Volume 10 • No 1 • June. 2022 • p-ISSN: 2410-9355 • e-ISSN: 2307-549X

# ARO

The Scientific Journal of Koya University

Wound Healing Properties and Structural Analysis of Four Geographical Areas' Natural Clays • Cement Percent Effect on the Shear and Interface Strength of Remolded Cement Treated Sand • Application of Experimental Design Methodology for Adsorption of Brilliant Blue onto Amberlite XAD-4/Agaricus campestris as a New Biocomposite Adsorbent • Detecting Deepfakes with Deep Learning and Gabor Filters • Suitability of the Carbonate Rocks of the Bekhme Formation Exposed in Shakrook Anticline, Iraqi Kurdistan region, for Cement Industry • Bioremediation Ability of the Local Isolate Enterobacter cloacae from Disposal Site • Network Transmission Flags Data Affinity-based Classification by K-Nearest Neighbor • Detection of SARS-CoV-2 Reinfections by Rapid Inexpensive Methods • Driver Drowsiness Detection Using Gray Wolf Optimizer Based on Face and Eye Tracking • Measuring the Voice Resemblance Extent of Identical (Monozygotic) Twins by Voiceprints Neutrosophic Domain • Identification DNA Methylation Change of ABCC8 Gene in Type 2 Diabetes Mellitus as Predictive Biomarkers • An Optimized SWCSP Technique for Feature Extraction in EEG-based BCI System • Investigating the Impact of Min-Max Data Normalization on the Regression Performance of K-Nearest Neighbor with Different Similarity Measurements • Effect of Static Magnetic Field on Bone Marrow Cellular Density • Extended-Spectrum β-lactamases and AmpC Production among Uropathogenic Isolates of Escherichia coli and Antibiogram Pattern • Role of Laser Produced Silver Nanoparticles in Reversing Antibiotic Resistance in Some Multidrug-Resistant Pathogenic Bacteria • Design, Modeling, and Characterization of Hot Electron Light Emission and Lasing in Semiconductor Heterostructure-VCSOA with Optical Gain up to 36dB • Detection of Sperm DNA Integrity and Some Immunological Aspects in Infertile Males • Synchro Software-Based Alternatives for Improving Traffic Operations at Signalized Intersections.

KOYA UNIVERSITY

ARO - DOI: 10.14500/2307-549X
Indexed by WoS-ESCI

**ARO-The Scientific Journal of Koya University**

The ARO ("Today" in Hewramí Kurdish), is an international scientific journal published by the Koya University with p-ISSN: 2410-9355, e-ISSN: 2307-549X and DOI: 10.14500/2307-549X. ARO is a journal of original scientific research, global news, and commentary. ARO Journal is an open access peer-reviewed journal that indexed by WoS-ESCI and publishes original research articles as well as review articles in areas of Science, Engineering and Technology. ARO Journal has no APC & ASC fees.





**ARO the Scientific Journal Office**

Koya University, University Park
Danielle Mitterrand Boulevard, Koya KOY45
Kurdistan Region - F.R. Iraq

**E-mail:** aro.journal@koyauniversity.org
**url:** aro.koyauniversity.org

June 2022

# ARO

## The Scientific Journal of Koya University

## Vol X, No 1(2022)

# Contents



DOI: 10.14500/2307-549X ARO p-ISSN: 2410-9355, e-ISSN: 2307-549X

# ARO Editorial Words

Dear readers,

ARO-the Scientific Journal of Koya University (KOU), is closing its 18th issue (Vol X, No 1, 2022). Our journal has had an exciting and yet dynamic season. ARO, an internationally renowned scientific journal, is publishing its 18th issue in the Kurdistan Region of Iraq (KRIQ). Notably, as of February 2016, ARO has been accepted for indexing in the Emerging Sources Citation Index (ESCI), a new edition of Web of Science™. The content in this index is being considered by WoS (Clarivate Analytics) for inclusion in the Science Citation Index Expanded™ (SCIE). ARO's individual articles are currently being listed by WoS (Clarivate Analytics) using the articles' unique DOI numbers, which is a historic accomplishment for our academic community. Aro is embarking on its ninth year of leading the quality of regional scientific publications with global impact. The editorial team has worked tirelessly to maintain the novel mission and ensure that ARO's future publications have greater impact and citations. It is exciting that ARO has been awarded the DOAJ Seal listing, which indicates that his work is of trusted high quality open access scientific work. ARO's life will be even more exciting in the coming new season, as WoS (Clarivate Analytics) will examine our journal for a full permanent listing.

Aro's mission remains to provide resources, support, and advice to researchers who are in the process of publishing their scientific papers, while also providing free public access to scientific research through open online access. This is a difficult task that we hope to complete in the coming years. As a result, in the sections that follow, we'd like to share and elaborate on the core elements that make up ARO. Finding dependable and skilled reviewers, on the other hand, remains a significant challenge for us. KOU is launching Adjunct Scholar Programs, which will allow non-resident scholars to affiliate with KOU and publish in ARO.

ARO was founded with the long-term goal of making science accessible to all researchers in Kurdistan and beyond, while also covering a wide range of scholarly disciplines. ARO is an open access, peer-reviewed journal that publishes original scientific research, global news, letters and commentary, and review articles in engineering, science and technology. You will find original research papers in a variety of fields in this issue.

The overwhelming response from researchers, academics, and professionals over the last nine years prompted us to form a larger Editorial Board to serve the greater number of submitted scientific manuscripts. It is clear, however, that having a committed and well-organized editorial board for the journal is only one side of the coin. The ability to attract submissions of high-quality research and scholarly work is the other. We thank everyone who put their faith in ARO and submitted their original research work for publication in Vol. X, No. 1 (2022) of the journal, as well as the 46 peer-reviewers from universities around the world who worked hard to review and enable this issue of ARO.

Your support and feedback are invited and appreciated.

Dilan M. Rostam
*Editor-in-Chief*

Mohammed H. Zangana
*Executive Publisher*

Salah I. Yahya
*Managing Editor*

Dilan M. Rostam, Salah I. Yahya, Basim M. Fadhil, Fahmi F. Muhammad, Wali M. Hamad, Jorge Correia, Fouad Mohammed, Jacek Binda, Nadhir Al-Ansari, Howri Mansurbeg, Tara F. Tahir and Yazen A. Khaleel.
*Executive Editorial Board*

DOI: 10.14500/2307-549X ARO p-ISSN: 2410-9355, e-ISSN: 2307-549X

# Wound Healing Properties and Structural Analysis of Four Geographical Areas' Natural Clays

Zahra A. Amin

Department of Pharmacognosy, College of Pharmacy, Hawler Medical University Erbil, Erbil 44001, Iraq

***Abstract*–Clays are fine particle materials that harden after drying. The difference in their structure is the key to their efficacy and their subsequent application. The current study aims to evaluate the wound healing property of four countries (C1:Iraq, C2:Turkey, C3:Azerbaijan and C4:Russia) clay samples by excision model using *Sprague dawley* rats also the chemical analysis of the samples was performed using X-ray diffraction (XRD) and X-ray Fluorescence (XRF) methods. Results revealed that the best wound healing activities were given by C1, C3, C4 and C2 respectively with healing percentages (76%, 71%, 62%, and 60%), respectively. XRD results revealed the presence of Calcium carbonate and Calcium-Magnesium carbonate in C1, Dolomite and Calcium-Magnesium carbonate in C2, Cobalt Tantalum Sulfide in C3, Finally Quartz and Silicon Oxide in C4. On the other hand, XRF analysis showed the appearance of different major and trace elements with different quantities in each clay type. We conclude that different countries clays enclose wound healing property with diverse ranges and this diversity is due to their chemical and mineral structures.**

***Index Terms*—Natural clay; wound healing; rats; X-ray diffraction; X-ray fluorescence.**

## I. Introduction

Worldwide many people are experiencing different types of skin wounds and the synthetic compounds are of less use day by day because they are environmental pollutants and take a long time circulating to the nature that is why there is an increase in the using of natural remedies for the treatment and healing of the wounds. In the developing countries, around 80% of their population are depending on the natural substances to treat their infections (Qureshi, Khatoon and Ahmed, 2015). The evolution and progress of wound therapies and advanced strategies with new techniques are observed over the years; however, skin wound treatments are categorized generally as "Regenerative" or "Conventional". Regenerative therapy aims to restore skin to its original function, reestablishing damaged cells and skin tissue without scarring while conventional therapy leads to the formation of scars (Tottoli, et al., 2020). Clay minerals healing efficacy were discovered many years ago and have been applied in Medicine for different purposes like spas, pharmaceutical formulations and aesthetic medicine. They are either orally administered for uses as laxatives, gastrointestinal protectors, anti-diarrhetics or as topical applications in cosmetics and dermatological protectors (Carretero, 2002) also clays were given to farm animals for the detoxification purposes and alleviation of gastrointestinal diseases. (Slamova, et al., 2011). Moreover, latest studies have documented the potential of clay minerals in the nanomedicine field regarding their beneficial effects on skin proliferation, cellular adhesion, and differentiation (Viseras, et al., 2019). In addition, the clay minerals were used to moisturize and clean the skin and to reduce acne, lipodystrophies and cellulite (Arab and Alshikh, 2012) (Williams and Haydel, 2010) investigated the antibacterial activity of natural clays and they found that the antioxidant state and the pH are the key of the reactions control and the chemistry of the bacterial cell wall. In addition, clays are proposed not to kill bacteria directly but may enclose soothing effects which are palliative (Williams, 2019). Other researchers proved that the clay material destroyed many bacterial strains, including Methicillin-resistant *Staphylococcus aureus*, *Escherichia coli*, *Pseudomonas aeruginosa*, and *Salmonella enterica* (Gaskell and Hamilton, 2014). Other pharmacological uses of clay include treatment of gastrointestinal diseases, applied topically to treat skin disorders, and have been taken orally to manage chronic or urgent diarrhea, and rheumatism. The mechanism of action was suggested to be due to their high porosity, large specific surface area, high adsorption and exchange capacities (Tang, et al., 2005). The chemical composition of natural clays includes silica, magnesium, aluminum, little iron substitutes and low quantities of sodium, potassium and calcium are existent as well. Depending on their ionic structure, these minerals can be classified into nine groups: pyrophyllite-talc, kaolin-serpentine, vermiculite, mica, chlorite, smectite, interstratified clay minerals (e.g., rectorite, tosudite, and corrensite), sepiolite-palygorskite, and allophane-imogolite (Wilson, 1994). These inorganic compositions of clays has been documented to improve and treat skin wounds through three different mechanisms, (1) physically by water vapor transmission and mechanical resistance, (2) chemically by hemostasis or adsorption of

ARO-The Scientific Journal of Koya University
Vol. X, No.1 (2022), Article ID: ARO.10889, 5 pages
DOI: 10.14500/aro.10889
Received: 08 October 2021; Accepted: 12 January 2022
Regular research paper: Published: 15 February 2022
Corresponding author's email: zahraa.alnajaar@hmu.edu.krd

http://dx.doi.org/10.14500/aro.10889

moisture and release of drugs, and (3) biologically by their antibacterial/antimicrobial effects and improving the healing process(García-Villén, et al., 2020). The aim of the present study was to compare the chemical composition of four clay samples obtained from different geographical areas and to evaluate the efficacy of the topical application of these clay samples in accelerating excision wound healing *in vivo* in experimental rat model.

## II. Materials and Methods

### *A. Clay Preparation and Analysis*

Four types of natural clays were collected from four different countries: Iraq (C1), Turkey (C2), Azerbaijan (C3), and Russia (C4), their different external views or appearances are shown in Fig. 1. The clays were grinded and prepared freshly every day by mixing with local mineral waters, which contain a unique balance of salts in a ratio of 2:1 water and clay, respectively. The mineral content of the clays were tested at Civil Engineering laboratory, Research Center, Koya University, to perform X-Ray Diffraction (XRD) technique type Panalytical Empyrean with CuKα radiation. The elemental composition and their energies were determined using energy dispersive X-ray Fluorescence (EDXRF).

### *B. In Vivo Wound Healing (Excision Model)*

Forty male Wistar rats (weighing 250–300 g) were randomly divided into 5 groups. Round seal was used to excise a uniform area of 2 cm in diameter from the nape of dorsal neck of all the rats. Then different treatments were applied as described in following:

Group 1 (Control) rats were topically applied with MEBO cream twice a day

Group 2 rats were topically dressed with 2 mL of C1 sample twice a day.

Group3 rats were topically dressed with 2 mL of C2 sample twice a day.

Group 4 rats were topically dressed with 2 mL of C3 sample twice a day.

Group 5 rats were topically dressed with 2 mL of C4 sample twice a day.

The wound area was noted by measuring the contraction area. Manually, the wound areas were traced and calculated in square millimeters. The wound closure area and closure percentage rate were measured at days 0, 5, and 10 of the experiment. The wound area was measured immediately by placing a transparent tracing paper over the wound and tracing it out. The tracing paper was placed on 1 mm 2 graph sheet and traced out. The squares were counted and the area recorded. Then, the percentage of wound closure was calculated following the formula: Wound closure (%) $=1-(Ad\ A0) * 100$, (1) where $A0$ is wound area at day zero and $Ad$ is wound area on corresponding day (Amin, et al., 2015).

### *C. Statistical Analysis*

All values are reported as mean ± SEM. and the statistical significance of differences among groups was assessed using one-way ANOVA. A value of (0.05) was considered significant.

## III. Results

Table 1 shows the effects of different treatments on the percentage of wound healing at different days after surgery, at day 0 no significant difference was found between groups that shows the accuracy of the work whereas significant results were found on day 5 of the treatment in which C1 and C3 clays showed wound closure percentage of (48% and 45%), respectively, which are comparable to MEBO group (43%). Moreover, remarkable results were observed at day 10$^{th}$ of the surgery in which the wound closure percentage were (76%, 60%, 71%, and 62%) for C1, C2, C3, and C4 groups, respectively. The C1 and C3 group's results were better than the MEBO control group (64%). These results confirmed macroscopically (as shown in Fig. 2), as seen groups C1


Fig. 1. The external view of the clay samples; C1 clay from Iraq, C2 clay from Turkey, C3 clay from Azerbaijan and C4 clay from Russia.

Table I
Wound Healing Measurements of Experimental Rats after Exposure to Different Treatments.

| Groups | Day 0 | Day 5 | | Day 10 | |
|---|---|---|---|---|---|
| | Wound area | Wound area | Wound closure % | Wound area | Wound closure % |
| MEBO | 332±2.4 | 190±2.1* | 43 | 120±2.1* | 64 |
| C1 | 339±0.9 | 175±1.7* | 48 | 81±1.6* | 76 |
| C2 | 340±0.7 | 231±1.4 | 32 | 137±1.5* | 60 |
| C3 | 342±2.1 | 187±1.1* | 45 | 100±1.3* | 71 |
| C4 | 338±1.4 | 225±3.1 | 33 | 130±3.3* | 62 |

Data expressed as Mean±SEM, *P* value considered significant when is <0.05

and C3 showed a significant re-epithelialization with sign of dermal healing as compared to MEBO group.

XRD results showed that the main peaks were related to magnesium calcite (chemical formula $C_1Ca_{0.94}Mg_{0.06}O_3$) and magnesium calcium carbonate (chemical formula $Mg_{0.06}Ca_{0.94}(CO_3)$) in C1 sample (density = 2.75 g/cm$^3$) as shown in Fig. 3a. Whereas, the peaks of C2 sample (density = 2.88 g/cm$^3$) were related to Dolomite (chemical formula $C_2Ca_1Mg_1O_6$) and Calcium Magnesium Carbonate (chemical formula $CaMg(CO_3)$) Fig. 3b. In addition to Cobalt Tantalum Sulfide (chemical formula $CO_2S_6Ta_9$) in C3 (density = 10.77 g/cm$^3$), finally Quartz (chemical formula

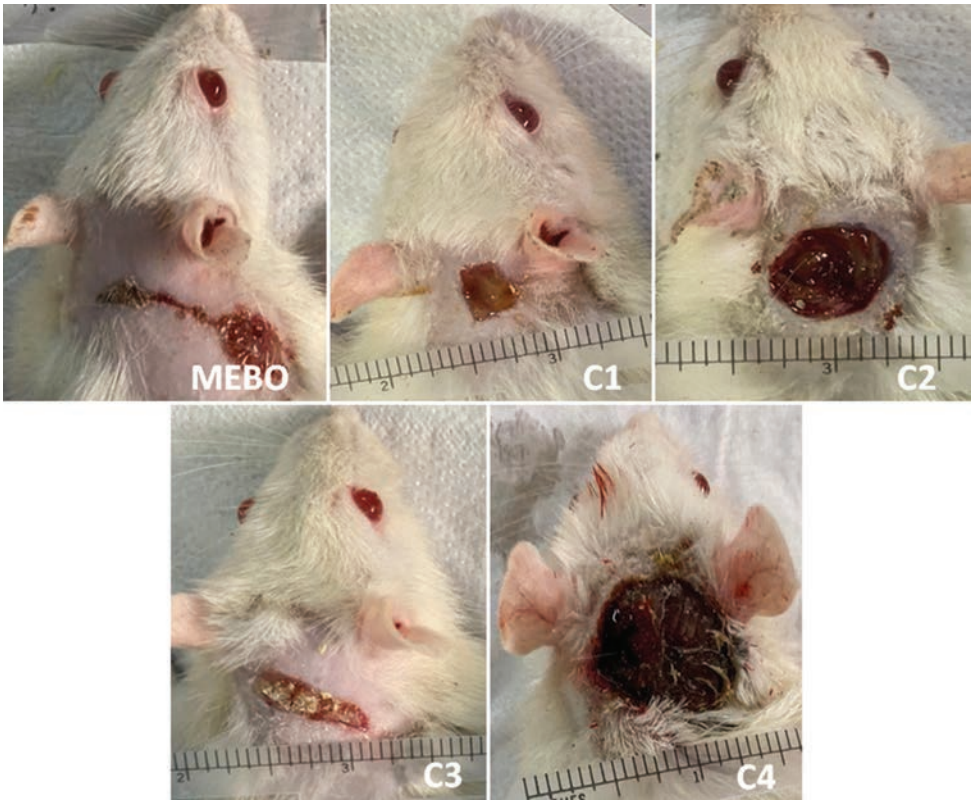


Fig. 2. Macroscopic appearance of excision wound healing area on rat skin at day 10 after surgery within different groups of treatments.

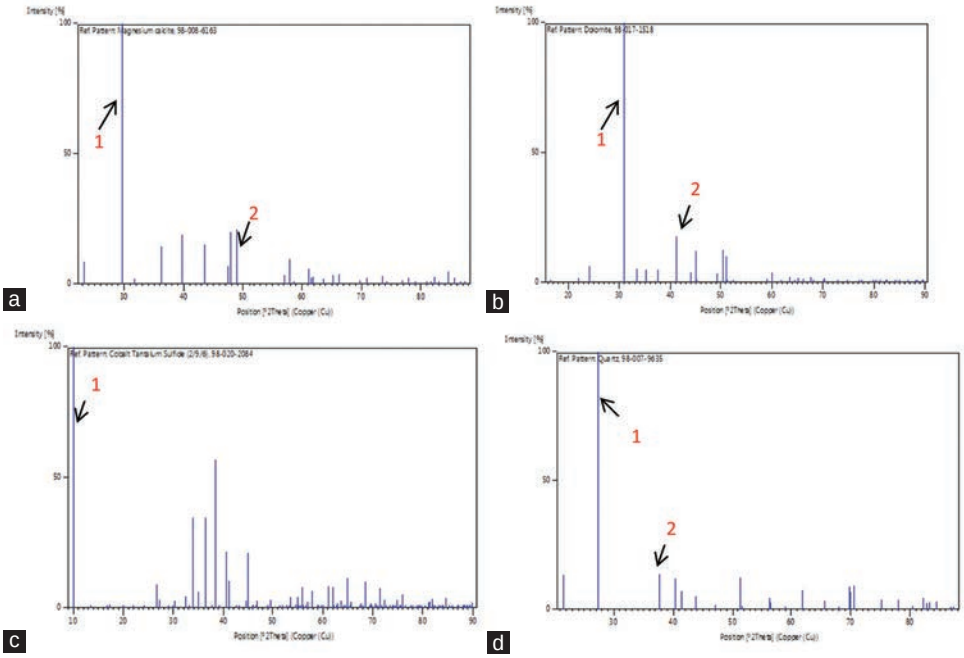


Fig. 3. The X-Ray Diffraction analysis of the clay samples. (a) C1 sample: peak 1 Magnesium Calcite peak 2 Magnesium Calcium carbonate, (b) C1 sample: peak 1 Dolomite peak 2 Calcium Magnesium Carbonate, (c) C3 sample: peak 1 Cobalt Tantalum Sulfide peak 2 Silica Oxide (d) C4 sample: peak 1 Quartz.

$O_2Si_1$), and Silicon Oxide (chemical formula $SiO_2$) in C4 sample (density = 2.75 g/cm$^3$), respectively.

On the other hand, the X-ray Fluorescence (XRF) analysis of the clay samples showed that the Silica or Quartz (SiO2), Calcium Oxide (CaO), Aluminum Oxide (Al2O3) and the Iron III or Ferric Oxide (Fe2O3) are the main elements of all types of clays with the appearance of few other trace elements in a lower quantities (Table 2).

## IV. Discussion

Experimental animals wound healing models have been studied widely in the last years. Nowadays, 80% of population depend on natural remedies to maintain wound care management (Qureshi, Khatoon and Ahmed, 2015). Indeed, the wound healing property of clays was well defined (Ferrell, 2008) *in vitro* and *in vivo* studies showed the therapeutic activities of clays (Ghadiri, Chrzanowski and Rohanizadeh, 2014b, Marinelli, et al., 2021). The inorganic contents of clay minerals, cations, zeolites, etc., were documented to have the ability to enhance cell proliferation, adhesion and cellular differentiation and uptake (García-Villén, et al., 2020). The results of the present study revealed the effective activity of four types of clays collected from different countries to the skin wounds induced *in vivo* on *Sprague Dawley* rats. The healing process characterized by declined wound area measurements and greater wound size reduction percentage as shown in Table 1 and Fig. 2. Whereas, it is obvious from Table 2 and Fig. 3 that all types of clays enclose different quantities of materials as performed by XRD and XRF analysis. Clay collected from Iraq (C1) and the one collected from Azerbaijan (C3) showed the best two results in healing rat's skin wounds (76% and 71%), respectively. The analysis of C1 clay showed the presence of Magnesium calcite and Magnesium calcium carbonate (Fig. 3a) whereas Cobalt Tantalum Sulfide was seen in C3 sample (Fig. 3c). Whereas elements analysis by XRF showed the presence of Calcium and Ferric Oxides C1 sample and Aluminum Oxide in C3 sample respectively. Other studies reported the same chemical ions and elements in clays (Ghadiri, Chrzanowski and Rohanizadeh, 2014c, Morrison, et al., 2014, Maniatis, et al., 1983) Williams et al. suggested that the biological effects of clays are due to their large surface area that buffers the oxidation state and the water pH also controlling the solubility of clay derived materials (Williams, et al., 2008).

Table II
The X-Ray Fluorescence Analysis of the Clays samples.

| | Elements | Mass % | | | |
|---|---|---|---|---|---|
| | | C1 | C2 | C3 | C4 |
| 1 | $SiO_2$ | 42.9 | 47.6 | 63.3 | 98.5 |
| 2 | CaO | 33.8 | 15.6 | 3.96 | 0.226 |
| 3 | $Al_2O_3$ | 11.8 | 12 | 15.5 | 0.874 |
| 4 | $Fe_2O_3$ | 5.19 | 4.62 | 4.29 | 0.123 |
| 5 | MgO | 4.22 | 16.2 | 3.9 | … |
| 6 | $K_2O$ | 1 | 2.96 | 1 | 0.0365 |
| 7 | $TiO_2$ | 0.709 | 0.512 | 0.804 | 0.0065 |
| 8 | MnO | 0.105 | 0.0837 | 0.0817 | 0.005 |
| 9 | $Cr_2O_3$ | 0.0993 | 0.0086 | … | 0.0028 |
| 10 | $SO_3$ | 0.0545 | 0.0598 | 1.85 | 0.0222 |
| 11 | $Co_2O_3$ | 0.0281 | 0.0172 | 0.0162 | 0.0011 |
| 12 | SrO | 0.0276 | 0.122 | 0.059 | 0.0006 |
| 13 | NiO | 0.0235 | 0.0083 | 0.0054 | … |
| 14 | BaO | 0.018 | 0.028 | 0.637 | … |
| 15 | $V_2O_5$ | 0.0165 | 0.0199 | 0.0556 | … |
| 16 | $SnO_2$ | 0.0101 | 0.0113 | 0.0091 | 0.0065 |
| 17 | ZnO | 0.0096 | 0.0092 | 0.0096 | 0.0006 |
| 18 | CuO | 0.0066 | 0.005 | 0.0071 | 0.0011 |
| 19 | $Rb_2O$ | 0.0048 | 0.0117 | 0.0055 | 0.0004 |
| 20 | $Y_2O_3$ | 0.0027 | 0.0023 | 0.0032 | … |
| 21 | $WO_3$ | 0.0016 | … | … | … |
| 22 | $Ga_2O_3$ | 0.0016 | 0.0012 | 0.0011 | … |
| 23 | $As_2O_3$ | 0.0015 | 0.0033 | … | 0.0001 |
| 24 | PbO | 0.0012 | 0.0024 | 0.145 | 0.0005 |
| 25 | $U_3O_8$ | … | 0.001 | … | … |
| 26 | $ThO_2$ | … | 0.0016 | 0.0021 | … |
| 27 | $HfO_2$ | … | 0.0019 | … | … |
| 28 | $Nb_2O_5$ | … | 0.0023 | … | … |
| 29 | $Ta_2O_5$ | … | 0.0028 | 0.0017 | … |
| 30 | $Cr_2O_3$ | … | 0.0086 | 0.0124 | 0.0028 |
| 31 | Na | … | … | 3.3 | … |
| 32 | Cl | … | … | 0.708 | 0.0143 |
| 33 | $P_2O_2$ | … | … | 0.251 | … |
| 34 | $Ir_2O_3$ | … | … | 0.0018 | … |
| 35 | $PtO_2$ | … | … | 0.001 | … |
| 36 | $Au_2O$ | … | … | 0.0005 | … |
| 37 | $TeO_2$ | … | … | … | 0.0008 |
| 38 | $GeO_2$ | … | … | … | 0.0004 |

Clay minerals were reported to establish interactions with biomolecules and permitting new possibilities for delivery of growth factors, matrix proteins and genes in tissue regeneration (Sandri, et al., 2016). The mechanism of wound healing property of the natural clays was documented to be due to regulation of macrophages and recruitment of monocytes into wounds. Moreover, in the healing wounds keratinocytes migrate through the wound area to maintain the epithelial integrity (Incledion, et al., 2021). In another study, the healing process of a synthetic clay has been studied when applied to wounds and the healing process was proposed to be through fibroblast cell proliferation (Ghadiri, et al., 2014a). Furthermore, clay mineral was investigated to promote collagen formation and angiogenesis on skin wounds (García-Villén, et al., 2020)

## V. Conclusion

This research has demonstrated the potential of different countries clays as wound healing agents. The difference in their activities was supposed to be due to their different structures; however, more studies are recommended to be performed to reveal the exact mechanism of their action.

## References

Arab, S. and Alshikh, A., 2012. The use of clay minerals of the dead sea as drugs. *Clay Minerals*, 5, pp.112-115.

Carretero, M.I., 2002. Clay minerals and their beneficial effects upon human health. A review. *Applied Clay Science*, 21, pp.155-163.

Ferrell, R., 2008. Medicinal clay and spiritual healing. *Clays and Clay Minerals,* 56, pp.751-760.

García-Villén, F., Souza, I., De Melo Barbosa, R., Borrego-Sánchez, A., Sánchez-Espejo, R., Ojeda-Riascos, S. and Iborra, C.V., 2020. Natural inorganic ingredients in wound healing. *Current Pharmaceutical Design,* 26, pp.621-641.

Gaskell, E.E. and Hamilton, A.R., 2014. Antimicrobial clay-based materials for wound care. *Future Medicinal Chemistry,* 6, pp.641-655.

Ghadiri, M., Chrzanowski, W., Lee, W. and Rohanizadeh, R., 2014a. Layered silicate clay functionalized with amino acids: Wound healing application. *RSC Advances,* 4, pp.35332-35343.

Ghadiri, M., Chrzanowski, W. and Rohanizadeh, R., 2014b. Antibiotic eluting clay mineral (Laponite®) for wound healing application: An *in vitro* study. *Journal of Materials Science: Materials in Medicine,* 25, pp.2513-2526.

Ghadiri, M., Chrzanowski, W. and Rohanizadeh, R., 2014c. Antibiotic eluting clay mineral (Laponite®) for wound healing application: An *in vitro* study. *Journal of Materials Science: Materials in Medicine,* 25, pp.2513-2526.

Incledion, A., Boseley, M., Moses, R., Moseley, R., Hill, K., Thomas, D., Adams, R., Jones, T. and Bérubé, K., 2021. A new look at the purported health benefits of commercial and natural clays. *Biomolecules,* 11, p.58.

Maniatis, Y., Simopoulos, A., Kostikas, A. and Perdikatsis, V., 1983. Effect of reducing atmosphere on minerals and iron oxides developed in fired clays: The role of Ca. *Journal of the American Ceramic Society,* 66, pp.773-781.

Marinelli, L., Cacciatore, I., Eusepi, P., Dimmito, M.P., Di Rienzo, A., Reale, M., Costantini, E., Borrego-Sánchez, A., García-Villén, F. and Viseras, C., 2021. *In vitro* wound-healing properties of water-soluble terpenoids loaded on halloysite clay. *Pharmaceutics,* 13, p.1117.

Morrison, K.D., Underwood, J.C., Metge, D.W., Eberl, D.D. and Williams, L.B., 2014. Mineralogical variables that control the antibacterial effectiveness of a natural clay deposit. *Environmental Geochemistry and Health,* 36, pp.613-631.

Qureshi, M., Khatoon, F. and Ahmed, S., 2015. An overview on wounds, their issue s and natural remedies for wound healing. *Biochemistry and Physiology,* 4, p.165.

Sandri, G., Bonferoni, M., Rossi, S., Ferrari, F., Aguzzi, C., Viseras, C. and Caramella, C., 2016. Clay minerals for tissue regeneration, repair, and engineering. In: *Wound Healing Biomaterials.* Elsevier, Amsterdam, Netherlands.

Slamova, R., Trckova, M., Vondruskova, H., Zraly, Z. and Pavlik, I., 2011. Clay minerals in animal nutrition. *Applied Clay Science,* 51, pp.395-398.

Tang, Q., Shen, S., Liang, J., Liang, G., Ou, X., Wang, L. and Ding, Y., 2005. Pharmacological effects and pharmaceutical application of clay minerals. *Journal-Chinese Ceramic Society,* 33, p.1036.

Tottoli, E., Dorati, R., Genta, I., Chiesa, E., Pisani, S. and Conti, B., 2020. Skin wound healing process and new emerging technologies for skin wound care and regeneration. *Pharmaceutics,* 12, p.735.

Viseras, C., Carazo, E., Borrego Sánchez, A., García-Villén, F., Sánchez Espejo, R., Cerezo, P. and Aguzzi, C., 2019. *Clay Minerals in Skin Drug Delivery*. Springer, Berlin, Germany.

Williams, L., 2019. Natural antibacterial clays: Historical uses and modern advances. *Clays and Clay Minerals,* 67, pp.7-24.

Williams, L.B. and Haydel, S.E., 2010. Evaluation of the medicinal use of clay minerals as antibacterial agents. *International Geology Review,* 52, pp.745-770.

Williams, L.B., Haydel, S.E., Giese, R.F. Jr. and Eberl, D.D., 2008. Chemical and mineralogical characteristics of French green clays used for healing. *Clays and Clay Minerals,* 56, pp.437.

Wilson, M.J., 1994. *Clay Mineralogy: Spectroscopic and Chemical Determinative Methods.* Chapman and Hall, London.

http://dx.doi.org/10.14500/aro.10805

# Cement Percent Effect on the Shear and Interface Strength of Remolded Cement Treated Sand

Zahraa N. Rashied

Department of Geotechnical Engineering, Faculty of Engineering, Koya University, Koya KOY45, Kurdistan Region - F.R. Iraq

***Abstract*—This research aims to simulate the behavior of remolded cement treated poorly graded sand in term of shear and interface strength using the direct shear test. Different percentages of cement up to 15% by weight are added to the soil samples. Compacted cement treated soil samples are prepared at the optimum moisture content and left for 28 days in the humidity room then distributed to use them for the remolding samples preparation. The shear strength parameters for both cases soil to soil interface and concrete to soil interface are predicted, where the results show that the interface strength parameters are higher than the shear strength parameters of the remolded soil samples. The increase in cement percent increases the cohesion (C) of the treated soil, whereas the interface cohesion ($C_{int.}$) has a maximum value at 10% of added cement, and the maximum percent between cohesion ($C_{int.}$) and soil cohesion (C) is of 76.2% at 0% added cement. Moreover, the results show an increase in the interface angle of friction (δ) and a decrease in the angle of friction (ϕ) as the percent of cement increases. The maximum percent between interface angle (δ) and angle of friction (ϕ) is 63.5% at 15% of the added cement. The hardened cement in the remolded case adheres to sand grains and works as soil grains with different sizes that lead to changes in the shear properties of the soil.**

***Index Terms*—Cement treated sand, Interface strength, Remolded soil, Shear strength.**

## I. Introduction

Placement of materials having different properties adjacent to each other led to generating the interface zone which can make it the weakest point of the overall system in terms of shear strength compared to that of neighboring materials. Soil structure interfaces are commonly controlling the overall design and stability of civil engineering structures.

Soils consist of particles with different sizes and properties which make them easy to undergo large deformation when being loaded (both compression and shear). Structural elements that made from concrete or steel can be treated as solid continuum materials compared with soils. The interfaces between these two types of materials are of unique properties. Many researchers were interested in finding the relationship between the soil angle of internal friction (ϕ) and the interface friction angle (δ).

Potyondy (1961) and Acar, et al. (1982) studied the effect of soil density on the interface angle of friction using direct shear apparatus with the sand on the top of concrete pad; they concluded that the interface angle increased as the density increased and the interface angle equal to the angle of internal friction. Uesugi, et al. (1990) used simple shear with the sand on top of the test material, their finding was same as that observed by Potyondy (1961) and Acar, et al. (1982). Sliding the material over the sand using direct shear mode was conducted by Broms (1963) and Noorany (1985) and they stated that the influence of sand density on the interface angle of friction is negligible. Recording the particle displacement at the interface between steel and sand using speed camera observed by Hu and Pu (2001), they stated that the shear failure is accompanied by strain softening and strong normal dilatancy. Feng (2012) used the multi-functional 3-D shear test equipment developed by Hou, et al. (2008) to observe the effect of different types of coarse-grained soils, structural plates and boundary conditions and loading conditions on the mechanism of interface between soil and structure. Their results (Hou, et al., 2008 and Feng, 2012) showed deeply constitutive interface laws between granular soil and structure. There were limited studies that discussed the effect of remolding on the behavior of cement treated soils, most of them were related to the effect of remolding for fine grain soils (Watabe, et al., 2016 and Suganya and Sivapullaiah, 2020). The present study is the first of its kind that discusses the effect of remolding on the strength and interface strength (soil-concrete) of cement treated granular soils. The effect of cement as treating material by dry weight of cohesion less soil up to 15% on the interface friction angle and cohesion between concrete and the compacted remolded cement treated soil will be discussed in this study by comparing them with the angle of internal friction and cohesion of the remolded cement treated samples. It is believed that the result observed in this study will be useful when the remolding of cement treated soils is required in some sits previously treated by cement.

## II. Materials and Testing Program

For the purpose of predicting the effect of remolding on the behavior of cement treated granular soil in term of cohesion

ARO-The Scientific Journal of Koya University
Vol. X, No.1 (2022), Article ID: ARO.10805, 4 pages
DOI: 10.14500/aro.10805
Received: 24 March 2021; Accepted: 29 January 2020
Regular research paper: Published: 19 February 2022
Corresponding author's e-mail: zahraa.noori@koyauniversity.org

and internal angle of friction (soil - soil) and interface cohesion and angle of friction between remolded cement treated soil and concrete (soil – concrete), granular soil samples were predicted from Drbandikhan, Sulaymaniyah (Kurdistan Religion-Iraq) used for this purpose, whereas the cement that used as improvement agent was ordinary Portland cement.

The soil mechanic laboratory of Koya University was used to conduct the material properties and shear tests, according to ASTM (American Society for Testing and Materials, 2020). Grain size analysis of the tested soil was carried out according to ASTM D 422, 2020, the grain size distribution for the soil used in this study is as shown in Fig. 1. The grain size analysis show that the percent passing from sieve No. 200 was about 1.9% whereas the percent of sand was of 75.4 %, the coefficients of uniformity and curvature were 3.3 and 0.7, respectively, so that soil classified as poorly graded sand (SP) according to the Unified Soil Classification System (USCS) (ASTM Test Designation D-2487). Specific gravity test was carried out on virgin soil according to ASTM D 854-00; the test result reflected that the specific gravity for the tested soil was 2.6. Compaction tests were confirmed according to ASTM D 698, 2020. The maximum dry density and optimum moisture content represent important parameters to preparing the samples for the direct shear test. Fig. 2 shows the variation of water content with dry density; the results showed that the maximum dry density was 1.71 kN/m$^2$ whereas the optimum moisture content was 14%.

Compacted soil samples at different cement content (0, 5, 10, and 15%) were prepared at optimum moisture continent and left for 28 day in the humidity room. After the 28 days, the samples disturbed to make them suitable for preparing remolded samples. Shear strength parameters of the virgin soil and also of all the soil mixed with different cement content were determined by direct shear tests on remolded samples obtained from compaction at optimum moisture content based on ASTM D 3080, 2020. The test is run several times for vertical-confining stresses of 70 kN/m$^2$, 138 kN/m$^2$, and 206 kN/m$^2$.

To prepare compacted soil samples for direct shear test purpose, the remolded soil passed from sieve No.16. Some soil placed in the mold and compacted in three equal layers. The number of drops of the plastic rammer that used to compact the soil was 25 drop per layer. The drops were applied at a uniform rate not exceeding around 1.5 s per drop, and the rammer provided uniform coverage of the specimen surface so that sample density must be represent the max density achieved from the standard compaction test.

For evaluating the shear strength parameters in case of sand-concrete interface, concrete interface element with dimension of (6×6×1) cm was prepared for this purpose. The mix proportions were (1 cement:3 aggregate) and the water – cement ratio (w/c) was 0.4. Direct shear test made by sliding the concrete element over the sand.

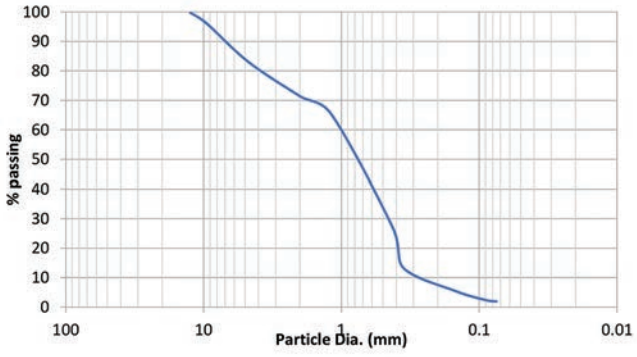


Fig. 1. Grain size analysis of the tested soil (0% of cement).

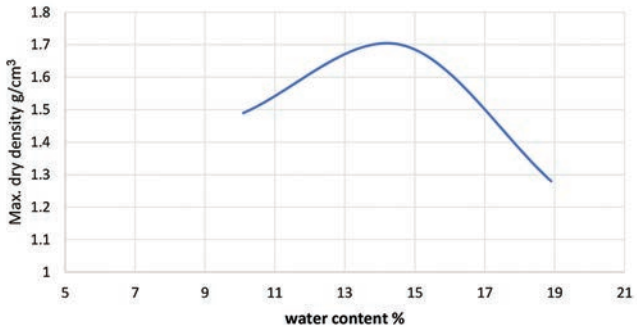


Fig. 2. Variation of maximum dry density with water content (standard compaction test).

## III. Results

A direct shear device used to determine the shear strength parameter of treated remolded compacted soil with different

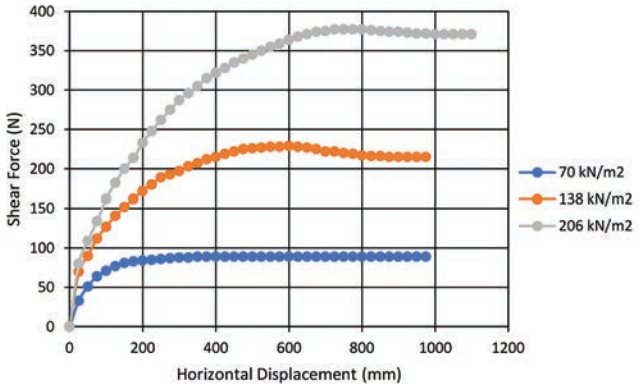


Fig. 3. Variation of shear force with horizontal displacement (10% of Cement).

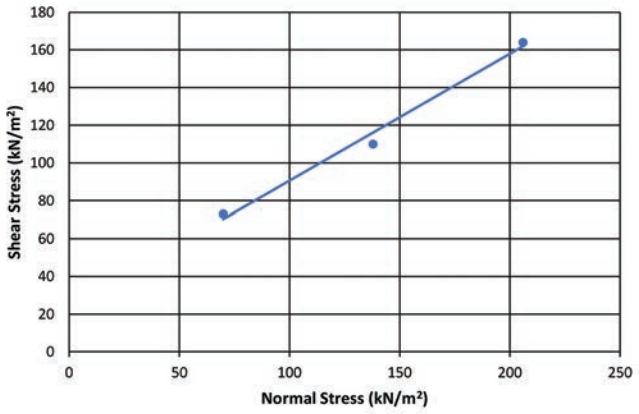


Fig. 4. Evaluation of angle of friction and cohesion of soil (10% cement).

http://dx.doi.org/10.14500/aro.10805

Table I
Results summary

| % of cement | Cohesion (C) ($KN/m^2$) | Friction angle (φ) (degree) | Interface cohesion ($C_{int.}$) ($kNlm^2$) | interface friction angle (δ) (degree) | Friction* (%) | Cohesion** (%) |
|---|---|---|---|---|---|---|
| 0 | 10.48 | 37.21 | 18.47 | 40 | 7.5 | 76.2 |
| 5 | 18.21 | 34.83 | 21.27 | 36.88 | 5.9 | 16.8 |
| 10 | 23.31 | 33.94 | 36.26 | 39.85 | 17.4 | 55.5 |
| 15 | 24.82 | 30.1 | 29.72 | 49.2 | 63.5 | 19.7 |

*Friction (%) = (δ-φ)/φ, **Cohesion (%) = ($C_{int.}$-C)/C

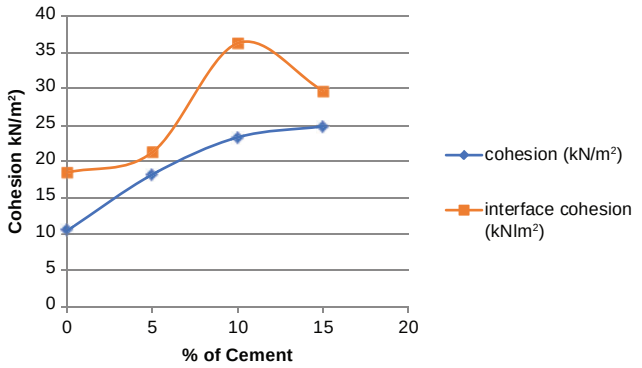


Fig. 5. Variation of the soil cohesion and interface cohesion with cement percent.

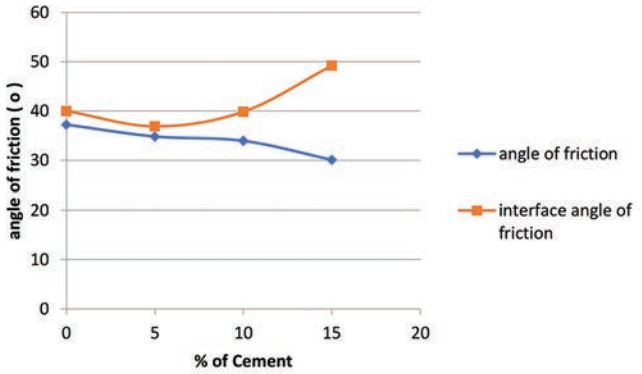


Fig. 6. Variation of the friction angle and interface friction angle with cement percent.

percent of cement up to 15%. Low strain rate of 0.01 mm/min were used to prevent rapid failure of the samples and as a result the observed data can simulate the exact behavior. The direct shear test was running three times for each percent to conform the observed results. The angle of friction and cohesion for both cases soil to soil interface and concrete to soil interface were predicted to find the ratio between the shear strength parameters at the same cement contamination percent for both cases. From the results of the shear stress versus the horizontal displacement, the maximum shear stress is obtained for a specific vertical confining stress. After the test is run several times for various vertical-confining stresses (70 $kN/m^2$, 138 $kN/m^2$, and 206 $kN/m^2$), the angle of friction and cohesion were obtained. Fig. 3 shows that the variation of shear force with horizontal displacement for 10% of cement soil sample as example whereas a plot of the maximum shear stresses versus the vertical (normal) confining stresses for 10% of cement shown if Fig. 4. Same procedure repeated for all samples treated by cement up to 15% for both cases (soil – soil) and (concrete – soil) interface. The summary of the results was as concluded in Table I.

As a conclusion from the predicated results of the direct shear test of the treated remolded poorly graded sand according to adding of different percent of cement up to 15%, Fig. 5 shows the variation of soil cohesion (C) and interface cohesion ($C_{int.}$) verse the increase in the percent of cement, the results showed that as the percent of cement increase the cohesion of soil increase, whereas the interface cohesion tends to increase then decrease its value beyond 10% of cement contaminations, the maximum percent cohesion percent was 76.2% according to 0% contamination as shown in Table I. Whereas Fig. 6 show the variation of the angle of friction (ϕ) and interface friction angle (δ) of the soil with cement percent, the results showed that as the percent of cement increase the angle of friction decrease, whereas the interface angle of friction increase, the maximum percent between interface angle of friction and angle of friction was 63.5%. As a conclusion interface cohesion ($C_{int.}$) and internal angle of friction (δ) are more than cohesion (C) and angles of friction (ϕ) of the untreated and remolded treated soil. It is believed that the cement in the remolded case adhered to sand particles and worked as soil grains with different sizes and as a result, the properties of the remolded soil changed as measured in term of cohesion and angle of friction.

## IV. Conclusion

The predicated results from the direct shear test of the untreated and treated remolded poorly graded sand according to adding of different percent of cement up to 15% reflect the following conclusions:

1. The results show that the interface cohesion ($C_{int.}$) and interface friction angle (δ) are more than cohesion (C) and angles of friction (ϕ) of the untreated and remolded treated soil whereas most of the previous studies concluded that interface friction angle and angles of friction are equal (δ = ϕ).
2. The increase in cement percent led to increase in the cohesion of soil (C), whereas the interface cohesion ($C_{int.}$) tends to increase then decrease its value beyond 10% of cement contaminations, the maximum percent between interface cohesion and soil cohesion was 76.2% according to 0% cement contamination.
3. The results also show that as the percent of cement increase the angle of friction decrease, whereas the interface angle

of friction increase, and the maximum percent between interface angle of friction and angle of friction was 63.5% at 15% of cement contamination.

4. It is believed that the cement in the remolded case adhered to sand particles and worked as soil grains with different sizes and as a result the properties of the soil changed as measured in term of cohesion and angle of friction.

## References


Acar, Y.B., Durgunoglu, H.T. and Tumay, M.T., 1982. Interface properties of sand. *Journal of Geotechnics*, 108, pp.648-654.

*ASTM, 2020. Annual Book of American Standards for Testing and Materials, Part 8.* Vol. 4. ASTM, United States.

*Braja, M.D. and Sobhan, K., 2014.In: Shortt CM, editor. Principles of Geotechnical Engineering.* 8th ed. Christopher M. Shortt.

Broms, B.B., 1963. Discussion on bearing capacity of piles in cohesionless soils. *Journal of the Soil Mechanics Division of the ASCE*, 89, pp.125-126.

Feng, D.K., 2012. *Three-Dimensional Constitutive Laws, Mechanism and Model of Gravel-Structure Interfaces, PhD Thesis, Tsinghua University, Beijing*.

Hou, W.J., 2008. *Research on monotonic and cyclic behavior and constitutive model of three-dimensional soil–structure interface, PhD thesis, Tsinghua University, Beijing*.

Hu, L.M. and Pu, J.L., 2001. Experimental study on mechanical characteristics of soil-structure interface. *Chinese Journal of Geotechnical Engineering*, 23, pp.431-435.

Hu, L.M. and Pu, J.L., 2003. Application of damage model for soil-structure interface. *Computers and Geotechnics*, 30, pp.165-183.

Noorany, I., 1985. *Side Friction of Piles in Calcareous Sands, Proceedings of the 11th International Conference of Soil Mechanics and Foundation Engineering, Cambridge, USA*, pp.12-16.

Potyondy, J.G., 1961. Skin friction between various soils and construction materials. *Geotechnique*, 11, pp.831-853.

Suganya, K. and Sivapullaiah, P.V., 2020. Compressibility of remolded and cement-treated Kuttanad soil. *Soils and Foundations*, 60, pp.697-704.

Uesugi, M., Kishida, H. and Uchikawa, Y., 1990. Friction between dry sand and concrete under monotonic and repeated loading. *Soils and Founds*, 30, pp.115-128.

Watabe, Y., Kaneko, T. and Wantanabe, Y., 2016. Cement mix proportion for treated soils recycled from a cement treated soil. *Japanese Geotechnical Society Special Publication*, 4, pp.168-172.

 http://dx.doi.org/10.14500/aro.10903

# Application of Experimental Design Methodology for Adsorption of Brilliant Blue onto Amberlite XAD-4/*Agaricus campestris* as a New Biocomposite Adsorbent

Ahmed A. Ahmed[1], Vahap Yönten[2]

[1]Department of Chemical Engineering, Faculty of Engineering, Koya University, Koya KOY45, Iraq

[2]Department of Chemical Engineering, Van Yuzuncu Yil University, 65080 Van, Turkey

***Abstract*–This research presents a new biocomposite adsorbents using response surface methodology (RSM) to find the best conditions for highest adsorption of Brilliant Blue G250 (BBG) from aqueous solution by Amberlite XAD-4/*Agaricus campestris*. The most effective parameters are determined by Plackett–Burman design (PBD) with specific ranges initial dye concentration (5–150 mg.L$^{-1}$), temperature (20–50°C), contact time (5–100 min), pH (3–11), shaking speed (150–300 rpm), sample volume (5–75 mL), and adsorbent dosage (0.05–0.6 g). Then, in the second step, the optimum condition of effective factors is predicted using steepest ascent design. Finally, optimal medium conditions of effective parameters with central composite design are located. According to RSM, the best adsorbent amount, contact time, initial dye concentration, and sample volume for maximum removal% of BBG (96.72%) are 0.38 g, 60.78 min, 107.13 mg.L$^{-1}$, and 28.6 mL, respectively. The adsorption of brilliant blue is approved by scanning electron microscopy. Under optimum conditions, it is concluded that XAD-4/*A. campestris* biocomposite is a suitable adsorbent for removing BBG from aqueous solution.**

***Index Terms*—Adsorption; Agaricus campestris; brilliant blue; biocomposite material; optimization.**

## I. Introduction

Water is essential to almost all life forms on the planet, and it is thought that life began in water. Although water covers more than 70% of the earth's surface, the majority of it is unfit for human consumption, and only a limited amount of potable water is available. The widespread use of chemicals for a variety of purposes in daily life, combined with increasing industrialization, has resulted in the unintentional contamination of our natural resources through the release of a variety of organic and inorganic pollutants into the water system (Mallampati, 2013).

Among the various pollutants found in industrial wastewaters, dye is regarded as a significant esthetic factor and is classified as a visible pollutant. Dyes are generally applied to color the products in the paper, food, textile, cosmetics, leather, and plastic industries. They are typically synthetic in origin and have complex aromatic molecular structures, making them hard to biodegrade and more stable (Aljebori and Alshirifi, 2012).

Many different types of adsorbents are used to remove dyes, but nowadays researchers are looking for the cheapest and most effective materials. Composite materials are one of the selected materials for adsorption because of the cost and high percent of removal dyes. They are made up of two materials that have distinct physical and chemical properties (Elhajjar, Valeria and Anastasia, 2013; Fazeli, Florez and Simão, 2019).

To remove dyes from wastewater, a variety of treatment methods have been used, including physical, biological, and chemical methods. One of the most efficient and cost-effective process is adsorption for dye removal from textile wastewater among physicochemical methods. In the literature, a number of natural adsorbents for dye removal have been reported (Beyene, 2014).

Empirical or statistical methods could be used to optimize the process. The empirical method takes time and does not always result in a successful optimization. Response surface methodology (RSM) is a statistics-based procedure and a useful tool for studying the interactions between two or more independent parameters (Ahmad and Alrozi, 2010; Öztürk and Şahan, 2015; Yönten and Aktaş, 2014).

The present study was intended to discover a new low cost biocomposite adsorbent material (XAD-4+*Agaricus campestris*) and its impact on removing Brilliant Blue G250 (BBG) dye from aqueous solutions. In batch adsorption techniques, the effects of pH, temperature, contact time, shaking speed, adsorbent dose, sample volume, and dye concentration were investigated, and RSM evaluated the

ARO-The Scientific Journal of Koya University
Vol. X, No. 1 (2022), Article ID: ARO.10903. 8 pages
DOI: 10.14500/aro.10903
Received: 04 November 2021; Accepted: 18 February 2022
Regular research paper: Published: 25 February 2022
Corresponding author's email: ahmed.abdulkareem@koyauniversity.org

equilibrium effective conditions for these parameters (Ince et al., 2016, and Yonten et al., 2016).

## II. Materials and Methods

### A. Chemicals and Apparatus

Sigma-Aldrich provided the Amberlite XAD-4 resins (20–60 meshes) (LOT: BCCB0646, Germany). BB G-250 (Table 1) was purchased from Fisher BioReagents (LOT: 154716, United States). In addition, Merck supplied the rest of the chemicals used in the study (Germany). To adjust the pH of BBG solutions, Thermo Orion digital pH meter (Germany) was applied. All chromatographic measurements were taken with a UV spectrometer (WTW 6100 UV spectrometer, Germany). The experiments were done in chemical engineering laboratories, Faculty of Engineering, Van Yuzuncu Yil University, Turkey.

### B. Fungus Preparation as an Adsorbent

The aboriginal fungus (*A. campestris*) was obtained from Van province in turkey to be used as a biosorbent. To remove contaminants, the fungus was washed with distilled water 2 times then dried at room temperature. A fine powder was made by grinding the dried fungus in a porcelain mortar. To certain that the dried cells of fungus had died completely, it was put in oven for 24 h at 70°C. The viability was tested by inoculation the cells into Sabouraud Dextrose Agar medium for 24 h at 27°C (Aksu et al., 2015).

### C. Biocomposite Material Preparation by Immobilization

The following procedure was used to immobilize the fungus (*A. campestris*) on the substrate: 1 g of Amberlite XAD-4 was mixed with 0.1 g of fungus powder. The mixture was wetted several times with 2 mL of ultra-pure water to improve immobilization efficiency and ensure thorough mixing. Then, put on a hot plate magnetic stirrer, set the temperature at 50°C and the stirring speed at 150 rpm. Following these steps, the mixture was dried in a 50°C oven for 24 h, for improving immobilization efficiency. The obtained sample was milled to minimize the particle size to <120 micrometer and used as an adsorbent for BBG. The turbidity analysis indicates that all of the fungus (0.1 g) immobilized on XAD-4 (Yonten et al., 2016).

### D. Characterization

Characterization of biocomposite materials is critical to determine the controlling mechanism of interaction betwixt the biocomposite material and BBG. Scanning electron microscopy-energy dispersive X-ray (SEM-EDX) was used to characterize the morphological structures of XAD-4/*A. campestris* before and after the biosorption process (Nicolet, Protege 460, Madison, WI, USA).

Table I
Properties of Brilliant Blue G-250.

| No. | Properties | Description |
|---|---|---|
| 1 | Chemical formula | $C_{47}H_{48}N_3O_7S_2Na$ |
| 2 | CAS Number | 6104-58-1 |
| 3 | Molar mass | 854.02 g/mol |
| 4 | Storage Temperature | 15–25°C |
| 5 | Synonyms | Brilliant Blue G, CBB G-250, Acid Blue 90 |

### E. Adsorption Studies

A biocomposite material was used in this study to remove BBG from aqueous solution. Batch adsorption was performed under various conditions. The adsorbent was treated with brilliant blue solution concentrations ranging from 5 to 150 mg $L^{-1}$ in sample volumes ranging from 15 to 75 mL. A digital pH meter (Jenco 6173) was used to adjust the pH from 3 to 11 using 0.1 M hydrochloric acid and sodium hydroxide. The dye solutions were stirred between 5 and 100 min at 150 and 300 rpm (WiseStir MSH-20D) and at temperatures ranging from 20 to 50°C. Before analysis, samples were centrifuged. The BBG in the supernatant was measured using a UV spectrometer set to 600 nm. The blanks were processed without any adsorbent.

### F. Evaluation Method of Chromatographic Experimentation

Before starting the experimental work the UV spectrophotometer calibrated regularly in some period. In addition, before experiments, a scan of dye solution was taken and compared with the literatures for checking the absorbance, when it is true, the analysis of supernatants was done. Furthermore, at the first of starting of researches, the dye solutions (known ppm) were scanned by the UV device to find maximum wavelength (nm) then compared to another UV device and literatures. Besides the continuing with calibration, the deviation of UV device reading also checked.

### G. Experimental Design

#### Plackett–Burman design (PBD)

The outputs of PBD were used in RSM to optimize the efficient factors influencing BBG removal percentage by biocomposite material. PBD performed an initial screening of the most important independent parameters affecting BBG removal by naturally powdered fungus/XAD-4. This technique assessed the determination of the factors that significantly influenced the specific response. The method is founded on the first-order polynomial model, as shown in Equation (1).

$$Y = \beta_0 + \sum(\beta_i X_i) \quad (1)$$

Where, Y represents the response (removal of BBG), β0 is the models intercept, $\beta_i$ symbolizes the linear coefficient, and $X_i$ denotes the level of the independent factor (Plackett and Burman, 1946). These seven parameters (temperature, shaking speed, pH, dye concentration adsorbent amount, contact time, and sample volume) were all investigated to determine the key factors influencing BBG removal. Based on PBD, the each factors prepared in the levels (−1: Low level and +1: High level). The PBD design model with seven parameters and responses is shown in Table 2.

 http://dx.doi.org/10.14500/aro.10903

Table II
Plackett-Burman Design and Responses.

| Runs | pH | Temperature (°C) | Adsorbent (g) | Shaking speed ( rpm) | Concentration (mg $L^{-1}$) | Contact time (min) | Sample volume (mL) | Y (%) |
|---|---|---|---|---|---|---|---|---|
| 1 | 3 | 20 | 0.05 | 300 | 5 | 100 | 75 | 73.77 |
| 2 | 3 | 50 | 0.6 | 150 | 150 | 100 | 75 | 71.27 |
| 3 | 11 | 20 | 0.05 | 150 | 150 | 5 | 75 | 54.51 |
| 4 | 11 | 50 | 0.6 | 150 | 5 | 5 | 75 | 86.37 |
| 5 | 3 | 50 | 0.05 | 300 | 150 | 5 | 75 | 55.27 |
| 6 | 11 | 20 | 0.6 | 300 | 150 | 5 | 15 | 94.20 |
| 7 | 3 | 50 | 0.6 | 300 | 5 | 5 | 15 | 59.05 |
| 8 | 11 | 50 | 0.05 | 150 | 5 | 100 | 15 | 82.87 |
| 9 | 11 | 50 | 0.05 | 300 | 150 | 100 | 15 | 94.65 |
| 10 | 11 | 20 | 0.6 | 300 | 5 | 100 | 75 | 84.62 |
| 11 | 3 | 20 | 0.05 | 150 | 5 | 5 | 15 | 86.73 |
| 12 | 3 | 20 | 0.6 | 150 | 150 | 100 | 15 | 96.97 |

### *H. Steepest Ascent Design (SAD)*

This design model used to determine the greatest increases in response. Finding points at the upper limit are more difficult in optimization. It depicts the relative amounts that should vary to maximize the yield of the direction and factors. SAD experiments were used to screen the impact of four effective parameters that were found by PBD to locate the optimum region in terms of response (Myers, Douglas and Christine, 2016). Table 3 represents the SAD experimental design and corresponding responses.

Table III
Steepest Ascent Design with Responses.

| Runs | Initial concentration (mg $L^{-1}$) | Sample volume (mL) | Time (min) | Adsorbent dosage (g) | Y (%) |
|---|---|---|---|---|---|
| 0 | 77.5 | 45 | 52.5 | 0.325 | 86.38 |
| 0+Δ1 | 85.25 | 41.30 | 54.78 | 0.339 | 90.09 |
| 0+Δ2 | 93 | 37.61 | 57.06 | 0.353 | 91.58 |
| 0+Δ3 | 100.75 | 33.92 | 59.35 | 0.367 | 97.38 |
| 0+Δ4 | 108.5 | 30.23 | 61.63 | 0.381 | 98.03 |
| 0+Δ5 | 116.25 | 26.53 | 63.92 | 0.395 | 97.51 |

### *I. Central composite design (CCD)*

RSM entails designing and testing experimental response surfaces through regression and optimization. The goal is to find the process's optimum operating conditions or a region that meets the operating requirements. This study used CCD with four factors at five levels. The total number of experiments was $30 = 2k + 2^k + 6$, where k represents the number of factors. Thirty experiments were supplemented at the center points to assess pure error. CCD experimental design is shown in Table 4. In quadratic models, the response can be related to selected factors during the optimization process. Equation (2) represents a quadratic model.

$$Y = \beta_0 + \sum_{i=1}^{3}\beta_i X_i + \sum_{i=1}^{3}\beta_{ii} X_i^2 + \sum_{i<1}^{3}\sum_{i=1}^{3}\beta_{ij} X_i X_j \quad (2)$$

Where, Y is response, $\beta_0$ is constant factor, $X_i$ (i = 1–3) are variables, $\beta_i$ is the linear, □$_{ii}$ is the quadratic, and $\beta_{ij}$ (i and j = 1–3) are second-order interaction factors. Design-Expert 7.0 was used to refine all of the data of PBD, SAD, and CCD (Ghaedi et al., 2015; Ince et al., 2016; Yonten et al., 2016).

Table IV
Parameters, Intervals and Results Perform in ccd.

| Runs | Initial concentration (mg $L^{-1}$) | Sample volume (mL) | Time (min) | Adsorbent dosage (g) | Y | |
|---|---|---|---|---|---|---|
| | | | | | Actual removal | Predicted % |
| 1 | 116 | 26 | 59 | 0.39 | 97.07 | 95.28 |
| 2 | 100 | 26 | 63 | 0.36 | 99.55 | 97.73 |
| 3 | 108 | 29.5 | 61 | 0.375 | 96.00 | 96.00 |
| 4 | 100 | 33 | 59 | 0.39 | 96.44 | 95.80 |
| 5 | 108 | 29.5 | 61 | 0.345 | 97.37 | 96.39 |
| 6 | 116 | 26 | 59 | 0.36 | 95.16 | 97.02 |
| 7 | 108 | 29.5 | 61 | 0.375 | 96.00 | 96.00 |
| 8 | 124 | 29.5 | 61 | 0.375 | 96.34 | 95.02 |
| 9 | 108 | 29.5 | 61 | 0.375 | 96.00 | 96.00 |
| 10 | 108 | 29.5 | 61 | 0.375 | 96.00 | 96.00 |
| 11 | 92 | 29.5 | 61 | 0.375 | 99.78 | 98.74 |
| 12 | 108 | 29.5 | 61 | 0.375 | 96.00 | 96.00 |
| 13 | 108 | 36.5 | 61 | 0.375 | 95.60 | 92.88 |
| 14 | 100 | 33 | 59 | 0.36 | 93.91 | 96.01 |
| 15 | 116 | 33 | 63 | 0.36 | 94.20 | 95.08 |
| 16 | 100 | 33 | 63 | 0.36 | 93.27 | 95.04 |
| 17 | 100 | 26 | 59 | 0.39 | 97.50 | 99.04 |
| 18 | 116 | 26 | 63 | 0.36 | 97.94 | 98.55 |
| 19 | 108 | 29.5 | 57 | 0.375 | 97.04 | 95.10 |
| 20 | 100 | 26 | 59 | 0.36 | 99.08 | 99.09 |
| 21 | 100 | 26 | 63 | 0.39 | 98.27 | 99.26 |
| 22 | 116 | 33 | 59 | 0.36 | 94.20 | 93.18 |
| 23 | 108 | 29.5 | 65 | 0.375 | 97.65 | 97.22 |
| 24 | 108 | 29.5 | 61 | 0.405 | 97.40 | 96.01 |
| 25 | 116 | 33 | 63 | 0.39 | 94.80 | 94.75 |
| 26 | 108 | 29.5 | 61 | 0.375 | 96.00 | 96.00 |
| 27 | 100 | 33 | 63 | 0.39 | 95.83 | 96.40 |
| 28 | 116 | 26 | 63 | 0.39 | 98.06 | 98.39 |
| 29 | 108 | 22.5 | 61 | 0.375 | 99.25 | 99.59 |
| 30 | 116 | 33 | 59 | 0.39 | 87.02 | 91.27 |

## III. Results and Discussion

### *A. PBD*

In statistical analysis, many scientists have recently carried out the impacts of the most important and independent factors (Öztürk and Şahan, 2015; Palanivelan, Ayyasamy and Ramya, 2019; Yönten and Aktaş, 2014). The minimum

and maximum values for the variables are given in Table 2 and their effects on the removal of BBG. The most effective response factors were determined on the basis of the Pareto graph (Fig. 1) and the half-normal plot (Fig. 2) which were the adsorbent dose (C), the dye concentration (E), the contact time (F), and the volume sample (G).

### *B. Pareto Plots*

For regression analysis, the effects of response parameters are important. The positive sign means increasing the response, whereas the negative sign reducing in response (Öztürk and Şahan, 2015; Yonten et al., 2016). There are positive effects of adsorbent quantity, pH and adsorbent quantity interaction, initial concentration and adsorbent quantity interaction, and negative impacts of pH and initial concentration interaction (Fig. 1). Pareto analysis clarified the results of the experiments as it will provide more important information on the percentage effect on the rate of adsorption (Bazrafshan et al., 2013; Haaland, 2020). Naturally, the weakness of bonds between dye molecules and adsorbing process can clarify this. The solution temperature effect is decreased and corrected by greater pH (Hassani et al., 2014).

Figs. 1 and 2 were shown in the Pareto graphical analysis. Efficient parameters for removing dye by XAD-4/*A. campestris* are the linear effect of initial dye concentration (40.57%), sample volume (27.31%), adsorbent dosage (7.55%), and contact time (7.68%).

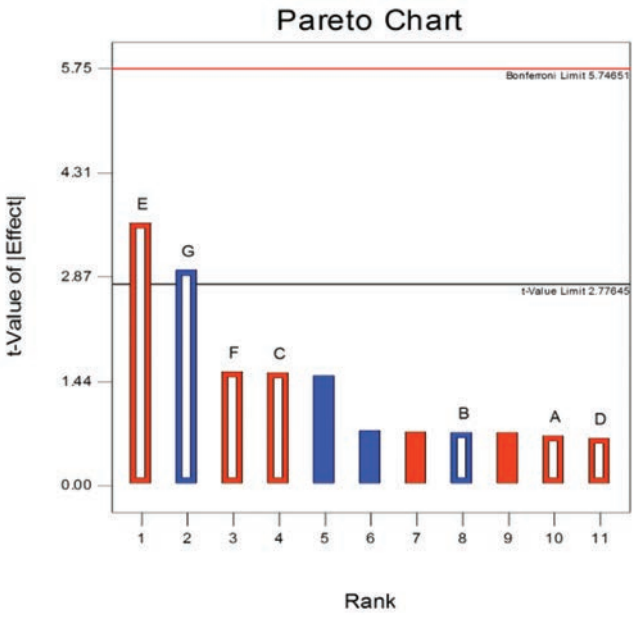


Fig. 1. Pareto graph.

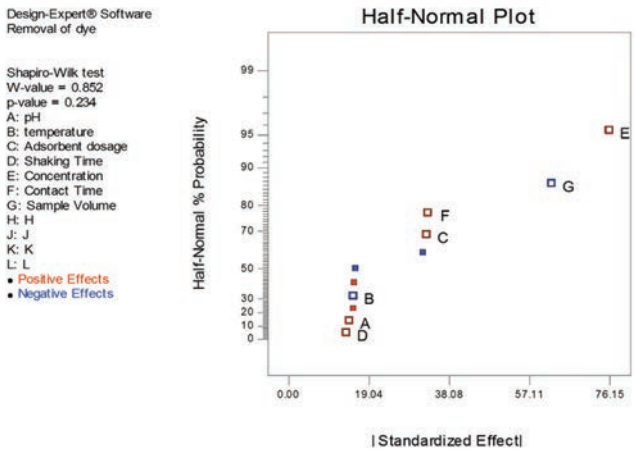


Fig. 2. Half-normal plots.

### *C. SAD*

The SAD method was determined by increasing (initial concentration (C), contact time (F), and adsorbent dosage [C]) and decreasing sample volume to find the correct direction for changing variables (G). The SAD path and the results obtained are shown in Table 3. When dye concentration, adsorbent dose, sample volume, and contacting time were 108.5 mg $L^{-1}$, 0.381 g, 30.23 mL, and 61.63 min, respectively, the plateau of the response was obtained as a 98.03% removal of BBG. The optimal points in that region were discovered to be.

### *D. CCD*

Table 4 illustrates the CCD and responses. The optimization by a linear model related to factors takes the response.

The figures below depict the parameters impact on BBG removal, as well as the interaction of four variables with the effect of the parameters. The linear model was used to organize the 3D response surface. In Fig. 3 which is three-dimensional response surface plot (TDRSP), some experiments were designed with sample volume (26–33 mL) and initial concentration (100–116 mg $L^{-1}$), fixed contact time amounts (61 min), and adsorbent amount (0.38 g) to explore the impact of dye concentration and sample volume on adsorption effectiveness. The removal of BBG has been strongly influenced by both variables in this figure.

The certain increase in initial concentration from 100 to 116 mg $L^{-1}$ had no statistically significant effect on the

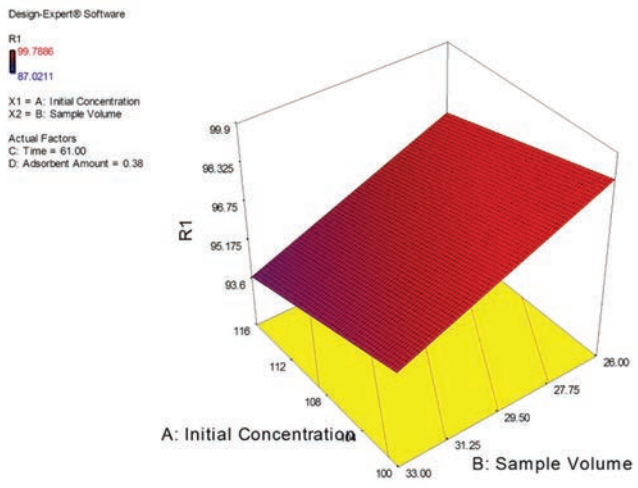


Fig. 3. TDRSP of the impact of the sample volume-dye concentration ratio on BBG removal percentage.

http://dx.doi.org/10.14500/aro.10903

percentage of BBG removal, which fell from 97.20% to 95.36% (Fig. 4). The optimum initial concentration was found to be 107.13 mg $L^{-1}$. The impact of sample volume is similar to the initial dye concentration. As shown in Fig. 5, any significant increase in sample volume from 26 to 33 mL reduced the percentage of BBG removal from 97.97% to 94.61%. The optimum volume for BBG removal was discovered to be 28.6 mL.

The same pattern has been achieved in some works. Adsorbent adsorption capacity was enhanced as the dye concentration increased. This might be due to a high mass transfer force. However, because the binding sites on the adsorbent are saturated, the percent removal decreases (Amin, Alazba and Shafiq, 2015). It can also be connected to the fact that the initial dye concentration had a limited impact on dye removal ability; at the same time, the adsorbent media had a specified range of active sites, which would have become saturated at a specific concentration. This has resulted in an increase in the number of dye molecules competing for available function groups on the adsorbent material's surface (Abbas, 2013). The removal percentage decreased as the initial dye concentration increased because the lower concentration solution contained fewer dye molecules than the higher concentration solution.

Furthermore, as the dye concentration increased, so also do the adsorbent's adsorption capacity. This influence could be caused by rising in the driving force of the ionic gradient with increasing dye concentration (Soni et al., 2012), which is justified by an increment in sorption capacity due to an increase in the amount of dye anion-adsorbent interactions. Santhi et al. (2010) discovered a similar phenomenon when they used agricultural waste (*Annona squamosa* seed) as an adsorbent to adsorb methyl red dye.

The effect of sample volume and contacting time on BBG removal% indicated by three dimensional plot as shown in Fig. 6. BBG removal percent tilted simultaneously with an increase in sample volume from 26 mL to 33 mL and contact time achieved a maximum of approximately 98.4% BBG removal at sample volume of approximately 33 mL and contact time of approximately 59 min and a slight increase at higher contact time values, as shown in Fig. 7.

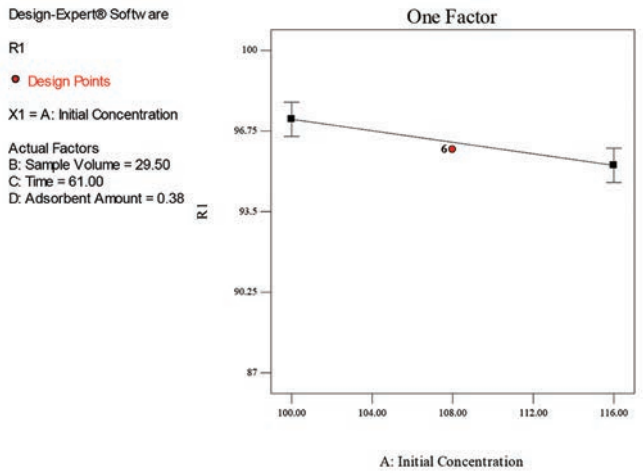


Fig. 4. Effect of initial concentration on removal % at mean value of other factors.

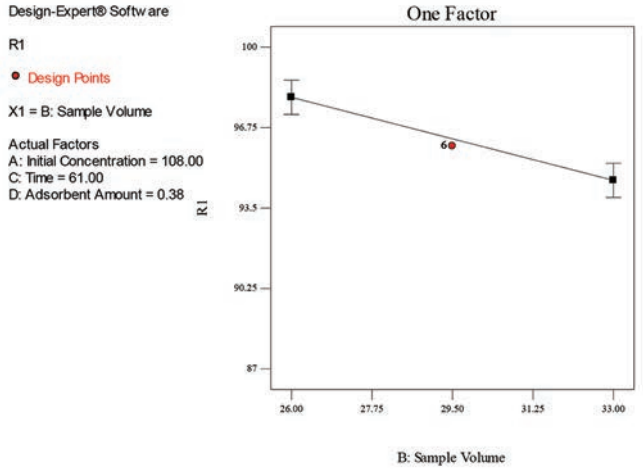


Fig. 5. Effect of sample volume on removal% at mean value of other factors.

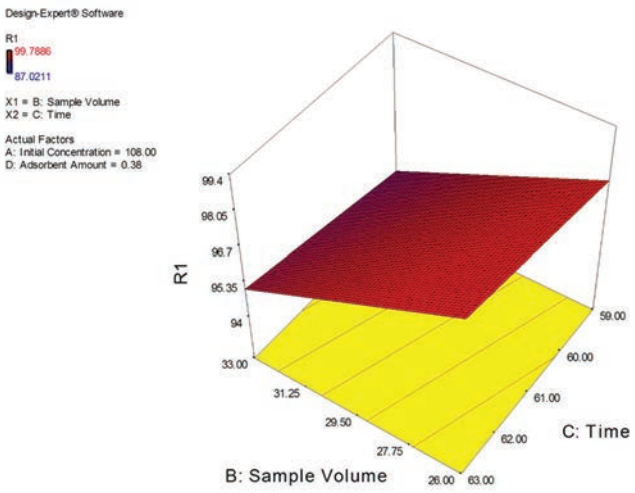


Fig. 6. TDRSP of the impact of sample volume-contact time ratio on removal% of BBG.

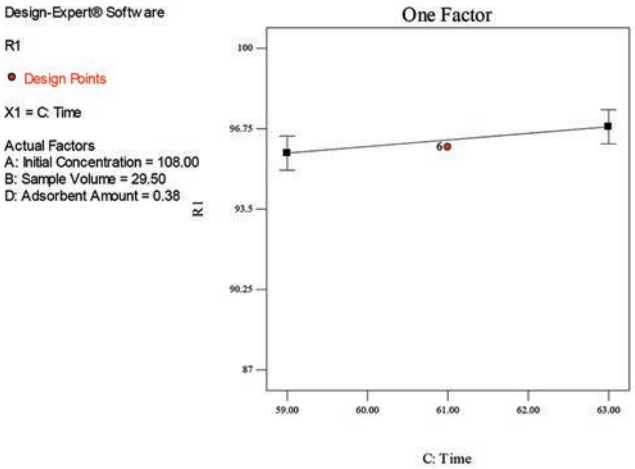


Fig. 7. Effect of contact time on removal% at mean value of other factors.

Moreover, enhancing the BBG concentration after reaching the saturated point, which can be attributed to a lack of vacant active sites, has little effect on the adsorption process. According to the Pareto graph results (Fig. 1), the removal process has a higher t-value of the initial concentration (E) than the other factors when compared to the initial BB concentration.

The interaction effect of contact time and adsorbent quantity ratio is given in Fig. 8. The removal percentage of BB increases as contact time increases from 59 to 63 min. The maximum contact time for the optimum yield was maintained at approximately 59.99 min (Daâssi et al., 2012; Şahan and Öztürk, 2014). The increase in removal percentage by adsorbent dose could be due to an increase in available surface area for sorption as well as the availability of additional adsorption sites. The increase in the removal of the adsorbent dose of methylene blue dye and linked it to an increase in surface area and sorption sites (Altaher and ElQada, 2011).

The results indicate that the rate of dye removal increased with contact time. For the higher dye concentration solution used, the longer balance time was required. Because of the large surface area of the adsorbent available for dye ion adsorption, the rate of dye removal is higher at first. Because the adsorbent surface has few active sites, only a poor increasing trend in color removal has been observed after a certain period (Soni et al., 2012).

The interaction of initial concentration and adsorbent quantity is depicted in Fig. 9. The removal percentage of BBG decreases as the initial concentration increases from 100 to 116 mg $L^{-1}$ and the amount of adsorbent increases from 0.36 to 0.39 g. As shown in Figs. 9 and 10, the maximum percentage of BBG removal was 96.38%.

According to the graphs, the optimum adsorption of 96.72% occurs at a sample volume of 28.60 mL, adsorbent quantity of 0.38 g, initial dye concentration of 107.13 mg. $L^{-1}$, and contact time of 60.78 min in accordance with the model, as shown in Fig. 11.

### *E. Characterization of Biocomposites*

EDX data (Table 5) and SEM micrographs (Fig. 12a-d) of pre- and post-sorption Amberlite XAD-4/*A. campestris* are presented. The results show that any of the elements, such as C, O, Na, Cl, Cu, and K, are present before adsorption in the biocomposite material with a percentage of weight (Table 5) of 81.40, 7.80, 3.37, 2.60, 3.72, and 1.11. After adsorption, all elements except K were present with a different percentage of weight (86.63, 7.71, 1.80, 0.62, and 3.23).

Fig. 12a and c shows Amberlite XAD-4 and fungal images at 100 and 300 μm before adsorption after bonding

TABLE V
PARAMETERS OF AMBERLITE XAD-4/*AGARICUS CAMPESTRIS* COMPOSITE MATERIAL.

| Before the adsorption | | | After the adsorption | | |
|---|---|---|---|---|---|
| Chemical elements | Weight % | Atomic % | Chemical elements | Weight % | Atomic % |
| C | 81.40 | 89.50 | C | 86.63 | 91.98 |
| O | 7.80 | 6.44 | O | 7.72 | 6.15 |
| Na | 3.37 | 1.94 | Na | 1.80 | 1.00 |
| Cl | 2.60 | 0.97 | Cl | 0.62 | 0.22 |
| Cu | 3.72 | 0.77 | Cu | 3.23 | 0.65 |
| K | 1.11 | 0.38 | - | - | - |

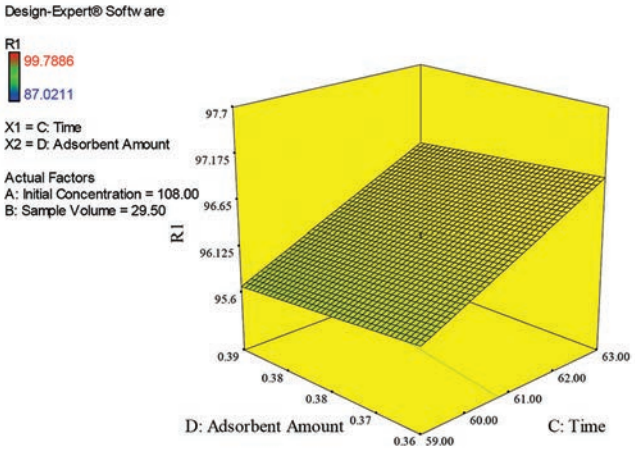


Fig. 8. TDRSP of the impact of adsorbent amount-contact time ratio on BBG removal %.

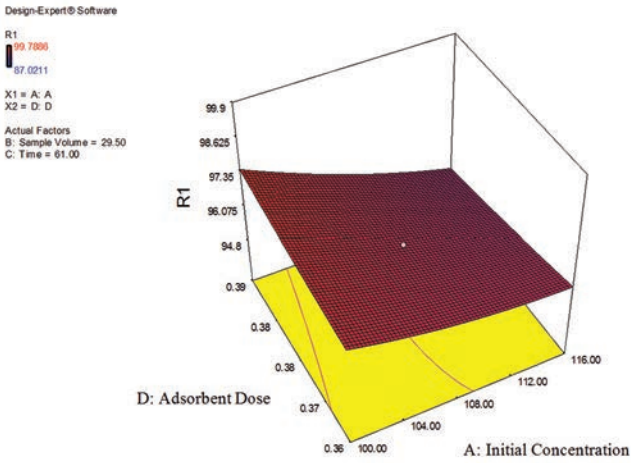


Fig. 9. TDRSP of the impact of initial concentration-adsorbent amount ratio on BBG removal %.

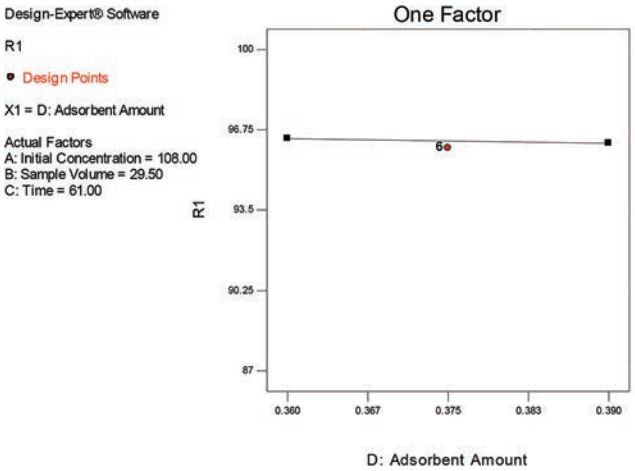


Fig. 10. Effect of adsorbent amount on removal% at mean value of other factors.

http://dx.doi.org/10.14500/aro.10903

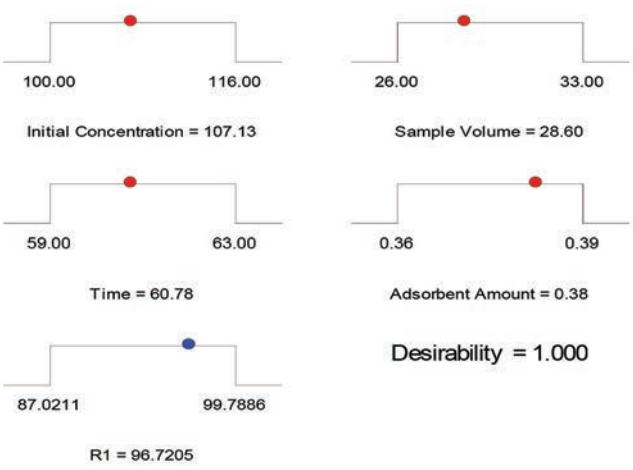


Fig. 11. Four variable parameters (adsorbent amount, contact time, initial concentration, and sample volume) numerical prediction graph.

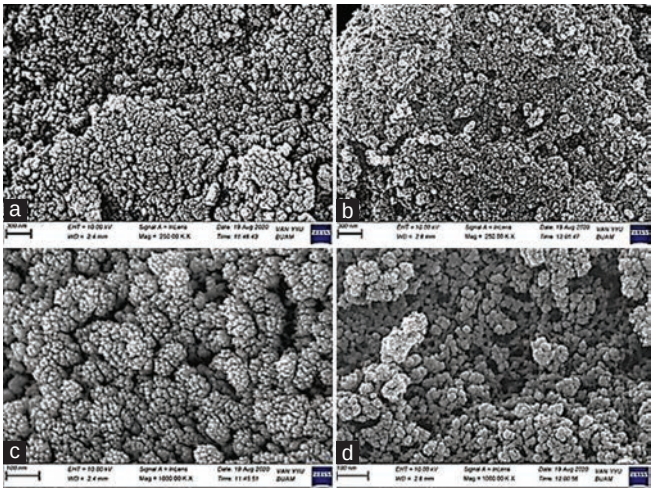


Fig. 12. SEM image at 100 and 300 µm (a and c) pre-adsorption and (b and d) post-adsorption.

with BBG, and these images are denser and BBG particles adhere to the surface more than the post-adsorption images (b and d). The simplicity observed before adsorption is visible in post-adsorption images, demonstrating the prevalence of adsorption (dye removal) in the present study.

## IV. Conclusion

It is possible to conclude:

1. Because of its sediment-free operation, simplicity and flexibility of design, and complete deletion of dyes even in low concentration solutions, the adsorption process has been demonstrated to be highly effective for dye removal from polluted water. Adsorbent surface modification is very useful in enhancing adsorption capacity and adsorbent selectivity by taking advantage of specific interactions between adsorbents and target molecules in the adsorption technique sector to remove dye from wastewater streams.
2. Based on the findings, the biocomposite material (Amberlite XAD-4/*A. campestris*) is an effective adsorbent for the removal of Brilliant Blue G250 from aqueous media.

## V. Recommendation

The following recommendations are made which can supplement the study performed in the future:

1. Using Amberlite XAD-4/*A. campestris* as a biocomposite adsorbent for the removal of other types of dyes, and it could be a viable alternative to low adsorption capacity materials.
2. RSM will be more economic and accurate way for finding the effective factors and optimizing the optimum point in adsorption process.

## References

Abbas, F.S., 2013. Dyes removal from wastewater using agricultural waste. *Advances in Environmental Biology*, 7, pp.1019-1026. Available from: https://www.citeseerx.ist.psu.edu/viewdoc/download?doi=10.1.1.1065.8042&rep=rep1&type=pdf [Last accessed on 2021 Oct 01].

Ahmad, A.M. and Alrozi, R., 2010. Optimization of preparation conditions for mangosteen peel based activated carbons for the removal of Remazol Brilliant Blue R using response surface methodology. *Chemical Engineering Journal*, 165, pp.883-890.

Aksu, O., Nuran, C.Y., Numan, Y., Durali, D. and Seval, D., 2015. Biochemical response of crayfish Astacus leptodactylus exposed to textile wastewater treated by indigenous white rot fungus *Coriolus versicolor*. *Environmental Science and Pollution Research*, 22(4), pp.2987-2993.

Aljebori, A.M.K. and Alshirifi, A.N., 2012. Effect of different parameters on the adsorption of textile dye maxilon blue GRL from aqueous solution by using white marble. *Asian Journal of Chemistry*, 24, pp.5813-5816.

Altaher, H. and ElQada, E., 2011. Investigation of the treatment of colored water using efficient locally available adsorbent. *International Journal of Energy and Environment*, 2(6), pp.1113-1124. Available from: https://www.ijee.ieefoundation.org/vol2/issue6/ijee_12_v2n6.pdf [Last accessed on 2021 Oct 01].

Amin, M.T., Alazba, A.A. and Shafiq, M., 2015. Adsorptive removal of reactive black 5 from wastewater using bentonite clay: Isotherms, kinetics and thermodynamics. *Sustainability (Switzerland)*, 7(11), pp.15302-15318.

Bazrafshan, E., Hossein, M., Ferdos, K.M. and Shima N., 2013. Application of electrocoagulation process for dairy wastewater treatment. *Journal of Chemistry*, 2013, pp.7-10.

Beyene, H.D., 2014. The potential of dyes removal from textile wastewater by using different treatment technology. A review. *International Journal of Environmental Monitoring and Analysis*, 2, pp.347-353.

Daâssi, D., Fakher, F., Hela, Z.M., Lassaad, B., Steve, W. and Tahar, M., 2012. Application of response surface methodology to optimize decolourization of dyes by the laccase mediator system. *Journal of Environmental Management*, 108, pp.84-91.

Elhajjar, R., Valeria, L.S. and Anastasia, M., 2013. *Smart Composites: Mechanics and Design*, CRC Press, Florida, United States.

Fazeli, M., Florez, J.P. and Simão, R.A., 2019. Improvement in adhesion of cellulose fibers to the thermoplastic starch matrix by plasma treatment modification. *Composites Part B: Engineering*, 163, pp.207-216.

Ghaedi, A.M., Ghaedi, M., Vafaei, A., Iravani, N., Keshavarz, M., Rad, M.,Tyagi, I., Agarwal, S. and Gupta, V.K., 2015. Adsorption of copper (II) using modified activated carbon prepared from Pomegranate wood: Optimization by bee algorithm and response surface methodology. *Journal of Molecular Liquids*, 206, pp.195-206.

Haaland, P.D., 2020. *Experimental Design in Biotechnology*, CRC Press, Florida, United States.

Hassani, A., Alidokht, L., Khataee, A.R. and Karaca, S., 2014. Optimization of comparative removal of two structurally different basic dyes using coal as a low cost and available adsorbent. *Journal of the Taiwan Institute of Chemical Engineers*, 45, pp.1597-1607.

Ince, O.K., Ince, M., Karaaslan, N.M. and Yonten, V., 2016. Optimization of cadmium removal from water by hydroxyapatite using experimental design methodology. *Analytical Letters*, 49(15), pp.2513-2524.

Mallampati, R., 2013. *Biomimetic Synthesis of Hybrid Materials for Potential Applications*. National University of Singapore, US. Available from: https://www.core.ac.uk/download/pdf/48682628.pdf [Last accessed on 2021 Oct 01].

Myers, R.H., Douglas, C.M. and Christine, M.A.C., 2016. *Response Surface Methodology: Process and Product Optimization using Designed Experiments*, John Wiley & Sons, New York, United States.

Öztürk, D. and Şahan, T., 2015. Design and optimization of Cu(II) adsorption conditions from aqueous solutions by low cost adsorbent pumice with response surface methodology. *Polish Journal of Environmental Studies*, 24, pp.1749-1756.

Palanivelan, R., Ayyasamy, P.M. and Ramya, S., 2019. Optimization of significant factors on the microbial decolorization of Azo Dye in an aqueous medium by design of experiments. *Pollution*, 5, pp.1-11.

Plackett, R.L. and Burman, J.P., 1946. The design of optimum multifactorial experiments. *Oxford University Press on Behalf of Biometrika Trust*, 33, pp.305-325. Available from: http://www.jstor.org/stable/2332195 [Last accessed on 2021 Oct 01].

Şahan, T. and Öztürk, D., 2014. Investigation of Pb(II) adsorption onto pumice samples: Application of optimization method based on fractional factorial design and response surface methodology. *Clean Technologies and Environmental Policy*, 16, pp.819-831.

Santhi, T., Manonmani, S. and Smitha, T., 2010. Removal of methyl red from aqueous solution by activated carbon prepared from the *Annona squmosa* seed by adsorption. *Chemical Engineering Research Bulletin*, 14, pp.11-18.

Soni, M., Ashok, K.S., Jitendra, K.S. and Yadav, J.S., 2012. Adsorptive removal of methylene blue dye from an aqueous solution using water hyacinth root powder as a low cost adsorbent. *International Journal of Chemical Sciences and Applications*, 3, pp.338-345.

Yönten, V. and Aktaş, N., 2014. Exploring the optimum conditions for maximizing the microbial growth of *Candida intermedia* by response surface methodology. *Preparative Biochemistry and Biotechnology*, 44, pp.26-39.

Yonten, V., Tanyol, M., Yildirim, N., Yildirim, N.C. and Ince, M., 2016. Optimization of remazol brilliant blue R dye removal by novel biosorbent *P. eryngii* immobilized on amberlite XAD-4 using response surface methodology. *Desalination and Water Treatment*, 57, pp.15592-15602.

 http://dx.doi.org/10.14500/aro.10917

# Detecting Deepfakes with Deep Learning and Gabor Filters

**Wildan J. Hadi[1], Suhad M. Kadhem[2], Ayad R. Abbas[2]**

[1]Department of Computer Science, College of Science for Women, University of Baghdad, Baghdad, Iraq.

[2]Department of Computer Science, University of Technology, Baghdad, Iraq.

***Abstract*–The proliferation of many editing programs based on artificial intelligence techniques has contributed to the emergence of deepfake technology. Deepfakes are committed to fabricating and falsifying facts by making a person do actions or say words that he never did or said. So that developing an algorithm for deepfakes detection is very important to discriminate real from fake media. Convolutional neural networks (CNNs) are among the most complex classifiers, but choosing the nature of the data fed to these networks is extremely important. For this reason, we capture fine texture details of input data frames using 16 Gabor filters in different directions and then feed them to a binary CNN classifier instead of using the red-green-blue color information. The purpose of this paper is to give the reader a deeper view of (1) enhancing the efficiency of distinguishing fake facial images from real facial images by developing a novel model based on deep learning and Gabor filters and (2) how deep learning (CNN) if combined with forensic tools (Gabor filters) contributed to the detection of deepfakes. Our experiment shows that the training accuracy reaches about 98.06% and 97.50% validation. Likened to the state-of-the-art methods, the proposed model has higher efficiency.**

***Index Terms*— Deepfake detection; deep learning; Gabor filter; VGG16.**

## I. Introduction

With the emergence of deep learning algorithms in artificial intelligence and its breakthrough in many areas such as Ghafoor, et al., 2021, Al-Talabani, 2020, Abdul, 2019, as well as computers' development in simulating reality, it has become possible to rely on them to create fake characters with scenes and recognize them as realistic. These represent primary reasons that have effectively contributed to the emergence of the so-called "deepfake" (deep learning + fake) technology. To make the fake video, we need the target video to use as a basis for the deepfake and then a set of videos of the person, we want to include in the fake video (Johnson, 2021). An example of deepfakes is shown in Fig. 1; this snapshot from a fake video starring Amy Adams in the film Man of Steel (Moran, 2021). Deepfakes rely mainly on deep learning algorithms, which are a form of artificial intelligence. One of these forms is called autoencoders (Zhu, et al., 2018, Zhou and Shi, 2017). Another form of artificial intelligence that has contributed to the emergence of deepfakes is generative adversarial networks (Mao and Li, 2021, Wang, et al., 2018, Karras, Laine and Aila, 2019, Yu, et al., 2017). These networks study large amounts of data to build new examples that mimic the original character incredibly.

Today, social media sites have become a good way to spread and promote fake clips, as many political figures, heads of state, and celebrity actors have been targeted (Lim, 2020). The widespread of deepfakes in social media can also provide new ways for deepfakes to target non-celebrities. The possibility of such things happening causes the loss of credibility for all published videos and their failure to use them as evidence or conviction in the courts. In general, the deepfakes technique, when directed at celebrities, some methods save them from such fabricated videos. Still, the real danger is when such technology targets the ordinary person who does not have an instrument to defend himself (Moran, 2021). Therefore, it has become necessary to build robust models in detecting deepfakes and proving the reliability of the spread data.

Inspired by the promising results achieved using deep learning in detecting deepfakes, we built a novel model for detecting deepfakes based on deep learning. Convolution neural network (CNN) is chosen to see the ability of this network to extract features from the input texture data instead of red-green-blue (RGB) image contents and to see how effective this system is in detecting deepfakes. Furthermore, the Gabor filter will be used to extract the texture properties of the input data before feeding input data to binary CNN classifier.

This paper processes the problem of deepfakes and is organized as follows: Section II presents related works. In Section III, methodology of the proposed model is described. The results of the proposed model with comparison to previous works are given in Section IV. Finally, Section V gives the conclusion of this work.

ARO-The Scientific Journal of Koya University
Vol. X, No. 1 (2022), Article ID: ARO.10917, 5 pages
DOI: https://doi.org/10.14500/aro.10917
Received: 13 December 2021; Accepted: 05 March 2022
Regular research paper: Published: 18 March 2022
Corresponding author's email: wildanjh_comp@csw.uobaghdad.edu.iq

## II. Related Work

This section describes previous work that was devoted to detecting manipulation, whether in images or videos. First, the methods based on multimedia forensic techniques will be discussed, and then, the methods based only on deep learning will be described:

### *A. Multimedia Forensic-based Approaches*

Several approaches are used to detect manipulation in the hidden structure of the media content by exploiting compression parameters, frequency domain parameters, noise maps, etc. These methods were previously relied on before deep learning algorithms appeared and depended on in the detection of forgery. For example, the author of Puglisi, et al., 2013, utilizes how implementing successive quantization followed by dequantizations introduces some arranges in the sequence of zeros and non-zeros in the coefficient distributions of the histogram. This method allows for recapturing the coefficients of the first compression in a double JPEC compression. Another form of exploiting multimedia forensic tools in detection manipulation is utilizing the statistical distribution of discrete cosine transform coefficients. In Battiato and Messina, 2009, this approach is used for forgery detection. Lens distortion is also exploited as a forensic tool. Each camera is fitted with a composite optical system; it cannot focus light at different wavelengths. These distortion signals are used to detect image manipulation (Fu and Cao, 2012). Noise residuals map also exploited for forgery detection. In Mullan, et al., 2017, a statistical comparison between two video sequences is implemented. In each sequence, noise residues within and between frames are calculated, and a statistical model is built for the first sequence to compare it with the second sequence.

### *B. Deep Learning-based Approaches*

After the emergence of deep learning algorithms, these algorithms entered into many areas, including the detection of manipulation and forgery. Many architectures based on deep learning have been used in detecting deepfakes as we have seen later. For example, two CNN architectures with a few layers and parameters are proposed in Afchar, et al., 2018, to detect deepfakes. The first network (Meso-4) consists of four layers of convolution and pooling fooled by one dense layer. A 5 × 5 kernel size is used in the convolution layer of the first network. The second network (MesoInception-4) is based on the inception module in its architecture. Rather than using 5 × 5 convolutions of the first network, the authors used 3 × 3 dilated convolutions combined with the inception module to avoid high semantic. Both networks are designed to utilize mesoscopic features. Montserrat, et al., 2020, combined two deep learning models, the CNN model and recurrent neural network (RNN), to detect facial manipulation in the video. The basic idea is to use the CNN network for extracting features from input frames and then feed them to RNN for temporal feature extraction. Another form of using deep learning is in Güera and Delp, 2018, first, CNN is used to learn frame-level features followed by RNN to classify if the input video is fake. The CNN model used is the inception V3 with removed fully connected layer to input the final feature vectors after final max-pooling layer to RNN network. A new attention mechanism has been proposed by Dang, et al., 2020, to enhance and process the feature maps of the classifier model. This attention-based layer concentrates the network direction to manipulated and discriminative regions only. The promising results are achieved using capsule networks paid researches to use this network in deepfakes detection. For example, Nguyen, Yamagishi and Echizen, 2019, used capsule network architectures for deepfakes detection and are obtained good results. Texture features give good results in image forgery detection. Based on this motivation, pixel gradient information combined with pixel intensity information to produce texture information is used in a Multi-scale Texture Difference model named as MTD-Net for robust face forgery detection (Deepfakes) (Yang, et al., 2021).

Fig. 1. Example of Deepfakes (Source YouTube).

## III. Methodology

The dataset that was relied on in this research is Deepfake Detection dataset from Google-and-Jigsaw (Dufour, et al., 2019). It is a large dataset consisting of about 3000 manipulated videos created using 28 actors with different actions and positions. Fig. 2 shows a few examples of this dataset.

The first step is to extract frames from fake and real videos loaded from the dataset and store them in separate folders. Then, the front face detector in dlib (an open-source library) is used to extract the facial area (Region of Interest). All cropped face images with categories real and fake normalized to size 224 × 224. The next step is to extract texture maps from real and fake face images using Gabor filters, then feed them to VGG 16 to classify real image from fake ones. The steps of our method are described on the flowchart, as shown in Fig. 3.

### *A. Gabor Filters*

In the field of image processing and computer vision, the Gabor filter has been widely used in texture analysis. When

http://dx.doi.org/10.14500/aro.10917

the Gabor filter convolves with an image, it gives a high response to areas where texture changes. Gabor filter depends on a certain number of parameters which are described in Equation (1).

$$g\left(x,y,\lambda,\theta,\psi,\sigma,\mathrm{Y}\right)=\exp(-\frac{x^{\sim 2}+\gamma^2 y^{\sim 2}}{2\sigma^2})\exp(i\ (2\pi\frac{x^{\sim}}{\lambda}+\psi)) \quad (1)$$

with:

$$x^{\sim}=x\cos\theta+y\sin\theta$$

$$y^{\sim}=-x\sin\theta+y\cos\theta$$

Where, λ (lambda) represents a wavelength of the sinusoidal factor, θ (theta) is the tendency of the normal to the parallel stripes of the Gabor function, ψ (psi) refers to phase offset, σ (sigma) is the standard deviation of the Gaussian function used in the Gabor filter, and finally, Y (gamma) refers to spatial aspect ratio (Dora, et al., 2017). The Gabor bank consists of 16 filters with different orientations; the values of the other parameters are kept unaltered because of the absence of scale variations in the cropped face image. The Gabor bank provides us with texture information that needs for the next step. Fig. 4 shows the workflow of processing cropped face images using Gabor bank filters.

Fig. 2. Examples of videos from deepfakes dataset (Dufour, et al., 2019).

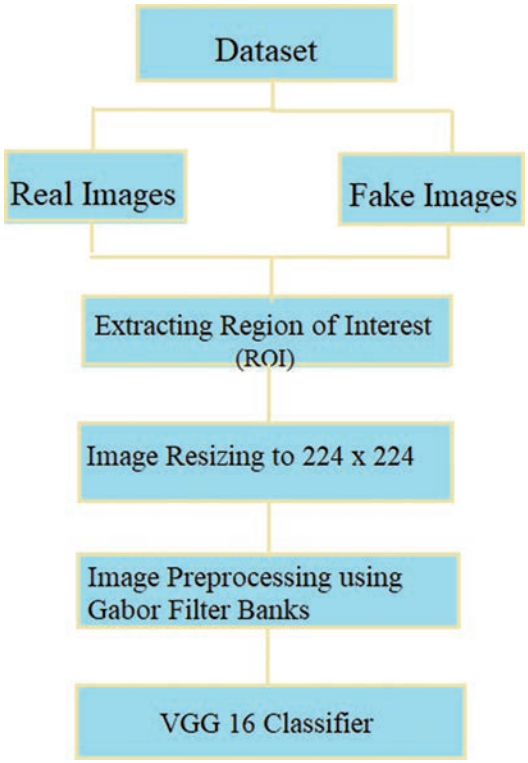


Fig. 3. The steps of proposed method.

*B. CNN (VGG16 Classifier)*

VGG 16 is a specified CNN intended for classification and localization. The VGG network model was first suggested by Simonyan and Zisserman, 2014. The architecture of the VGG16 network is shown in Fig. 5, which includes five blocks of convolution layer and max-pooling layer followed by three fully connected layers. Convolution layers depend on a 3 × 3 kernel with the value of 1 for both padding and stride to ensure that the resulting map has the same length of dimensions as the activation map in the previous layer. Also to guarantee the spatial dimension of the activation map from the previous layer is halved, the max-pooling layer uses a 2 × 2 kernel size, a stride of 2, and no padding. This differentiates the CNN when it is compared with the size of backpropagation networks of the same number of layers. At the end of each block of convolution and max pooling, a rectified linear unit activation is used to reduce the spatial dimension. Finally, three fully connected layers are used in VGG16 architecture for final classification.

The fully connected layers predict the real and fake classes based on the input layer. The softmax function is used to squash the outputs of each neuron between 0 and 1 by applying the following equation:

$$S(y)_i=\frac{\exp(y_i)}{\sum_{j=1}^{n}\exp(y_i)} \quad (2)$$

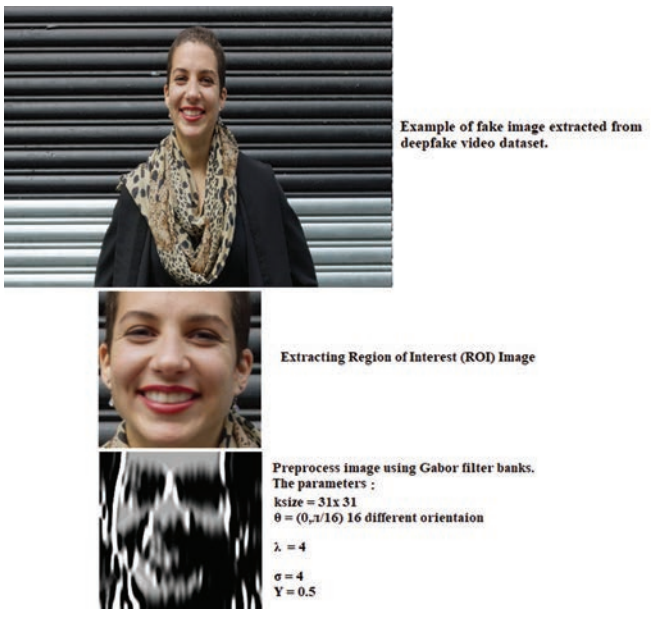


Fig. 4. The workflow of applying Gabor bank and its parameter description.

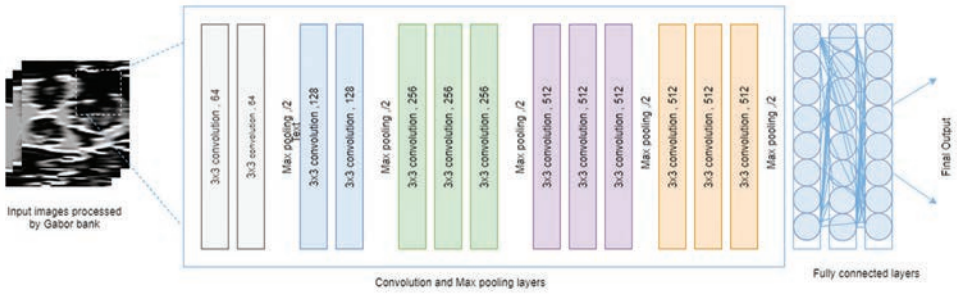


Fig. 5. The architecture of VGG 16 network.

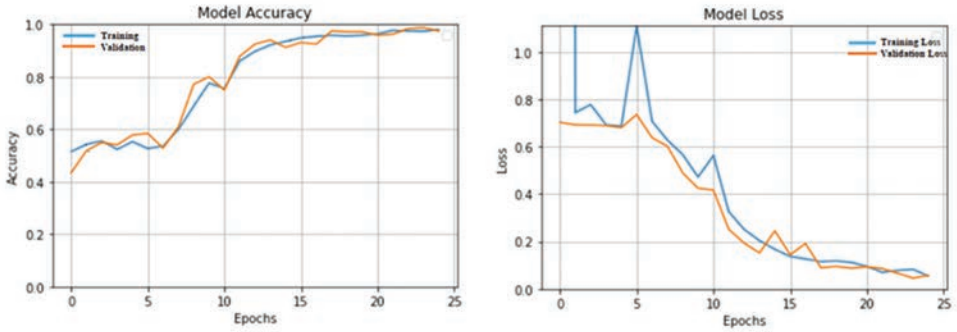


Fig. 6. The accuracy and loss of the proposed model.

Where, $y_i$ is the i-th element of input vector (Sudiatmika and Rahman, 2019).

## IV. Results and Discussion

In this section, the experimental results of the proposed deepfake detection algorithm will be described. The images extracted from the deepfake video dataset are divided using 80–20% for training and testing. As shown in Fig. 6, the accuracy of training ranges between 50 and 90, which means that the proposed method can learn this type of data.

From the results above, we find that the training accuracy of the model has reached 98% and for validation 97% employing 25 epochs. As a result, the use of the VGG16 model in learning texture features from the input data processed by the Gabor filter contributed to detecting deepfakes.

The execution of the proposed model compared with alternate methods such as MesoNet (Afchar, et al., 2018) and automatic face weighting (Montserrat, et al., 2020). The performance of these methods reached 84.3 and 91.88, respectively. The advantages of our system involve minimizing the required numbers of epochs for training also the high accuracy values for both training and testing. These advantages are satisfied due to using texture maps instead of RGB maps as input to the CNN classifier. However, the GPU environment is necessary for other methods, but our model can be implemented in the CPU environment. Furthermore, the principles on which other methods relied are not recognized, but our proposed model is based on texture maps in detecting deepfakes.

## V. Conclusion

In this study, a novel method for deepfakes detection is proposed. It is shown that using Gabor bank filters to extract texture features in 16 different orientations and feeding them to the VGG model provide good results. This means that combining techniques from forensic tools such as Gabor filters and deep learning methods such as the VGG model affect deepfake detection accuracy. Therefore, the new oriented takes advantage of the methods used in both areas (multimedia forensics + deep learning) and uses them in deepfakes detection.

For the future work, some considerations can be taken into account such as creating a hybrid dataset by combining two or more deepfakes datasets to enable the proposed CNN model to be trained on it and then increase its ability to recognize unseen data. Furthermore, we can use Gabor transform (which is a 1-D transform used to processes 1d signals) for detecting deepfakes audio due to the promising results, we have achieved from using Gabor filters in this work.

## References

Abdul, Z.K., 2019. Kurdish speaker identification based on one dimensional convolutional neural network. *Computational Methods for Differential Equations*, 7, pp.566-572.

Afchar, D., Nozick, V., Yamagishi, J. and Echizen, I., 2018 Mesonet: A compact facial video forgery detection network. In: *2018 IEEE International Workshop on Information Forensics and Security* (*WIFS*). IEEE, pp.1-7.

Al-Talabani, A.K., 2020. Automatic recognition of arabic poetry meter from speech signal using long short-term memory and support vector machine. *ARO-The Scientific Journal of Koya University*, 8(1), pp.50-54.

Battiato, S. and Messina, G., 2009. Digital forgery estimation into DCT domain:

A critical analysis. In: *Proceedings of the First ACM Workshop on Multimedia in Forensics*, pp.37-42.

Dang, H., Liu, F., Stehouwer, J., Liu, X. and Jain, A.K., 2020. On the Detection of Digital Face Manipulation. In: *Proceedings of the IEEE/CVF Conference on Computer Vision and Pattern recognition*, pp.5781-5790.

Dora, L., Agrawal, S., Panda, R. and Abraham, A., 2017. An evolutionary single Gabor kernel based filter approach to face recognition. *Engineering Applications of Artificial Intelligence*, 62, pp.286-301.

Dufour, N., (2019) 'Deepfakes Detection Dataset'.

Fu, H. and Cao, X., 2012. Forgery authentication in extreme wide-angle lens using distortion cue and fake saliency map. *IEEE Transactions on Information Forensics and Security*, 7(4), pp.1301-1314.

Ghafoor, K.J., Rawf, K.M.M., Abdulrahman,A.O., Taher, S.H., 2021. Kurdish dialect recognition using 1D CNN. *ARO-The Scientific Journal of Koya University*, 9(2), pp.10-14.

Güera, D. and Delp, E.J., 2018. Deepfake video detection using recurrent neural networks. In: *2018 15th IEEE International Conference on Advanced Video and Signal Based Surveillance* (*AVSS*). IEEE, pp.1-6.

Johnson, D., 2021. *What is a Deepfake? Everything you need to Know*. Available from: https://www.businessinsider.com/what-is-deepfake [Last accessed on 2021 Sep 07].

Karras, T., Laine, S. and Aila, T., 2019. A style-based generator architecture for generative adversarial networks. In: *Proceedings of the IEEE/CVF Conference on Computer Vision and Pattern Recognition*, pp.4401-4410.

Lim, H., 2021. *The Best* (*and worst*) *Deepfakes Developments in 2020, Lionbridge AI*. Available from: https://lionbridge.ai/articles/a-look-at-deepfakes-in-2020 [Last accessed on 2020 Apr 24].

Mao, X. and Li, Q., 2021. *Generative Adversarial Networks for Image Generation*. Springer Nature. Available from: https://books.google.com/books?hl=en&lr=&id=u9oeEAAAQBAJ&oi=fnd&pg=PR7&dq=generative+adversarial+networks+%2Bface2face%2Bimage+synthesis&ots=TwOl2AJx0K&sig=emvISr6kpl5okeSBjPDMcYT6iZM

Montserrat, D.M., Hao, H., Yarlagadda, S.K., Baireddy, S., Shao, R., Horvath, J., Bartusiak, E., Yang, J., Guera, D., Zhu, F. and Delp, E.J., 2020. Deepfakes detection with automatic face weighting. In: *Proceedings of the IEEE/CVF Conference on Computer Vision and Pattern Recognition Workshops*, pp.668-669.

Moran, T.B., 2021, *What is a deep Fake and how are they made?* Available from: https://www.smh.com.au/technology/what-is-the-difference-between-a-fake-and-a-deepfake-20200729-p55ghi.html [Last accessed on 2021 Nov 30].

Mullan, P., Cozzolino, D., Verdoliva, L. and Riess., C, 2017. Residual-based forensic comparison of video sequences. In: *2017 IEEE International Conference on Image Processing* (*ICIP*). IEEE, pp.1507-1511.

Nguyen, H.H., Yamagishi, J. and Echizen, I., 2019. Capsule-forensics: Using capsule networks to detect forged images and videos. In: *ICASSP 2019-2019 IEEE International Conference on Acoustics, Speech and Signal Processing* (*ICASSP*). IEEE, pp.2307-2311.

Puglisi, G., Bruna, A.R., Galvan, F. and Battiato, S., 2013. First JPEG quantization matrix estimation based on histogram analysis. In: *2013 IEEE International Conference on Image Processing*. IEEE, pp.4502-4506.

Simonyan, K. and Zisserman, A., 2014. Very deep convolutional networks for large-scale image recognition. *arXiv*, 2014, p.14091556.

Sudiatmika, I.B.K. and Rahman, F., 2019. Image forgery detection using error level analysis and deep learning. *Telkomnika*, 17(2), pp.653-659.

Wang, X., Li, W., Mu, G., Huang, D. and Wang, Y., 2018. Facial expression synthesis by u-net conditional generative adversarial networks. In: *Proceedings of the 2018 ACM on International Conference on Multimedia Retrieval*, pp.283-290.

Yang, J., Li, A., Xiao, S., Lu, W. and Gao, X., 2021. MTD-net: Learning to detect deepfakes images by multi-scale texture difference. *IEEE Transactions on Information Forensics and Security*, 16, pp.4234-4245.

Yu, Y., Gong, Z., Zhong, P. and Shan, J., 2017. Unsupervised representation learning with deep convolutional neural network for remote sensing images. In: *International Conference on Image and Graphics*. Springer, Berlin. pp.97-108.

Zhou, Y. and Shi, B.E., 2017. Photorealistic facial expression synthesis by the conditional difference adversarial autoencoder. In: *2017 7th International Conference on Affective Computing and Intelligent Interaction* (*ACII*). IEEE, pp.370-376.

Zhu, H., Zhou, Q., Zhang, J. and Wang, J.Z., 2018. Facial aging and rejuvenation by conditional multi-adversarial autoencoder with ordinal regression. *arXiv*, 2018, p.180402740.

# Suitability of the Carbonate Rocks of the Bekhme Formation Exposed in Shakrook Anticline, Iraqi Kurdistan region, for Cement Industry

Mohammed J. Hamwandy[1], Rahel Kh. Ibrahim[1], Varoujan K. Sissakian[2]

[1]Department of Civil Engineering, Faculty of Engineering, Koya University, Koya KOY45, Kurdistan region – F.R. Iraq

[2]Natural Resource Engineering and Management Department, University of Kurdistan Hewler, Kurdistan region – F.R. Iraq

***Abstract*–The Bekhme Formation forms almost the bulk of the Shakrook anticline, especially the limbs. The current research deals with studying the exposed beds within the Bekhme Formation at the Shakrook anticline to check the suitability of the exposed rocks at the northeastern limb of the anticline for the cement industry. Twenty rock samples from a section which lies along a deeply cut valley that crosses the northeastern limb of the Shakrook anticline within the Bekhme Formation were collected. The channel sampling method was applied; therefore, each sample represents the concerned sampling interval and to be representative for the thickness of the sampled interval. The total thickness of the sampled section is 110 m with a covered interval of 15 m, totaling to 125 m. The collected 20 samples were prepared at the laboratory of the Koya University and were subjected to XRF test at the Tarbiat Modares University, Iran, to indicate the concentration of the main oxides (CaO, MgO, $Al_2O_3$, $Fe_2O_3$, $Na_2O$, $K_2O$, and $SO_3$), and Cl and L.O.I. The indicated concentrations at each sample, from both universities, were compared and were found to be almost coinciding. The average concentrations at each sample were changed to weighted averages and the results were compared with the Iraqi standards for cement industry. The results revealed that the sampled rocks are excellent for cement production.**

***Index Terms*—Bekhme formation, Cement production, Limestone, Geological reserve, Shakrook anticline, Weighted average, Iraqi Kurdistan Region.**

## I. Introduction

There is only one cement factory in the Erbil Governorate, which is the capital of the Iraqi Kurdistan Region (IKR). Since it is witnessing great developments in infrastructure; large quantities of cement are highly needed. Therefore, construction of cement plants in the governorate is very significant. In contrast, there are five cement plants at the Sulaimaniyah Governorate. This is attributed to the fact that the exposed rocks in Erbil Governorate were less studied as compared to those that were exposed in Sulaimaniyah Governorate. However, the existing reconnaissance studies have proved that there are enormous amounts of limestone that is suitable for the construction of cement plants in the Erbil Governorate.

### *A. Aim*

The aim of this research is to check the suitability of the carbonate rocks that are exposed within the Bekhme Formation for cement production in the Shakrook anticline. The large thickness of the exposed rocks, quarrying conditions, and preexisting data encouraged the research team to select a relevant section within the Bekhme Formation at Shakrook Mountain to perform the current research.

### *B. Location*

The sampled section is located in a deep cut valley along the northeastern limb of Shakrook anticline, about 10 km southeast of Hareer town (Fig. 1) and about 70 km NE of Erbil city. It can be reached from Erbil city through a paved road that leads to Ranya city. The section is limited by the following coordinates (from bottom to top): At elevation of 978 m, coordinates 36° 25' 59.66″ N, 44° 27' 36.57″ E, and elevation of 998 m with coordinates of 36° 26' 09.59″ N, 44° 27' 36.05″ E, respectively.

### *C. Previous Works*

Since the past decade, many studies were performed to evaluate the carbonate rocks for different industrial uses, especially for cement production. These studies were briefed hereinafter.

Sissakian, et al. (2019) studied the carbonate rocks that are exposed within the Pila Spi Formation in the southwestern limb of Permam anticline, near Al-Maseef. They reported about the presence of excellent quality and quantity of limestone. Ghafur, et al. (2020) studied and evaluated the exposed beds of the Bekhme Formation at Galley Ali Beg gorge. They concluded that excellent deposit for cement industry exists at the studied location. Sissakian, et al. (2020)

ARO-The Scientific Journal of Koya University
Vol. X, No. 1 (2022), Article ID: ARO.10907. 8 pages
DOI: 10.14500/aro.10907
Received: 21 November 2021; Accepted: 03 March 2022
Regular research paper: Published: 25 March 2022
Corresponding author's email: f.khajeek@ukh.edu.krd

http://dx.doi.org/10.14500/aro.10907

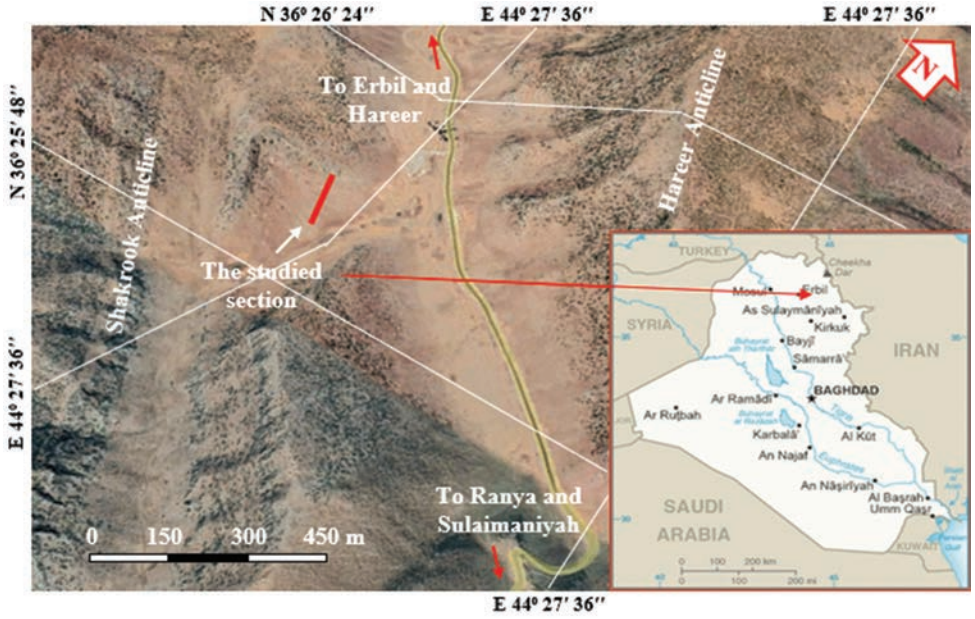


Fig. 1. Satellite image showing the location of the studied section.

studied and evaluated the exposed rocks within the Pila Spi Formation at Haibat Sultan Mountain, along a section that is located 17 km east of Koya town. They concluded that excellent deposit exists for cement production. Sissakian, et al. (2021) studied the rocks of the Bekhme Formation at the Hareer anticline and have found that the rocks are excellent for cement plant.

## II. Geological Setting

The geological setting of the studied section at the Shakrook anticline is briefly described hereinafter including the following main topics based on Fouad (2015) and Sissakian and Al-Jiburi (2014).

### *A. Geomorphology*

The main geomorphological units that are developed near the studied section are as follows:

- Structural denudational unit, the anticlinal ridges are well developed in hard to very hard limestone beds of the Bekhme Formation. The anticlinal ridges represent excellent locations for quarrying.
- Denudational unit, slope sediments are well developed; usually of large fallen blocks that attain few cubic meters.

### *B. Stratigraphy*

The studied and sampled section is within the Bekhme Formation (Fig. 2). The Bekhme Formation is described briefly hereinafter.

Bekhme Formation (Upper Cretaceous) consists of well bedded (30–70 cm) to massive (1–1.5 m) limestone and very rare dolomitic limestone, light gray and brown in color, hard to very hard, usually splintery. The exposed thickness of the formation in the studied site is about 180 m.

### *A. Tectonics and structural Geology*

The Shakrook anticline is located in the High Folded Zone. The High Folded Zone belongs to the Outer Platform of the Arabian Plate. The zone is also a part of the Zagros Fold – Thrust Belt. The belt is developed due to the collision of the Arabian and Iranian plates since the Late Cretaceous Period. It is still ongoing with a convergent plate contact (Alavi, 2004, and Fouad, 2015). The Shakrook anticline is a double plunging anticline with a NW-SE trend, it is very complicated due to four thrust faults (Sissakian, et al., 2022).

## III. Materials and Methods

The studied section for sampling was chosen along the northeastern limb of the Shakrook anticline with the Bekhme Formation based on the experience of the authors and previously performed works. The exposed rocks along the studied section were sampled and described in the field (Fig. 2a) and tested by HCl acid to indicate their reaction (Fig. 2b). The sampling interval was measured by a measuring tape and kept constant; 5 m, apart from samples No. 19 and 20, where the interval was changed to 10 m (Table 1). Within the section, there is a covered slope (about 15 m) by fallen limestone rocks up to 1 cubic meter (Fig. 3). Each sample was collected in the form of small chips to be a representative sample of the completely sampled interval.

Samples were kept in nylon sacks, numbered, and well documented (Table 1). Totally, 20 samples were collected representing 110 m, beside the covered slope of 15 m, which exists along the uppermost part of the sampled section. The authors believe that the covered slope also includes limestone bed like those above and below the covered interval. The Iraqi Standard No. 5 (1984) (Table 2) for the cement production was used to indicate the suitability of the collected samples for the cement industry.

*C. Sample Preparation*

The collected 20 samples were ground to powder, using an electrical grinder. The powdered sample was well mixed to have a homogeneous representative sample. Then, 10 g of each powdered sample was pressed into a special pellet. The pressed pellet was dried in an electrical oven for 2 h. The prepared pellets were mounted in an XRF instrument (XRF PW2404) at the Analytical Laboratories of the Faculty of Science at the Tarbiat Modares University, Iran, to indicate the main oxides (CaO, MgO, $Al_2O_3$, $Fe_2O_3$, $Na_2O$, $K_2O$, and $SO_3$), and Cl and L.O.I., which are used to indicate the suitability of the sampled rocks for cement industry. The used XRF instrument is calibrated with Philips Analytical X-Ray B.V. standards and has a certificate of the secondary for the *SEMIQ*. The detection limit of the instrument is 20 ppm–100%. The monitoring system is repeated every week with SRM samples. Moreover, the internal method of QC is used by means of SRM samples every month.

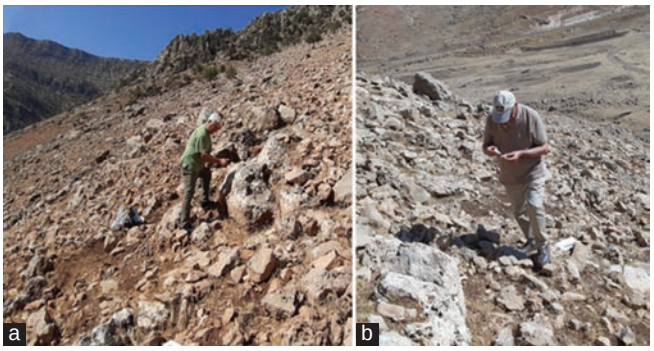


Fig. 2. Sample collection, (a) sample collecting and description, (b) sample testing by HCl.

Fig. 3. General view of the sampled section, note the absence of overburden and the covered space below the top ridge (Photo looking NW).

For the industrial assessment purpose, the concentrations of all indicated oxides, Cl, and L.O.I. (Table 3) of each sample were changed to a weighted average. This is because the sampling interval is not uniform; accordingly, for industrial assessment, the weighted average should be calculated.

To indicate the proper concentration of the oxides, Cl, and L.O.I. within each sample, the weighted percentage of each oxide in each sample is calculated by the following equation (IET, 2021)

$$Weighted\ Percentage = \frac{\sum C1 + C2 + C3 + C4 + Ci}{\sum T1 + T2 + T3 + T4 + Ti} \quad (1)$$

Where, C = the percentage of each oxide multiplied by the sample's thickness (T),

The weighted average is calculated as follows:

$$Weighted\ Avergae = \frac{\sum W1 + W2 + W3 + W4 + Wi}{\sum T1 + T2 + T3 + T4 + Ti} \quad (2)$$

Where, W = the weighted percentage of each oxide multiplied by the sample's thickness (T),

TABLE I
FIELD DESCRIPTION OF THE COLLECTED 20 SAMPLES.

| Sample No. | Rock name | Color | Hardness | Thick (m) | Reaction with HCl | Description |
|---|---|---|---|---|---|---|
| 1 | Limestone | Light brown | Very hard | 5 | High | Well bedded |
| 2 | Limestone | Dark gray | Very hard | 5 | High | Massive |
| 3 | Dolomitic limestone | Dark gray | Very hard | 5 | Low | Thickly bedded |
| 4 | Limestone | Light gray | Very hard | 5 | High | Thickly bedded |
| 5 | Limestone | Light gray | Hard | 5 | High | Well bedded |
| 6 | Limestone | Light gray | Very hard | 5 | High | Well bedded |
| 7 | Limestone | Light gray | Hard | 5 | Low | Well bedded |
| 8 | Limestone | Light gray | Hard | 5 | Low | Well bedded |
| 9 | Limestone | Light gray | Hard | 5 | Low | Well bedded |
| 10 | Limestone | Gray | Very hard | 5 | High | Thickly bedded |
| 11 | Limestone | Gray | Hard | 5 | Low | Thickly bedded |
| 12 | Dolomitic limestone | Gray | Hard | 5 | Low | Thickly bedded |
| 13 | Limestone | Dark gray | Hard | 5 | Low | Massive |
| 14 | Limestone | Gray | Hard | 5 | High | Massive |
| 15 | Limestone | Gray | Very hard | 5 | Low | Thickly bedded |
| 16 | Limestone | Gray | Hard | 5 | High | Thickly bedded |
| 17 | Limestone | Light gray | Very hard | 5 | High | Thickly bedded |
| Covered slope (about 15 m) by scree of large fallen blocks of limestone | | | | | | |
| 18 | Limestone | Gray | Very hard | 5 | High | Massive |
| 19 | Limestone | Gray | Very hard | 10 | High | Thickly bedded |
| 20 | Limestone | Gray | Very hard | 10 | High | Thickly bedded |
| Total thickness of the sampled rocks | | | | | 110 m | |
| Total thickness of the sampled section | | | | | 125 m | |

 http://dx.doi.org/10.14500/aro.10907

Table II
Iraqi Standard No. 5 for Cement Production, 1984 (Iraqi Standardization and Quality Control, 2016) and other specification.

| Specifications of industries (%) (After Sissakian, 2018) | | | | | | | | |
|---|---|---|---|---|---|---|---|---|
| Cement industry | | Current study | Paint industry | | Current study | Sugar industry | | Current study |
| CaO | >45.00 | 50.622 | $CaCO_3$ | >99.5 | 94.042 | MgO | < 4.00 | 1.477 |
| MgO | <2.00 | 1.477 | $SiO_2$ | <1.00 | 0.602 | CaO | >55.0 | 54.5 |
| $Fe_2O_3$ | <0.10* | 0.101 | $Al_2O_3$ | <0.05 | 0.214 | $Al_2O_3$ | <0.27 | 0.214 |
| $SO_3$ | <1.00 | | $Fe_2O_3$ | <0.05 | 0.101 | Fe2O3 | <0.09 | 0.101 |
| Cl | 0.50–1.00 | | L.O.I. | >43.00 | 43.42 | $SiO_2$ | <0.66 | 0.602 |
| L.O.I. | >43.00 | 43.42 | | | $CaCO_3$=CaO+L.O.I. | | | |
| * For white cement only | | | | | $MgCO_3$=MgO L.O.I. | | | |
| Glass industry | | Current study | Paper industry | | Current study | Legend | | |
| $CaCO_3$ | >98.00 | 99.43 | $CaCO_3$ | >90 | 99.43 | | | |
| $SiO_2$ | <2.00 | 0.602 | MgO | <1.5 | 1.477 | Fit with the standard | | |
| MgO | <0.05 | 1.477 | SiO2 | <1.5 | 0.602 | Near to the standard | | |
| $Fe_2O_3$ | <0.06 | 0.31 | $SO_3$ | <1.0 | | Out of the standard | | |
| L.O.I. | >43.00 | 43.42 | I.R. | <4.5 | 0.35 | Not analyzed or detected | | |

Table III
Chemical Composition of the Analyzed 20 Samples by Means of XRF.

| Sample No. | CaO % | MgO % | $SiO_2$ % | $Fe_2O_3$ % | $Al_2O_3$ % | $Na_2O$ % | $K_2O$ % | $SO_3$ % | Cl % | L.O.I. % |
|---|---|---|---|---|---|---|---|---|---|---|
| 1 | 51.561 | 1.224 | 2.396 | 0.27 | 0.527 | 0.032 | N.D. | 0.063 | 0.015 | 43.81 |
| 2 | 54.272 | 1.036 | 0.345 | 0.059 | 0.075 | 0.029 | N.D. | 0.040 | 0.019 | 43.81 |
| 3 | 48.780 | 2.269 | 0.634 | 0.093 | 0.264 | 0.022 | 0.044 | 0.082 | 0.024 | 46.72 |
| 4 | 54.271 | 1.362 | 0.343 | 0.063 | 0.075 | 0.027 | 0.031 | 0.037 | 0.023 | 43.80 |
| 5 | 54.200 | 1.108 | 0.347 | 0.059 | 0.075 | 0.027 | N.D | 0.041 | 0.019 | 43.78 |
| 6 | 50.454 | 3.753 | 0.518 | 0.096 | 0.232 | 0.031 | 0.035 | 0.072 | 0.013 | 44.76 |
| 7 | 49.745 | 3.115 | 0.608 | 0.115 | 0.295 | 0.023 | 0.031 | 0.093 | 0.023 | 45.88 |
| 8 | 50.886 | 2.005 | 0.096 | 0.062 | 0.170 | 0.042 | 0.027 | 0.050 | 0.025 | 46.28 |
| 9 | 50.745 | 2.115 | 0.606 | 0.117 | 0.290 | 0.028 | 0.033 | 0.091 | 0.022 | 45.83 |
| 10 | 51.443 | 1.981 | 1.500 | 0.338 | 0.681 | 0.045 | 0.145 | 0.075 | 0.005 | 43.73 |
| 11 | 50.637 | 2.160 | 1.087 | 0.127 | 0.302 | 0.058 | 0.052 | 0.067 | 0.036 | 46.40 |
| 12 | 45.567 | 3.885 | 1.080 | 0.145 | 0.518 | 0.067 | 0.062 | 0.055 | 0.035 | 46.87 |
| 13 | 53.495 | 2.049 | 0.574 | 0.058 | 0.217 | 0.049 | N.D. | 0.039 | 0.031 | 46.44 |
| 14 | 53.138 | 1.072 | 0.723 | 0.132 | 0.231 | 0.040 | 0.038 | 0.089 | 0.006 | 44.42 |
| 15 | 52.660 | 1.277 | 0.788 | 0.156 | 0.297 | 0.031 | 0.052 | 0.043 | 0.018 | 44.66 |
| 16 | 51.440 | 2.213 | 0.430 | 0.094 | 0.191 | 0.029 | 0.039 | 0.020 | 0.014 | 44.99 |
| 17 | 54.288 | 1.344 | 0.341 | 0.067 | 0.080 | 0.032 | 0.058 | 0.036 | 0.029 | 43.88 |
| Covered slope by large limestone blocks | | | | | | | | | | |
| 18 | 55.201 | 0.423 | 0.240 | 0.055 | 0.086 | 0.028 | N.D. | 0.044 | 0.014 | 55.27 |
| 19 | 54.275 | 1.358 | 0.345 | 0.061 | 0.073 | 0.029 | 0.054 | 0.039 | 0.021 | 43.80 |
| 20 | 55.275 | 0.358 | 0.245 | 0.050 | 0.083 | 0.025 | N.D. | 0.041 | 0.017 | 43.82 |

N.D.: Not detected

Table IV
Weighted Averages of the Oxides in the 20 Collected Samples.

| Sample No. | Thick. (m) | Weighted averages (%) | | | | | | | | | |
|---|---|---|---|---|---|---|---|---|---|---|---|
| | | CaO | MgO | $SiO_2$ | $Fe_2O_3$ | $Al_2O_3$ | $Na_2O$ | $K_2O$ | $SO_3$ | Cl | L.O.I. |
| 1 | 5 | 257.805 | 6.120 | 11.98 | 1.35 | 2.635 | 0.16 | N.D. | 0.32 | 0.075 | 219.05 |
| 2 | 5 | 271.36 | 5.180 | 1.725 | 0.295 | 0.375 | 0.15 | N.D. | 0.20 | 0.095 | 219.05 |
| 3 | 5 | 243.900 | 1.345 | 3.17 | 0.465 | 1.32 | 0.11 | 0.22 | 0.41 | 0.120 | 233.60 |
| 4 | 5 | 271.355 | 6.810 | 1.72 | 0.315 | 0.375 | 0.14 | 0.16 | 0.19 | 0.115 | 219.00 |
| 5 | 5 | 271.000 | 5.540 | 1.74 | 0.295 | 0.375 | 0.14 | N.D. | 0.21 | 0.095 | 218.90 |
| 6 | 5 | 252.270 | 18.765 | 2.59 | 0.48 | 1.16 | 0.16 | 0.18 | 0.36 | 0.065 | 223.80 |
| 7 | 5 | 248.725 | 15.575 | 3.04 | 0.575 | 1.475 | 0.12 | 0.16 | 0.47 | 0.115 | 229.40 |
| 8 | 5 | 254.430 | 10.025 | 0.48 | 0.31 | 0.85 | 0.21 | 0.14 | 0.25 | 0.125 | 231.40 |
| 9 | 5 | 253.725 | 10.575 | 3.03 | 0.585 | 1.45 | 0.14 | 0.17 | 0.46 | 0.110 | 229.15 |
| 10 | 5 | 257.215 | 9.905 | 7.50 | 1.69 | 3.405 | 0.23 | 0.73 | 0.38 | 0.025 | 218.65 |
| 11 | 5 | 253.185 | 10.800 | 5.44 | 0.635 | 1.51 | 0.29 | 0.26 | 0.34 | 0.180 | 232.00 |
| 12 | 5 | 227.835 | 19.425 | 5.40 | 0.725 | 2.59 | 0.34 | 0.31 | 0.28 | 0.175 | 234.35 |
| 13 | 5 | 267.475 | 10.245 | 2.87 | 0.29 | 1.085 | 0.25 | N.D. | 0.19 | 0.155 | 232.20 |
| 14 | 5 | 265.69 | 5.360 | 3.62 | 0.66 | 1.155 | 0.20 | 0.19 | 0.45 | 0.030 | 232.10 |
| 15 | 5 | 263.300 | 6.385 | 3.94 | 0.78 | 1.485 | 0.16 | 0.26 | 0.22 | 0.090 | 223.30 |
| 16 | 5 | 257.200 | 11.065 | 2.15 | 0.47 | 0.955 | 0.15 | 0.19 | 0.10 | 0.070 | 224.95 |
| 17 | 5 | 271.440 | 6.720 | 1.71 | 0.335 | 0.4 | 0.16 | 0.29 | 0.18 | 0.145 | 219.40 |
| Covered slope by large limestone blocks | | | | | | | | | | | |
| 18 | 5 | 276.005 | 2.115 | 1.20 | 0.275 | 0.43 | 0.14 | N.D. | 0.22 | 0.070 | 276.35 |
| 19 | 10 | 542.750 | 13.580 | 3.45 | 0.61 | 0.73 | 0.29 | 0.54 | 0.39 | 0.210 | 438.00 |
| 20 | 10 | 552.750 | 3.580 | 2.45 | 0.5 | 0.83 | 0.25 | N.D. | 0.41 | 0.170 | 438.20 |
| Average | | 50.082 | 1.557 | 0.602 | 0.101 | 0.214 | 0.033 | 0.033 | 0.052 | 0.019 | 43.42 |
| $CaCO_3$ = (CaO+L.O.I.) | | | | | | | | | 93.502 | | |

N.D.: Not detected

The acquired results of the weighted averages of all tested oxides and other elements are presented in Table 4. Then, the results were compared with the Iraqi Standard No.5 (1984) (Table 2) for the cement production to indicate their suitability for cement production.

## IV. Results

The acquired results of the weighted averages from the 20 collected and analyzed samples (Table 4) were compared with the Iraqi Standard No.5 (1984) for cement industry, which is shown in Table 2 to indicate the suitability of the sampled limestone beds to be used in cement industry and other industries. Hereinafter are the details of the requirements of cement production; as the raw materials are concerned.

### *A. Limestone*

The acquired results (Table 4) of the 20 samples from the Shakrook anticline showed excellent matching with the Iraqi Standard No.5 (1984) for cement industry (Table 2). The average CaO is 50.082% and that of the MgO is 1.557% (Table 4). However, when adding the average concentrations of CaO and MgO of the covered slope of 15 m from calculation of the average concentrations of the CaO and MgO for the sample Nos. 17, 18, 19, and 20, the average concentrations will be as shown in Table 5. In addition, when adding the acquired averages of CaO and MgO to the covered slope, then the average concentrations will be as shown in Table 6.

It is clear there is a slight positive improvement in the concentrations of CaO and MgO (Table 6) as compared to the results of the concentrations without considering of the covered slope results (Table 4).

The $Fe_2O_3$ average content is 0.101% which is almost the same as for white cement production (Table 2); therefore, the exposed rocks in the sampled section can be used for the production of white cement too.

### *B. Clay Deposit*

In the cement production, the second main raw material is clay, which may account up to 40% of the raw mix (MRP, 2020). This percentage depends on the chemical composition of the used limestone. Clay is added as raw material to produce the cement clinker as a supplement to the adjusting of a kiln input. The best content of calcium carbonate in the raw material for the clinker firing is 75–80%. When the composition of the raw materials is not the same as these values, then many additives are used. Adding clay raw materials will reduce the calcium carbonate content in the mix and increase the contents of $SiO_2$, $Al_2O_3$, and $Fe_2O_3$ (MRP, 2020).

An enormous clay deposit occurs within the alluvial fan sediments, which are developed opposite to the Shakrook anticline, along the whole foot slopes of the Hareer Mountain (Fig. 4). These deposits are rich in limestone fragments of different sizes that derived from the weathering and erosion of the limestone beds of the Bekhme Formation.

The alluvial fan deposits can be divided easily into two main parts, coarse, and fine grained. The former is deposited along and near the foothills of the Hareer Mountain, whereas the latter is deposited after the coarse materials and the break in the slope forming gently sloping areas (Fig. 4). The thickness of these deposits' ranges from 1 m up to about 10 m, but the coverage area (Fig. 4) is huge.

It is worth mentioning that, west of the sampled section, the Gercus, Fatha, Injana, Mukdadiya and Bai Hassan formations are exposed and include huge thicknesses of claystone that has produced reddish-brown clayey soil (Fig. 5), which can be used as the clay raw material. All those cement plants in the Bazian vicinity in the Sulaimaniyah Governorate use claystone from the Injana, Mukdadiya, and Bai Hassan formation as the clay raw material.

### *C. Gypsum Deposit*

Gypsum is added to the clinker by about 5% depending on the chemical composition of the clinker. The main role of the gypsum is to retard the consolidation time of the concrete (Shmitt, 2012). Therefore, gypsum is very essential for cement production. However, no gypsum as deposit occurs neither in the Shakrook Mountain nor nearby areas, and this is the only disadvantage in the studied area as far as cement production is concerned.

Table V
Weighted Averages for the Sample Nos. 17–20.

| Sample No. | Thick. (m) | Weighted averages (%) | | | | | | | | | |
|---|---|---|---|---|---|---|---|---|---|---|---|
| | | CaO | MgO | $SiO_2$ | $Fe_2O_3$ | $Al_2O_3$ | $Na_2O$ | $K_2O$ | $SO_3$ | Cl | L.O.I. |
| 17 | 5 | 271.440 | 6.720 | 1.71 | 0.335 | 0.4 | 0.16 | 0.29 | 0.18 | 0.145 | 219.40 |
| Covered slope by large limestone blocks | | | | | | | | | | | |
| 18 | 5 | 276.005 | 2.115 | 1.20 | 0.275 | 0.43 | 0.14 | N.D. | 0.22 | 0.070 | 276.35 |
| 19 | 10 | 542.750 | 13.580 | 3.45 | 0.61 | 0.73 | 0.29 | 0.54 | 0.39 | 0.210 | 438.00 |
| 20 | 10 | 552.750 | 3.580 | 2.45 | 0.5 | 0.83 | 0.25 | N.D. | 0.41 | 0.170 | 438.20 |
| Total | | 1642.945 | 25.995 | | | | | | | | |
| Average A | | 54.765 | 0.867 | | | | | | | | |

Table VI
Weighted Averages for the Sample Nos. (1–20) + the Covered Slope.

| Sample No. | Thick (m) | Weighted averages (%) | | | | | | | | | |
|---|---|---|---|---|---|---|---|---|---|---|---|
| | | CaO | MgO | $SiO_2$ | $Fe_2O_3$ | $Al_2O_3$ | $Na_2O$ | $K_2O$ | $SO_3$ | Cl | L.O.I. |
| 1 | 5 | 257.805 | 6.120 | 11.98 | 1.35 | 2.635 | 0.16 | N.D. | 0.32 | 0.075 | 219.05 |
| 2 | 5 | 271.36 | 5.180 | 1.725 | 0.295 | 0.375 | 0.15 | N.D. | 0.20 | 0.095 | 219.05 |
| 3 | 5 | 243.900 | 1.345 | 3.17 | 0.465 | 1.32 | 0.11 | 0.22 | 0.41 | 0.120 | 233.60 |
| 4 | 5 | 271.355 | 6.810 | 1.72 | 0.315 | 0.375 | 0.14 | 0.16 | 0.19 | 0.115 | 219.00 |
| 5 | 5 | 271.000 | 5.540 | 1.74 | 0.295 | 0.375 | 0.14 | N.D. | 0.21 | 0.095 | 218.90 |
| 6 | 5 | 252.270 | 18.765 | 2.59 | 0.48 | 1.16 | 0.16 | 0.18 | 0.36 | 0.065 | 223.80 |
| 7 | 5 | 248.725 | 15.575 | 3.04 | 0.575 | 1.475 | 0.12 | 0.16 | 0.47 | 0.115 | 229.40 |
| 8 | 5 | 254.430 | 10.025 | 0.48 | 0.31 | 0.85 | 0.21 | 0.14 | 0.25 | 0.125 | 231.40 |
| 9 | 5 | 253.725 | 10.575 | 3.03 | 0.585 | 1.45 | 0.14 | 0.17 | 0.46 | 0.110 | 229.15 |
| 10 | 5 | 257.215 | 9.905 | 7.5 | 1.69 | 3.405 | 0.23 | 0.73 | 0.38 | 0.025 | 218.65 |
| 11 | 5 | 253.185 | 10.800 | 5.44 | 0.635 | 1.51 | 0.29 | 0.26 | 0.34 | 0.180 | 232.00 |
| 12 | 5 | 227.835 | 19.425 | 5.40 | 0.725 | 2.59 | 0.34 | 0.31 | 0.28 | 0.175 | 234.35 |
| 13 | 5 | 267.475 | 10.245 | 2.87 | 0.29 | 1.085 | 0.25 | N.D. | 0.19 | 0.155 | 232.20 |
| 14 | 5 | 265.69 | 5.360 | 3.62 | 0.66 | 1.155 | 0.20 | 0.19 | 0.45 | 0.030 | 232.10 |
| 15 | 5 | 263.300 | 6.385 | 3.94 | 0.78 | 1.485 | 0.16 | 0.26 | 0.22 | 0.090 | 223.30 |
| 16 | 5 | 257.200 | 11.065 | 2.15 | 0.47 | 0.955 | 0.15 | 0.19 | 0.10 | 0.070 | 224.95 |
| 17 | 5 | 271.440 | 6.720 | 1.71 | 0.335 | 0.4 | 0.16 | 0.29 | 0.18 | 0.145 | 219.40 |
| C. S. | 15 | 821.475 | 13.005 | | | | | | | | |
| 18 | 5 | 276.005 | 2.115 | 1.20 | 0.275 | 0.43 | 0.14 | N.D. | 0.22 | 0.070 | 276.35 |
| 19 | 10 | 542.750 | 13.580 | 3.45 | 0.61 | 0.73 | 0.29 | 0.54 | 0.39 | 0.210 | 438.00 |
| 20 | 10 | 552.750 | 3.580 | 2.45 | 0.5 | 0.83 | 0.25 | N.D. | 0.41 | 0.170 | 438.20 |
| Average | | 50.622 | 1.477 | 0.602 | 0.101 | 0.214 | 0.033 | 0.033 | 0.052 | 0.019 | 43.42 |
| $CaCO_3$ = (CaO+L.O.I.) | | | | | | | | | 94.042 | | |

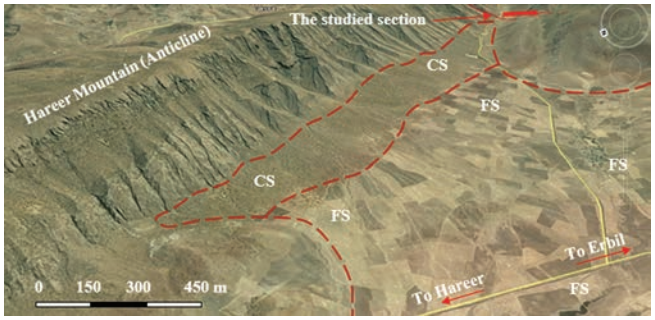


Fig. 4. Satellite image of the Hareer Mountain with the clay sediments, CS= Coarse sediments, FS= Fine sediments.

Fig. 5. The reddish-brown soil developed along the Hareer Mountain (Photo looking NE).

http://dx.doi.org/10.14500/aro.10907

The nearest gypsum to the Shakrook Mountain, which is used as a deposit is at the Aghjalar vicinity; along the Qara Dagh Mountain, it is southwest of the Sulaimaniyah city about 100 km away from the sampled section (Sissakian and Fouad, 2015). However, another gypsum deposit occurs at Qara Chough Mountain which is about 50 km south of the Erbil city and 120 km south of the Shakrook Mountain.

## V. Discussion

### *A. Cement Production*

In the IKR, there are six cement plants (Fig. 6). Five of them are located in the Sulaimaniyah Governorate, whereas the sixth plant is located in the Erbil Governorate near the Makhmour town, which is about 45 km SW of the capital Erbil. The whole IKR is witnessing an enormous development in the infrastructure besides, tens of the recently constructed residential sites. Accordingly, an enormous amount of cement is required to construct those industrial sites and develop the infrastructure. However, since there is only one cement plant within the Erbil Governorate, it is very crucial to construct cement plants within the Erbil Governorate. To plan locations for cement plants, it should be significant to find limestone beds that are suitable for cement industry and to encourage investors to utilize the found limestone beds for the construction of cement plants.

With the bulk of the carried out work; however, it is not possible to consider the studied section in the Shakrook anticline as a deposit. Detailed exploration should be carried out to estimate the reserve of the deposit following JORC (1999) instructions. Moreover, a relevant location for the cement plant should be considered when choosing a site for sampling, besides the quarrying conditions. Therefore, the selected section for sampling fulfills all the requirements including: (1) The quality of the limestone, (2) the quarrying conditions, (3) available clay deposits, and (4) available and relevant area for the cement plant. The mentioned aspects are discussed hereinafter.

- Quality of the Limestone: The acquired results from XRF of the tested 20 samples (Table 4) indicate excellent quality of limestone for cement production according to the Iraqi specification for cement industry (Table 2).-
- Quarrying Conditions: The selected site for sampling fulfills the following conditions:
- There is no overburden not only at the sampling site (Fig. 3) but also the whole Shakrook Mountain (Fig. 7)
- The presence of high cliffs and anticlinal ridges (Figs. 7 and 8) will facilitate the quarrying of the limestone beds,
- The plunge of the Shakrook anticline can be the start point of the quarry (Fig. 9),
- The widely exposed Bekhme Formation along both limbs of the Shakrook anticline (Figs. 7 and 8) will give a very high limestone reserve and encourage the construction of a cement plant,
- The well-bedded nature of the exposed limestone (Fig. 10) will facilitate the quarrying,


Fig. 6. Locations of the six existing cement plants in the IKR. Cement Plants: T= Taslouja, M= Mass, L= Lafarge, D= Delta, G= Gasin, and K = Kar.

Fig. 7. (Top) General view of the Shakrook anticline, note the bare anticlinal ridges (Photo looking toward SE), and (Bottom) the opposite site of the sampled location, note the large valley that can be used as service road to reach the huge reserves of the limestone (above photo) (Photo looking toward SE).

- The absence of villages near the sampled site and near surrounding will decrease the negative environmental impact on the villagers.
- Available Clay Deposit: The clayey soil within the alluvial fans' sediments (Figs. 4-6), and within many geological formations, which has produced red clayey soil due to weathering (Fig. 5) can be used as clay deposit for cement industry.
- Available Site for the Cement Plant: The presence of wide and vast flat area near the plunge of the Shakrook anticline (Fig. 9) can be used as a site for construction of a cement plant. The main road to the Erbil city and to the Hareer and Aqra towns passes just near the recommended site.

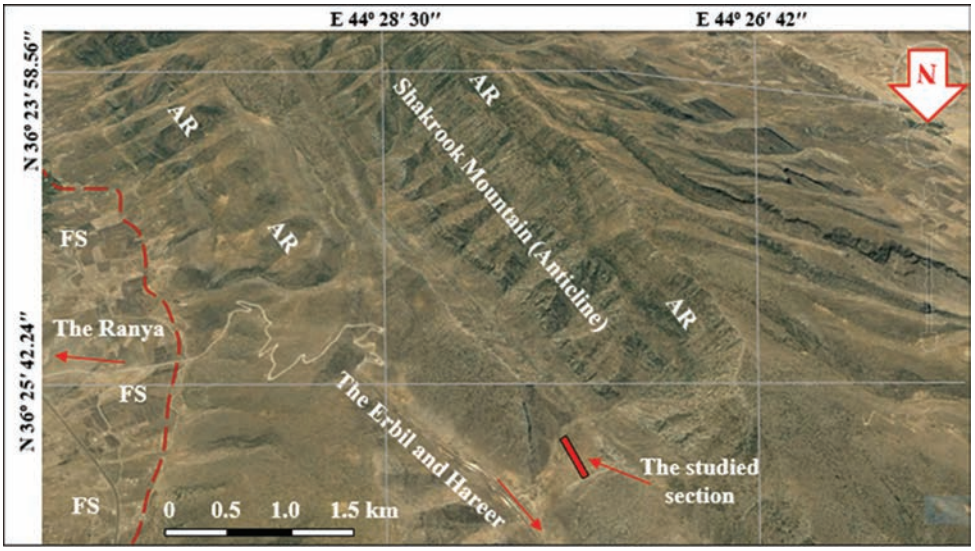


Fig. 8. Satellite image of the sampled section and part of the Shakrook anticline. AR= Anticlinal ridge, FS= Fine sediments (soil). Note the huge amount of the exposed limestone beds without overburden.

Fig. 9. A wide plain in front of the Shakrook Mountain. The sampled section is behind the plunge of the anticline shown in the left side (Photo looking toward SE).

*B. Drug Industry and Human's Health*

Pure limestone can also be used in drug industry (CONGAL, 2021). The acquired results from the tested samples showed that the weighted average of the calcium carbonate ($CaCO_3$) concentration is high 94.042 %, which means a pure calcium carbonate with very low concentrations of other oxides (Table 6). Therefore, such pure calcium carbonate can be used in drug industry (CONGAL, 2021).

Calcium has different functions for the human's health, it helps in having healthy bones, muscles, nervous system, and heart. It is also used as an antacid to relieve heartburn, acid indigestion, and stomach upset. Calcium carbonate is a dietary supplement for the human, especially when the amount of calcium taken in the diet is not enough.

Pure calcium carbonate can also be used for the treatment of cancer cases, it will gradually dissolve in the weal acidic microenvironment of cancer cells, since the loaded doxorubicin can be released over the period of 14 days with pH responsive and sustained manner to treat cancers specifically and significantly (Render, et al., 2016).

*C. Miscellaneous*

The exposed limestone beds in the sampled section and surrounding area can also be used as mineral fillers in many industries such as plastics, paper, paint, and rubber industries (Table 2) and are used in various applications from tires, wire cable, flexible PVC, pipes, flooring, coatings, and adhesives.

The main advantages of using the calcium carbonate as filler include a high surface gloss or opacity. Moreover, when the particle size is carefully controlled, then $CaCO_3$ helps to increase both impact strength and flexural modulus (i.e., stiffness) (CONGAL, 2021).

*D. Geological Reserve Estimation for a Cement Plant*

We have added this attempt to estimate the reserve of the limestone along the sampled section and near surrounding, since the XRF results are very encouraging (Tables 4 and 6). Moreover, the quarrying conditions are very favorable.

Accordingly, we will assume a quarry area of 1.0 $km^2$, then the geological reserve can be estimated as follows:

The surface area = 1,000,000 $m^2$

The thickness of the sampled part = 115 + 15 (covered slope) m, then the total thickness will be 130 m. We have added the covered area also because the rocks below the slope (sample Nos. 17 and 18) and above the slope (sample nos. 19 and 20) have high CaO content and low MgO content (Table 6).

The volume of the limestone within the supposed quarry = 1,000,000 × 130 = 13 × $10^7$ $m^3$

The average density of the limestone is about 2400 kg/$m^3$,

The weight of the limestone which can be quarried = 2400×13×$10^7$ = 312×$10^9$ kg

= 312,000,000 tons.

The second significant raw material that is used in the raw mix for cement production is the clay, which is available near to the sampled area where huge alluvial fans cover large flat area (Figs. 4, 5 and 9). The added clay to the raw mix is about 30–40 % of the used limestone.

Therefore, 35% of 312,000,000 tons = 109,200,000 tons

Total used raw mix = 312,000,000 + 109,200,000 = 421,200,000 tons

If the daily production of a cement plant is 5000 tons, then the used quantity of the raw mix is about 10,000 tons/day, this means that the estimated reserve can be used for about

421,200,000 ÷ 10,000 = about 42,120 days, which is about 127 years. We have considered 330 days, as 30 days are supposed to be for maintenance and other irrelevant working days.

The exposed limestone beds within the Bekhme Formation surrounding the sampled section even in Hareer anticline, which is few hundred meters north of the sampled section, have almost the same chemical composition (Sissakian, et al., 2021). Therefore, the area of the suggested quarry as $1^2$ km can be extended; consequently, the calculated geologic reserve will be more than the estimated. It is worth to mention; however, that this is a preliminary geological reserve estimation with a low level of confidence according to JORC (1999). Therefore, the acquired results cannot be used for investments, unless relevant site investigation is carried out to estimate the true reserve which can be invested with high level of confidence according to JORC (1999). The detailed site investigation should include boreholes' drilling of continuous core with core recovery not <90%, and with spacing not more than 150 m and core sampling of 1 m interval, and the analyzing of all collected samples for the main oxides and other elements as mentioned in Table 2.

## VI. Conclusions

The acquired results from the XRF test, which was applied on the collected 20 rock samples from the Bekhme Formation at the Shakrook anticlines, showed excellent limestone with average concentrations of CaO and MgO at 50.622% and 1.4777%, respectively, that the sampled rocks are excellent for cement production. Moreover, the average concentration of the $CaCO_3$ is 94.042%, which means that the exposed limestone beds can be used for drug industry and other human's health concerns. From the author's experience, the exposed rocks in the sampled section can also be used for paint, paper, rubber, and plastic industries.

## VII. Acknowledgments

The authors would like to pass their sincere thanks to the authorities at the Faculty of Engineering/Koya University and the University of Kurdistan Hewler for providing logistics during this research work.

## References

Alavi, M., 2004. Regional stratigraphy of the Zagros Fold-thrust belt of Iran and its proforel and evolution. *American Journal of Science*, 304, pp.1-20.

CONGAL, 2021. C*alcium Carbonate. Plastic, Rubber, Paint. Internet data*. Available form: https://www.congcal.com/markets/plastics-rubber [Last accessed on 2021 Mar 29].

Fouad, S.F., 2015. Tectonic map of Iraq, scale 1: 1000000. 3rd edition. *Iraqi Bulletin of Geology and Mining*, 11(1), pp.1-8.

Ghafur, A.A., Sissakian, V.K. and Bapir, A.M., 2020. Industrial assessment of the rocks of the Bekhme formation in Korek mountain, Iraqi Kurdistan Region. *Carbonates and Evaporates*, 36(1), pp.1-10.

Indeed Educational Team, 2021. *How to Calculate Weighted Average in 3 Steps (with Example). Internet Data*. Available from: https://www.indeed.com/career-advice/career-development/how-to-calculate-weighted-average [Last accessed on 2021 Aug 12].

Iraqi Standardization and Quality Control, 2016. *Iraqi Standards for cement Production, 1984. Internet Data*. Available from: http://www.uokufa.edu.iq/qclab/wp-content/uploads/2016/03 [Last accessed on 2016 Aug 31].

JORC, 1999. *Australian Code for Reporting of Mineral Resources*. Available form: http://www.jorc.org/docs/historical_documents/1999_jorc_code.pdf [Last accessed on 2021 Sep 21].

Mineral Resources of Polland, 2020. *Clay Raw Materials for Cement Production. General Information and Occurrence. Internet Data*. Available from: http://www.geoportal.pgi.gov.pl/surowce/skalne/ilaste_cement [Last accessed on 2020 Oct 03].

Render, D., Samuel, T., King, H., Vig, M., Jeelani,S., Jayachandra Babu, R. and Rangari, V., 2016. Biomaterial-derived calcium carbonate nanoparticles for enteric drug delivery. *Journal of Nanomaterials*, 2016, p.3170248.

Shmitt, H., 2012. *Gypsum as a Raw Material in the Gypsum and Cement Industry. Global CemTrader conference*. *Internet Data*. Available from: https://www.youtube.com/watch?v=Zr_kHHl4-IE [Last accessed on 2021 Oct 03].

Sissakian, V.K. and Al-Jiburi, B.M., 2014. Stratigraphy of the high folded zone. *Iraqi Bulletin of Geology and Mining*, 6, pp.73-16.

Sissakian, V.K. and Fouad, S.F., 2015. Geological map of Iraq, scale 1: 1000 000, 4th edition. *Iraqi Bulleting of Geology and Mining*, 11(1), pp.9-18.

Sissakian, V.K., 2018. The minerals wealth in Kurdistan region: A critical review. *UKHJSE*, 2(2), pp.23-36.

Sissakian, V.K., Ahmed, J.M. and Ibrahem, R.K., 2020. Industrial assessment of the carbonate rocks of the Pila Spi formation at Haibat Sultan Mountain, Iraqi Kurdistan Region. *ARO*, 8(1), pp.24-30.

Sissakian, V.K., Ghafur, A.A., Ibrahem, F.I., Abdulhaq, H.A., Hamoodi, D.A. and Omer, H.O., 2021. Suitability of the carbonate rocks of the Bekhme formation for cement industry, Hareer Mountain, Iraqi Kurdistan Region. *Iraqi Geological Journal*, 54(C), pp.59-67.

Sissakian, V.K., Hamoudi, D.A., Omer, H.O. and Niazi, S.A., 2019. Assessment of the Carbonate Rocks of the Pila Spi Formation for Cement Industry, in Permam Mountain, Erbil, Iraqi Kurdistan Region. *UKHJSE*, 3(1), pp.1-9.

# Bioremediation Ability of the Local Isolate *Enterobacter cloacae* from Disposal Site

Hanaa A. Muhammad[1], Hanan T. Subhi[1], Khalid N. Sediq[2]

[1]Department of Biology, Faculty of Science and Health, Koya University, Koya KOY45, Kurdistan Region – F.R. Iraq
[2]Department of Physics, Faculty of Science and Health, Koya University, Koya KOY45, Kurdistan Region – F.R. Iraq

***Abstract*—Illegal dumping is a serious problem that needs to be addressed immediately to preserve human health and the environment as if the pollution that arises from it reaches the groundwater, complications of the remediation processes will increase. To decontaminate the organic and inorganic components, bioremediation seems to be the most environmentally friendly and economically viable technique without further treatment as reported by many studies. In this investigation, samples were taken from the soil of the main dumping area in Koysinjaq in Kurdistan Region of Iraq to determine the most potent bacteria to remediate the existed pollutants. The existence of non-essential minerals and organic compounds in the soil sample was detected using X-ray fluorescence device, and ethane and 1,2-dichloroethane solvents separating technique, respectively. Then, from the same samples, three different naturally occurring bacteria were isolated and cultured under optimized conditions then stimulated for a good result. Finally, spectrophotometer was set at wavelength of 600 nm and used to detect the heaviest growth of bacteria after incubating the cultured bacteria on a mineral salt broth medium with the extracted pollutants at pH 7.0 overnight at 32°C. Based on the highest absorbance, the most effective type of bacteria (*Enterobacter cloacae*) was chosen among others to remediate the organic components in which approximately 90% of them are plastics, medical waste, municipal waste, electrical items, and hydrocarbons, and some heavy metals, for instance aluminum and lead, which were found in the soil.**

***Index Terms*—Bioremediation, Enterobacter cloacae, Organic matter, Dumping area.**

## I. Introduction

Dumping areas cause some significant negative impacts on the environment, therefore, managing and remediating it should be any country's priority (Chandler, 2017). Hence, bioremediation is chosen to be one of the most effective, environmentally friendly, and less expensive treatment options to purify water and soil from organic matters and some metals (Tyagi and Kumar, 2021) (Ganguly, 2018; Jardine and Taylor, 1995; Shen and Wang, 1994; Tyagi and Kumar, 2021), whereas landfills are considered to be necessary to store almost about 55% the partially degradable and undegradable wastes, for example, plastic wrappers, take-out containers, Band-Aids, newspapers and water bottles, and glasses (Chandler, 2017; CHEJ, 2016).

Recently, microbial systems are frequently been used for both soil and water remediation, which can reduce the mass, concentration, and toxicity of the contaminants (Head, 1998) with the consideration of some crucial environmental conditions, for example, the presence of carbon source, pH, temperature, dissolved oxygen, oxidation-reduction potential, and presence of other oxyanions and metal cations (Chandler, 2017; Chen and Hao, 1998; Xia and Boufadel, 2010). Besides, the final product from this process is mainly $CO_2$ and water (Boopathy, 2000; Thomas, Hughes and Daly, 2006). Thus, there is a possibility of complete mineralization of organic pollutants to inorganic materials (Head, 1998). For an organism to survive, electron donors (BTEX, PAHs, phenols, and cresol) and electron acceptors (oxygen, nitrate, sulfate, manganese, iron, and $CO_2$) are required (Bewley and Webb, 2001; Kracke, Vassilev and Krömer, 2015). Frische in 2003 also declared that introducing organisms to the soil can enhance bioremediation, as a certain organism can only degrade specific contaminants. The most common applications of soil bioremediation are stimulating the naturally occurring microorganisms to pollutant by enhancing nutrients concentration, oxygen supply, and moisture content (Frische, 2003).

The aim of this study is to remediate the existed pollutants, such as plastics, medical waste, municipal waste, electrical items, and hydrocarbons and some toxic heavy metals in the main damping area in Koya city (Fig. 1) through bioremediation using *Enterobacter cloacae*. In spite of the fact that, the performance of this system with the optimum condition for the bacteria is necessary to be monitored and observed as the rate of the biodegradation of each contamination is different so that the remediation time could be reduced (Margesin, Zimmerbauer and Schinner, 2000). In addition, the microbial activity could be increased due to the association of some other techniques, namely, the addition of biosurfactants, biostimulation, and bioaugmentation, as the mobility and the access to nutrients of the microbes in the soil are limited (de Rizzo, et al., 2010). The eco-toxicological tests can be used to evaluate the environmental toxicity of

ARO-The Scientific Journal of Koya University
Vol. X, No. 1 (2022), Article ID: ARO.10948. 4 pages
DOI: 10.14500/aro.10948
Received: 20 November 2021; Accepted: 29 March 2022
Regular research paper: Published: 10 April 2022
Corresponding author's email: hanaa.muhammad@koyauniversity.org

http://dx.doi.org/10.14500/aro.10948

the treated soil using plant or survival earthworm (Hund and Traunspurger, 1994).

## II. Materials and Methods

### A. Soil Sample Collection

Based on International Atomic Energy Agency in 2004 of soil sampling for environmental contaminants, three samples (100 g) were collected from the depth of 25 cm of the contaminated site in Koya city, in which the upper 5 cm of the soil surface was discarded, then the rest of the sample was kept in a sterilized plastic bag for about an hour.

### B. Contamination Found

According to the site investigation, which was done through sampling processes, from digging pits across the site in a regular grid for soil; most of the contaminants exist in the soil caused by continuous dumping, therefore, it's considered to be the main source of the contamination (Fig. 1). These two methods were used to detect the pollutants in the site:

1. X-ray fluorescence (XRF Rigaku 50 KV in Koya University) was used to detect the existence of metals in the soil samples (Fig. 2). This device provides the most accurate compositional analysis that based on the emission of a characteristic X-rays by a specific chemical components (Pinto, 2018).

Fig. 1: The main disposal site that located in the city of Koya (Koysinjaq) in Kurdistan region of Iraq.

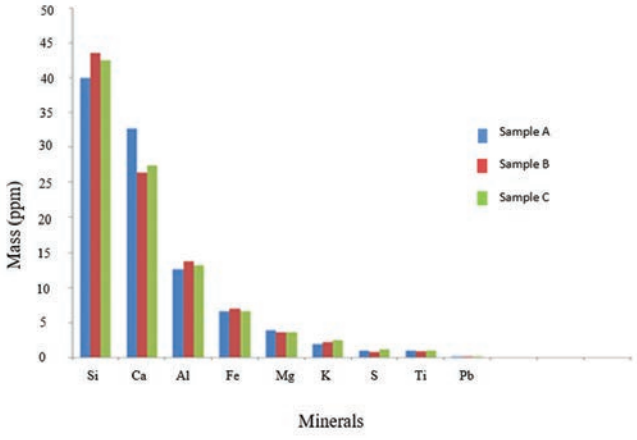


Fig. 2: X-ray fluorescence result analyzes for minerals existed in collected samples from the disposal site in Koya city.

2. Following the methodology of Osman and Saim in 2013 to extract the organic compounds from the soil, the samples were air-dried at room temperature to evaporate water to less than 5% and sieved through a 600 m pore sieve. Then, each sample was split into two equal weight (50 g). Next, each part was mixed with 250 ml of ethane and 1,2-dichloroethane solvents (Ke, et al., 2014). These mixtures were stirred and stored for 48 h in a screw cap glass specimen jar. To extract the organic compounds, solvent was completely evaporated by stirring the soil sample inside the chamber hood for nearly 6 h.

### C. Bacterial Isolation

Bacterial isolates were developed on mineral salt broth medium (Zajic and Supplisson, 1972) that was prepared by dissolving 1.8 g K2HPO4, 4.0 g NH4 CI, 0.2 g MgSO4.7H2O, 0.1 g NaCl, and 0.01 g FeSO4.7H2O in 1 L of distilled water.

Using the methods mentioned by Zhang, Pab and Li in 2010, briefly, 1 g of each specimen was added to 10 ml of sterile distilled water and then vortexed carefully to homogenize the soil suspension. Following this, a 1/10 serial dilution of this suspension was prepared from the above culture by taking 1 ml and adding it to 9 ml of sterile media to $10^{-4}$, which was used to inoculate mineral salt broth medium agar plates.

From each dilution, 0.1 ml were spread on nutrient agar plates at pH 7.0, to check the growth of bacteria, incubation was conducted in Petri plates at 28 ± 1°C for 72 h. Then the types of the bacteria were classified based on the colony morphology, such as color, shape, and size.

### D. Bioremediation Assay

Three different bacterial colonies were primarily selected for further studies, as they grew better compared to the rest of the colonies (Fig. 3). Next, the three different colonies were taken and cultured on slant nutrient agar separately to be used as reference (Fig. 4). To observe which bacterial strain manifests the highest tolerance level, the three isolates were taken from each colony which was resuspended in 10 mL saline to give the inoculums suspension at absorbance of 0.5 and wavelength at 600 nm and then cultured in a mineral salt broth medium

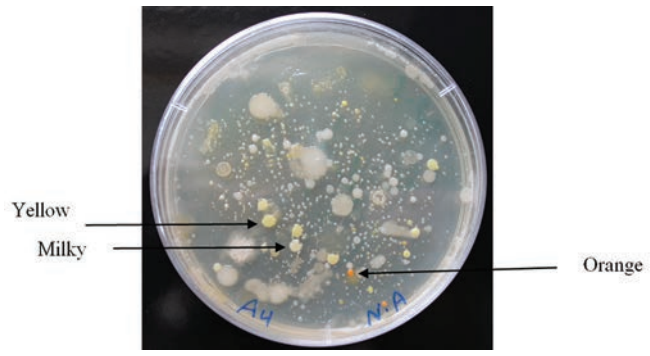


Fig. 3: Bacterial colonies morphology which were extracted from the contaminated soil of Koya city in Kurdistan region of Iraq.

at pH 7.0 with adding the same concentration of the organic matter which was found in the site and incubated overnight at 32°C. The results were recorded after 48 h by spectrophotometer on 600 nm.

### *E. Bacterial Identification*

To characterize the selected bacteria, these techniques were used (by Medya Diagnostic Center in Erbil city).

1. Gram stain test was performed for the isolate.
2. Biomerieux Analytical Profile Index (API) 20E.

## III. Results and Discussion

In this present study, the isolated bacteria were Gram-negative rods and Biomerieux API 20E showed that there was a heavy growth of *E. cloacae* (Fig. 5).

*Enterobacter* is a Gram-negative, facultatively anaerobic, rod-shaped, non-spore-forming bacteria, which can grow best at the temperature of 37°C (Mezzatesta, Gona and Stefani, 2012). Since this microorganism is oxidase negative but catalase positive and facultative anaerobic, therefore, for making ATP, it can switch between aerobic respirations to fermentation in the absence of oxygen (Ren, et al., 2010).

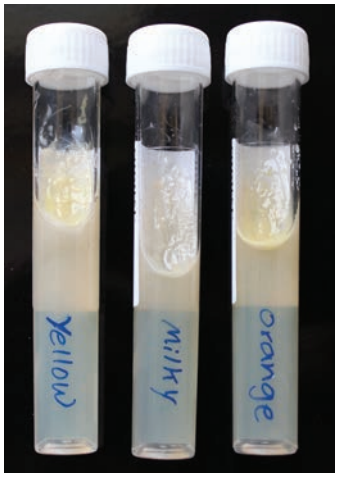


Fig. 4: Three different types of bacteria colonies cultured on slant nutrient agar, which were extracted from the contaminated site in Koya city.


Fig. 5: *Enterobacter cloacae* local isolate from Koya city dumping area on nutrient agar.

In our study, we have isolated one potent organic matter and heavy metal-resistant bacteria in polluted soil from one of the main dumping areas at Koya city to be used in the process to treat the existed pollutants. That bacterium was chosen as it has the heaviest growth in a mineral salt broth medium with the added pollutants from the soil at pH 7.0 after incubating overnight at 32°C. The analysis identified the bacterial isolate as *E. cloacae*.

Since there is a great possibility of leaking the organic compounds in which nearly 90% of them come from plastics, medical waste, municipal waste, electrical items, and hydrocarbons that are found in the site can reach the water bodies eventually, besides, heavy metal toxicity and municipal wastes in the environment due to global industrialization are increasing significantly, for instance, lead (Pb) and cadmium are existed in the site. These two heavy metals are biologically nonessential and non-degradable and tend to accumulate in exposed organisms which are the two most abundant toxic heavy metals in the environment that are reported in the Priority List of Hazardous Substances on the 2$^{nd}$ and 7$^{th}$ places, respectively (Kirillova, et al., 2017). Therefore, without treating and processing the waste, there is a major possibility of releasing a colossal amount of toxic heavy metals into water bodies (Batta, et al., 2013; Hookoom and Puchooa, 2013; Kafilzadeh, et al., 2012). Mechanical treatment of the pollutant can be costly and time consuming, hence, bioremediation is a great alternative (Head, 1998). Thus, developing and applying an efficient and promising technology, such as bioremediation to remediate pollution, are urgent (Chandler, 2017; Olga, et al., 2008).

## IV. Conclusion

As dumping areas which caused by the low rate of waste collection and dispersing the garbage in the streets were never been a solution to the clean environment, therefore, some suitable techniques should be applied to deal with this problem that most developing countries might face recently due to the improvement in living standards of people and the proliferation of suburbs. Hence, biodegradation was found to be one of the most effective techniques in Koysinjaq in Kurdistan region of Iraq to destroy hazardous contaminants or transform them into less harmful forms before it was too late to deal with.

In this study, the biodegradation efficiency for the organic compounds in which about 90% of them come from plastics, medical waste, municipal waste, electrical items, and hydrocarbons (as Iraq economically depends mainly on petroleum) that were extracted from the soil samples using ethane and 1,2-dichloroethane solvents organic compounds separation technique, and some of the toxic heavy metals, such as aluminum and Pb, which were detected by XRF analysis, indicates that the proposed remediation technique using local isolated bacteria *E. cloacae* reflects the treatment

costs and minimizes the health and environmental risks associated with prolonged exposure to those residues. However, pollutant bioavailability and biodegradation are critical to the success of this technique. Along with that, the operational conditions (pH, temperature, aeration, and moisture content) are essential to the possibility of the effectiveness of this process. Hence, introducing additives to the soil (water, microorganisms, surfactants, nutrients, pH corrections, and cosubstrates) are important as it can enhance bioremediation.

## References


Batta, N., Subudhi, S., Lal, B., Devi, A., 2013. Isolation of a lead tolerant novel bacterial species, *Achromobacte* sp. TL-3: Assessment of bioflocculant activity. *Indian Journal of Experimental Biology*, 51(11), pp.1004-1011.

Bewley, R.J.F., Webb, G., 2001. *In situ* bioremediation of groundwater contaminated with phenols, BTEX and PAHs using nitrate as electron acceptor. *Land Contamination and Reclamation*, 9(4), p.14.

Boopathy, R., 2000. Factors limiting bioremediation technologies. *Bioresource Technology*, 74, pp.63-67.

Chandler, N., 2017. *Landfills Environmental Impacts, Assessment and Management*. Nova Science Publishers, Hauppauge, New York.

CHEJ, 2016. *Landfills Trashing the Earth*. Center for Health, Environment and Justice, Idylwood, Virginia.

Chen, J.M., Hao, O.J., 1998. Microbial chromium (VI) reduction. *Critical Reviews in Environmental Science and Technology*, 28, pp.219-251.

de Rizzo, A.C.L., da dos Santos, R.M., dos Santos, R.L.C., Soriano, A.U., da Cunha, C.D., Rosado, A.S., dos Sobral, L.G.S., Leite, S.G.F., 2010. Petroleum-contaminated soil remediation in a new solid phase bioreactor. *Journal of Chemical Technology and Biotechnology*, 85, pp.1260-1267.

Frische, T., 2003. Ecotoxicological evaluation of in situ bioremediation of soils contaminated by the explosive 2,4,6-trinitrotoluene (TNT). *Environmental Pollution*, 121, pp.103-113.

Ganguly, S., 2018. *Plastic Pollution and its Adverse Impact on Environment and Ecosystem*. International Conference on Recent Trends in Arts, Science, Engineering and Technology.

Head, I.M., 1998. Bioremediation: Towards a credible technology. *Microbiology*, 144, pp.599-608.

Hookoom, M., Puchooa, D., 2013. Isolation and identification of heavy metals tolerant bacteria from industrial and agricultural areas in mauritius. *Current Research in Microbiology and Biotechnology*, 1, pp.119-123.

Hund, K., Traunspurger, W., 1994. Ecotox-evaluation strategy for soil bioremediation exemplified for a PAH-contaminated site. *Chemosphere*, 29, pp.371-390.

International Atomic Energy Agency, 2004. *Soil Sampling for Environmental Contaminants*. International Atomic Energy Agency, Vienna.

Jardine, P.M., Taylor, D.L., 1995. Kinetics and mechanisms of Co(II) EDTA oxidation by pyrolusite. *Geochimica et Cosmochimica Acta*, 59, pp.4193-4203.

Kafilzadeh, F., Afrough, R., Johari, H., Tahery, Y., 2012. Range determination for resistance/tolerance and growth kinetic of indigenous bacteria isolated from lead contaminated soils near gas stations (Iran). *European Journal of Experimental Biology*, 2, pp.62-69.

Ke, Q., Jin, Y., Jiang, P., Yu, J., 2014. Oil/water separation performances of superhydrophobic and superoleophilic sponges. *Langmuir*, 30, pp.13137-13142.

Kirillova, A.V., Danilushkina, A.A., Irisov, D.S., Bruslik, N.L., Fakhrullin, R.F., Zakharov, Y.A., Bukhmin, V.S., Yarullina, D.R., 2017. Assessment of resistance and bioremediation ability of *Lactobacillus* strains to lead and cadmium. *International Journal of Microbiology*, 2017, p.9869145.

Kracke, F., Vassilev, I., Krömer, J.O., 2015. Microbial electron transport and energy conservation the foundation for optimizing bioelectrochemical systems. *Frontiers in Microbiology*, 6, p.575.

Margesin, R., Zimmerbauer, A., Schinner, F., 2000. Monitoring of bioremediation by soil biological activities. *Chemosphere*, 40, pp.339-346.

Mezzatesta, M.L., Gona, F., Stefani, S., 2012. Enterobacter cloacae complex: clinical impact and emerging antibiotic resistance. *Future Microbiology*, 7, pp.887-902.

Olga, P., Petar, K., Jelena, M., Srdjan, R., 2008. Screening method for detection of hydrocarbon-oxidizing bacteria in oil-contaminated water and soil specimens. *The Journal of Microbiological Methods*, 74, pp.110-113.

Osman, R., Saim, N., 2013. Selective extraction of organic contaminants from soil using pressurised liquid extraction. *Journal of Chemistry*, 2013, p.357252.

Pinto, A., 2018. Portable X-ray fluorescence spectrometry: Principles and applications for analysis of mineralogical and environmental materials. *Aspects Mining Mineral Science*, 1, pp.1-6.

Ren, Y., Ren, Y., Zhou, Z., Guo, X., Li, Y., Feng, L., Wang, L., 2010. Complete Genome Sequence of *Enterobacter cloacae* subsp. *cloacae* Type Strain ATCC 13047. *Journal of Bacteriology*, 192, pp.2463-2464.

Shen, H., Wang, Y.T., 1994. Biological reduction of chromium by *E. coli*. *Journal of Environmental Engineering*, 120, pp.560-572.

Thomas, R.A.P., Hughes, D.E., Daly, P., 2006. The use of slurry phase bioreactor technology for the remediation of coal tars. *Land Contamination and Reclamation*, 14, pp.235-240.

Tyagi, B., Kumar, N., 2021. Bioremediation: Principles and applications in environmental management. In: Saxena, G., Kumar, V., Shah, M.P. (Eds.), *Bioremediation for Environmental Sustainability*. Ch. 1. Elsevier, Amsterdam, Netherlands, pp.3-28.

Xia, Y., Boufadel, M.C., 2010. Lessons from the Exxon Valdez oil spill disaster in Alaska. *Disaster Advances*, 3(4), pp.270-273.

Zajic, J.E., Supplisson, B., 1972. Emulsification and degradation of "Bunker C" fuel oil by microorganisms. *Biotechnology and Bioengineering*, 14, pp.331-343.

Zhang, Z.Y., Pab, L.P., Li, H., H., 2010. Isolation, identification and characterization of soil microbes which degrade phenolic allelochemicals. *Journal of Applied Microbiology*, 108, pp.1839-1849.

# Network Transmission Flags Data Affinity-based Classification by K-Nearest Neighbor

Nahla Aljojo

Department of Information System and Technology, College of Computer Science and Engineering, University of Jeddah, Jeddah, Saudi Arabia

***Abstract*—This research is concerned with the data generated during a network transmission session to understand how to extract value from the data generated and be able to conduct tasks. Instead of comparing all of the transmission flags for a transmission session at the same time to conduct any analysis, this paper conceptualized the influence of each transmission flag on network-aware applications by comparing the flags one by one on their impact to the application during the transmission session, rather than comparing all of the transmission flags at the same time. The K-nearest neighbor (KNN) type classification was used because it is a simple distance-based learning algorithm that remembers earlier training samples and is suitable for taking various flags with their effect on application protocols by comparing each new sample with the K-nearest points to make a decision. We used transmission session datasets received from Kaggle for IP flow with 87 features and 3.577.296 instances. We picked 13 features from the datasets and ran them through KNN. RapidMiner was used for the study, and the results of the experiments revealed that the KNN-based model was not only significantly more accurate in categorizing data, but it was also significantly more efficient due to the decreased processing costs.**

***Index Terms*—Transmission control protocol flags, K-nearest neighbors, Investment, Financial risk, Deep learning.**

## I. Introduction

The transmission control protocol (TCP) operations is conducted with the use of flags which are very important component of the TCP protocol that must be understood to perform transmission of data over a network and for the network to function properly (Hartpence and Kwasinski, 2020). Those transmission flags are contained within the seventh field of the TCP header and can be set to either 0 or 1 depending on the situation, which they regulate and determine how connection states are managed as well as the manner in which packet transfers are carried out (Kadhim and Abed, 2017). It is also possible to use flags to control the establishment of connections as well as the closure and termination of connections; in other words, when a flag is turned on, it is referred to as being set; conversely, when a flag is turned off, it is referred to as being unset. A total of nine TCP flags can be set, six of which are commonly used in network communications and the other three are not. When a flag is set to 1, it indicates that a control was set for the function of that flag in the and when it is set to 0, it means it's off. One of the major functions of TCP in transmission is to "control" the transmission process in general. A TCP segment should be processed first, for example, if there is a problem with priority, TCP would be able to give priority of one segment over other segments with the use of flag. Similarly, TCP would be able to provide control over transmission and retransmission and many other transmission tasks.

The main research problems that this present study highlighted lie with the use of data. That is in this study, the usage of data created during the transmission session linked with the activities of flags was identified as one of the most significant research problems that needed to be addressed. When the sending computer sends, for example, a "push flag," it is usually to inform the receiving computer that the sending computer should flush the TCP buffers and send whatever data are still present in them at the time the push flag is sent. The push flag can be used to indicate a variety of different things associated with the payload in different circumstances. It means gathering such scenarios, there will be some insight that will be gain in order to properly understand the transmission operations fully. In addition, it is usual for the transmitting computer to send a "push flag" to inform the receiving computer that it should flush the TCP buffers and deliver any data that are still present in them at the time the push flag is sent. When used in a variety of various contexts, the push flag can be used to convey a variety of different things that are linked to the payload. By analyzing such circumstances, some information can be gathered that can then be used to correctly identify the transmission flaws as well. Moreover, given that these flags must be toggled on or off, their impact on various application layer protocols on different transmission sessions will be extremely significant for understanding network communication in general, something that has hitherto been overlooked by the academic community.

ARO-The Scientific Journal of Koya University
Vol. X, No. 1 (2022), Article ID: ARO.10880. 43 pages
DOI: 10.14500/aro.10880
Received: 17 September 2021; Accepted: 21 February 2022
Regular research paper: Published: 25 April 2022
Corresponding author's email: nmaljojo@uj.edu.sa

 http://dx.doi.org/10.14500/aro.10880

Considering the research problems highlighted above, the objective of the present study is to examine the use of data generated during the transmission session in conjunction with the activities of transmission flags, based on the fact that this has been outline as the current research gaps and as one of the most critical research concerns that required more investigation. There are many motivations for achieving this objective. The crucial one lies with the use of reset flag. Consider a transmission where an attempt to establish a connection result in the return of a reset flag; however, it is possible that an attempt will be made and a reset flag will be returned because a port may not be open at the time of the attempt. It means that information will be generated in various aspects that would require further analysis. Furthermore, the previous research studies have identified that TCP flags can be used in packet analysis to determine the state of the communications process at any given point in the TCP conversation or to trace a session from its inception to its conclusion, depending on the protocol (Kumar, et al., 2018; Chow, Li, Mountrouidou, 2017; Muelas, et al., 2017; Kushwah, et al., 2019; Hartpence and Kwasinski, 2020; Tomar, 2019; Sahi, et al., 2017; D'souza, et al., 2020).

The present study makes it obvious that the unit of analysis is "data," and as a result, the problem of connection construction between two TCP segments is handled as the core major problem. TCP flags can be used to determine the current state of the communication process at any given point in the conversation by studying the contents of the flags (Gital, et al., 2016). In reality, malicious users can take advantage of TCP flags to their own advantage; they can be configured in such a way that they can be used to launch denial of service attacks and other malicious actions on the network (Amanowicz and Jankowski, 2021). Considering a network scenario, where a central source and four destinations are in transmission (Fig. 1). In all the four cases, the various TCP flags can be found in the TCP header, despite coming from a single source and they are responsible for the transmission and flow of packets across the network connection. As a result, they are approximately in control of how data are transmitted, and how data are processed. Each of the TCP flags is on its way out to carry out its responsibilities on the target in all the four connections. The urgent flag is used to specify that a packet must be processed immediately, and you're attempting to pass that information along to the target or to any other device that will be processing that packet. The push flag is used to transmit data as soon as it is received. The Fin brings the transmission to a close. The ACK flag indicates that a packet has been successfully received. To initialize the connection between two devices, the SYN or synchronization flag is used.

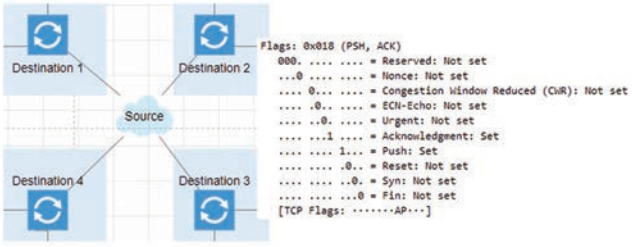


Fig. 1. The types of TCP flags in a transmission session.

## II. Related Work

Analyzing transmission session data are mostly carried out in response to network monitoring (Demertzis, et al., 2021), crucial to that is employing an architecture that monitors the entire traffic and analyzes them for identification of either attacks or real-time problems. Data are generated within a network operation for various reason, an organization's network activity generates data, such as new benchmark datasets for evaluating data-driven intrusion detection systems (Abubakar, et al., 2015). The generation of data from any network process or operation is necessary, but the analysis of that data is much more crucial. Poorzare and Calveras (2021) generate network transmission data to reveals an understanding of why TCP cannot differentiate between congestion and other network flaws that can cause packet drops. Atan, et al. (2021) utilized some traffic data to gain an understanding of degradation attacks and TCP performance. Although data can be collected from various area of network, the analysis of such kind of data is the key problems. That is why there are many machine learning approaches to analysis data to draw out some values from such data.

The K-nearest neighbors (KNN) classifier has been used in a number of the previous studies to better understand the functioning of networks. Gordon et al. (2021) revealed that to identify and classify Internet of Things devices, as well as to detect several types of DDoS attacks, including TCP-SYN, UDP, and ICMP, KNN has performed. Dini and Saponara (2021) utilized KNN for instruction detection in a network transmission session. In analysis with data, the amount of recorded patterns makes the approach more efficient. KNN provides a set of patterns in the training set. Given KNN and other machine learning algorithms operations, it is easy to see how the KNN method of classification is a simple but extremely effective method of categorizing network data associated with network transmission (Nikam, 2015). In a similar vein, it has been demonstrated that a classification algorithm known as the KNN is critical in the solution of fundamental classification problems for network transmission operations (Alweshah, et al., 2020). KNN has also been recognized as the most appropriate option when dealing with long-term network operations datasets (Jannach and Ludewig, 2017). Despite having a wide acceptance, KNN also faces some drawbacks.

It has been recognized that analysis associated with KNN is mostly affected by the preparation of the "good value" for the parameter k, which is also required before constructing a network of nodes. It's a significant problem in the KNN algorithm because it makes selecting a "good value" for k more difficult than it should be, which makes it less efficient (Zhang, et al., 2017). Furthermore, another significant shortcoming of the algorithm is that it does not take into consideration any of the input data, which is another serious

flaw in the algorithm (Liao, et al., 2021). In a survey of a techniques, datasets, and challenges in intrusion detection systems, KNN has been identified to be among the crucial intrusion detection technique (Khraisat, et al., 2019), several points were highlighted on the reason why KNN retains all of the training data for classification, which many other algorithms discard those portions of it to improving their performance.

Using KNN for anomaly detection in TCP/IP networks, Zanero and Savaresi (2004) did a critical classification analysis for the aim of anomaly detection in TCP/IP networks, and the findings were published. To perform their analysis, the research team used a clustering approach followed by normal anomaly detection techniques. In a network transmission session, Ponmaniraj and Anand (2018) were able to analyses both the usual traffic pattern and the anonymous traffic pattern using KNN. Wenke and Stolfo (1998) developed an established framework capable of taking a classification and clustering techniques for detection intrusion detection on specific network scenarios with the purpose of detecting hostile activity and applying them to specific network situations. A better grasp of how many potentially harmful patterns can be discovered by an intrusion detection system was demonstrated to gain a better comprehension of the concept. A majority distance-based weighting (Zhang, 2020) has been demonstrated to extend the application of KNN to the setting of classification in a variety of situations, as demonstrated by Zhang, et al. KNNs in network management and analysis, on the other hand, have gained widespread acceptance as a result of the demand for the selection of a suitable value for k, which has a substantial impact on the performance of the classification method when it is combined with other algorithms. A recent study on KNN suggests that an alternative KNN technique should be used. To summarize, the KNN model approximately recalls all of the training samples and compares the current sample with the k nearest points to draw conclusions from the data. Whereas there are a variety of approaches for determining the k value, the easiest is to run the algorithm several times with different k values and then choose the one that performs the best on average.

## III. The KNN Model

It was discovered over the course of adoption of KNN, there are many ways to implement it. This study utilized two KNN-related algorithms (Algorithm 1 and Algorithm 2). The algorithms are concerned with the cost of categorizing the datasets with all of the information associated with transmission flags and network application layer protocols, and the techniques are designed to minimize this cost to the greatest extent possible, according to the requirements of the specifications. As a result, the conceptualization process follows a similar pattern to the classification process. It has been previously stated that the reason for this is due to the simple fact that practically all the computation that occurs during the classification process depend on the computational resources and value of k, and also the size of the training samples. Algorithm 1 entails running KNN for the first round and then following the procedure where the k in KNN was picked at random with no consideration for its impact on the outcome.

**Algorithm 1:** The first round KNN Algorithm
Input: *s, x, y*;
Output: *Class of I*
Initialize the distance *d* (*x*′λ′) between the points (x, xi)" in the dataset
*Set s*{*I*} where 1, 2, 3., *n*
*d* within points (1+*n*, ∞,).
set *n*⟶ ∞ and find *k* distances
$k \geq 1$
*end*.
*match k*-points & *d*
*if* ($k_i$>$k_j$) and *I* > j,
set *x* ϵ 1
*end*
*end*

On completion of the successful implementation of Algorithm 1, it was discovered that the KNN had been implemented, but not in the most efficient manner. Because it cannot be used to areas where dynamic categorization is required for a where the value of k is required, the first model can be seen as pre-modeling to maximize its efficiency. As a result, in Algorithm 2, validation was accomplished by maximizing the value of k. Attempts are made to tackle these concerns, and an optimization parameter is presented to obtain the desired value of k.

**Algorithm 2:** The second round KNN Algorithm
Input: *s, x, y*;
Output: *Class of s*
Initialization: *f*or (*x*′λ′) ϵ *y* set task and do
Normalize *x* and *y*;
*match* flags labels;
*end*
*for each* set of s;
*set* the distance(*d*) within (*x*, *y*) ϵ R
*sort (d)*
*Obtaining class labels k-nearest point to (d)*
*end*
*end*

## IV. Experimental Analysis and Evaluation Technique

This section of the study describes in detail the experimental analysis processes that were carried out on the basis of the conceptualization of transmission flags that had an impact on the network-aware application (application layer protocols). Preparation of data, pre-processing of data, and final analysis are all necessary steps in the experimental analysis and evaluation of outcomes. The KNN was used to forecast the classification of the model before it was implemented.

 http://dx.doi.org/10.14500/aro.10880

### *A. Dataset*

Kaggle provided the raw data for this study, which contained some transmission sessions through IP flow with 87 features and 3.577.296 occurrences, which were employed in this investigation. Imagine that we are looking at a transmission pool, which is primarily concerned with the transmission of data via specific ways; once the data have been processed, it will be transferred to one or more networks, for example (processes). Because of the unpredictability of the data gathering technique, the amount of data collected will vary from session to session. Furthermore, it is critical to emphasize the amount of information that can be obtained through network transmission, as this allows any filtering and aggregation capabilities to be performed to any of the packets that were delivered as a result of the transmission operation to be highlighted. Remember that the information gathered is primarily intended for the development of models that classify the interplay between network transmission flags associated with network-aware applications on transmission sessions, which will then be used to construct models based on the classification models. The dataset indicates that only 13 of the 87 features associated with flags were utilized, out of a total number of 87 features in the dataset overall (Table I). A number of variables must be considered, including: The number of times the push flag was set in packets transmitting in the forward direction (Fwd.PSH. Flags), the number of times the push flag was set in packets transmitting in the backward direction (Bwd.PSH.Flags), the number of times the urgent flag was set in packets transmitting in the forward direction (Fwd.URG.Flags), and the number of times the push flag was set in packet (Bwd. URG.Flags). Following that, is the count of the finish flag (FIN.Flag.Count), the count of the starting communication flag (SYN.Flag.Count), the count of the reset flag (RST.Flag. Count), the count of the push count flag (PSH.Flag.Count), the count of the acknowledgement flag (ACK.Flag.Count), the count of the urgent flag (URG.Flag.Count), and the count of the common weakness enumeration flag, which follows by the (ECN-Echo ECE.Flag. Count). The goal of all of them is to have some sort of impact on the network-aware application in some form, which means that they are conceptualized to have some sort of influence on the network-aware application (application layer protocols).

The network-aware apps are the most significant aspects of a network because they are at the heart of the underlying applications over IP flow, and they are responsible for either monitoring the status of the underlying network or receiving information about the status of the underlying network from network monitors. Although less important, the ability of the network to change its behavior in response to the information it receives is equally important, and it is associated with transmission flags, which are used to identify which protocols are being used at the application layer and are associated with transmission flags. A network transmission session is defined as a period of time during which an application delivers acceptable and predictable performance. A total of 60 of these applications were acquired during a transmission session, and they are included in the current dataset (Table II). Google was determined to have the greatest number of transmission sessions, whilst NFS count only had one, making it the least amount of transmission sessions among the dataset's participants. This study hypothesized that transmission flags had an impact on these protocols.

### *B. Data Pre-processing*

KNN method uses a distance measure, which is determined by the scale of the variables being compared, to get classification results. When the unit of measurement

TABLE I
FEATURES ASSOCIATED WITH FLAGS IN THE DATASET

| Fwd. PSH. Flags | Bwd. PSH. Flags | Fwd. URG. Flags | Bwd. URG. Flags | FIN. Flag. Count | SYN. Flag. Count | RST. Flag. Count | PSH. Flag. Count | ACK. Flag. Count | URG. Flag. Count | CWE. Flag. Count | ECE. Flag. Count | ProtocolName |
|---|---|---|---|---|---|---|---|---|---|---|---|---|
| 0 | 0 | 0 | 0 | 0 | 0 | 0 | 0 | 1 | 0 | 0 | 0 | HTTP_PROXY |
| 0 | 0 | 0 | 0 | 0 | 0 | 0 | 0 | 1 | 1 | 0 | 0 | HTTP_PROXY |
| 1 | 0 | 0 | 0 | 0 | 1 | 0 | 0 | 1 | 0 | 0 | 0 | HTTP |
| 0 | 0 | 0 | 0 | 0 | 0 | 0 | 0 | 1 | 1 | 0 | 0 | HTTP |
| 1 | 0 | 0 | 0 | 0 | 1 | 0 | 0 | 1 | 0 | 0 | 0 | HTTP_PROXY |
| 0 | 0 | 0 | 0 | 0 | 0 | 0 | 0 | 1 | 0 | 0 | 0 | HTTP_PROXY |
| 1 | 0 | 0 | 0 | 0 | 1 | 0 | 0 | 1 | 0 | 0 | 0 | HTTP_PROXY |
| 0 | 0 | 0 | 0 | 0 | 0 | 0 | 1 | 0 | 0 | 0 | 0 | HTTP_CONNECT |
| 1 | 0 | 0 | 0 | 0 | 1 | 0 | 0 | 1 | 0 | 0 | 0 | SSL |
| 0 | 0 | 0 | 0 | 0 | 0 | 0 | 1 | 0 | 0 | 0 | 0 | GOOGLE |
| 1 | 0 | 0 | 0 | 0 | 1 | 0 | 0 | 1 | 0 | 0 | 0 | HTTP_PROXY |
| 0 | 0 | 0 | 0 | 0 | 0 | 0 | 0 | 1 | 0 | 0 | 0 | HTTP_PROXY |
| 0 | 0 | 0 | 0 | 0 | 0 | 0 | 0 | 1 | 0 | 0 | 0 | HTTP_PROXY |
| 0 | 0 | 0 | 0 | 0 | 0 | 0 | 0 | 1 | 0 | 0 | 0 | HTTP_PROXY |
| 0 | 0 | 0 | 0 | 0 | 0 | 0 | 1 | 1 | 0 | 0 | 0 | HTTP_PROXY |
| 0 | 0 | 0 | 0 | 0 | 0 | 0 | 1 | 1 | 0 | 0 | 0 | SSL |
| 1 | 0 | 0 | 0 | 0 | 1 | 0 | 0 | 1 | 0 | 0 | 0 | HTTP |
| 1 | 0 | 0 | 0 | 0 | 1 | 0 | 0 | 1 | 0 | 0 | 0 | HTTP |
| 1 | 0 | 0 | 0 | 0 | 1 | 0 | 0 | 1 | 0 | 0 | 0 | HTTP |

Table II
The underlying applications over IP flow in the dataset

| # | Protocol Name | Transmission Sessions | # | Protocol Name | Transmission Sessions | # | Protocol Name | Transmission session |
|---|---|---|---|---|---|---|---|---|
| 1 | Google | 256726 | 21 | Instagram | 1159 | 41 | WAZE | 52 |
| 2 | HTTP | 254525 | 22 | WhatsApp | 829 | 42 | NTP | 40 |
| 3 | HTTP_Proxy | 154026 | 23 | Wikipedia | 741 | 43 | Easytaxi | 34 |
| 4 | SSL | 131461 | 24 | Netflix | 699 | 44 | Twitch | 24 |
| 5 | HTTP_Connect | 94362 | 25 | MS_One_Drive | 654 | 45 | Unencryped_Jabber | 19 |
| 6 | Youtube | 46236 | 26 | DNS | 516 | 46 | Deezer | 16 |
| 7 | Microsoft | 19389 | 27 | IP_ICMP | 503 | 47 | Citrix | 11 |
| 8 | Amazon | 15495 | 28 | Apple_Itunes | 376 | 48 | Whois_Das | 10 |
| 9 | Windows_Update | 11996 | 29 | Ebay | 345 | 49 | Opensignal | 9 |
| 10 | Gmail | 9565 | 30 | Apple_Icloud | 322 | 50 | Skinny | 8 |
| 11 | Skype | 7497 | 31 | SSL_NO_CERT | 300 | 51 | Oracle | 7 |
| 12 | Yahoo | 7450 | 32 | HTTP_Download | 157 | 52 | Edonkey | 6 |
| 13 | Facebook | 7020 | 33 | Spotify | 136 | 53 | MSSQL | 4 |
| 14 | Dropbox | 6780 | 34 | Teamviewer | 130 | 54 | UPNP | 4 |
| 15 | Twitter | 5315 | 35 | TOR | 110 | 55 | Mail_Imaps | 3 |
| 16 | Cloudflare | 4228 | 36 | Google_Maps | 102 | 56 | Openvpn | 2 |
| 17 | MSN | 3791 | 37 | Ubuntuone | 93 | 57 | Oscar | 2 |
| 18 | Apple | 2103 | 38 | SSH | 74 | 58 | Simet | 2 |
| 19 | Content_Flash | 1610 | 39 | MQTT | 72 | 59 | Starcraft | 2 |
| 20 | Office_365 | 1373 | 40 | FTP_Data | 53 | 60 | NFS | 1 |

is changed, the distance between two objects with the same length and mass will change dramatically. Because of this, all variables should be brought into the same range to be able to compare values that have been measured with more consistency. Finding any anomalies in the data, such as null values and outliers, was the first step in the process, which took several hours. A number of columns were omitted from the dataset because they were judged unimportant for analysis and prediction, such as those requiring natural language processing. Additional columns from the dataset were excluded from the dataset since they were deemed to be unrelated to the research on the basis of the problem domain.

### *C. Performance Evaluation*

The performance of the classification algorithms is presented in Table III, it relies on the evaluation metrics such as accuracy, recall, precision.

The evaluation is critical when estimating the performance of a machine learning algorithm. Typically, performance is measured using indicators such as precision and recall. Precision and recall are two different metrics that describe how well a prediction algorithm performs when rejecting a non-relevant class, and precision and recall are two different metrics that describe how well the algorithm finds all relevant classes. A binary label is used to differentiate between what happened in real life and what happened in the prediction when evaluating precision and recall.

Finally, the evaluation of the model will follow using the sensitivity and specificity measures. Considering that substantial research studies on prediction utilized rules based scores, sensitivity and specificity in identifying and predicting problems, the sensitivity-based approach reveals the efforts of each flags contribution and the least effect on the protocol. Hence, the positive and negative class of performance measure present true positives (TP), false positives (FP), true negatives (TN), and false negatives (FN). TP: Precisely predict, FP: Erroneously predict, FN: Erroneously rejected, TN: Precisely rejected. This is used for measuring the "Sensitivity ($S_e$)," and "Specificity ($S_p$)," based on the following evaluates the performance measure of the models used:

Table III
Performance evaluation metrics

| | True+ve | True –ve | Precision |
|---|---|---|---|
| Pred+ve | Count of TP | Count of FP | PPV |
| Pred–ve | Count of FN | Count of TN | NPV |
| Recall | Sensitivity | Specificity | Accuracy |

- Accuracy $=TP+TN/TP+FP+FN+TN$
- Classification error =1−Accuracy
- Positive precision value (PPV) $=TP/TP+FP$
- Negative precision value (NPV) $=TN/FN+TN$
- Sensitivity/true positive rate (TPR) $=TP/TP+FN$
- Specificity/true negative rate (TNR) $=TN/FP+TN$.

### *D. Experimental Simulations*

RapidMiner Studio 9.9 was used for the processing component of the analysis, which allowed for a wide range of options to be used in the data preparation and analysis. Under all conditions in this experiment, the ideal numbers split (0.7–0.3) was employed for both training and testing in all situations, respectively, irrespective of the context. All of the model's attributes were implemented as a result of the model's correctness being determined. To conduct this experiment, an Intel® CoreTM i7-10750H CPU running at 5.0 GHz and 16 GB of total RAM were employed in a computer system powered by an Intel® CoreTM i7-10750H processor. When it comes to network-aware application variables, the envisioned influencing of transmission flags

http://dx.doi.org/10.14500/aro.10880

is based on comparing multiple flags one after another in terms of their impact on the protocol for throughout the transmission session, which is why KNN was utilized. The simplicity of the KNN algorithm's design makes it an easy distance-based supervised learning algorithm that merely remembers earlier training samples and compares a new sample with the K-nearest points to make a decision.

## V. Presentation of the Results and Discussion

There was a large amount of data entered into the training dataset, and there are no missing data records inside the record. This set of datasets was divided into training and testing datasets using a variety of percentage splits. A series of investigations were conducted; the model is presented in Fig. 2. The performance of the prediction model for each partition was recorded and analyzed in detail. Algorithm 1 was used to conduct the first round of analysis. The accuracy of the model's performance was greater than 80%, and the sensitivity and specificity of the model were all reported in Table IV to demonstrate their effectiveness.

As a result, the value of k was adjusted in the following round of analysis, but not in accordance with the optimization prediction; as a result, the analysis with the same large amount of data entered into the training dataset, where it was divided into training and testing datasets using a model presented in Fig. 3 shows that the performance of the prediction model for each partition was recorded and analyzed. The first phase of analysis was carried out with the help of Algorithm 1. Performance of the model was more than 80% accurate; the model's sensitivity and specificity were all presented in Table V to indicate its efficacy.

The successful implementation of Algorithm 1 was followed by the discovery that the KNN had been implemented, but that it had not been done in the most efficient manner.

Table V
The performance of implementation of the modified Algorithm 1

| | True SF | True S0 | True REJ | Class precision |
|---|---|---|---|---|
| Pred. SF | 4244 | 269 | 306 | 88.07% |
| Pred. S0 | 246 | 1820 | 640 | 67.26% |
| Pred. REJ | 2 | 14 | 17 | 51.52% |
| Class recall | 94.48% | 86.54% | 1.77% | |

Table IV
The performance of implementation of the Algorithm 1

| | True SF | True S0 | True REJ | Class precision |
|---|---|---|---|---|
| Pred. SF | 4244 | 269 | 306 | 88.07% |
| Pred. S0 | 246 | 1820 | 640 | 67.26% |
| Pred. REJ | 2 | 14 | 17 | 51.52% |
| Class recall | 94.48% | 86.54% | 1.77% | |

Table VI
The performance of the final implemented Algorithm 2

| | True SF | True S0 | True REJ | Class precision (%) |
|---|---|---|---|---|
| Pred. SF | 2959 | 184 | 228 | 87.78 |
| Pred. S0 | 185 | 1287 | 439 | 67.35 |
| Pred. REJ | 0 | 1 | 7 | 87.50 |
| Class recall | 94.12% | 87.43% | 1.04% | |

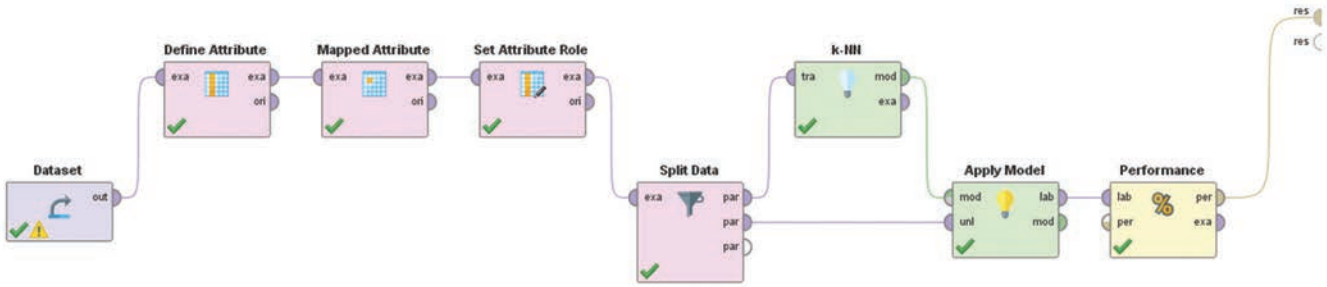


Fig. 2. The model for implementation of the Algorithm 1.

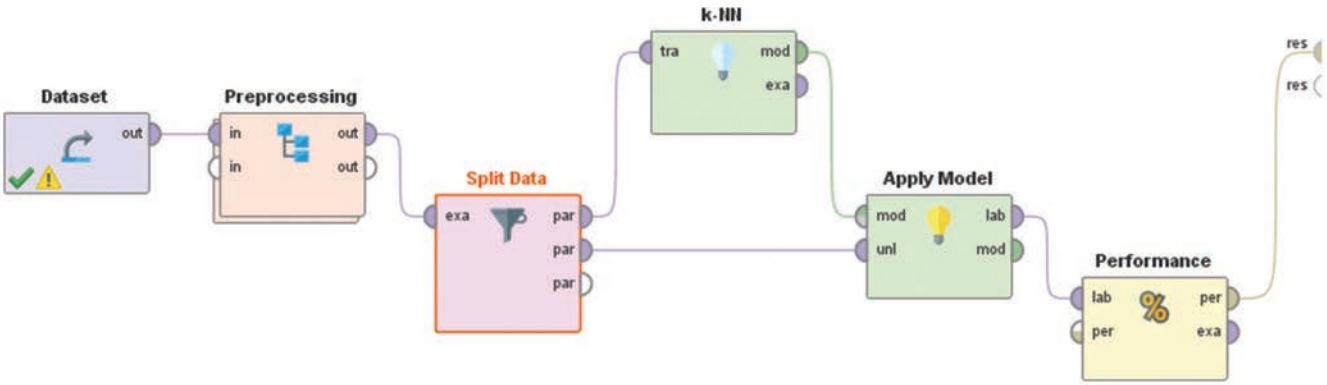


Fig. 3. The model for implementation of the modified Algorithm 1.

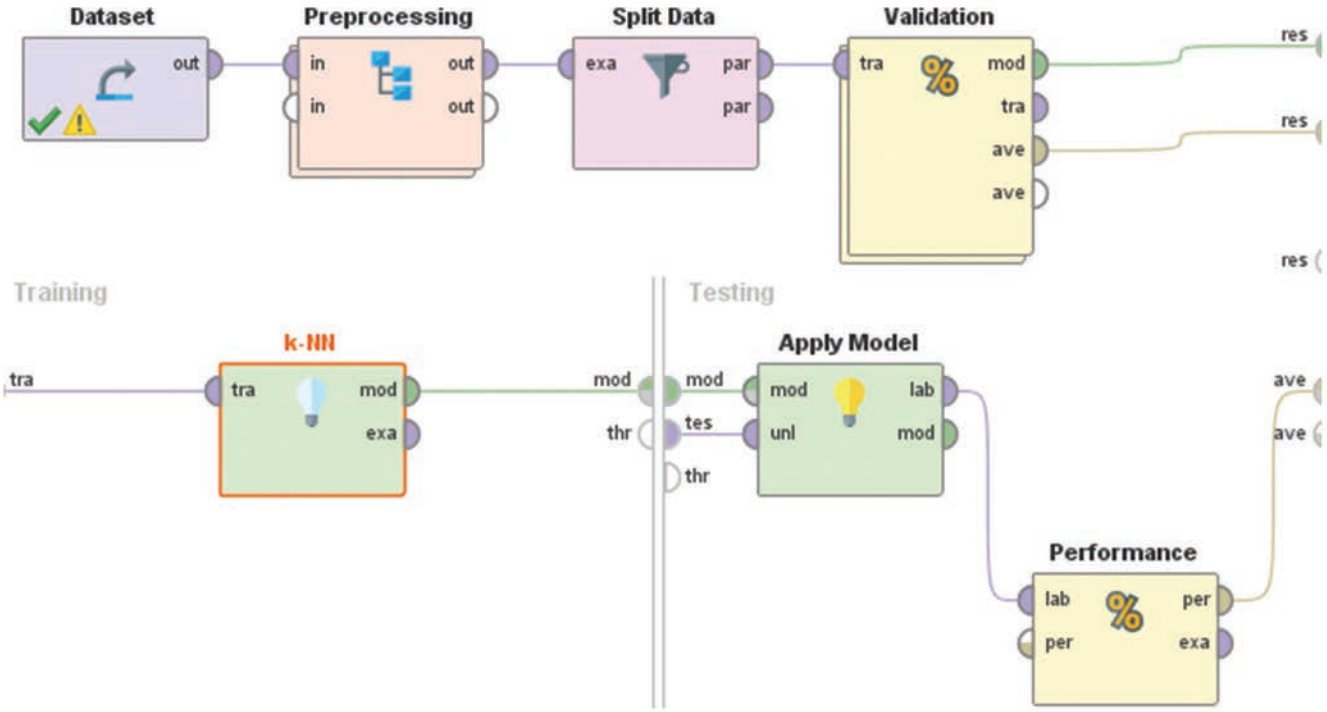


Fig. 4. The final model for implementation of the Algorithm 2.

It is possible to think of the first model as pre-modeling to maximize its efficiency because it cannot be applied to areas where dynamic categorization is necessary and where the value of k is required. As a result, Algorithm 2 was developed, in which the optimization was performed by increasing the value of k to its maximum. Following the completion of the optimization, the required value of k was determined, and this value was utilized to modify the model (Fig. 4).

The model's sensitivity and specificity were all provided in Table VI to demonstrate its effectiveness, and as a result, we obtain the greatest performance scores of the model, which was more than 80% accurate.

## VI. Discussion

According to the findings of this study, there are six different most essential transmission flags that TCP uses (the push flag, the reset flag, the fin flag, the synchronization flag, the acknowledgement flag, and the urgent flag). These flats are critical for the transmission session to be successful. Typically, to terminate a connection, the fin flag must be used, whereas the syn flag must be used when sending a connection request, and the ACK flag must be used if we wish to send an acknowledgment of a request. An instance of the push flag is one in which the sender and receiver intend to engage in interactive conversation, which may begin with the transmission of two bytes. When a sender's payload is 2 bytes, a minimum of 20 bytes IPv4 header and a maximum of 60 bytes will be appended at the transport layer, resulting in a total of [2+20=22] bytes. A minimum of 20 bytes IPv4 header will be added at the network layer, and a maximum of 60 bytes will be added at the application layer, so let's assume the minimum, which will result in 22+20=42 bytes. It is expected that an extra minimum of 48 bytes will be added at the data connection layer, increasing the total amount of bytes received at the receiver to 90 bytes. To put it another way, to convey two bytes of information, a total of 90 bytes of information must be sent out. And what is the efficiency of sending 2 bytes over a 90 byte transmission, to put it another way. This is when the usage of a push flag proves to be quite advantageous. Rather of waiting until a particular amount of data has been compiled into a segment, it enables the transmission to push the two bytes immediately after they are received. Following the arrival of a pair of bytes in a given transmission session, they are sent out using the push flat method. When the push flag is set to the first position, this occurs. When the current connection fails, the reset flag is used to attempt to re-establish the connection with the server again. It is possible to priorities interconnected transmissions by referring to them as urgent and urgent pointer, respectively.

The classification of the interrelationships among the variables was accomplished through the application of KNN. There was a significant amount of data entered into the training dataset, and there are no missing data records contained inside the record itself. With the help of a number of percentage splits, this collection of datasets was divided into training and testing datasets. Investigations were carried out in a number of different ways. The outcome of the prediction model's performance for each partition was recorded and studied in great detail. Both algorithms outperformed their counterparts.

It's also worth noting that the network transmission session is considered a data generating tool, because it generates data and adds some value to the organization and management in the long run. Numerous solutions can be derived from this data. Some key qualities linked with them can be found

using those data in this essential area of data science. Since the data created during a network transmission session might be used to extract value, our research addressed the problem. So that any study could be conducted, this research conceptualized the influence of each transmission flag on network-aware applications by comparing the flags one by one on their impact to the application during the transmission session rather than comparing all of them at the same time.

## VII. Conclusion

Data generated during a network transmission session is studied to discover the optimal method of extracting value from the data provided and being able to perform actions. However, instead of comparing them all simultaneously, this paper conceptualized each transmission flag's impact on network-aware apps by comparing each flag's effects one by one during the transmission session. By comparing each flag's impact on the application during the transmission session, this article conceptualized the impact of each transmission flag on network-aware apps. Because it is an easy-to-use distance-based learning algorithm that remembers prior training samples and can be applied to a variety of flags that have variable effects on application protocols, KNN type classification was chosen. Researchers found that the KNN machine learning algorithm was more accurate at categorizing data, but it was also more efficient due to the reduction in processing costs. Denoted as a data-generating instrument, the network transmission session generates valuable information for the company. These data can be used to find a variety of solutions. Those data can be used in this crucial area of data science to discover some of their most important characteristics. This was a concern of ours because the data generated during a network transmission session could be utilized to extract value. Therefore, to conduct a study on the impact of each transmission flag on network-aware apps, this research evaluated each flag individually, rather than comparing them all at once, to determine their impact on the programmer during the transmission session.

## References

Abubakar, A.I., Chiroma, H., Muaz, S.A. and Ila, L.B., 2015. A review of the advances in cyber security benchmark datasets for evaluating data-driven based intrusion detection systems. *Procedia Computer Science*, 62, pp.221-227.

Alweshah, M., Al Khalaileh, S., Gupta, B.B., Almomani, A., Hammouri, A.I. and Al-Betar, M.A., 2020. The monarch butterfly optimization algorithm for solving feature selection problems. *Neural Computing and Applications*, 32(13), pp.1-15.

Amanowicz, M. and Jankowski, D., 2021. Detection and classification of malicious flows in software-defined networks using data mining techniques. *Sensors*, 21(9), pp.2972.

Atan, F.M., Zulkifl, N., Idrus, S.M., Ismail, N.A. and Zin, A.M., 2021. Understanding degradation attack and TCP performance in next generation passive optical network. *Journal of Physics: Conference Series*, 1933, p.012107.

Available from: https://www.kaggle.com/jsrojas/ip-network-traffic-flows-labeled-with-87-apps [Last accessed 2021 Jun 20].

Chow, J., Li, X. and Mountrouidou, X., 2017. Raising flags: Detecting covert storage channels using relative entropy. In: *2017 IEEE International Conference on Intelligence and Security Informatics* (*ISI*), pp.25-30.

D'souza, J., Kaur, M.J., Mohamad, H.A. and Maheshwari, P., 2020. Transmission Control Protocol (TCP) Delay Analysis in Real Time Network. In: *2020 Advances in Science and Engineering Technology International Conferences* (*ASET*), pp.1-6.

Demertzis, K., Tsiknas, K., Takezis, D., Skianis, C. and Iliadis, L., 2021. Darknet traffic big-data analysis and network management for real-time automating of the malicious intent detection process by a weight agnostic neural networks framework. *Electronics*, 10(7), p.781.

Dini, P. and Saponara, S., 2021. Analysis, design, and comparison of machine-learning techniques for networking intrusion detection. *Designs*, 5(1), p.9.

Gital, A.Y.U., Ismail, A.S., Chiroma, H. and Abubakar, A., 2016. TCP Skudai: A High Performance TCP Variant for Collaborative Virtual Environment Systems. In: *2016 6th International Conference on Information and Communication Technology for The Muslim World* (*ICT4M*), pp.118-121.

Gordon, H., Batula, C., Tushir, B., Dezfouli, B. and Liu, Y., 2021. Securing smart homes via software-defined networking and low-cost traffic classification. *arXiv*, 2021, p.00296.

Hartpence, B. and Kwasinski, A., 2020. Combating TCP Port Scan Attacks Using Sequential Neural Networks. In: *2020 International Conference on Computing, Networking and Communications* (*ICNC*), pp.256-260.

Hartpence, B. and Kwasinski, A., 2020. Combating TCP Port Scan Attacks Using Sequential Neural Networks. In: *2020 International Conference on Computing, Networking and Communications* (*ICNC*), pp.256-260.

Jannach, D. and Ludewig, M., 2017. When Recurrent Neural Networks Meet the Neighborhood for Session-based Recommendation. In: *Proceedings of the Eleventh ACM Conference on Recommender Systems*, pp.306-310.

Kadhim, J.M. and Abed, A.E., 2017. Steganography Using TCP/IP's Sequence Number. *Al-Nahrain Journal of Science*, 20(4), pp.102-108.

Khraisat, A., Gondal, I., Vamplew, P. and Kamruzzaman, J., 2019, Survey of intrusion detection systems: Techniques, datasets, and challenges. *Cybersecurity*, 2, p.20.

Kumar, P., Tripathi, M., Nehra, A., Conti, M. and Lal, C., 2018. SAFETY: Early detection and mitigation of TCP SYN flood utilizing entropy in SDN. *IEEE Transactions on Network and Service Management*, 15(4), pp.1545-1559.

Kushwah, D., Singh, R.R. and Tomar, D.S., 2019. An Approach to Meta-Alert Generation for Anomalous TCP Traffic. In: *International Conference on Security and Privacy*. Springer, Singapore, pp.193-216.

Liao, T., Lei, Z., Zhu, T., Zeng, S., Li, Y. and Yuan, C., 2021. *Deep Metric Learning for K Nearest Neighbor Classication*. IEEE Transactions on Knowledge and Data Engineering.

Muelas, D., de Vergara, J.E.L., Ramos, J., García-Dorado, J.L. and Aracil, J., 2017, On the impact of TCP segmentation: Experience in VoIP monitoring. In: *2017 IFIP/IEEE Symposium on Integrated Network and Service Management* (*IM*), pp.708-713.

Nikam, S.S., 2015. A comparative study of classification techniques in data mining algorithms. *Oriental Journal of Computer Science and Technology*, 8(1), pp.13-19.

Ponmaniraj, S., Rashmi, R. and Anand, M.V. 2018, IDS Based Network Security Architecture with TCP/IP Parameters Using Machine Learning, *2018 International Conference on Computing, Power and Communication Technologies* (*GUCON*), 2018, pp.111-114.

Poorzare, R. and Calveras, A., 2021. FB-TCP: A 5G mm wave friendly TCP for urban deployments. *IEEE Access*, 9, pp.82812-82832.

Sahi, A., Lai, D., Li, Y. and Diykh, M., 2017. An efficient DDoS TCP flood attack detection and prevention system in a cloud environment. *IEEE Access*, 5, pp.6036-6048.

Tomar, D.S., 2019. An Approach to Meta-Alert Generation for Anomalous TCP Traffic. Vol. 939. In: *Security and Privacy: Second ISEA International Conference, ISEA-ISAP 2018*, Jaipur, India, January, 9-11, 2019. Springer, Berlin, p.193.

Wenke, L. and Stolfo, S.J., 1998. Data mining approaches for intrusion detection. In: *Proceedings of the 7th USENIX Security Symposium*, 7, pp.6-6.

Zanero S. and Savaresi, S.M., 2004. Unsupervised learning techniques for an intrusion detection system. In: *Proceedings of the 2004 ACM symposium on Applied computing SAC* 04, pp.412-419.

Zhang, S., 2020. Cost-sensitive KNN classification. *Neurocomputing*, 391, pp.234-242.

Zhang, S., Li, X., Zong, M., Zhu, X., and Cheng, D., 2017. Learning k for knn classification. *ACM Transactions on Intelligent Systems and Technology*, 8(3), pp.1-19.

http://dx.doi.org/10.14500/aro.10916

# Detection of SARS-CoV-2 Reinfections by Rapid Inexpensive Methods

Sherko S. Niranji[1,2] and Sirwan M. A. Al-Jaf[1,2]

[1]College of Medicine, University of Garmian,
Kurdistan Region – F.R. Iraq
[2]Department of Biology, College of Education, University of Garmian,
Kurdistan Region – F.R. Iraq

***Abstract*—New SARS-CoV-2 infections are difficult to be verified, whether they are reinfections or persistent infections. The most prominent factors used for differentiating reinfections from persistent infections are whole-genome sequencing and phylogenetic analyses that require time and funds, which may not be feasible in most developing countries. This study explores reinfections with COVID-19 that harbors D614G and N501Y mutations by rapid inexpensive methods. It exploits the previously developed rapid economic methods that identified both D614G and N501Y mutations in clinical samples using real-time reverse transcriptase polymerase chain reaction (rRT-PCR) probes and conventional PCR specific primers. In the present study, an immunocompetent patient has been found with a SARS-CoV-2 N501Y reinfection without comorbidities. According to the obtained results, this study suggests that the initial infection was due to a variant that contained only D614G mutation whereas the reinfection was potentially a result of alpha variant contained three mutations confirmed by DNA sequencing, including D614G, N501Y, and A570D mutations. These techniques will support rapid detection of SARS-CoV-2 reinfections through the identification of common spike mutations in the developing countries where sequencing tools are unavailable. Furthermore, seven cases of reinfections were also confirmed by these methods. These rapid methods can also be applied to large samples of reinfections that may increase our understanding epidemiology of the pandemic.**

***Index Terms*—Alpha variant, Iraq, Reinfections, SARS-CoV-2.**

## I. Introduction

SARS-CoV-2 reinfections occur as a result of declining antibodies in convalescent people (Qureshi, *et al.*, 2021). However, a recent study found that reinfection occurs in an immunocompetent person who had neutralizing antibodies produced from the initial infections due to the patients moderate immune response (Brehm, *et al.*, 2021). The infections generally persist in immunosuppressed patients but the reinfections occur in immunocompetent individuals in regions where different variants are circulating (Choudhary, *et al.*, 2021). Immunosuppressed can be defined as the loss or deficiency in the quality of humoral or cellular immune components (CDC, 2022). These researchers concluded that in immunosuppressed individuals, accumulation of mutations is linked to viral evolution (Weigang, *et al.*, 2021). This is often perplexing to differentiate between reinfections and persistent infections. The reinfections can be differentiated from persistent infections by identifications of the viral variants in the clinical samples taken from both first and second infections. Viral variants are usually identified by phylogenetic analysis of the viral whole-genome sequences which are difficult to obtain as quickly as possible for both initial and second infections (Stokel-Walker, 2021). In other words, confirmations of reinfections have been under investigation. CDC recommends several criteria for suspecting SARS-CoV-2 reinfections including collecting respiratory samples daily for 7 days and serum samples in different times points on days 3, 7, 14, 21, and 60 (CDC, 2020). Therefore, alternative, rapid, molecular biological methods can also be exploited for variant identifications using real-time reverse transcriptase polymerase chain reaction (rRT-PCR) probes, particularly when whole-genome sequencings are not available in poor or developing countries. Several methods have recently been developed (Al-Jaf and Niranji, 2021; Al-Jaf, *et al.*, 2021; Banada, *et al.*, 2021; Durner *et al.*, 2021; Sandoval Torrientes, *et al.*, 2021). These methods, such as, specific primers, TaqMan probe-based method, and melting curve analysis, are more inexpensive and feasible than whole-genome sequencing.

Before emergence of SARS-CoV-2 variants of concerns (VOCs) such as B.1.1.7, B.1.351, P1, and B.1.617, reinfections were seldomly reported in the world. For example, reinfection with SARS-CoV-2 has first reported in a person from Hong Kong who migrated to Europe that was confirmed to be caused by a different lineage of the virus (Parry, 2020). Later on, several cases of reinfections have been reported worldwide (Choudhary, *et al.*, 2021). However, the variants of most of these reinfections were not confirmed by genomic sequencings; this makes reporting reinfections controversial and confusing with persistent

ARO-The Scientific Journal of Koya University
Vol. X, No. 1 (2022), Article ID: ARO.10916. 5 pages
DOI: 10.14500/aro.10916
Received: 08 December 2021; Accepted: 15 April 2022
Regular research paper: Published: 03 May 2022
Corresponding author's email: sirwan@garmian.edu.krd

infections (Costa, *et al.*, 2021). In other words, the majority of the global SARS-CoV-2 reinfections may have been a persistent infection not even reinfections (Simmonds, *et al*., 2021). This highlights the importance of reinfection confirmation and persistent infection exclusions using either whole-genome sequencings or rapid techniques to identify the virus's variants. Meanwhile, false-negative tests should be considered to avoid prolonged viral shedding from the patient (Falahi and Kenarkoohi, 2020) and emergence of new variants.

SARS-CoV-2 has several major VOC, which have been known to influence on the transmissibility, infectivity, and fatality of the virus, including B.1.1.7 (alpha variant) (Challen, *et al.*, 2021; Davies, *et al.*, 2021), B.1.351 (beta variant), P.1 (gamma variant), and B.1.617 (delta variant). Up to our best knowledge, there are few case reports of reinfections in Iraq (Hussein, *et al.*, 2020, 2021). Nonetheless, no studies have confirmed reinfection using DNA sequencings, particularly with the alpha variant and few reports in the world. This was possibly due to difficulties in comparing the whole-genome sequencings between the initial infections and reinfections. In this study, we aim to investigate reinfections in eight individuals reported in Kalar town, Sulaymaniyah Province, Kurdistan regional government of Iraq, where sequencing facilities are hardly obtained. We also aim to apply the previous rapid methods to confirm reinfections with variants carrying N501Y mutations that have occurred in the region.

## II. Materials and Methods

Seventy-eight out of 255 individuals who visited Coronavirus Research and Identification Lab, University of Garmian, Kurdistan Region, Iraq, were positive for COVID-19 rRT-PCR test ((MutaPLEX® Immundiagnostik, Germany). Eleven persons revisited the laboratory, after 5–10 months, having COVID-19 symptoms, but only eight of them were tested positive. Only the patients were included in the current study that has their tests negative after 2 weeks of first infection. All positive samples were tested for D614G and N501Y mutations using the methods that described previously by Al-Jaf and Niranji, 2021; Al-Jaf, *et al*., 2021.

Nasopharyngeal samples were tested by rRT-PCR kits (MutaPLEX® Immundiagnostik, Germany). The positive samples were tested for mutations from both initial infections and reinfections. Specific primers method was applied for identification of both N501Y and D614G that can detect both mutations utilizing conventional PCR and electrophoresis. rRT PCR method was applied for the identification of both N501Y and D614G mutations (TaqMan probes designed to detect both N501Y and D614G mutations). Spike 748 primers were used to amplify a 748 nucleotides region of the spike protein. The PCR products from this region were sequenced to detect the common mutations that occurred in the VOCs including (K417N, L452R, T478K, E484K, N501Y, A570D, and D614G). These methods were previously described by Al-Jaf and Niranji, 2021; Al-Jaf, *et al*., 2021.

Initially, a person was presented to the Coronavirus Research and Identification Lab, University of Garmian, Kurdistan Region, Iraq. He agreed to fill a consent form as a participant of this study, which was approved by an ethical committee at the Department of Biology, University of Garmian (Ethical approval code: 00087, October 01, 2020) that follows the rules adhered to the Declaration of Helsinki for human and animal research. He was 42 years old, his body weight was 70, height = 170 cm. A nasopharyngeal swab was taken in viral transport medium (VTM) on October 7, 2020. The initial infection was tested for diagnosis as SARS-CoV-2 using a coronavirus real-time RT-PCR kit (MutaPLEX® Immundiagnostik, Germany). Blood tests were performed to observe complete blood counts (CBC), ferritin, D-dimer, LDH, CRP, and ESR. The patient had no comorbidities without receiving vaccination. The reinfection was diagnosed on March 23, 2021 (after 5.5 months), using the same protocol as the initial infection.

Identifications of SARS-CoV-2 N501Y and D614G mutations were performed for both initial infection and reinfection, using rapid molecular biological methods (TaqMan probes, Macrogen, South Korea) as previously developed (Al-Jaf and Niranji, 2021; Al-Jaf, *et al*., 2021) and illustrated in Fig. 1. In addition, a pair of primers (F-AGAGGTGATGAAGTCAGACAAAT) and (R- CTATTAAACAGCCTGCACGT) amplifying a region of 748 nucleotides (22768-23516) that cover common mutations of VOC (including K417N, L452R, T478K, E484K, N501Y, A570D, and D614G) in the spike protein gene of SARS-CoV-2 were used (Al-Jaf and Niranji, 2021) and the PCR products were confirmed by DNA sequencings (Sanger sequencing, Macrogen Co., Seoul, KR). ELISA test for SARS-CoV-2 IgG and IgM (Ideal Tashkhis Atieh Co., Iran) was performed a day post reinfection to reveal antibody state of the patient against the virus. The rapid molecular methods were also applied to seven persons suspected of either reinfections or persistent infections. They agreed to fill consent forms and were approved by the ethical committee as previously mentioned.

## III. Results

### *A. Initial Infection*

The clinical features were as follows: Severe sore throat with excessive cough for 2 weeks that were initially dry but wet and purulent at the end. Sneezing, malaise, fatigue, and diarrhea were also present. Oxygenation saturation was normal as indicated by normal $SPO_2$ more than 96%. The results of the rapid methods showed that the initial infection resulted from a SARS-CoV-2 variant, which has had N501 wild type and D614G mutant. The Ct value of 17.14 was obtained. The sequencing result also confirmed amino acids N501 wild type, A570 wild type, and D614G mutant in the

http://dx.doi.org/10.14500/aro.10916

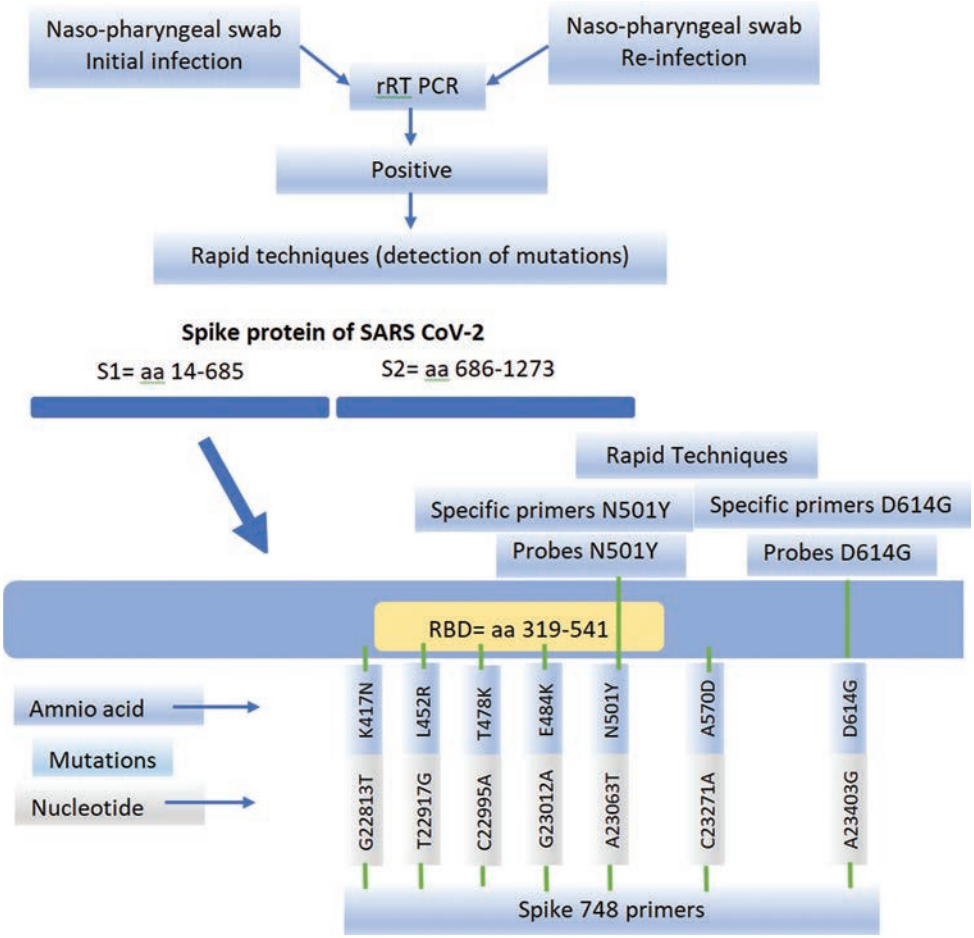


Fig. 1. Rapid detection of reinfections by identifying spike mutations of variants of concerns. S1: Spike 1, S2: Spike 2, RBD: Receptor-binding domain of the spike protein, WT: Wild type, MT: Mutant, CT: Threshold cycle for rRT-PCR.

initial variant (MW897351). Treatment was Vitamin D, zinc, Vitamin C, paracetamol, and azithromycin for 10 days. PCR result was negative after 2 weeks. Another PCR test was performed 4 months later.

### *B. Reinfection*

The clinical features were as follows: Moderate sore throat with mild coughs for 10 days. Dry mouth was much more than the initial infection. Malaise and fatigue were less prominent than the previous infection, and the patient had no diarrhea. He had normal $SPO_2$. The rapid methods and sequencing result (MW897356) found two amino acid changes N501Y and A570D, in addition to the D614G which was also present in the initial infection. The presence of Y501, D570, and G614 mutations in the reinfection suggested alpha variant. Other parameters are as follows: Ct value = 17.9, normal CBC, ferritin, D-dimer, LDH, and ESR, but CRP was 15 mg/dl (normal CRP titer <5 mg/dl). Treatment was Vitamin D, zinc, Vitamin C, paracetamol, and azithromycin for 7 days. The patient recovered with negative PCR after 2 weeks with no clinical signs. Both IgG and IgM were considered as negative results with very low titers, 0.28 and 0.182, respectively (antibody titer above 1 is considered as positive).

### *C. Application of the Rapid Molecular Biological Methods on Other Reinfections*

Seven persons, who were previously positive for SARS-CoV-2 from June to September 2020 where no N501Y mutations were present in the region, were tested for reinfections by the same molecular methods as previously mentioned. Results of the rapid methods showed that all the eight persons were reinfected with a variant having both D614G and N501Y mutations, as shown in Table I. The patients' demographic and clinical information are shown in Table II. The results revealed that one out of eight reinfections carried the wild-type N501 variant (Case No. 3); these were confirmed by DNA sequencings. Whereas other 7 persons were re-infected with N501Y mutated variants. This mutation is present in the Alpha, Beta and Gamma variants of COVID-19.

## IV. Discussion

This study has reported SARS-CoV-2 reinfections using rapid inexpensive techniques that can be used to discriminate between reinfections and persistent infections. The reinfections occurred in different ages ranging between 26 and 55 years, with either having comorbidities or not. In

addition, the manifestation and the severity of the symptoms were variable among different individuals and between the initial and second infections in the same patient. The first case reported in this study was confirmed by the rapid tests and DNA sequencings in the Kurdistan Region of Iraq. In addition, these rapid methods, which can detect both D614G and N501Y mutations, were applied to eight clinical samples. Out of eight persons, one (Case No. 3, Table II) was suspected to be either reinfected or suffered from persistent infections because she carried only D614G but not N510Y mutations in both initial and second infections as confirmed by DNA sequencings too. However, she seemed to be reinfected rather than persistent infection as the time between both infections was more than 6 months (Stokel-Walker, 2021). The other seven individuals carried both D614G and N501Y mutations; the latter was not present in the first infection that suggested reinfections. The reinfected patients include different ages with or without comorbidities suggested that reinfections with alpha variant may occur in various ages with or without comorbidities. The comorbidities were obesity, hypertension, diabetes, and asthma.

SARS-CoV-2 reinfections were previously rare in the world as in a study conducted in approximately 9 thousands of positive samples in the USA from December 2019 to November 2020, only 63 samples (0.7%) were reported as reinfections, which were linked with low antibody responses in the initial infection (Qureshi, *et al.*, 2021). However, recent research has reported 58 out of 1300 suspected reinfections among about 700,000 positive individuals in India (Mukherjee, *et al.*, 2021). Likewise, 138 out of 28,875 positive cases were reported as reinfections in Denmark (Hansen, *et al.*, 2021). An ecological research conducted in the UK concluded no evidence of increasing rate of reinfections with the alpha variant (B.1.1.17) which were confirmed by whole-genome sequencings (Graham, *et al.*, 2021). During the writing of this manuscript, several cases of SARS-CoV-2 reinfections were reported in the USA, Italy, Columbia, Brazil, and Luxemburg, in which their second infections were due to B.1.1.7, B.1.1.7, B.1.1.269, P1, and B.1.351 variants (Marquez, *et al.*, 2021; Novazzi, *et al.*, 2021; Ramírez, *et al.*, 2021; Staub, *et al.*, 2021).

For how long antibodies persisted in previously infected persons is uncertain. However, studies suggested that antibodies may remain for approximately 6 months (Stokel-Walker, 2021). The persistence of antibodies varies from an individual to another or it depends on the severity of the disease or the type of the variants. The antibody status of the first case was performed a day of the reinfection indicated that his adaptive immunity had no response yet and results showed that both IgG and IgM were negative. This suggested that the reinfected person has had no protective antibodies to prevent the reinfection. Limitations of the present study were lack of checking antibodies in all cases. Despite the small number of samples, this study reported reinfections with SARS-CoV-2 N501Y mutant.

Table I
SARS-CoV-2 Mutations in Initial and Reinfection Confirmed by the Rapid Methods and Sequencing

| Cases | Initial infections | | Reinfections | |
|---|---|---|---|---|
| | Mutations | Date | Mutations | Date |
| 1 | G614, A570 and N501 MW897351 | 07/10/2020 | G614, D570, and Y501 MW897356 | 23/03/2021 |
| 2 | G614 and N501 | 10/09/2020 | G614 and Y501 | 22/04/2021 |
| 3 | G614 and N501 sequencings: MW897353.1 | 10/07/2020. | G614 and N501 sequencings: MW897354 | 10/02/2021 |
| 4 | G614 and N501 | 10/07/2020 | G614 and Y501 | 24/04/2021 |
| 5 | G614 and N501 | 10/07/2020 | G614 and Y501 | 24/04/2021 |
| 6 | G614 and N501 | 25/06/2020 | G614 and Y501 | 26/04/2021 |
| 7 | G614 and N501 | 10/07/2020 | G614 and Y501 | 26/04/2021 |
| 8 | G614 and N501 | 10/07/2020 | G614 and Y501 | 26/04/2021 |

Table 2
Demographics and Clinical Information of the Patients in Both Initial Infection and Reinfections

| Cases | Demography | | Comorbidities | Clinical manifestations | |
|---|---|---|---|---|---|
| | Age | Sex | | Initial infections | Reinfections |
| 1 | 42 | M | None | Severe sore throat, excessive cough, sneezing, malaise, fatigue, diarrhea, normal $SPO_2$ more than 96% | Moderate sore throat, mild coughs, dry mouth, malaise, fatigue. Normal CBC, ferritin, D-dimer, LDH and ESR, CRP (15 mg/dl). Negative IgG and IgM |
| 2 | 43 | M | None | Asymptomatic with normal CBC and acute phase parameters | Severe dry cough, malaise for 3 weeks. Loss of taste and smell |
| 3 | 35 | F | Obese | Tiredness, fever, headache, and loss of taste and smell | Tiredness, fever, and headache for 4 days |
| 4 | 55 | M | Hypertension, diabetes, obesity | Malaise, fever | Malaise, hypoglycemia, and diarrhea |
| 5 | 26 | F | None | Fever, tiredness, sore throat, headache, loss of taste and smell | Fever, tiredness, sore throat, headache, loss of taste and smell |
| 6 | 41 | M | Obese | Myalgia, fever, headache, loss of appetite. High platelet and WBC count | Tiredness and headache |
| 7 | 54 | F | None | Dry cough, myalgia, fever, headache, loss of appetite | Dry cough, tiredness, and fever |
| 8 | 34 | F | Asthma | Malaise, sore throat, headache | Malaise, sore throat, headache |

## V. Conclusion

This research explores SARS-CoV-2 reinfections using rapid low-cost methods and reported first reinfections with a SARS-CoV-2 N501Y mutant variant in the Kurdistan region of Iraq. Further study is required to apply these methods in a large number of samples. This will open our understandings of the epidemiology and reinfections of the virus.

## Acknowledgment

We are grateful to the individuals (patients) who gave clinical samples to this study.

## References

Al-Jaf, S.M.A., Niranji, S.S., 2021. Rapid detection of SARS CoV-2 N501Y mutation in clinical samples. *medRxiv* 2021, p.21255656.

Al-Jaf, S.M.A., Niranji, S.S., and Mahmood, Z.H., 2021. Rapid, inexpensive methods for exploring SARS CoV-2 D614G mutation. *Meta Gene*, 30, p. 100950.

Banada, P., Green, R., Banik, S., Chopoorian, A., Streck, D., Jones, R., Chakravorty, S., Alland, D., 2021. A simple RT-PCR melting temperature assay to rapidly screen for widely circulating SARS-CoV-2 variants. *MedRxiv*, 2021, p.21252709.

Brehm, T.T., Pfefferle, S., von Possel, R., Kobbe, R., Nörz, D., Schmiedel, S., Grundhoff, A., Olearo, F., Emmerich, P., Robitaille, P., Günther, T., Braun, P., Andersen, G., Knobloch, J.K., Addo, M.M., Lohse, A.W., Aepfelbacher, M., Fischer, N., Wiesch, J.S.Z., and Lütgehetmann, M., 2021. SARS-CoV-2 reinfection in a healthcare worker despite the presence of detectable neutralizing antibodies. *Viruses*, 13(4), p. 661.

CDC, 2020. Common Investigation Protocol for Investigating Suspected SARS-CoV-2 Reinfection. Available from: https://www.cdc.gov/coronavirus/2019-ncov/php/reinfection.html#print [Last accessed on 2021 May 05].

CDC, 2022. Altered Immunocompetence. Available from: https://www.cdc.gov/vaccines/hcp/acip-recs/general-recs/immunocompetence.html [Last accessed on 2022 Mar 15].

Challen, R., Brooks-Pollock, E., Read, J.M., Dyson, L., Tsaneva-Atanasova, K., and Danon, L., 2021. Risk of mortality in patients infected with SARS-CoV-2 variant of concern 202012/1: Matched cohort study.*BMJ*, 372, p.n579.

Choudhary, M.C., Crain, C.R., Qiu, X., Hanage, W., and Li, J.Z., 2021. SARS-CoV-2 sequence characteristics of COVID-19 persistence and reinfection. *MedRxiv*, 2021, p.21252750.

Costa, A.O.C., de Carvalho Aragão Neto, H., Nunes, A.P.L., de Castro,R.D., 2021. Covid-19: Is reinfection possible?. *EXCLI Journal*, 20, pp.522-536.

Davies, N.G., Jarvis, C.I., Edmunds, W.J., Jewell, N.P., Diaz-Ordaz, K., and Keogh, R.H., 2021. Increased mortality in community-tested cases of SARS-CoV-2 lineage B.1.1.7. *Nature*, 593(7858), pp.270-274.

Durner, J., Burggraf, S., Czibere, L., Tehrani, A., Watts, D.C., and Becker, M., 2021. Fast and cost-effective screening for SARS-CoV-2 variants in a routine diagnostic setting. *Dental Materials*, 37(3), pp.e95-e97.

Falahi, S., and Kenarkoohi, A., 2020. COVID-19 reinfection: Prolonged shedding or true reinfection? *New Microbes and New Infections*, 38, p.100812.

Graham, M.S., Sudre, C.H., May, A., Antonelli, M., Murray, B., Varsavsky, D., Kläser, K., Canas, L.S., Molteni, E., Modat, M., Drew, D.A., Nguyen, L.H., Polidori, L., Selvachandran, S., Hu, C., Capdevila, J., Hammers, A., Chan, A.T., Wolf, J., Spector, T.D., Steves, C.J., and Ourselin, S., 2021. Changes in symptomatology, reinfection, and transmissibility associated with the SARS-CoV-2 variant B.1.1.7: An ecological study. *The Lancet Public Health*, 6(5), pp.e335-e345.

Hansen, C.H., Mumoli, N., Clerici, P., De Paschale, M., Evangelista, I., Cei, M., and Mazzone, A., 2021. Assessment of protection against reinfection with SARS-CoV-2 among 4 million PCR-tested individuals in Denmark in 2020: A population-level observational study. *Lancet*, 397(10280), pp.1204-1212.

Hussein, N.R., Musa, D.H., Ibrahim, N., Saleem, Z.S.M., and Naqid I.A., 2021. COVID-19 Reinfection in a Nurse Working in Emergency Hospital in Duhok City, Kurdistan Region of Iraq. *Asian Journal of Case Reports in Medicine and Health*, 5(1), pp.27-30.

Hussein, N.R., Musa, D.H., Saleem, Z.S.M., Naqid, I.A., and Ibrahim, N., 2020. The first case of COVID-19 reinfection in Duhok city, Kurdistan region of Iraq: A case report. *Journal of Kermanshah University of Medical Sciences*, 24(4), p.111454.

Marquez, L., Koy, T., Spinler, J.K., Luna, R.A., Tocco, L., Fasciano, L., Dunn, J. and Campbell, J.R., 2021. Reinfection with severe acute respiratory syndrome coronavirus 2 (SARS-CoV-2) B. 1.1. 7 variant in an immunocompromised adolescent. *Infection Control and Hospital Epidemiology*, 1-2, pp. 1-6.

Mukherjee, A., Anand, T., Agarwal, A., Singh, H., Chatterjee, P., Narayan, J., Rana, S., Gupta, N., Bhargava, B., Panda, S., 2021. SARS-CoV-2 re-infection: Development of an epidemiological definition from India. *Epidemiology and Infection*, 149, p.e82.

Novazzi, F., Baj, A., Genoni, A., Spezia, P.G., Colombo, A., Cassani, G., Zago, C., Pasciuta, R., Gasperina, D.D., Ageno, W., Severgnini, P., Dentali, F., Focosi, D., and Maggi, F., 2021. SARS-CoV-2 B.1.1.7 reinfection after previous Covid-19 in two immunocompetent italian patients. *Journal of Medical Virology*, 93(9), pp.5648-5649.

Parry, J., 2020. Covid-19: Hong Kong scientists report first confirmed case of reinfection. *BMJ*, 370. p.m3340.

Qureshi, A.I., I Baskett, W., Huang, W., Lobanova. I., Naqvi, S.H., and Shyu, C.R., 2021. Re-infection with SARS-CoV-2 in patients undergoing serial laboratory testing. *Clinical Infectious Diseases*, 74(2), pp.294-300.

Ramírez, J.D., Muñoz, M., Ballesteros, N., Patiño, L.H., Castañeda, S., Rincón, C.A., Mendez, C., Oliveros, C., Perez, J., Márquez, E.K., de Los Santos Ortiz, F., Correa-Cárdenas, C.A., Duque, M.C., and Paniz-Mondolfi, A., 2021. Phylogenomic evidence of reinfection and persistence of sars-cov-2: First report from Colombia. *Vaccines*, 9(3), p.9030282.

Sandoval Torrientes, M., Abietar, C.C., Riveiro, J.B., Álvarez-Argüelles, M.E., Rojo-Alba, S., Salinas, F.A., González, I.C., Martínez, Z.P., Rodríguez, G.M., de Oña, J.G., García, E.C., and García, S.M., 2021. A novel single nucleotide polymorphism assay for the detection of N501Y SARS-CoV-2 variants. *Journal of Virological Methods*, 294, p.114143.

Simmonds, P., Williams, S., and Harvala, H., 2021. Understanding the outcomes of COVID-19-does the current model of an acute respiratory infection really fit? *The Journal of General Virology*, 102(3), p001545.

Staub, T., Arendt, V., de la Vega, E.C.L., Braquet, P., Michaux, C., Kohnen, M., Tsobo, C., Abdelrahman, T., Wienecke-Baldacchino, A., and Francois, J.H., 2021. Case series of four re-infections with a SARS-CoV-2 B.1.351 variant, Luxembourg, February 2021. *Euro Surveillance*, 26(18), p.2100423.

Stokel-Walker, C., 2021, What we know about covid-19 reinfection so far. *The BMJ*, 372, pp.1-2.

Weigang, S., Fuchs, J., Zimmer, G., Schnepf, D., Kern, L., Beer, J., Luxenburger, H., Ankerhold, J., Falcone, V., Kemming, J, Hofmann, M., Thimme, R., Neumann-Haefelin, C., Ulferts, S., Grosse, R., Hornuss, D., Tanriver, Y., Rieg, S., Wagner, D., Huzly, D., Schwemmle, M., Panning, M., and Kochs, G., 2021. Within-host evolution of SARS-CoV-2 in an immunosuppressed COVID-19 patient as a source of immune escape variants. *Nature Communications*, 12(1), p.6405.

# Driver Drowsiness Detection Using Gray Wolf Optimizer Based on Face and Eye Tracking

Sarah S. Jasim[1], Alia K. Abdul Hassan[2] and Scott Turner[3]

[1]Department of IT, Technical College of Management-Baghdad, Middle Technical University, Baghdad, Iraq
[2]Department of Computer Science, University of Technology, Baghdad, Iraq
[3]Director of Computing, School of Engineering, Design, and Technology, Church Christ Church University, Kent, United Kingdom

***Abstract*—It is critical today to provide safe and collision-free transport. As a result, identifying the driver's drowsiness before their capacity to drive is jeopardized. An automated hybrid drowsiness classification method that incorporates the artificial neural network (ANN) and the gray wolf optimizer (GWO) is presented to discriminate human drowsiness and fatigue for this aim. The proposed method is evaluated in alert and sleep-deprived settings on the driver drowsiness detection of video dataset from the National Tsing Hua University Computer Vision Lab. The video was subjected to various video and image processing techniques to detect the drivers' eye condition. Four features of the eye were extracted to determine the condition of drowsiness, the percentage of eyelid closure (PERCLOS), blink frequency, maximum closure duration of the eyes, and eye aspect ratio (ARE). These parameters were then integrated into an ANN and combined with the proposed method (gray wolf optimizer with ANN [GWOANN]) for drowsiness classification. The accuracy of these models was calculated, and the results demonstrate that the proposed method is the best. An Adadelta optimizer with 3 and 4 hidden layer networks of (13, 9, 7, and 5) and (200, 150, 100, 50, and 25) neurons was utilized. The GWOANN technique had 91.18% and 97.06% accuracy, whereas the ANN model had 82.35% and 86.76%.**

***Index Terms*—Artificial neural network, Drowsiness, Feature extraction, Gray wolf optimizer, Normalization, Segmentation.**

## I. Introduction

An essential in modern society is safe and collision-free travel. The rapid growth of traffic accidents impacts society and the individual level (Zhang, et al., 2017). Rapid eye movement is a signal for sleeping, one of the leading causes of traffic accidents. It is possible that using eye-tracking to alert drivers when their focus has strayed from the road could reduce the likelihood of collisions. Finding behavioral drivers and devising methods for classifying drivers that require an artificial neural network (Priddy and Keller, 2005) requires flexibility, competence, the ability to simplify and overcome categorization challenges, as well as the ability to determine similarities in patterns. Several governments have already concentrated interest in driving safety in modern norms. For example, DAISY (Driver Assisting System), a monitoring and alert system for drivers on German highways, and the Robotics Institute at Carnegie Mellon University created Copilot (Wang, et al.). Therefore, drowsiness detection research for drivers has critical importance. Computer vision has the potential to be a non-intrusive means of detecting drowsiness. It can be used to determine the facial characteristics analyzed by changing face manifestations, such as blinking of an eye, eye closure, yawning, and tracking the head position is also crucial in this area (Zhang, et al., 2017).

Nevertheless, this strategy needs to be implemented at a minimal cost; the current methods tend to use only high-quality and costly cameras (Lawoyin, et al., 2014). Moreover, despite substantial research on driver drowsiness detection (DDD), the impact of these discoveries appears to be waning in the actual world because only a few concepts are applied in real life (Bamidele, et al., 2019).

Because of the diversity of faces, developing a reliable face detection method is complex (e.g., size, location, stance, orientation, and expression) and environmental changes (e.g., illumination, exposure, and occlusion). Several effective ways (e.g., Wang, et al., Lawoyin, et al., 2014) have been created to designate pixels as human skin, and color spaces such as RGB, HSV, and YCrCb have been used. To identify more difficult face features, you often need to use complicated tools, but balancing the behavior of complex ones can take too long. Many powerful algorithms, including neural networks (Rowley, et al., 1998), support vector machines (SVMs) (Kadhm and Hassan, 2015), hidden Markov model (Hong, et al., 2005), and active shape model, can detect faces in complex backdrops. However, these procedures are difficult and costly in terms of time. Viola and Jones created an Adaboost face detection system that uses rectangular features, integral pictures, and cascade classifier architectures to detect faces in photos quickly. Moreover, this method's false detection rate is still high in drowsiness detection systems (Liu, et al., 2012).

ARO-The Scientific Journal of Koya University
Vol. X, No.1 (2022), Article ID: ARO.10928, 8 pages
DOI: 10.14500/aro.10928
Received: 14 January 2022; Accepted: 18 April 2022
Regular research paper: 05 May 2022
Corresponding author's email: sara-sm@mtu.edu.iq

 http://dx.doi.org/10.14500/aro.10928

Fig. 1. Image data samples for normal and abnormal cases.

This study developed a technique for acquiring images of a driver's face, including a recognition process on the driver's eye state, utilizing videos. The approach is divided into three phases, as illustrated in Fig. 1: extracting the eye's region, determining the state of eye recognition, and detecting sleepiness.

The remainder of the paper is organized as follows: First, the proposed system is presented in Section 3. Then, Section 4 shows the experiment's Results and Discussion. Final Section 5 presented the essay conclusion and works for the future.

## II. Related Work

Recent developments in artificial intelligence, or machine learning, have made enormous strides in image and signal recognition (Yu, et al., 2021). In recent years, a lot of research has shown that behavioral approaches are non-intrusive, such that they can capture the driver's alertness without any physical interaction with the driver. One of the first behavioral methods used in DDD was Percentage of Eyelid Closure (PERCLOS), which describes a threshold for the validation of subsequent systems (Alshaqaqi, et al., 2013). Furthermore, intricate interconnections of neuronal elements through electrical activity will influence functional linkages between biological neural networks, potentially allowing us to comprehend neurons better (Chen, et al., 2018).

Kumar and Patra, 2018, computed the eye aspect ratio (EAR) and mouth opening ratio (MOR) to detect driver's drowsiness. Logistic regression (LR) and Haar cascade classifier were investigated to detect drowsiness and achieved 92% and 86% accuracy, respectively.

Mehta, et al., 2019b, extracted the EAR, nose length ratio (NLR), and MOR. All features were fed into their advanced DDD system (AD3S) and applied to different types of classifiers (boosting technique [BT], Naïve Bayes, SVM, random forest [RF], Bagging, and Voting). The results show that the BT had the best accuracy (89.5%) compared to the other classifiers tested.

The work by Costa, 2019, describes an approach based on combining eye and head trackers, smart eye pro technique. SVM and decision tree (DT) were used to detect driver sleepiness. The study demonstrates that DT has 93% accuracy score compared to SVM has 91%.

Another work in de Naurois, et al., 2019, eyelid closure (EC), gaze (G), head movements (HM), and driving time was measured. Artificial neural networks (ANNs) were investigated to detect drowsiness and achieved an accuracy of 95% to detect drivers' drowsiness.

Combining EAR and eye closure ratio (ECR) to detect driver's drowsiness based on a RF classifier has been investigated (Mehta, et al., 2019a), with an overall accuracy was 84%.

Whereas authors in Gwak, et al., 2020, calculated the number of eye blinks (EB) and the percentage closure of eyes (PERCLOS), the features were fed into two classifiers a majority voting classifier and RF. In general, the best accuracy (89.8%) was obtained using RF.

The work in Dreißig, et al., 2020, extracted multiple behavioral features. In addition, some features related to HM and blinking (BM) evaluated the K-NN classifier's classification. The results show that the model achieves 84.2% and 70.0% in the binary and multiclass classification, respectively. Table I illustrates a brief utilization of behavioral techniques.

It is necessary to detect drowsiness in drivers before their driving ability is threatened. The problem of providing safe and collision-free transportation is crucial. For this purpose, an automated hybrid drowsiness classification technique includes the ANN and the GWO to distinguish human drowsiness and weariness.

## III. The Proposed System

At present, researchers in pattern recognition and machine learning are increasingly recognizing the importance of swarm optimization for reducing data dimensionality and improving classification accuracy. Features can be selected using various swarm optimization techniques, such as Particle Swarm Optimization or Ant Colony Optimization. New swarm-inspired algorithms, such as GWO, have recently appeared (Hassan and Mohammed, 2020). Gray wolf optimization (GWO) is a new metaheuristic algorithm based on how gray wolves behave in the wild. To keep order, the group used to have two species: Wolf males and wolf females (Xu, et al., 2019). Any herd has a social hierarchy that looks like this:

1. The leaders, known as alphas (decide ($\alpha$)), are male, and a female dominates wolves. The wolves problem them
2. Beta wolves ($\beta$) are second-level wolves. Beta's support dominant decisions
3. Delta's wolves ($\delta$) are the third-level wolves who obey the alphas and betas

TABLE I
SUMMARY OF ARTWORKS UTILIZING BEHAVIORAL TECHNIQUES

| References | Year | Behavioral features | Datasets | Machine learning methods | Accuracy (%) |
|---|---|---|---|---|---|
| Ghourabi, et al. | 2018 | EAR + MOR | Images of the driver's face in real time | LR | 92.0 |
| Gwak, et al. | 2019 | EAR + MOR + NLR | 1200 images in real time of application users | BT | 89.5 |
| Hassan and Mohammed | 2019 | Eye, Head | The real-time images of 20 volunteers | DT | 93.0 |
| Hassan and Jasim | 2019 | EC + G + HM | The real-time image of 21 participants (11 men and 10 women) | ANN | 95.0 |
| Heidari, et al. | 2019 | EAR + ECR | The real-time images of 50 volunteers | RF | 84.0 |
| Hong, et al. | 2020 | EB + PERCLOS | The real dataset of 16 males | RF | 89.8 |
| Huang, et al. | 2020 | HM + BM | A large real-time dataset | K-NN | 84.2 |

4. The omegas wolves (ω) signify the pack's most minor alpha, beta, and delta wolves' scheme. The GWO algorithm ranks alpha wolves best first, followed by beta and delta wolves. Omegas (ω) make up this population cluster (Heidari and Pahlavani, 2017). Algorithm I lists the pseudo-code of the gray wolf.

**Algorithm I**

THE PSEUDO-CODE OF THE GWO ALGORITHM

| | |
|---|---|
| Input | Start the gray wolf population $Xi$, in which $i$=1, 2, 3, 4.<br>Start α, $A$, and C<br>Number total of iterations for optimization.<br>The fitness of each candidate solution is computed through equations:<br>$X(t+1)=X(t)-A.D$ (1)<br>$D=\|C.X_p(_t)-X(t)\|$ (2)<br>$A=2a.r_1-a$ (3)<br>$X\alpha$, is the first finest search agent<br>$X\beta$, is the second finest search agent<br>$X\delta$, is the third finest search agent |
| Output | Optimal gray wolf position ($\alpha$); and the best fitness value $f(X\alpha)$. |
| | Begin |
| | Generate the GRAY wolf population Xi randomly. |
| | While (iteration<Maximum iteration number) |
| | { |
| | for each search agent |
| | Modify the current search agent's position throuh equation |
| | $X(t+1)=\frac{(X1+X2+X3)}{3}$ |
| | end for |
| | Modify A, C, and α |
| | The fitness for all search agent is computed |
| | Modify $X\alpha$, $X\beta$, and $X\delta$ |
| | iteration=iteration+1 |
| | return $X\alpha$ |
| | } |
| | End |

*A. Proposed Drowsiness Detection System Based on the Optimized ANN using Gray Wolf Optimizer (GWO)*

First stage: Using GWO for ANN training:

Selection: Size of individuals (Packs),

Improvement: Largest iterations are identified,

Formation: Using the backpropagation algorithm in NN, implementation: GWO in as (5) used to get the better value of weights and bias,

$$RMSE=\sqrt{\frac{1}{n}\sum_{i=1}^{n}\left(T_i-Y_i\right)^2} \quad (5)$$

Restoring: Optimum of weights and bias,

Second stage: GWO used to optimize backpropagation algorithms for training ANN:

Selection: GWO outputs as the beginning of weights and bias,

Restoring: Optimum training of ANN model.

*B. Dataset*

The dataset was a DDD video for this experiment provided by the National Tsing Hua University (NTHU) Computer Vision Lab and the link of download is available at Computer Vision Lab, November 2016. The total dataset (training, evaluation, and testing) includes 36 individuals of various nationalities. Table II explains the dataset. Using infrared lighting (IR) has been captured in videos. The resolution of the movie is AVI 640 × 480.

The total number of persons in the proposal is 17 of the international dataset (NTHU-DDD Dataset). The collection states normal and abnormal cases, as explained in Fig. 1.

*C. Initial Pre-processing of Data*

A data processing diagram is shown in Fig. 2. Pre-processing seeks to filter raw data and remove noise. Each frame tracks the driver's face before tracking his eyes to reduce the input dimension. One value represents each of the 307,200 inputs because the raw data currently at hand are a 640x480 pixel 15/30 fps video collection and each frame's respective drowsiness annotation. If this data were to be used, proposed machine learning classifiers would have 307,200 inputs/dimension values for each sample, which is very expensive. Then, each video's eye states that data were divided into 4 s segments. If 30 fps is employed, a 3 min video (180 s) would include 45 segments, each with 120 values. The 4-s duration was chosen since it is expected to elicit significant responses indicative of changes in alertness (Weng, et al., 2016). Finally, pupil eye detection is used to detect an open or closed eye to standardize the data. The following sections briefly describe these steps.

*Face and eye detection*

To assist the detection of a pupil of the eye from a dataset containing video frames; it is appropriate to convert into the grayscale image, after that an Adaptive Histogram

http://dx.doi.org/10.14500/aro.10928

Equalization (AHE) is used, Viola-Johns applied to detect the face and eyes (this algorithm has high accuracy for object detection); alongside using contours and morphological operations (erosion and dilation). Erosion removes the image's white region while dilatation adds it. This model's binarized eye performs closing (dilation followed by erosion), erosion, and ultimately opening (erosion followed by dilation). The opening function removed noise (scanty white pixels) from the visual image, whereas the closing function closed small black dots in the image. The output will be confined to four values:

- A value of (0) indicates face detection
- A value of (0.50) indicates no face detection
- A value of (0.75) indicates one eye detection
- A value of (1) indicates (left and right) eye detection.

*Segmentation and label of a video frame*

The eye data are divided into 4 s segments in 3 min, and this means that each segment is treated as 120 values. Each eye contains 480 labels (3 min multiplied by 120 values). Therefore, each video will have four labels. Drowsiness, eye, head, and mouth are the four labels for each eye state, and each of these labels could have a distinct value. Like sleepiness and eyes labels, head and mouth labels have a value of 2 and are changed to 0.1. It eliminated the scenario of looking away while chatting or laughing because it does not represent sleep. As a result, if a threshold is the biggest from value (0.25), it is changed to 1, whereas if it is the smallest, it is turned to 0.

*D. Extraction and Normalization of Features*

Four features were derived from the eye state data. The features were calculated every 4 s within the video frame. The percentages of eyelid closure (PERCLOS), blink frequency (BF), maximum closure duration (MCD), and aspect ratio eye are the features calculated (ARE) using the following as 6, 7, 8, 9, and 10.

$$PERCLOS = \left( t_1 + t_2 + \ldots + t_n \Big/ T \right) * 100 \quad (6)$$

$$BF = n \Big/ T \quad (7)$$

$$MCD = MAX\left(t_1, t_2, \ldots, t_n\right) \quad (8)$$

$$ARE\ in\ Left\ Eye = \left(p2 - p6\right) + \left(p3 - p5\right) \Big/ 2*(p4 - p1) \quad (9)$$

$$ARE\ in\ Right\ Eye = \left(p8 - p12\right) + \left(p9 - p11\right) \Big/ 2*(p10 - p7) \quad (10)$$

Where, $(t_1+t_2+.+t_n)/T$ is a percentage of eyelid closure, $T$=120; $n/T$ is the number of blinks per minute, and Max ($t_1$, $t_2$., $t_n$) is the longest allowed of eye closure, as explained in Figs. 3 and 4.

After extracting the characteristics, the next and last step was to scale the data to normalize its range. This procedure is essential because machine learning models employ the Euclidean distance to calculate the distance between two values during the learning process. Moreover, the characteristics for this data were as follows: MCD is 0–120 because the length of each segment is 120, which

TABLE II
DESCRIPTION OF NTHU DATASET (BAMIDELE, ET AL., 2019)

| Dataset category | Training group and evaluation group |
|---|---|
| Gender of driver | Female and male |
| Type of scenario | No glasses, glasses, sunglasses, night-no glasses, and night-glasses |
| Driver's behaviors | Yawning, nodding, looking aside, talking and laughing, sleepy eyes, drowsy, and stillness |
| Videos | Yawning.avi, slowBlinkWithNodding.avi, sleepyCombination.avi, and nonsleepyCombination.avi |
| Labels | Drowsiness.txt, head.txt, mouth.txt, and eye.txt |
| Labels No. | 0, 1, and 2 |

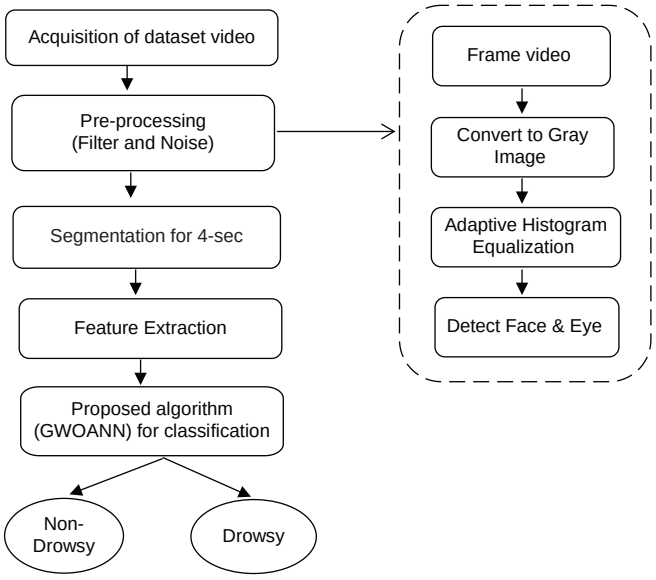


Fig. 2. Data processing protocol and classification model.

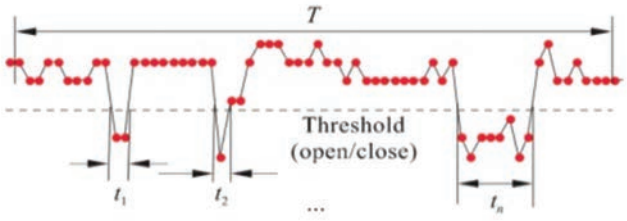


Fig. 3. PERCLOS, BF, and MCD Features (Zhang, et al., 2012).

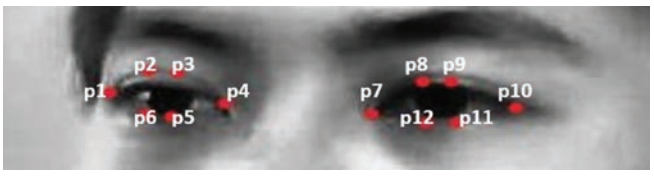


Fig. 4. Points in AER features.

is also the maximum time a person could have their eyes closed in a segment. PERCLOS is 0 to 100 since it is a percentage, and BF is 0–40. In machine learning, there are numerous techniques to normalize features. For example, standardization, as in Equation (11), rescales features to have a zero mean and unit variance. Because it is the most extensively used normalization technique for collecting machine learning algorithms employed, it was chosen.

$$Standardization = {x - \mu}/{\sigma} \quad (11)$$

Where, ($x$) is the data point, ($\propto$) is the mean, and ($\sigma$) is the standard deviation.

*E. Classification of Drowsiness*

Only two states, namely, the state of sleepiness (1) and the state of alertness (0), are used to classify binary drowsiness. They employ machine learning technologies, for example, to identify DDD using machine learning methods, for example, SVM, KNN, ANN, DT, etc. The proposed approach (GWOANN) and the (ANN) were depended on in this study because they successfully solved problems of non-linearity, high-dimensional classifications, and even classification in EOG signals.

*ANN*

A neural network is a collection of processing units designed to produce human-like outcomes. On the other hand, one subdivision performs its computations and sends them to a second (Yusiong, 2012; Abdulwahed, 2018; Rashid and Abdullah, 2018). The network has three layers: Input, hidden, and output (Huang, et al., 2021; Nwobi-Okoye and Ochieze, 2018). ANN models have been developed for a long time. Even when people or other computer algorithms cannot find patterns and trends in complex or confusing data, neural networks can disclose them; ANN has good classification and performance approximation performance (Abed, 2019). As a result, a qualified neural network can be seen as an "Expert" in the knowledge category for which it has received only an assessment. This expert can then be utilized to make forecasts in new situations of concern and respond to "what if" queries (Bati and Adam, 2006, Hassan and Jasim, 2010).

*The proposed GWOANN*

In the starting, GWO algorithms are used to train ANN to identify the best weights and biases, as shown in Algorithm II. An effective backpropagation network is then used to equip the neural network. Finally, check to see if the network has reached the correct error rate or if the number of generations required to finish the algorithm has been surpassed, as shown in Algorithm III. Fig. 2 depicts the method's main flowchart. For the depiction of the ANN, consider using a two-layered network, as follows in Equation (12).

$$\sum_{k=1}^{N} w_k f\left(\sum_{i=1}^{m} w_i x_i + b\right) \quad (12)$$

Where, ($N$) represents the number of neurons in the hidden layer, ($w$) represents the weight of a net, $b$ represents the bias value, and ($f$) represents the activation function of each neuron in this example. As in Equation (13) is the mean squared error (MSE):

$$MSE = {\sum_{t}^{z}\left(d^t - y^t\right)^2}/{z} \quad (13)$$

If ($d$) is the desired output and ($y$) is the actual output, $z$ is the number of testing outcomes, $T$ is the goal value, and $Y$ is the projected output, then as in Equation (14) indicates a superior model.

$$RMSE = \sqrt{\frac{1}{n}\sum_{i=1}\left(T_i - Y_i\right)^2} \quad (14)$$

**Algorithm II**

The hybrid GWOANN method

| Using GWO to train ANN: | |
|---|---|
| Input | Selection of number of people in the population (Pack),<br>Optimization by defining the maximum number of iterations,<br>Creation of the ANN shape by backpropagation technique<br>Execution GWO to discover the best value for weight and biases in Equation (9), |
| Output | Return the optimum weight and biases at the outset, |

**Algorithm III**

GWO's optimal backpropagation technique was used to train an ANN

| | |
|---|---|
| Input | GWO's initial weight and biases are used in the selection process. |
| Output | Return the best ANN shape for training, |

## IV. Experiments Results and Discussion

The dataset has been used in several experiments, one of which used a video from the Computer Vision Lab at National Tsing Hua University (NTHU) to detect driver drowsiness. The following stages are included in each experiment:

- Pre-processing
- Features extraction
- Classification by ANN and GWOANN.

Discovering the parameters that work well for each classifier is critical. There were a set of predetermined values used. Three trials were run for each classifier, with a different training-testing proportion. These were 90–10%; 80–20%; and 70–30%. The suggested approach requires data on PERCLOS, BF, MCD, and ARE of eye movement. This research tested two classification categories (drowsy or not).

http://dx.doi.org/10.14500/aro.10928

TABLE III
PARAMETERS USED FOR A STANDALONE ANN MODEL

| Parameters | Value |
|---|---|
| Max iteration | 1000 |
| Number of (neurons in the I/P layer) | 4 |
| Number of (hidden layer) | 4 and 5 |
| Number of (neurons in each hidden layer) | (13, 9, 7, and 5) and (200, 150, 100, 50, and 25) |
| Number of (neurons in O/P layer) | 2 |

TABLE IV
THE RESULTS PROVIDED BY STANDALONE ANN

| No. hidden neurons | 13, 9, 7, and 5 | | | 200, 150, 100, 50, and 25 | | |
|---|---|---|---|---|---|---|
| Run number | Acc. (90–10%) | Acc. (80–20%) | Acc. (70–30%) | Acc. (90–10%) | Acc. (80%–20%) | Acc. (70%–30%) |
| 1 | 76.47 | 66.91 | 74.02 | 83.82 | 84.56 | 82.35 |
| 2 | 63.24 | 70.59 | 74.02 | 82.35 | 80.15 | 86.76 |
| 3 | 72.06 | 75.74 | 74.51 | 86.76 | 91.91 | 88.71 |
| 4 | 67.65 | 64.71 | 72.06 | 82.35 | 86.76 | 86.24 |
| 5 | 64.71 | 80.88 | 76.96 | 85.29 | 83.09 | 80.24 |
| 6 | 67.65 | 75 | 73.53 | 82.35 | 85.29 | 84.80 |
| 7 | 79.41 | 67.65 | 70.59 | 85.29 | 84.56 | 86.76 |
| 8 | 82.35 | 76.47 | 73.04 | 85.29 | 86.03 | 83.25 |
| 9 | 63.24 | 79.41 | 79.41 | 80.88 | 84.56 | 85.78 |
| 10 | 75 | 70.59 | 73.04 | 80.88 | 86.03 | 80.88 |

TABLE V
PARAMETERS BASED ON GWO AND ANN

| Parameters | Value |
|---|---|
| Parameters based on GWO | |
| Iteration no. | 100 |
| Population size | 100 |
| Parameters based on ANN | |
| Number of (neurons in the I/P Layer) | 4 |
| Number of (hidden layer) | 4 and 5 |
| Number of (neurons in each hidden layer) | (13, 9, 7, and 5) and (200, 150, 100, 50, and 25) |
| Number of (neurons in O/P layer) | 2 |
| Max iteration | 10,000 and 12,000 |

### *A. Using ANN Classifier*

It is used to classify the driver's sleepiness using MLP. Unsupervised learning is used to build an ANN that can classify driver drowsiness. The parameters used in Table III determine the standalone ANN classifier.

Table IV illustrates the results of utilizing a standalone ANN classifier with 90–10%, 80–20%, and 70–30% training-testing percentages. The ANN classifier had the best accuracy when the training-testing percentages were 70–30%. Table III shows that the accuracy percentages have reduced by 90–10% and 80–20%.

### *B. Using GWOANN*

GWO swarm is used to find the best weights and biases in the training phase of the ANN. The suggested method involves first training the network with starting weights and biases, then updating the findings. Hence, the global optima backpropagation is sped up. The suggested technique includes weights and biases.

TABLE VI
THE RESULTS PROVIDED BY GWOANN

| No. hidden neurons | 13, 9, 7, and 5 | | | 200, 150, 100, 50, and 25 | | |
|---|---|---|---|---|---|---|
| Run number | Acc. (90–10%) | Acc. (80–20%) | Acc. (70–30%) | Acc. (90–10%) | Acc. (80–20%) | Acc. (70–30%) |
| 1 | 91.18 | 86.76 | 87.43 | 88.24 | 88.97 | 88.24 |
| 2 | 82.35 | 89.71 | 86.76 | 82.35 | 91.18 | 86.76 |
| 3 | 86.76 | 86.03 | 77.45 | 77.94 | 88.97 | 85.29 |
| 4 | 80.88 | 82.35 | 77.45 | 94.18 | 83.82 | 88.73 |
| 5 | 85.29 | 80.88 | 81.86 | 92.65 | 81.62 | 81.86 |
| 6 | 77.94 | 77.94 | 75.49 | 97.06 | 88.24 | 84.31 |
| 7 | 89.71 | 83.82 | 87.75 | 85.29 | 90.44 | 85.78 |
| 8 | 88.24 | 86.03 | 81.37 | 88.24 | 84.56 | 81.27 |
| 9 | 83.82 | 84.56 | 86.76 | 83.82 | 85.29 | 83.82 |
| 10 | 88.24 | 80.88 | 78.92 | 88.24 | 86.03 | 84.31 |

It is based on RMSE. This classification is more accurate than the ANN classifier, as shown in Tables V and VI.

Table VI demonstrates the outcomes of implementing the proposed hybrid approach (GWOANN) with 90–10%, 80–20%, and 70–30% training-testing percentages. The GWOANN approach, once again, achieved balanced accuracy in all percentages of training and testing. To avoid overfitting, the algorithm's lower number of parameters was used. It achieved higher simplicity and, reasonably, the lower the risk of overfitting, where it's trained with more data can help the algorithm detect the signal better or using early stopping.

Tables VII and VIII display the best, worst, mean, and standard deviation of two classifiers employing 90–10%, 80–20%, and 70–30% training-testing percentages with neurons in hidden layers (13, 9, 7, and 5) and (200, 150, 100, 50, and 25). The proposed method's STD value was the lowest compared to the ANN classifier. Compared to the ANN classifier, the value of best, worst, and mean achieved the highest value. Thus, the proposed approach (GWOANN) is stable and specific.

In addition, all classifications considered in this work have reasonable precision, but the GWOANN classificatory reaches 99.6% with the highest rating accuracy. Therefore, the proposed solution may be essential for future studies or future "systems" vehicles as reference work. Table IX compares the proposed method's improvement rate with the ANN classifier in 90-10%, 80-20%, and 70-30% training-testing percentages.

$$Improvement\ rate = \frac{A1 - A2}{A2} \quad (15)$$

Where, (A1) represents the accuracy of the proposed algorithm and (A2) represents the accuracy of another classifier.

## C. COMPARATIVE ANALYSIS OF RESULTS

Comparisons are made between the outcomes of the ANN and GWOANN algorithms and the findings of prior works using the labeled NTHU-DDD dataset. Results of this comparison are provided in Table X. It was observed that the results of the proposed paper had obtained high accuracy compared to previous works.

TABLE VII
THE RESULTS OF CLASSIFIERS MODELS

| No. hidden neurons | 13, 9, 7, and 5 | | | | | | | | | | | |
|---|---|---|---|---|---|---|---|---|---|---|---|---|
| Name classifier | (90% training, 10% testing) | | | | (80% training, 20% testing) | | | | (70% training, 30% testing) | | | |
| | Best Acc. (%) | Worst Acc. (%) | Mean (%) | STD. | Best Acc. (%) | Worst Acc. (%) | Mean (%) | STD. | Best Acc. (%) | Worst Acc. (%) | Mean (%) | STD. |
| ANN | 82.35 | 63.24 | 71.18 | 0.065477 | 80.88 | 64.71 | 72.80 | 0.052188 | 79.41 | 70.59 | 74.12 | 0.023581 |
| GWOANN | 91.18 | 77.94 | 85.44 | 0.03973 | 89.71 | 77.94 | 83.90 | 0.03280 | 87.75 | 75.49 | 82.12 | 0.04488 |

TABLE VIII
THE RESULTS OF CLASSIFIERS MODELS

| No. hidden neurons | 200, 150, 100, 50, and 25 | | | | | | | | | | | |
|---|---|---|---|---|---|---|---|---|---|---|---|---|
| Name classifier | (90% training, 10% testing) | | | | (80% training, 20% testing) | | | | (70% training, 30% testing) | | | |
| | Best Acc. (%) | Worst Acc. (%) | Mean (%) | STD. | Best Acc. (%) | Worst Acc. (%) | Mean (%) | STD. | Best Acc. (%) | Worst Acc. (%) | Mean (%) | STD. |
| ANN | 86.76 | 80.88 | 83.53 | 0.019502 | 91.91 | 80.15 | 85.29 | 0.028273 | 88.71 | 80.24 | 84.58 | 0.02647 |
| GWOANN | 97.06 | 77.94 | 87.80 | 0.05474 | 91.18 | 81.62 | 86.91 | 0.02956 | 88.73 | 81.27 | 85.04 | 0.023303 |

TABLE IX
IMPROVEMENT RATE OF GWOANN OVER STANDALONE ANN

| Classifier | 90–10% | | | 80–20% | | | 70–30% | | |
|---|---|---|---|---|---|---|---|---|---|
| | IR of best (%) | IR of worst (%) | IR of mean (%) | IR of best (%) | IR of worst (%) | IR of mean (%) | IR of best (%) | IR of worst (%) | IR of mean (%) |
| Hidden neurons in ANN (13, 9, 7, and 5) | 11 | 23 | 15 | 13 | 20 | 13 | 15 | 10 | 11 |
| Hidden neurons in ANN (200, 150, 100, 50, and 25) | 12 | 1 | 2 | 6 | 2 | 0 | 9 | 2 | 1 |

TABLE X
COMPARATIVE ANALYSIS OF THE NTHU DATASET TO OTHER RECENT STATE-OF-THE-ARTS

| Method | Accuracy % |
|---|---|
| Alex Net (Krizhevsky, et al., 2012) | 70.4 |
| VGC-Face Net (Parkhi, et al., 2015) | 63.8 |
| LRCN (Donahue, et al., 2015) | 68.7 |
| Flow ImageNet (Donahue, et al., 2015) | 56.3 |
| DDD-FFA (Park, et al., 2016) | 78.2 |
| DDD-IAA (Park, et al., 2016) | 69.8 |
| CARL 3D DCNN (Yu, et al., 2018) | 79.6 |
| 3D DCNN (Yu, et al., 2016) | 75.1 |
| K-NN (Ghourabi, et al., 2020) | 72.55 |
| MLP (Ghourabi, et al., 2020) | 72.47 |
| DNN (Vu, et al., 2019) | 84.81 |
| LeNet-5 CNN (Islam, et al., 2020) | 93.57 |
| CNN (Ravi Teja, et al., 2021) | 89.00 |
| Proposed ANN | 86.76 |
| Proposed GWOANN | 97.06 |

## V. CONCLUSION

This paper sought a low-cost, non-intrusive method of detecting driver drowsiness using face and eye monitoring by placing a good and inexpensive camera that types (CAM 313). Such eye state recognition is a highly accurate technology. This study examines the results of the input parameters that can be detected driver drowsiness early by measuring the percentage of eyelid closure (PERCLOS), blink frequency (BF), maximum closure duration (MCD), and aspect ratio eye (ARE) characteristics. To prevent accidents, they can detect driver drowsiness early on. To compare, we found that using a hybrid approach gives us 91.18% and 97.06% accuracy, whereas using only an ANN gives us an accuracy of 82.35% and 86.76%, making the hybrid approach superior to the ANN algorithm. Even though the proposed method produced great accuracy results, there is still scope for change. Behavioral approaches combined with physiological strategies can provide a significant advantage in the future.

## REFERENCES

Abdulwahed, M.N., 2018. Analysis of image noise reduction using neural network. *Engineering and Technology Journal*, 36, pp.76-87.

Abed, I.S., 2019. Lung cancer detection from X-ray images by combined Backpropagation neural network and PCA. *Engineering and Technology Journal*, 37, pp.166-171.

Alshaqaqi, B., Baquhaizel, A.S., Ouis, M.E.A., Boumehed, M., Ouamri, A. and Keche, M., 2013. Driver drowsiness detection system. In: *8th International Workshop on Systems, Signal Processing and their Applications* (*WoSSPA*), pp.151-155.

Bagci, A.M., Ansari, R., Khokhar, A. and Cetin, E., 2004. Eye tracking using Markov models. In: *Proceedings of the 17th International Conference on Pattern Recognition*, IEEE, pp.818-821.

Bamidele, A., Kamardin, K., Syazarin, N., Mohd, S., Shafi, I., Azizan, A., Aini, N. and Mad, H., 2019. Non-intrusive driver drowsiness detection based

on face and eye tracking. *International Journal of Advanced Computer Science and Applications*, 10, pp.549-569.

Bati, A.F. and Adam, N.E., 2006. Hybrid neuro-genetic based controller of power system. *Iraqi Journal of Computers, Communication, Control and Systems Engineering*, 6, pp.112-125.

Chen, J., Wang, H. and Hua, C. 2018. Assessment of driver drowsiness using electroencephalogram signals based on multiple functional brain networks. *International Journal of Psychophysiology*, 133, pp.120-130.

Computer Vision Lab, 2016. *Driver Drowsiness Detection Dataset*. Available from: http://cv.cs.nthu.edu.tw/php/callforpaper/datasets/DDD [Last accessed on 2016 Nov 12].

Costa, M., 2019. Detecting driver's fatigue, distraction and activity using a non-intrusive ai-based monitoring system. *Journal of Artificial Intelligence and Soft Computing Research*, 9, pp.247-266.

De Naurois, C.J., Bourdin, C., Stratulat, A., Diaz, E. and Vercher, J.L., 2019. Detection and prediction of driver drowsiness using artificial neural network models. *Accident Analysis and Prevention*, 126, pp.95-104.

Donahue, J., Anne Hendricks, L., Guadarrama, S., Rohrbach, M., Venugopalan, S., Saenko, K. and Darrell, T., 2015, Long-term recurrent convolutional networks for visual recognition and description. *Proceedings of the IEEE Conference on Computer Vision and Pattern Recognition*, 2015, pp.2625-2634.

Dreißig, M., Baccour, M.H., Schäck, T. and Kasneci, E., 2020. Driver Drowsiness Classification Based on Eye Blink and Head Movement Features Using the k-NN Algorithm. In: *IEEE Symposium Series on Computational Intelligence* (*SSCI*). p889-896.

Ghourabi, A., Ghazouani, H. and Barhoumi, W., 2020. Driver drowsiness detection based on joint monitoring of yawning, blinking and nodding. In: *IEEE 16th International Conference on Intelligent Computer Communication and Processing* (*ICCP*). p407-414.

Gwak, J., Hirao, A. and Shino, M., 2020. An investigation of early detection of driver drowsiness using ensemble machine learning based on hybrid sensing. *Applied Sciences*, 10, p.2890.

Hassan, A.K. and Mohammed, S.N., 2020. A novel facial emotion recognition scheme based on graph mining. *Defence Technology*, 16, pp.1062-1072.

Hassan, A.K.A. and Jasim, S.S., 2010. Integrating neural network with genetic algorithms for the classification plant disease. *Engineering and Technology Journal*, 28, pp.686-702.

Heidari, A.A. and Pahlavani, P., 2017. An efficient modified grey wolf optimizer with Lévy flight for optimization tasks. *Applied Soft Computing*, 60, pp.115-134.

Hong, K., Min, J., Lee, W. and Kim, J., 2005. Real time face detection and recognition system using Haar-like feature/HMM in ubiquitous network environments. In: *International Conference on Computational Science and its Applications*, Springer, Berlin. p1154-1161.

Huang, X., Cheng, C. and Zhang, X.B., 2021. Machine learning and numerical investigation on drag reduction of underwater serial multi-projectiles. *Defence Technology*, 18, pp.229-237.

Islam, M.R., Matin, A. and Kamruzzaman, T., 2020. Automatic Identification of Driver Inattentiveness Using Convolutional Neural Networks. In: *IEEE International Women in Engineering (WIE) Conference on Electrical and Computer Engineering* (*WIECON-ECE*). pp.21-24.

Kadhm, M.S. and Hassan, A.K.A., 2015. Handwriting word recognition based on SVM classifier. *International Journal of Advanced Computer Science and Applications*, 1, pp.64-68.

Krizhevsky, A., Sutskever, I. and Hinton, G.E., 2012. Imagenet classification with deep convolutional neural networks. *Advances in Neural Information Processing Systems*, 25, pp.1097-1105.

Kumar, A. and Patra, R., 2018. Driver drowsiness monitoring system using visual behaviour and machine learning. In: *2018 IEEE Symposium on Computer Applications and Industrial Electronics* (*ISCAIE*), IEEE. pp.339-344.

Lawoyin, S., Liu, X., Fei, D.Y. and Bai, O., 2014. Detection methods for a low-cost accelerometer-based approach for driver drowsiness detection. In: *IEEE International Conference on Systems, Man, and Cybernetics* (*SMC*), IEEE. pp. 1636-1641.

Liu, T., Xie, J., Yan, W. and Li, P., 2012. Driver's face detection using space-time restrained adaboost method. *KSII Transactions on Internet and Information Systems* (*TIIS*), 6, pp.2341-2350.

Mehta, S., Dadhich, S., Gumber, S. and Jadhav Bhatt, A., 2019a. Real-time Driver Drowsiness Detection System Using Eye Aspect Ratio and Eye Closure Ratio. In: *Proceedings of international conference on sustainable computing in science, technology and management* (*SUSCOM*), Amity University Rajasthan, Jaipur, India.

Mehta, S., Mishra, P., Bhatt, A.J. and Agarwal, P., 2019. AD3S: Advanced driver drowsiness detection system using machine learning. In: *5th International Conference on Image Information Processing* (*ICIIP*), IEEE. pp. 108-113.

Nwobi-Okoye, C.C. and Ochieze, B.Q., 2018. Age hardening process modeling and optimization of aluminum alloy A356/Cow horn particulate composite for brake drum application using RSM, ANN and simulated annealing. *Defence Technology*, 14, pp.336-345.

Park, S., Pan, F., Kang, S. and Yoo, C.D., 2016. Driver Drowsiness Detection System Based on Feature Representation Learning Using Various Deep Networks. In: Asian Conference on Computer Vision. Springer, Berlin. pp. 154-164.

Parkhi, O.M., Vedaldi, A. and Zisserman, A., 2015. *Deep Face Recognitio*n.

Rashid, T.A. and Abdullah, S.M., 2018. A hybrid of artificial bee colony, genetic algorithm, and neural network for diabetic mellitus diagnosing. *ARO The Scientific Journal of Koya University*, 6, pp.55-64.

Ravi Teja, P., Anjana Gowri, G., Preethi Lalithya, G., Ajay, R., Anuradha, T. and Kumar, P., 2021. Driver drowsiness detection using convolution neural networks. In: *Smart Computing Techniques and Applications*. Springer, Berlin.

Rowley, H.A., Baluja, S. and Kanade, T., 1998. Neural network-based face detection. *IEEE Transactions on Pattern Analysis and Machine Intelligence*, 20, pp.23-38.

Vu, T.H., Dang, A. and Wang, J.C., 2019. A deep neural network for real-time driver drowsiness detection. *IEICE Transactions on Information and Systems*, 102, pp.2637-2641.

Wang, Q., Yang, J., Ren, M. and Zheng, Y., 2006. Driver Fatigue Detection: A Survey. *6th World Congress on Intelligent Control and Automation*.

Weng, C.H., Lai, Y.H. and Lai, S.H., 2016. Driver drowsiness detection via a hierarchical temporal deep belief network. In: *Asian Conference on Computer Vision*. Springer, Berlin. pp. 117-133.

Xu, L., Wang, H., Lin, W., Gulliver, T.A. and Le, K.N., 2019. GWO-BP neural network based OP performance prediction for mobile multiuser communication networks. *IEEE Access*, 7, pp.152690-152700.

Yu, J., Park, S., Lee, S. and Jeon, M., 2016. Representation learning, scene understanding, and feature fusion for drowsiness detection. In: *Asian Conference on Computer Vision*, Springer, Berlin. pp. 165-177.

Yu, J., Park, S., Lee, S. and Jeon, M., 2018. Driver drowsiness detection using condition-adaptive representation learning framework. *IEEE Transactions on Intelligent Transportation Systems*, 20, pp.4206-4218.

Yu, X., Wang, S.H. and Zhang, Y.D., 2021. CGNet: A graph-knowledge embedded convolutional neural network for detection of pneumonia. *Information Processing and Management*, 58, p.102411.

Yusiong, J.P.T., 2012. Optimizing artificial neural networks using cat swarm optimization algorithm. *International Journal of Intelligent Systems and Applications*, 5, p.69.

Zhang, F., Su, J., Geng, L. and Xiao, Z., 2017. Driver fatigue detection based on eye state recognition. In: *International Conference on Machine Vision and Information Technology* (*CMVIT*), IEEE. pp. 105-110.

Zhang, W., Cheng, B. and Lin, Y., 2012. Driver drowsiness recognition based on computer vision technology. *Tsinghua Science and Technology*, 17, pp.354-362.

# Measuring the Voice Resemblance Extent of Identical (Monozygotic) Twins by Voiceprints Neutrosophic Domain

Yazen A. Khaleel[1], Caroline Y. Daniel[1] and Salah I. Yahya[1,2]

[1]Department of Software Engineering, Faculty of Engineering, Koya University, Koya, Kurdistan Region – F.R. Iraq

[2]Department of Communication and Computer Engineering, Cihan University-Erbil, Erbil, Kurdistan Region – F.R. Iraq

***Abstract*—The identical twins (monozygotic) are siblings (sib) created from the division of one fertilized egg (zygote), so they will be identical in their genetic characteristics and therefore in their phenotypic traits to a very large extent. The voiceprint of the twins is one of these traits. This paper proposed a method to determine the extent of the similarity and dis-similarity between the voiceprints for the brothers of identical twin and thus it is possible to distinguish between their voices. The proposed method adopts the use of the spectrogram as two-dimensional function with neutrosophic transformation. The neutrosophy theory is applied to all spectrogram elements that belong to the first sibling to determine to what extent this element belongs to the spectrogram of the second sibling for the same utterance. This study relied on the use of a number of voice clips collected from 35 identical twins. The neutrosophic transformation is used to convert the voiceprints into the neutrosophic domain represented by three membership functions (true, false, and indeterminate). The results showed that the average extent of the similarity ratio between twins' voices (true membership) is 68.15%, the difference ratio (false membership) is 31.84%, and the indeterminacy membership function ratio is 18.83%.**

***Index Terms*—Identical Twins, Monozygotic, Neutrosophic domain, Voiceprint.**

## I. Introduction

Monozygotic (MZ) twins (identical twins) come from one fertilized egg (zygote). The identical twins are well-known to show the most extreme form of anatomical, physiological match among human beings. Identical twins cannot be distinguished using DNA, which has caused problems in creating evidence in many forensic cases Künzel (2011). It is recommended that the biometric identifiers, such as fingerprints, iris, palm prints (Kong, Zhang, Lu, 2006), face, and voice (Kong, Zhang, Lu, 2006); (Kodate, et al., 2002), can still be used to discriminate them.

The physical features of the laryngeal, such as vocal fold length and structure, shape and size of the supraglottic vocal tract, and vocal mechanism, are genetically determined (Sataloff, Herman-Ackah, Hawkshaw, 2007). The excitation vocal signal which is generated by the human vocal cords is filtered by the shape of the vocal tract that includes the tongue and teeth. This shape specifies what sound comes out (Khaleel, 2020).

Although voice is unique to individuals, researches show perceptive similarity in MZ twins (Van Gysel, Vercammen, and Debruyne, 2001). Many studies showed that MZ twins have similar voice characteristics, leading to perceived similarity (Whiteside and Rixon, 2000).

Fuchs, et al. (2000) presented a study to identify parameters of voice performance and acoustic features in MZ twins. They compared intrapair differences with data from a control group. Moreover, they examined the correlation of intrapair differences with the age of the MZ twins. A more significant difference in older twin pairs than in younger pairs could show the effect of an exogenous influence. They inspected seven parameters of voice performance and three acoustic features in 31 MZ twin pairs (median age 36 years, range 18–75 years) and compared them with control group pairs, which consisted of non-related persons of the same sex and age. In Cielo, et al. (2012) research, two pairs of adult twins participated, one pair of each sex. They found no differences in vocal attack, articulation, loudness, resonance, respiratory mode, and type in both pairs of MZ twins evaluated, and the results were within normal limits.

Sebastian, et al. (2013) have a study aimed at perceptually and acoustically discriminating the voices of identical twins from each other. A perception test was done to find whether the voices of identical twins could be perceived as the same or different voices. Ten MZ twin pairs, five females and five males between the ages of 10 and 15 years old participated as speakers. Five native listeners were requested to judge whether each pair belonged to the same speaker or to different

ARO-The Scientific Journal of Koya University
Vol. X, No.1 (2022), Article ID: ARO.10925, 6 pages
DOI: 10.14500/aro.10925
Received: 10 January 2022; Accepted: 14 May 2022
Regular research paper: Published: 25 May 2022
Corresponding author's e-mail: yazen.adnan@koyauniversity.org

speakers. The acoustic analysis exposed that shimmer values are more sensitive in discriminating twin voices among each other. This study can contribute to automatic speaker recognition.

The study of Segundo, et al. (2017), explores the forensic potential of voice features combining source and filter characteristics. A set of features have been extracted from pause fillers. Speaker similarity was measured using standardized Euclidean distances (EDs) between pairs of speakers: 54 different-speaker (DS) comparisons, 54 same-speaker (SS) comparisons, and 12 comparisons between MZ twins. Their results revealed that the differences between DS and SS comparisons were significant in both high-quality and telephone-filtered recordings, with no false rejections and limited false acceptances. Mean ED for MZ pairs lies between the average ED for SS and DS comparisons.

Cavalcanti, Eriksson, Barbosa (2021) evaluate the speaker-discriminatory potential of a set of fundamental frequency ($f_o$) estimates in intraidentical twin pair comparisons and cross-pair comparisons (i.e., among all speakers). Ten male identical twin pairs aged between 19 and 35 were subjected. Acoustic measurements were done on the speech samples. Although identical twins were very closely related regarding their f0 patterns, the outcomes suggest that some pairs could still be differentiated acoustically.

The neutrosophic logic (NL) is a non-classical logic which can be used to represent a mathematical model of an uncertainty, fuzzy, vagueness, or ambiguity cases. Because of the fuzzy nature (non-crisp) in the similarity extent between the voices of the twins, so the neutrosophic theory was chosen to determine the extent of similarity (true membership), difference (false membership), or it might be the indeterminacy membership (neutrality).

The current research aims to determine whether it is possible to numerically measure the extent of similarity between the voices of identical twins using the fuzzy neutrosophic transformation (NS-T) theory. It also looks more carefully at the speech voiceprints features to determine the similarities and differences between identical twins' voices.

## II. Materials and Dataset

This study used an audiovisual twins database that is collected at the Sixth Mojiang International Twins Festival held on May 1, 2010, China (Li, 2015). This database contains 39 MZ twin pairs subjects (aged 7 up to 54 years), however, only 35 pairs (16 males and 19 females) were selected and participated as speakers in the current research. The excluded samples were children twins who did not clearly perform the vocal clips as required so they are not suitable for our study. The dataset has several face images, facial motion videos, and speech records for each subject. The ages of the participants ranged from 7 to 54 years old. The used audio voice records in this dataset uttered by the participants are one speech sample. Each one for both siblings of a twin utters 10 words as he counts from 1 to 10. The audio clip record lasts for about 8 s on average. Each uttered word is processed individually.

## III. Neutrosophic Transformation

Real-world applications provide massive information which is incomplete, imprecise, fuzzy, conflict, and inconsistent. The uncertainty may originate from acquisition errors, insufficient knowledge, or stochasticity. Biometric applications are an example of a field that deals with these kinds of information. These human biometrics types have characteristics that may or may not be completely identical to the original entity or may be indeterminate (neutrality).

Neutrosophy, a branch of philosophy that generalizes dialectics, was introduced by Smarandache in 1980. It studies neutralities' source, nature, and scope. In neutrosophy theory, every event has a substantial degree of truth (T), falsity (F), and indeterminacy (I) that have to be considered independently from each other. Therefore, A is an idea, theory, event, concept, or entity; Anti-A is the opposite of A; and the neutrality Neut-A means neither A nor anti-A, that is, the neutrality between the two extremes (Smarandache, 2001).

Neutrosophic set is a generalization of the fuzzy set theory, where each element of the universe has a degree of truth, falsity, and indeterminacy. Unlike in fuzzy sets, the neutrosophic set includes the additional domain (I), which offers a more effective method to deal with the higher degrees of ambiguity.

Let U be a universe of discourse set. A neutrosophic set A in U is described by three neutrosophic components: T, F, and I are defined to represent the truth membership degree, falsity membership degree (non-membership degree), and the indeterminacy membership degree of an element, respectively, and independently.

## IV. Methodology of Twin's Voice Discrimination

The proposed method is to measure how similar and then distinguishes the voices of the identical twins from each other using the neutrosophic theory. In the beginning, it is assumed that the twins' voices are similar to the exact spoken words. Through the proposed method, the correctness or wrongness of this assumption will be proved. The technique depends on extracting some features from the speech clips recorded for the twins. One of the most important features is the spectrogram, called "*voiceprint.*"

The speech signals are transformed to the spectral domain and then the spectrogram is interpreted and handled in NS domain. In NS domain, a filter is considered with the spectral and time domains.

The proposed method deals with the extracted spectrogram as a two-dimensional entity that maps the speech loudness to the frequencies and specific points of time. The neutrosophy theory is applied to all spectrogram elements that belong to the first sibling to determine to what extent this element belongs to the spectrogram of the second sibling for the same

utterance. In addition, slight differences between the siblings of the identical twins are noticed, when they are classified according to their gender and age in the examined voiceprints.

### *A. Preprocessing Step*

The preprocessing step includes segmentation each speech records into 10 individual uttered words for the both siblings of all participated twin pairs. These segmented words are the spoken counted numbers from 1 to 10.

### *B. Voice Analysis in Frequency Domain*

An essential part of this paper is the audio processing that involves a frequency voice analysis. The algorithms do not take the raw audio files as input; hence, extracting features from the audio files are mandatory. This helps to build the required model. An audio signal can be represented using a three-dimensional signal where these three axes represent amplitude, frequency, and time which are called spectrogram or voiceprint (vp).

MATLAB provides toolboxes for the analysis of audio. In this work, the spectrogram toolbox uses a Short-Time Fourier Transform (STFT) of the speech signal specified by a vector. The obtained spectrogram is represented in a matrix which is divided into eight segments with 50% overlap and each segment is windowed with a Hamming window. Each column of the spectrogram matrix estimates the input speech vector's short-term, time-localized frequency content. The amplitude (loudness) of an audio file can be shown in Fig. 1 that is an example of the raw speech signal uttered by both siblings of a twin.

The spectrogram is used to map different frequencies at a given point of time to their amplitudes. It is a graphical representation of the spectrum of frequencies of a voice. An example is shown in Fig. 2.

### *C. The Voice in the Neutrosophic Domain*

A voice spectrogram is defined in the neutrosophic domain as: Let U be a universe of discourse and A is a set included in U, representing the highly valued elements. The spectrogram in the neutrosophic domain ($S_{NS}$) is characterized using three distinctive membership components (T), (I), and (F), where T defines the truth scale, F as the scale of false, and I characterizes the scale of intermediate. All considered components are independent of each other. The element (S) of a spectrogram in the neutrosophic domain can be described as *S* (*T, I, F*) (Smarandache, 2001). Each element belongs to set A in the following way: It is t% true membership function in the high-valued element set (similarity indicator), the i% indeterminacy membership function in the set, and the f% a falsity-membership function in the set (dissimilarity indicator). There is a valuation for each component in [0, 1].

The logic of the neutrosophic concept is an obvious frame trying to calculate the truth, indeterminacy, and falsity. Smarandache notes the dissimilarity of fuzzy logic and NL. NL could differentiate absolute truth (AT) and relative truth (RT) by assigning $1^+$ for AT and 1 for RT and is also applied in the field of philosophy. Hence, the standard interval [0,1] used in IFS is extended to non-standard [$^-0$, $1^+$] in NL. There is no condition on truth, indeterminacy, and falsity, which are all the subsets of a non-standard unitary interval (Broumi, et al., 2019).

In the spectral domain, element *S* (*j, k*) is transformed into a neutrosophic domain by calculating $S_{NS}$ (*j,k*) = {*T* (*j,k*), *I* (*j,k*), *F* (*j,k*)} in Eqs. (1–6), where *T* (*j,k*), *I* (*j,k*), and *F* (*j,k*) are considered as a probability of that element *S* (*j, k*) belongs to a highly valued set, indeterminate-valued set, and low-valued set, respectively. This is the primary benefit of neutrosophic in colormap processing, and it can be taken at the same time when the decision is made for each element in the spectrogram. The following basic equations were used for transforming voiceprint from a spectral domain into the neutrosophic domain (Ali, 2018):

$$S_{NS}(j,k)=\{T(j,k),I(j,k),F(j,k)\} \tag{1}$$

$$T(j,k)=\frac{\bar{s}(j,k)-\bar{s}_{min}}{\bar{s}_{max}-\bar{s}_{min}} \tag{2}$$

$$\bar{s}(j,k)=\frac{1}{L^2}\sum_{m=j-\frac{L}{2}}^{j+\frac{L}{2}}\sum_{n=k-\frac{L}{2}}^{k+\frac{L}{2}}s(m,n) \tag{3}$$

$$I(j,k)=\frac{h(j,k)-h_{min}}{h_{max}-h_{min}} \tag{4}$$

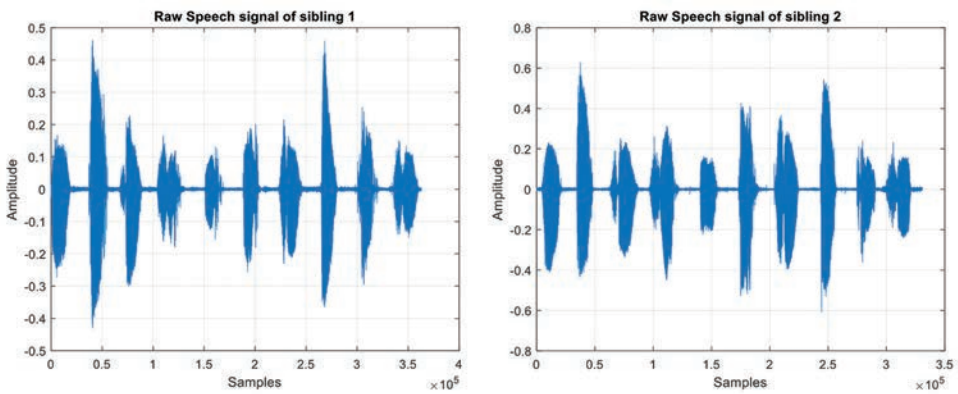


Fig. 1. Example of the raw audio signal record of an identical twin uttering the same words sample. Each column is from one sibling of the twin.

http://dx.doi.org/10.14500/aro.10925

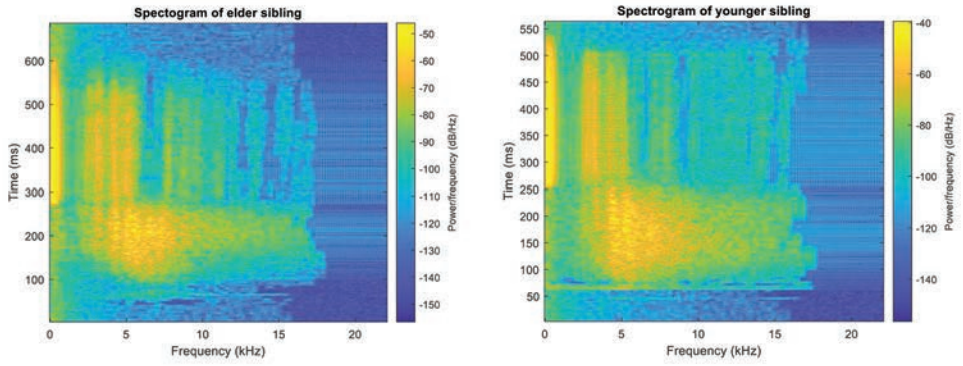


Fig. 2. The corresponding spectrograms of identical twins for a same uttered word shown in Fig. 1. Each column is from one sibling of the twin.

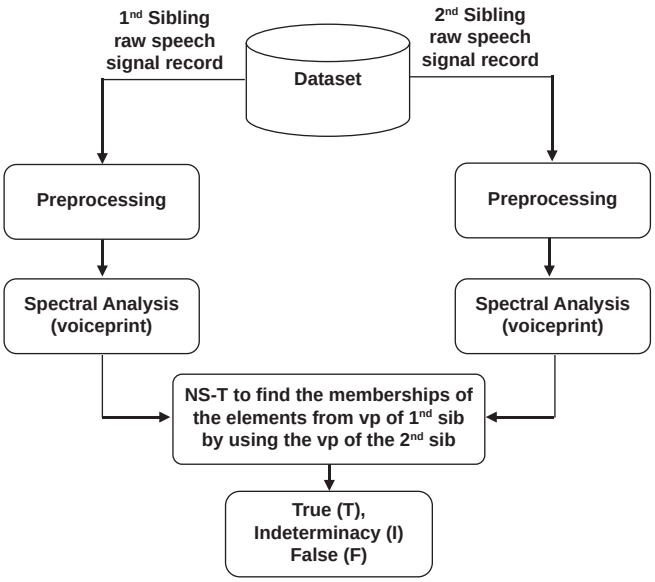


Fig. 3. General flow block diagram of the proposed method.

$$h(j,k) = \left| s(j,k) - \bar{s}(j,k) \right| \tag{5}$$

$$F(j,k)=1-T(j,k) \tag{6}$$

Where:

- $s(j,k)$ represents the amplitude value of the element in the domain
- T, I, and F are true, indeterminacy, and false sets, respectively, in the neutrosophic domain
- $\bar{s}(j,k)$ can be defined as the local average (mean) value of $s(j,k)$
- $L$ is the length of the averaging window, for the current research, $L$=5
- $h(j,k)$ is the homogeneity value of T at $(j,k)$, which is described by the absolute value of the difference between the amplitude value of the spectrogram $s(j,k)$ and its local average value $\bar{s}(j,k)$.

The output of the proposed process is the true, indeterminacy, and false membership functions (t%, i%, and f%, respectively). They are calculated for each element in the spectrogram function of the uttered word (1–10). This process is repeated for all the participated twins. Finally, the average for each membership is calculated. Fig. 3 shows a general block diagram of the proposed method.

TABLE I
TRUE, INDETERMINACY, AND FALSE MEMBERSHIP VALUES FOR ONE TWIN FOR EACH UTTERED WORD

| Uttered Word | T | I | F |
|---|---|---|---|
| One | 0.749 | 0.154 | 0.251 |
| Two | 0.642 | 0.156 | 0.358 |
| Three | 0.622 | 0.152 | 0.378 |
| Four | 0.643 | 0.142 | 0.357 |
| Five | 0.739 | 0.156 | 0.261 |
| Six | 0.739 | 0.220 | 0.261 |
| Seven | 0.696 | 0.205 | 0.304 |
| Eight | 0.789 | 0.195 | 0.211 |
| Nine | 0.702 | 0.168 | 0.298 |
| Ten | 0.699 | 0.208 | 0.301 |
| Average | 0.702 | 0.176 | 0.298 |

## V. RESULTS AND DISCUSSION

The output of this process is the calculated probability of the true membership function in the set t%, indeterminacy membership function in the set i%, and a falsity-membership function in the set f% for each uttered word, as shown in Table I. This process is repeated for all the participated twins.

Then, the average of each membership value is calculated as in the last row in Table I. The mean values of T, I, and F memberships are computed for each twin, as shown in Fig. 4. Finally, the total average is calculated, showing the mean values of each probability value of the three membership functions for all the 35 twins that participated in the process, as shown in Fig. 5.

Fig. 4 shows that the average true membership value (similarity indicator) equals 0.6815, the average indeterminacy membership value equals 0.1883, and the false membership value (dissimilarity indicator) equals 0.3184. These results indicate that the extent of similarity between the voiceprints of the two siblings of a twin is about 68.15% and the dissimilarity is about 31.84%. At the same time, the indeterminacy probability is 18.83%. These results were obtained for a text-dependent utterance. The maximum

Table II
Comparison with the Previous Literature Works

| Ref. | No. of MZ twin pairs | Technique | Conclusion |
|---|---|---|---|
| Fuchs, et al., 2000 | 31 | Identify 10 parameters of voice performance and acoustic features | They found significant differences in seven of 10 parameters |
| Cielo, et al., 2012 | 2 | Auditory, auditory-perceptual vocal, and glottic source acoustic evaluations | No differences in vocal attack, articulation, loudness, resonance, respiratory mode, and type in both pairs of monozygotic twins evaluated, and the results were within normal limits |
| Sebastian, et al., 2013 | 10 | Acoustic analysis and five native listeners were requested to judge | The measured values are more sensitive in discriminating twin voices among each other |
| Segundo, et al., 2016 | 12 | Extraction a set of features. Speaker similarity was measured using standardized Euclidean distances | Mean ED for MZ pairs lies between the average ED for SS comparisons and DS comparisons |
| Cavalcanti, Eriksson, Barbosa, 2021 | 10 | Assess the speaker-discriminatory potential of a set of fundamental frequency ($f_0$) estimates in intra identical twin pair comparisons and cross-pair comparisons | Although identical twins were very closely related regarding their $f_0$ patterns, some pairs could still be differentiated acoustically |
| Current research | 35 | Neutrosophic domain transformation of the voiceprints | The extent of similarity between the voiceprints of the two siblings of a twin is about 68.15%, and the dissimilarity is about 31.84%. At the same time, the indeterminacy probability is 18.83% |

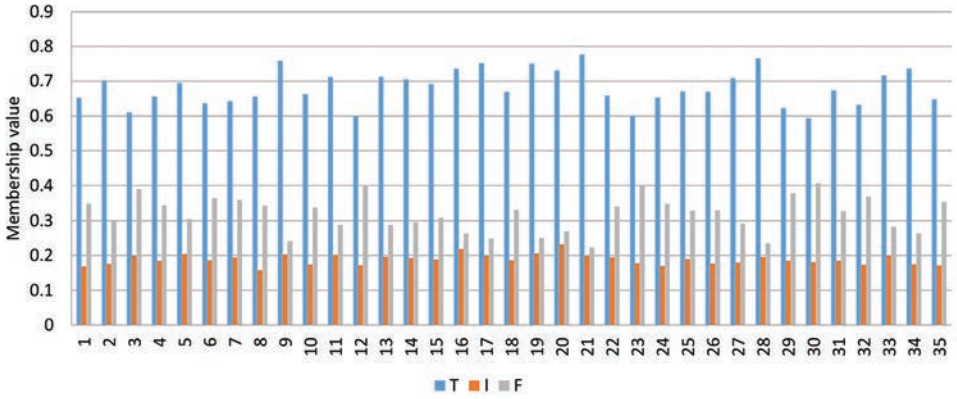


Fig. 4. True (T), indeterminacy (I), and false (F) membership values for each participating twin.

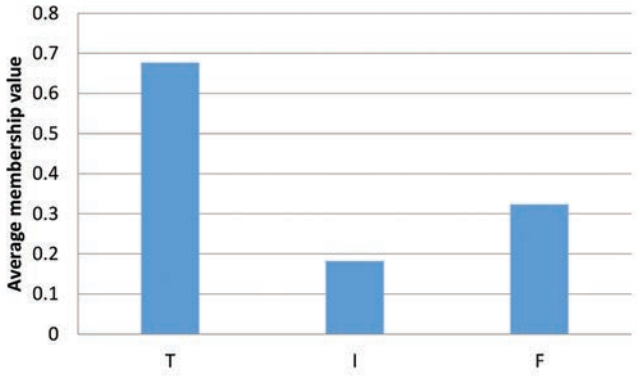


Fig. 5. The total average of true (T), indeterminacy (I), and false (F) membership values membership value for all 35 twins.

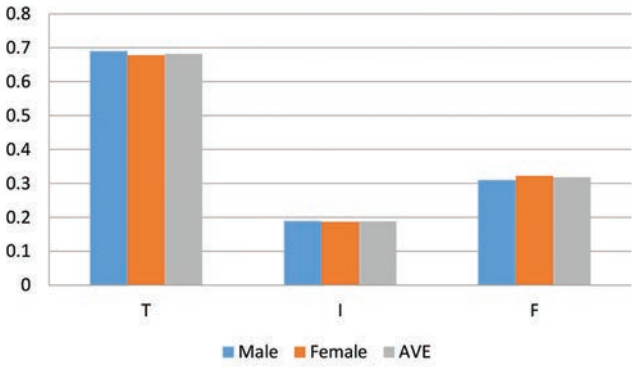


Fig. 6. True (T), indeterminacy (I), and false (F) membership values membership value for 16 males versus 19 females.

true membership value is 93.13% for the individual spoken words, whereas the minimum is 47.79%. At the average level for each twin, the maximum true membership value is 77.7%, whereas the minimum is 59.3%.

A comparison of T, I, and F membership values was made, but this time the data were classified by gender (male/female). Fig. 6 shows the average true (T), indeterminacy (I), and false (F) membership values membership value for 16 males versus 19 females. The obtained values are compared with total average of all 35 pairs results. It is noticed clearly, that is, no significant effect between the results relating the gender difference when compared with total average. However, for the male, it is slightly bigger in the true membership value.

Another comparison was carried out after classifying the participants according to their age groups (children,

http://dx.doi.org/10.14500/aro.10925

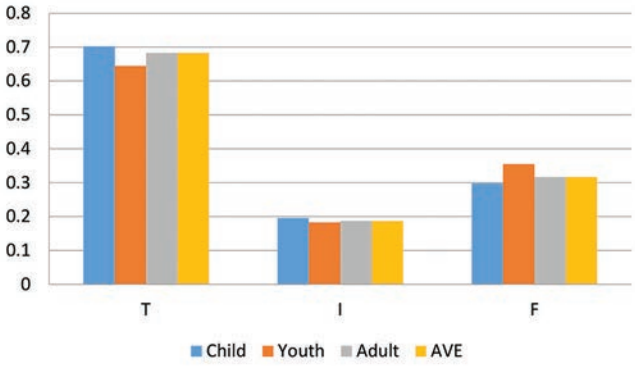


Fig. 7. True (T), indeterminacy (I), and false (F) membership values membership values according to the age categories of the participants twin pairs.

youth, and adults). The T, I, and F membership values were compared for these three age categories and with the total average as well. Fig. 7 shows the results for the true (T), indeterminacy (I), and false (F) membership values according to the age of the participants twin pairs.

There is a small impact relating to the ages of the twin pairs. The average true membership value for the children group is slightly greater than the other groups, and in the youth category, it takes the least true membership value among them. Table 2 shows a comparison between the suggested method in the current research and some of the previous literatures. The comparison is focused on the used technique and the with the main obtained conclusions.

## VI. Conclusion

The identical twins come from one fertilized egg (zygote), and therefore, their genetic personalities are expected to be very similar. The voice is one of these traits. This paper proposed a method to measure the degree of similarity or difference between the voiceprint between twin siblings. The audio clips of 35 twins were collected during the twins' festival held in 2010. During these audio clips, the participants count from 1 to 10. The neutrosophic transformation is applied to the voice spectrograms "voiceprints" of the twin brothers. The outputs of this process are three functions: t% true membership function (similarity indicator), the i% indeterminacy membership function, and the f% a falsity-membership function (dissimilarity indicator). These results indicate that the extent of similarity between the voiceprints of the two siblings of a twin is about 68.15%, and the dissimilarity is about 31.84%. At the same time, the indeterminacy probability is 18.83%. These results were obtained for a text-dependent utterance. In addition, slight differences between the siblings of the identical twins are noticed, when they are classified according to their gender and age in the examined voiceprints.

## References

Ali, M.L., Son, H., Khan, M. and Tung, N.T., 2018. Segmentation of dental X-ray images in medical imaging using neutrosophic orthogonal matrices. *Expert Systems With Applications*, 91, pp.434-441.

Ariyaeeinia, A., Morrison, C., Malegaonkar, A. and Black, S., 2008. A test of the effectiveness of speaker verification for differentiating between identical twins. *Science and Justice*, 48, pp.182-186.

Broumi, S., Nagarajan, D., Bakali, A. and Talea, M., 2019. Implementation of neutrosophic function memberships using MATLAB program. *Neutrosophic Sets and Systems*, 27(1), pp.44-52.

Cavalcanti, J.C., Eriksson, A. and Barbosa, P.A., 2021. Multiparametric analysis of speaking fundamental frequency in genetically related speakers using different speech materials: Some forensic implications, *Journal of Voice*, In Press.

Cielo, A.C., Agustini, R. and Finger, L.S., 2012. *Vocal Characteristics of Monozygotic Twins*. Revista CEFAC, pp.1234-1243.

Fuchs, M., Oeken, J., Hotopp, T., Täschner, R., Hentschel, B. and Behrendt, W., 2000. Similarity of monozygotic twins regarding vocal performance and acoustic markers and possible clinical significance. *HNO*, 48(6), p.462.

Khaleel, Y.A., 2020. High security and capacity of image steganography for hiding human speech based on spatial and cepstral domains. *ARO Journal*, 8(1), pp.95-106.

Kodate, K., Inaba, R., Watanabe, E. and Kamiya, T., 2002. Facial recognition by a compact parallel optical correlator. *Measurement Science and Technology*, 13, pp.1756-1766.

Kong, A.W.K., Zhang, D. and Lu, G., 2006. A study of identical twins' palmprints for personal verification. *Pattern Recognition*, 39, pp.2149-2156.

Künzel, H.J., 2011. Automatic speaker recognition of identical twins. *The International Journal of Speech, Language and the Law*, 17(2), pp.251-277.

Li, J., Zhang, L., Guo, D., Zhuo, S. and Sim,T., 2015. Audio-visual twins database. International Conference on Biometrics, 2015, pp.493-500.

Sataloff, R.T., Herman-Ackah, Y.D. and Hawkshaw, M.J., 2007. Clinical Anatomy and physiology of the voice. *Otolaryngologic Clinics of North America*, 40(5), pp.909-929.

Sebastian, S., Benadict, A.S., Sunny, G.K. and Balraj, A., 2013. An investigation into the voice of identical twins. *Otolaryngology Online Journal*, 3(2), pp.1-7.

Segundo, E.S., Tsanas, A. and Vilda, P.G., 2017. Euclidean Distances as measures of speaker similarity including identical twin pairs: A forensic investigation using source and filter voice characteristics. *Forensic Science International*, 270, pp.25-38.

Smarandache, F., 2001. An introduction to neutrosophy, neutrosophic logic, neutrosophic set, and neutrosophic probability and statistics. *1st International Conference on Neutrosophy, Neutrosophic Logic, Neutrosophic Set, Neutrosophic Probability and Statistics*, University of New Mexico-Gallup 1-3 December, pp.1-17.

Van Gysel, W.D., Vercammen, J. and Debruyne, F., 2001. Voice similarity in identical twins. *Acta Otorhinolaryngologica Belg*, 55(1), pp.49-55.

Whiteside, S.P. and Rixon, E., 2000. The identification of twins from pure (single speaker) syllables and hybrid (fused) syllables: An acoustic and perceptual case study. *Perceptual and Motor Skills*, 91, pp.933-947.

# Identification DNA Methylation Change of ABCC8 Gene in Type 2 Diabetes Mellitus as Predictive Biomarkers

Harem O. Smail[1,2], Dlnya A. Mohamad[2]

[1]Department of Biology, Faculty of Science and Health, Koya University, Koya KOY45, Kurdistan Region – F.R. Iraq

[2]Department of Biology, College of Science, University of Sulaimani, Sulaymanyah,Kurdistan Region – F.R. Iraq

***Abstract*—Type 2 diabetes mellitus is the most common chronic endocrine disorder that affecting 5%–10% of adults globally. Recently, the disease has rapidly spread throughout the Kurdistan Region. This study investigates DNA methylation status in the ABCC8 gene among the study population, and it possibly used as a biomarker. One hundred and thirteen individuals were included in this study, and they were divided into three categories (47 diabetes, 36 prediabetic, and 30 controls). Blood samples were collected to investigate DNA methylation status in patients who attended private clinical sectors in Koya city, Kurdistan Region of Iraq, between August and December 2021. Methylation-specific PCR (MSP) uses paired primers for each methylated and unmethylated region. In addition, the X2 Kruskal–Wallis statistical and Wilcoxon signed-rank tests were run with a significance level of p 0.05. In comparison to the healthy group, hypermethylation of DNA is detected in the promoter region of diabetes and prediabetes. In addition, age, gender, BMI, alcohol use, family history, and physical activity all influence the degree of DNA methylation in people who have had coronavirus illness. The above-mentioned findings suggest that DNA methylation alterations in the ABCC8 promoter region might be exploited as a possible predictive biomarker for type 2 diabetes mellitus diagnosis.**

***Index Terms*—ABCC8 gene, Diabetes mellitus, DNA methylation, Methylated primer, Unmethylated primer.**

## I. Introduction

Diabetes mellitus (DM) is a leading cause of death and disability worldwide, affecting 415 million people in 2017, and this is expected to increase to 592 million by 2035 (Willmer, et al., 2018). The disease is the most common chronic endocrine disorder, affecting 5%–10% of adults worldwide. Type 2 diabetes mellitus (T2DM) is associated with resistance to insulin action and inadequate compensatory insulin secretory response (ADA 2019). Type 2 diabetes affects both the old and the youth (Asiimwe, Mauti and Kiconco, 2020).

The study of epigenetic mechanisms can provide novel insights into the pathophysiology of diabetes and its complications, which may result in the identification of new drug targets. In addition, the investigation of associations with DNA methylation (DNAm)in peripheral blood may identify novel biomarkers for noninvasive early disease detection since P.B. (Florath, et al., 2016). Multiple genes and their interactions are involved in the insulin secretion pathway. For example, sulfonylurea receptor encoded by ABCC8(ATP Binding Cassette Subfamily C Member 8) gene, together with inward-rectifier potassium ion channel (Kir6.2), regulates insulin secretion by ATP-sensitive K+ (KATP) channel located in the plasma membranes (Haghverdizadeh, et al., 2014). In T2D, the ABCC8 gene is an essential target for candidate gene association studies. Single nucleotide polymorphism (SNP) in these genes has been associated with metabolic syndrome features across various populations (Matharoo, Arora and Bhanwer, 2013).

## II. Material and Methods

### *A. Study Design and Sample Collection*

A cross-sectional study consisting of 113 blood samples was collected from both men and women who visited clinical sectors in the Koya city Kurdistan area of Iraq between August and December 2021 after taking approval and instructions institutional of the scientific Committee. The study population was divided into 47 diabetes, 36 prediabetes, and 30 apparently healthy individuals according to medical history and clinical and laboratory examination. All blood samples were placed in a test tube containing anticoagulant ethylene diamine tetraacetic acid (EDTA) to prevent clotting of the blood (Smail, 2016), which were diagnosed by the HbA1c analyzer, (HbA1c) parameter to determine the prediabetes and diabetic groups. For people without diabetes, the normal range for the hemoglobin A1C level is between 4% and 5.6%. Hemoglobin A1C levels between 5.7% and 6.4% mean you have a higher chance of getting

ARO-The Scientific Journal of Koya University
Vol. X, No. 1 (2022), Article ID: ARO.10947, 5 pages
DOI: 10.14500/aro.10947
Received: 28 February 2022; Accepted: 24 April 2022
Regular research paper: Published: 30 May 2022
Corresponding author's e-mail: Harem.othman@koyauniversity.org

http://dx.doi.org/10.14500/aro.10947

diabetes. Levels of 6.5% or higher mean you have diabetes. Besides the blood collection, also asked the participants about age, gender, body max index, smoking, family history, and alcohol with measured random blood sugar (RBS).

### *B. DNA Extraction*

The ReliaPrep™ Blood gDNA Miniprep System performed DNA extraction (Cat. No. A5081, Promega Compa Promega, USA) according to the manufacturer's instructions, briefly included four essential steps, homogenizing the whole blood to release. The DNA, Binding DNA to the ReliaPrep™ Binding Column, Removing impurities with wash solution repeated three times, and Eluting purified DNA

### *C. Bisulfite DNA Conversion*

MethylEdge™ Bisulfite Conversion System (Promega Compa Promega, USA) was perfumed according to manufactures instructions (N1301). The bisulfite-converted reaction was based on the unmethylated cytosine converted to uracil whereas methylated cytosine was unaffected.

### *D. Determination DNA Quality and Quantitates*

Typical nucleic acid concentration ranges for direct A280 absorbance measurements using nanodrops were used to determine quantities of bisulfite-converted DNA. The sample type was set to RNA-40 because bisulfite-converted DNA contains uracil and is widely single-stranded. DNA samples (100 ng of each sample) were run on the 1% agarose gel and stained with Diamond Nucleic™ Acid Dye. To evaluate the level of fragmentation following conversion, but nanodrop was set to DNA-50 to estimate DNA concentration before bisulfite conversion and stained with ethidium bromide

### *E. Methylation Specific PCR Primer*

MethPrimer is a tool for creating methylation PCR primers based on bisulfite conversion. It is currently possible to develop methylation-specific PCR, as it is shown in Table I.

PCR products were analyzed on 2% agarose gel electrophoresis, stained with ethidium bromide, and visualized under U.V. illumination, as shown in Tables II and III. The methylation band was present at 135 base pairs and the unmethylation band at 136 base pairs. Control reactions were prepared using pre-qualified methylated DNA from a source similar to the source of the experimental samples. Converted Methylated Human Control has been bisulfite-converted. High percent methylation of CpG sites run opposite with samples (N1231 Promega Compa Promega, USA), as demonstrated in Table IV.

### *F. Statistical Analysis*

Methylation-specific PCR results were determined by deviation from the Normal pattern. Next, the difference in methylation percentage expression between all groups and normal ones was analyzed. According to Shapiro–Wilk and Kolmogorov–Smirnov's nonparametric test, the study data were nonparametric (Non-Normal Distribution) using the Kruskal–Wallis and Wilcoxon signed-rank test. For categorical variables, frequencies were chosen. Descriptive statistics (mean and standard deviation) are used for continuous variables. The receiver operating characteristic curve (ROC curve) estimated the biomarker test. $P<0.05$ was considered statistically significant. In addition, GraphPad Prism 8 was used for statistical data analysis.

## III. Results

Several variables were studied; body max index random blood sugar and hemoglobin A1c showed highly significant differences ($P = 0.000$), significant differences were noticed within age, gender, and alcohol, while non-significant with others as shown in Table V.

Table I
Primer Sequence for Methylation-Specific Pcr

| No | Primer | Length | Product size | Sequence (5'->3' |
|---|---|---|---|---|
| 1 | Forward methylated primer | 24 | 135 | TTTGTGTGAAAGTGTTAGATACGT |
| 2 | Reverse methylated primer | 25 | 135 | AATAAAAAAAATAAAACAAAACGTT |
| 3 | Forward un unmethylated primer | 25 | 136 | TTTTGTGTGAAAGTGTTAGATATGT |
| 4 | Reverse unmethylated primer | 25 | 136 | AATAAAAAAAATAAAACAAAACATT |

Table II
Prepare the Pcr Master Mix with the Primer Sets Specific to the Methylated Primer for Bisulfited Converted DNA

| Component | Volume (µl) | Final concentration |
|---|---|---|
| 2X PCR master mix | 12.5 | 1X |
| M forward primer | 1 | 10 picomole |
| M reverse primer | 1 | 10 picomole |
| DNA template | 3 | 10-50 ng |
| DNA nuclease-free water | 7.5 | The final volume of 25 µl |

Table III
Prepare the Pcr Master Mix with the Primer Sets Specific to the Unmethylated Primer for Bisulfited Converted DNA

| Component | Volume (µl) | Final concentration |
|---|---|---|
| 2X PCR Master Mix | 12.5 | 1X |
| U forward primer | 1 | 10 picomole |
| U reverse primer | 1 | 10 picomole |
| DNA template | 3 | 10–50 ng |
| DNA nuclease-free water | 7.5 | The final volume of 25 µl |

Table IV
Cycling Conditions for Methylation-Specific Pcr of Bisulfite-Converted DNA

| Steps | Temperature | Time | Number of cycle |
|---|---|---|---|
| Enzyme inactivation | 95°C | 5 min | 1 |
| Denaturation | 95°C | 30 s | 35 |
| Annealing | 52°C | 30 s | 35 |
| Extension | 72°C | 30 s | 35 |
| Holder time | 72°C | 5 min | 1 |

Regarding the methylation status, methylated was more frequent in diabetes and prediabetes than in the control group with 23, 23, and 10 cases, respectively, while 10, 7, and 17 cases in unmethylated. On the other hand, the methylated and methylated as 14 and 6 then 3 cases in control with highly significant differences ($P$ = 0.000) as shown in Table VI.

In the same group association between DNA methylation status and some clinicopathologic characteristics showed that there was highly significant between DNA methylation and HbA1c and as well as blood sugar with highly significant differences ($P$=0.000), whereas less significant was observed among other parametric such as smoking, age, and alcohol as shown in Table VII.

## IV. Discussion

The present study has investigated diabetes-related ABCC8 methylation qualitatively using methylation-specific PCR on blood. Interestingly, ABCC8 methylation was detected at a high frequency, which was 23 (48.9%)out of 47 samples of diabetes, 23(63.9%) prediabetes out of 36 samples, and 10 (33.3%) of control out of 30 samples limited studies have done regards identifying ABCC8 gene methylation in Kurdistan region of Iraq. DNAm marks mainly occur at the 5′ position of the cytosine residues of cytidine-guanine dinucleotides (CpG). Clustered CpG dinucleotides forming dense repeat sequences in the genome are termed CpG islands. Islands are located especially in promoter regions. However, they can also be found in intragenic and enhancer regions (Jones 2012). Many studies have revealed that DNAm also occurs at sites other than the CpG sequences (non-CpG methylation). Non-CpG methylation has been suggested to be prevalent in human embryonic stem cells and the brain. (Jang, et al., 2017). Methylation of cytosine residues in DNA (DNA methylation) are the most studied epigenetic trait. Recent data show significant influences of age and lifestyle-related risk factors such as overweight and physical activity on site-specific DNAm in blood and tissues relevant to T2D (Dayeh, et al., 2014; Smail, 2019).

Table V
General Characteristics of the Studied Population

| Variable | Diabetes (47) | Prediabetes (36) | Control (30) | *P* value |
|---|---|---|---|---|
| Age | 49.4±12.5 | 46.4±11.4 | 41±10.6 | 0.012 |
| Gender | | | | |
| Male | (18) 38.3% | 16 (44.4%) | 21 (70%) | 0.022 |
| Female | (29) 61.7 | 20 (50.6%) | 9 (30%) | |
| BMI (body max index ) | 30.5±2.8 | 26±4.1 | 23.8±4.3 | 0.000 |
| Smoking | 5 (10.6) | 5 (13.9%) | 5 (16.7) | 0.74 |
| Family history | 7 (14.9%) | 2 (5.6%) | 5 (16.7%) | 0.316 |
| Covid 19 | 7 (14.9%) | 9 (25%) | 3 (10%) | 0.244 |
| alcohol | 1 (2.1%) | 0 (0%) | 4 (13.3%) | 0.020 |
| Physical Activity | 13 (27.7%) | 13 (36.1%) | 15 (50%) | 0.141 |
| RBC (random blood sugar) mg/dL | 248.7±84.6 | 145.8±26.8 | 113.1±23.7 | 0.000 |
| HBA1C (hemoglobin A1c)% | 9.5±2 | 6.1±0.3 | 4.7±0.4 | 0.000 |

Sig=($P$≤0.05), NS: ($P$≥0.05) using Kruskal–Wallis test.

Table VI
Correlation Methylation Status with the Control Groups

| Groups | Methylated state | | | Total (%) | *P* value |
|---|---|---|---|---|---|
| | Unmethylated (100%) | Methylated (100%) | Methylated and methylated (partially methylated) (%) | | |
| Diabetes | 10 (21.3) | 23 (48.9) | 14 (29.8) | 47 (100) | 0.002 |
| Prediabests | 7 (19.4) | 23 (63.9) | 6 (16.7) | 36 (100) | |
| Control | 17 (56.7) | 10 (33.3) | 3 (10) | 30 (100) | |

Sig= ($P$≤0.05) using Kruskal–Wallis test.

Methylation-specific PCR can rapidly determine virtually any cytosine methylation status from CpG sites within a CpG island. MSP requires very small amounts of DNA, is susceptible to 0.1% of a given CpG island locus methylated alleles and can be carried out in paraffin-embedded DNA extracted samples (Herman, et al., 1996). Nested MSP can be conducted if an experiment could not amplify the product abundantly for analysis by direct MSP. A different primer set is required for Nested MSP, which covers the amplified product sequence with two selected pairs of primers. A second PCR with two pairs of primers (each primer set for different methylation states) is carried out after the first PCR with nested MSP primers using the amplified products from the first PCR (Hanaei, et al., 2020). In the current study, there were significant differences between DNA methylation changes in diabetes and prediabetes with control, as shown in Table VI; there was a strong relationship between DNA methylation in all three groups; the p-value was 0.002. Our data demonstrated that higher DNA methylation was detected in females in diabetes and prediabetes groups.

In contrast, minimum DNA methylation was recorded in the male of the healthy group (Table VII). Identifying CpG loci of which DNAm levels are under genetic control or are related to age or gender will facilitate further studies into the role of DNAm and disease (Boks, et al., 2009). Associations between age acceleration and body mass index, total cholesterol to high-density lipoprotein cholesterol ratios, socioeconomic status, high blood pressure, and smoking behavior (McCartney, et al., 2018). With the advent of microarray technology, it became possible to assess many specific genomic sites for age-related changes in DNAm. Microarray studies confirmed a decrease in DNAmwith age, whereas site-specific analysis indicated an increase in variability of DNA methylation with age (Jones, et al., 2015). Furthermore, demonstrate that genotype state at methylation quantitative trait loci (meQTLs) can affect some age-associated CpG sites (Gopalan, et al., 2017).

The statistical analysis showed an association between MSP results with BMI, HbA1c, and random blood sugar, and the p-value was 0.000, as analyzed in Table VII. Moreover, recent studies have shown that changes in body weight and increased physical activity seem to impact the DNAm of certain genes related to T2D (de Mello, et al., 2014). Thus, the search for new biomarkers is ongoing. There is great interest in epigenetic biomarkers such as DNAm, which can influence the environment and potentially improve T2D prediction (Dayeh, et al., 2016). Data demonstrate highly significant correlations between DNAm and the most important risk

http://dx.doi.org/10.14500/aro.10947

Table VII
Association of Promoter Region Methylation Clinic Pathologic Characteristics Within Same Groups

| | Diabetes | | | | Prediabetes | | | | Control | | | |
|---|---|---|---|---|---|---|---|---|---|---|---|---|
| | U | M | UM | *P* value | U | M | Um | *P* value | U | M | UM | *P* value |
| Age | 54.1±10.8 | 44.4±8.7 | 54.1±15.9 | 0.000 | 52.2±11.8 | 45.3±11.9 | 43.8±7.9 | 0.000 | 40.9±7.2 | 36.5±7.4 | 56.6±22.1 | 0.000 |
| Gender | | | | | | | | | | | | |
| Male | 1 | 9 | 8 | 0.003 | 2 | 11 | 3 | 0.007 | 13 | 0 | 0 | 0.106 |
| Female | 9 | 14 | 6 | | 5 | 12 | 3 | | 4 | 10 | 3 | |
| BMI (body max index ) | 18±4.2 | 30.7±1.8 | 32.2±1.8 | 0.000 | 25.4±2.2 | 26.7±4.5 | 24.3±4.2 | 0.000 | 25.0±15.8 | 21.7±3.3 | 24.2±7.5 | 0.000 |
| Smoking | 0 | 3 | 2 | 0.106 | 1 | 3 | 1 | 0.346 | 2 | 2 | 1 | 0.061 |
| Family history | 1 | 4 | 2 | 0.055 | 0 | 2 | 0 | 0.796 | 3 | 2 | 0 | 0.039 |
| Covid 19 | 1 | 3 | 3 | 0.061 | 1 | 6 | 2 | 0.101 | 2 | 1 | 0 | 0.012 |
| Alcohol | 0 | 1 | 0 | 0.317 | 0 | 0 | 0 | 0.782 | 3 | 1 | 0 | 0.018 |
| Physical activity | 1 | 10 | 2 | 0.006 | 3 | 8 | 2 | 0.014 | 12 | 1 | 2 | 0.755 |
| RBC (random blood sugar) mg/dL | 233.9±91.5 | 243.3±91.8 | 268.2±67.9 | 0.000 | 148.8±5.7 | 144.8±31 | 146±274 | 0.000 | 114.6±22.6 | 102.7±21.4 | 139±13.0 | 0.000 |
| HbA1c (hemoglobin A1c)% | 9.1±2.5 | 8.9±1.2 | 10.6±5.7 | 0.000 | 6.3±0.1 | 6.0±0.0 | 6.0±0.2 | 0.000 | 4.9±0.3 | 4.7±0.2 | 4.8±0.2 | 0.000 |

M: Methylated, U: Unmethylated, UM: Unmethylated and methylated (partial), significant difference Wilcoxon signed-rank test

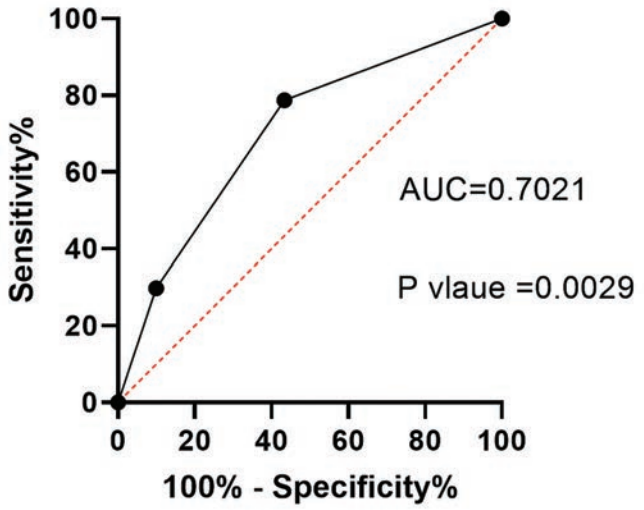


Fig. 1: ROC curve of MSP results in diabetes.

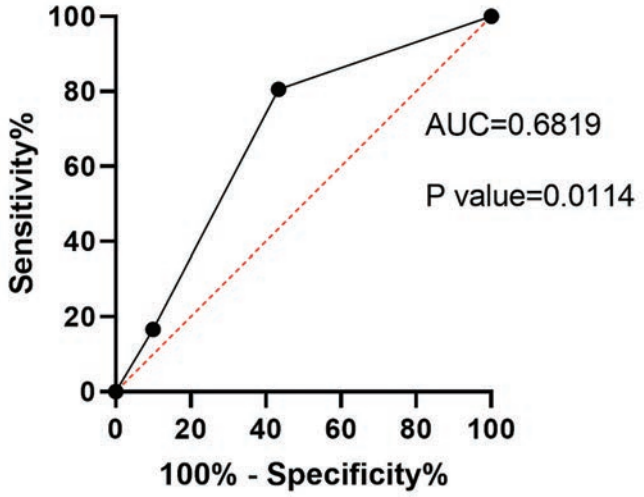


Fig. 2: ROC curve of MSP results in prediabetes.

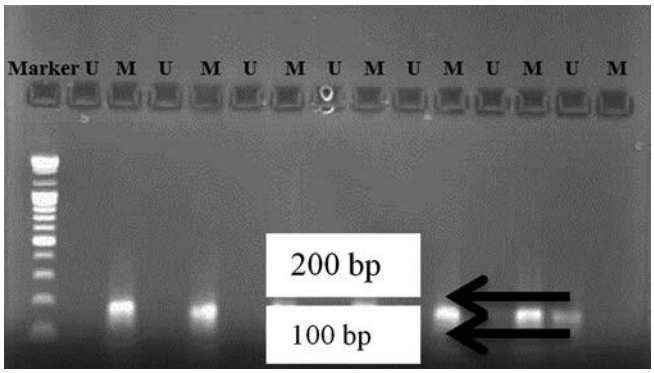


Fig. 3: Methylation-specific PCR (MSP) analysis of ABCC8 gene. *Lane 1: DNA Marker ((3kb. DNA ladder). Agarose gel electrophoresis (2%) of MSP Products are both an excellent demonstration. M refers to a methylated specific primer; U refers to an unmethylated-specific primer. The expected product size was 136 bp for unmethylated primer and 135 bp for methylated primer.

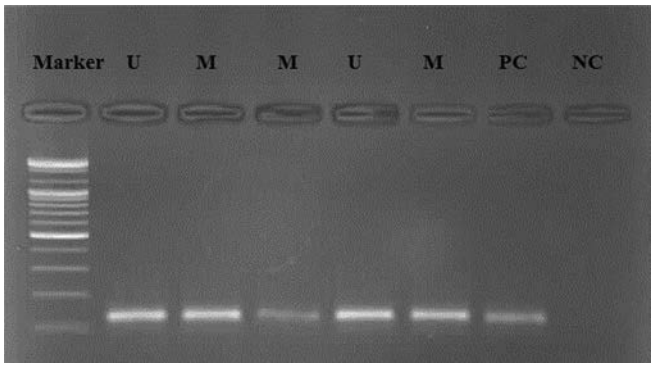


Fig. 4: Methylation-specific PCR (MSP) analysis of ABCC8 gene. *Lane 1: DNA Marker ((3kb. DNA ladder). Agarose gel electrophoresis (2%) of MSP Products is both an excellent demonstration. M refers as a methylated specific primer; U refers to unmethylated-specific primer. P.C.: Positive control(Methylated Human Control) and NC: negative control (Distil water) The expected product size was 136 bp for unmethylated primer and 135 bp for methylated primer.

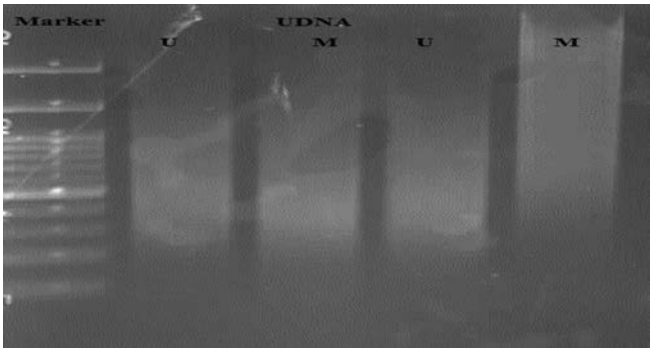


Fig. 5: Methylation-specific PCR (MSP) analysis of ABCC8 gene. *Lanes 1 and 6: DNA marker ((3kb. DNA ladder). Agarose gel electrophoresis (2%) MSP products are an excellent demonstration. M refers to methylated-specific primer; U refers to unmethylated-specific primer. Using unconverted DNA (UDNA) instead of converted DNA demonstrated that the primer was only specific for the converted DNA; the agarose gel showed not any PCR product either for methylated or unmethylated ABCC8 gene.

factors of T2D, including age and body mass index, in blood and human tissues relevant to insulin resistance and T2D. Furthermore, T2D patients and individuals with increased risk of the disease display differential DNAm profiles and plasticity compared to controls (Gillberg and Ling, 2015). ABCC8 ROC curve showed that both are under the curve and the p-value was significant for both diabetes and prediabetes groups, as illustrated in Figs. 1 and 2. The methylation-specific PCR primer, demonstrated in Figs. 3-5, shows that the size of the product is 136 bp for unmethylated primer and 135 bp for a methylated primer in addition to the methylated control. However, the MSP primers have not been amplified unconverted DNA, and negative control (distill water).

## V. Conclusion

Increased DNA methylation in type 2 diabetes patients may have correlated with pathogenesis and developed symptoms of diabetes, and the results of this study demonstrated that the hypermethylation of the ABCC8 gene is associated with BMI, HbA1c, and Random blood sugar. Industrially may be used commercial kits to diagnose diabetes in its early stages.

## VI. Acknowledgments

We thank the Science and Health Research Center staff, especially their laboratory technicians, Mr. Hiwa Abdurahman and Mr. Shwan Salih, for their help and support in doing this research.

## References

American Diabetes Association, 2019. Classification and diagnosis of diabetes: standards of medical care in diabetes 2019. *Diabetes Care*, 42, pp.S13-S28.

Asiimwe, D., Mauti, G.O. and Kiconco, R., 2020. Prevalence and risk factors associated with Type 2 diabetes in elderly patients aged 45-80 years at Kanungu District. *Journal of Diabetes Research*, 2020, p.5152146.

Boks, M.P., Derks, E.M., Weisenberger, D.J., Strengman, E., Janson, E., Sommer, I.E., Kahn, R.S. and Ophoff, R.A., 2009. The relationship of DNA methylation with age, gender and genotype in twins and healthy controls. *PLoS One,* 4, p.e6767.

Dayeh, T., Tuomi, T., Almgren, P., Perfilyev, A., Jansson, P.A., de Mello, V.D., Pihlajamäki, J., Vaag, A., Groop, L., Nilsson, E. and Ling, C., 2016. DNA methylation of loci within ABCG1 and PHOSPHO1 in blood DNA is associated with future Type 2 diabetes risk. *Epigenetics*, 11, pp.482-488.

Dayeh, T., Volkov, P., Salö, S., Hall, E., Nilsson, E., Olsson, A.H., Kirkpatrick, C.L., Wollheim, C.B., Eliasson, L., Rönn, T. and Bacos, K., 2014. Genome-wide DNA methylation analysis of human pancreatic islets from Type 2 diabetic and non-diabetic donors identifies candidate genes that influence insulin secretion. *PLoS Genetics*, 10(3), p.e1004160.

de Mello, V.D.F., Pulkkinen, L., Lalli, M., Kolehmainen, M., Pihlajamäki, J. and Uusitupa, M., 2014. DNA methylation in obesity and Type 2 diabetes. *Annals of Medicine*, 46(3), pp.103-113.

Florath, I., Butterbach, K., Heiss, J., Bewerunge-Hudler, M., Zhang, Y., Schoettker, B. and Brenner, H., 2016. Type 2 diabetes and leucocyte DNA methylation: an epigenome-wide association study in over 1,500 older adults. *Diabetologia*, 59(1), pp.130-138.

Gillberg, L. and Ling, C., 2015. The potential use of DNA methylation biomarkers to identify risk and progression of Type 2 diabetes. *Frontiers in Endocrinology*, 6, p.43.

Gopalan, S., Carja, O., Fagny, M., Patin, E., Myrick, J.W., McEwen, L.M., Mah, S.M., Kobor, M.S., Froment, A., Feldman, M.W. and Quintana-Murci, L., 2017. Trends in DNA methylation with age replicate across diverse human populations. *Genetics*, 206, pp.1659-1674.

Haghverdizadeh, P., Haerian, M.S., Haghverdizadeh, P. and Haerian, B.S., 2014. ABCC8 genetic variants and risk of diabetes mellitus. *Gene*, 545, pp.198-204.

Hanaei, S., Sanati, G., Zoghi, S., Gharibzadeh, S., Ziaee, V. and Rezaei, N., 2020. The status of FOXP3 gene methylation in pediatric systemic lupus erythematosus. *Allergologia et Immunopathologia*, 48, pp.332-338.

Herman, J.G., Graff, J.R., Myöhänen, S.B.D.N., Nelkin, B.D. and Baylin, S.B., 1996. Methylation-specific PCR: A novel PCR assay for methylation status of CpG islands. *Proceedings of the National Academy of Sciences*, 93, pp.9821-9826.

Jang, H.S., Shin, W.J., Lee, J.E. and Do, J.T., 2017. CpG and non-CpG methylation in epigenetic gene regulation and brain function. *Genes*, 8(6), p.148.

Jones, M.J., Goodman, S.J. and Kobor, M.S., 2015. DNA methylation and healthy human aging. *Aging Cell*, 14(6), pp.924-932.

Jones, P.A., 2012. Functions of DNA methylation: islands, start sites, gene bodies and beyond. *Nature Reviews Genetics*, 13(7), pp.484-492.

Matharoo, K., Arora, P. and Bhanwer, A.J.S., 2013. Association of adiponectin (AdipoQ) and sulphonylurea receptor (ABCC8) gene polymorphisms with Type 2 Diabetes in North Indian population of Punjab. *Gene*, 527(1), pp.228-234.

McCartney, D.L., Stevenson, A.J., Walker, R.M., Gibson, J., Morris, S.W., Campbell, A., Murray, A.D., Whalley, H.C., Porteous, D.J., McIntosh, A.M. and Evans, K.L., 2018. Investigating the relationship between DNA methylation age acceleration and risk factors for Alzheimer's disease. *Alzheimers and Dementia: Diagnosis, Assessment and Disease Monitoring*, 10, pp.429-437.

Smail, H.O., 2016. *Qualitative and Quantitative Identification of DNA Methylation Changes in Blood of the Breast Cancer Patients*. (MSC Thesis, University of Sulaimani).

Smail, H.O., 2019. The epigenetics of diabetes, obesity, overweight and cardiovascular disease. *AIMS Genetics*, 6, pp.36-45.

Willmer, T., Johnson, R., Louw, J. and Pheiffer, C., 2018. Blood-based DNA methylation biomarkers for Type 2 diabetes: Potential for clinical applications. *Frontiers in Endocrinology*, 9, p.744.

 http://dx.doi.org/10.14500/aro.10926

# An Optimized SWCSP Technique for Feature Extraction in EEG-based BCI System

Navtej S. Ghumman[1] and Balkrishan Jindal[2]

[1]Department of Computer Science and Engineering, Punjabi University
Patiala, Punjab, India

[2]Department of Computer Engineering, YCoE, Punjabi University Guru Kashi Campus
Talwandi Sabo, Punjab, India

***Abstract*–Multichannel electroencephalography (EEG) is an often used non-invasive method of providing input signals to motor imagery (MI)-based brain-computer interface (BCI) systems. At present, its use is severely limited due to lack of the required level of classification accuracy. Machine learning is used in BCIs to identify hidden patterns in EEG data and then classify them into appropriate MI tasks. In this study, an approach called optimized spectrally weighted common spatial pattern is proposed to improve feature extraction in an EEG-based BCI system. It enhances information gain by optimizing weights of spectral and spatial coefficients, to extract discriminating features from event-related desynchronization (ERD) brain activity. The proposed approach is evaluated by executing it on benchmark dataset 2a of BCI Competition IV. The independent component analysis method is used for the removal of noise whereas the linear discriminant analysis method is used for classification. The experimental results using the proposed approach yield higher classification accuracy as compared to other approaches reported in the literature.**

***Index Terms*—Brain-computer interface; Common spatial pattern; Electroencephalogram; Feature extraction, Motor imagery.**

## I. Introduction

Brain-computer interface (BCI) is a technique for establishing a direct communication interface between the brain of a user and an external device, without using normal nerve pathways (Dai, et al., 2019). It is an advanced technology that can be used for the rehabilitation of patients suffering from nervous system disorders, by directly translating their intention into corresponding commands (Mason and Birch, 2003). The human brain controls and coordinates different body parts by the transmission of neural signals. Electroencephalography (EEG) can be used for recording functional brain activity as it is non-invasive, safe, and easy to use, as compared to invasive techniques in which sensors are implanted directly into the brain during neurosurgery (Bernardi, Pimenta, and Moreno, 2019). These signals reflect a particular motor imagery (MI) activity of hands, foot, or tongue movements (Lotte, et al., 2018). The past decades have seen the advent of powerful computer hardware and software, which have encouraged researchers to provide more efficient, robust, and efficient BCIs for rehabilitation (Wolpow, et al., 2002). Although the field of BCI research has seen many advances, the desired level of accuracy in the estimation of MI tasks is not yet achieved. The EEG signals are adversely affected by noise from external environmental and physiological resources. These signals are then preprocessed to improve their signal-to-noise ratio. It is then followed by spatial and/or spectral domain-based feature extraction techniques to extract discriminating features from the denoised signals. Finally, a classification algorithm is used for estimating the class of the brain activity pattern. Various state-of-the-art algorithms can be used for the implementation of the various BCI stages. The improvement in classification accuracy achieved can enhance the reliability of BCI systems, which are then safe to use for health-related purposes. The users of an MI-based BCI system produce various brain activity patterns corresponding to MI tasks, by following experimental protocols as per visual clues flashed on the screen. The subject is signaled to envisage moving a particular limb but withholding its physical movement. Spontaneously, EEG signals are fetched whereas the subject executes specific MI tasks of the left hand, right hand, both feet, tongue movement, etc. (Gaur, et al., 2018). It generates a reduction in mu and beta rhythms, called event-related desynchronization (ERD). These rhythms called event-related synchronization (ERS) subsequently increase after the completion of such a task. The pattern in changes of ERD and ERS can be used for input to a BCI system. The ongoing research in BCI primarily emphasizes improving classification accuracy to attain sufficient robustness in MI-based BCI systems. Its overall performance is dependent on efficiency attained at its different sequential stages of acquiring signals, their preprocessing, extraction of features, and classification, as shown in Fig. 1. The EEG signals are acquired from different positions of the scalp of a

ARO-The Scientific Journal of Koya University
Vol. X, No.1 (2022), Article ID: ARO.10926, 7 pages
DOI: 10.14500/aro.10926
Received: 11 January 2022; Accepted: 12 May 2022
Regular research paper: Published: 30 May 2022
Corresponding author's email: navtejghumman@sbsstc.ac.in

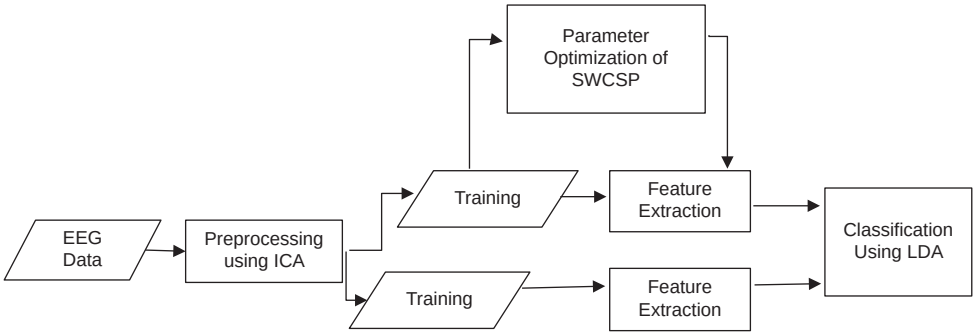


Fig. 1. A block diagram representing the proposed optimized spectrally weighted common spatial patterns.

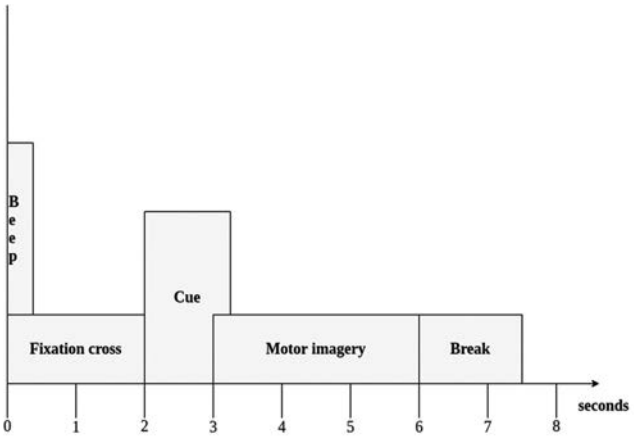


Fig. 2. Timing of dataset 2a from BCI Competition IV (Liu, et al., 2017).

human subject, by placing electrodes, as shown in Fig. 2. The acquired signals are prone to huge quantities of noise, which is eliminated in the next stage of preprocessing before these are fed to the feature extraction stage. Overall performance of a BCI system can be enhanced by the selection and execution of a combination of algorithms to implement preprocessing, feature extraction, and classification stages.

CSP and its variants are widely used feature extraction technique using spatial filtering to enhance the discriminability of two classes (Zhang, et al., 2015, 2018; Kirar and Agrawal, 2016, pp. 14–21). Their performance is limited as they manually establish frequency bands for successfully discriminating between two classes of tasks, as explained in Section 2C.

In this work, the performance of the feature extraction stage of BCI implementation is enhanced, by identifying and optimizing parameters of SWCSP, which is a popularly used variant of CSP. It focuses on the performance of the feature extraction component of the EEG-based BCI system, as it has a direct bearing on the overall performance of a BCI system. Spatial and spectral parameters are optimized and the prior filter band of SWCSP is varied to improve feature extraction. The performance of the proposed approach is measured by executing it on a benchmark dataset and compared with reported literature.

### *A. Related Work*

In recent years, many EEG signal feature extraction and feature classification techniques are proposed by the researchers. In this part, recent studies on feature extraction from EEG signal are briefly discussed.

Alam, Ibrahimy, and Motakabber, 2021, have employed the power spectral density to extract features on the basis of frequency transformation to enhance the classification accuracy. However, they have used dataset 2b of BCI Competition IV, which is only a two-class MI of the left and right movement. In our study, four-class MI of the left and right hand besides foot and tongue movement is considered, for more effective BCI.

The authors in Rashid, et al., 2020, have reviewed many popular BCI applications and analyzed methods used for feature extraction, classification, and evaluated their performance. They have opined that most of the current BCI applications are at a nascent stage, adoption of common BCI framework by the research community, and commercialization of BCI technology, which can enhance its acceptance and popularity in near future. They have also reported that CSP and its variants such as common spatial-spectral patterns and regularized CSP are popularly used feature extraction methods.

Other BCI researchers have experimented with and proposed several alternative methods to implement BCIs, which widely vary from simple binary capabilities (Wolpaw, McFarland, and Vaughan, 2000), to state-of-art applications such as Talk Assist (Kennedy, et al., 2000). This has enabled patients suffering from a neurological disorder to compose words by contributing a limited input, for useful communication with the outside world by controlling external devices. They have recommended improvements in learning during training phase of the BCI model and identification of reliable techniques for meaningful implementation of the BCI model.

A wide number of studies in the past have focused on improving methodologies to implement various stages of BCI implementations. The data acquired in EEG-based BCIs are bulky and contain a lot of artifacts. Various preprocessing methods can be used to identify and remove noise. Multichannel EEG signals are non-stationary and non-linear; hence, information of interest has to be identified efficiently (She, et al., 2017). They have proposed a novel method of identifying intrinsic mode functions that contain information of interest. This has increased classification accuracy, but only for some of the subjects, leaving scope for further improvement in the future work.

Feature extraction methods can be used for reducing the number of features in a dataset, which summarizes most of

http://dx.doi.org/10.14500/aro.10926

the information contained in the original set of features, by selecting task-specific features from EEG signals in spectral and spatial domains (Tan, et al., 2017). It identifies important features of the data using spectral methods such as Fourier transform, wavelet transform (Lemm, et al., 2005), and spatial methods like common spatial pattern (Selim, et al., 2018) (Yang and Wu, 2014). The authors in Tan, et al., 2017, have proposed EEG classification by fusing multiple features in an orchestrated way to enhance accuracy. This approach has additional computational overheads as multiple Siuly and Li, 2012, have proposed a cross-correlation-based feature extraction method for two-class MI signal recognition. They have reported an improvement in classification accuracy by 7.40%, by evaluating it on benchmark datasets of BCI Competition III. However, a two-class classification is not enough for implementing a useful BCI.

In the classification stage, classifier algorithms are used for assigning classes to the features extracted from the previous stage. The designers of a multiclass classification BCI system choose an appropriate classifier for attaining a requisite level of efficiency (Padfield, et al., 2019). Various classifiers such as artificial neural network, linear discriminant analysis (LDA), fuzzy logic, K-nearest neighbor algorithm, and support vector machine may be employed for the classification of the selected features. However, their classification accuracy attainment is not at the desired level.

The authors in Nguyen, et al., 2018, introduced a new model of BCI consisting of feature extraction and fuzzy classification to handle uncertainty, noise, and outliers in EEG data. They have used a common spatial pattern algorithm to extract discriminant features from multiclass data. They have reported performance attained using different popularly used algorithms, which are used in this study to compare the performance of the proposed approach.

It is analyzed from the study of the related work that CSP and its variant SWCSP are widely used feature extraction techniques. Hence, the authors in this work have focused on improving performance by optimizing its parameters. The efficiency gained at the feature extraction stage will be reflected by an increase in classification accuracy achieved using the proposed approach.

## II. Methodology

The effectiveness of the proposed approach is verified by implementing preprocessing, feature extraction, and classification stages of an EEG-based BCI system. In this study, MATLAB-based open-source toolkit BCILAB is used for the development, testing, and evaluation of new BCI methods (Kothe and Makeig, 2013).

### *A. EEG Dataset*

An EEG-based BCI system analyzes signals fetched by electrodes positioned according to the standard international 10–20 system of EEG, as shown in Fig. 3, on designated parts of the scalp (Costantini, et al., 2009).

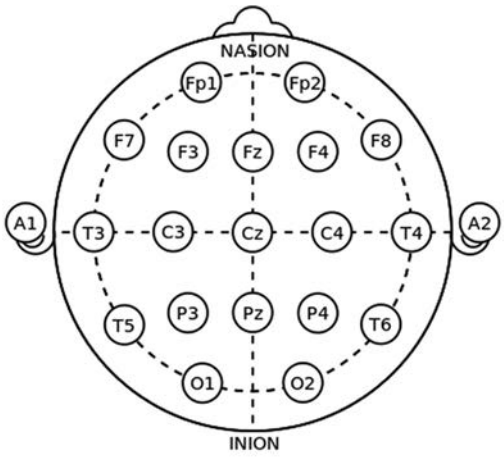


Fig. 3. International 10–20 system of electrode placement (Tangermann, et al., 2012).

In this work, benchmark dataset 2a of BCI Competition IV (Brunner, et al., 2008) is used. This dataset is publicly accessible and is vastly used by the research community to validate signal processing and classification methods for BCIs. It consists of trials of spontaneous EEG activity recorded from nine healthy subjects. One part is labeled, which is used for training and another part is unlabeled, which is used as test data. It contains 22 EEG Ag/AgCl channels besides three electrooculography (EOG) channels and the left mastoid acts as a reference while executing one of the four stipulated MI tasks. Each subject performs one training session and another test session. Each of the two sessions consists of six runs and each of the runs has 48 trials consisting of 12 trials for every four MI classes. The subject is shown a cue on the screen for performing the MI tasks of the left, right hands, both feet, or tongue movement (Tangermann, et al., 2012). Every trial starts with a short warning sound with a fixation cross, which is shown on a computer screen. It is followed by a small arrow signaling the subject to begin the execution of a corresponding MI task. The arrow sign switches back to the sign of fixation cross after 1.25 s and the MI task is continued for 6 s, after which the signaling fixation crossfades away from the screen. Then, there is a short break turning the screen black again. The experiment duration for each trial was 8 s, as shown in timing Fig. 2.Each subject's data set consisted of a training set and an evaluation set. The signals fetched in the above trials are sampled at 250 Hz, followed by bandpass filtering between 0.5 and 100 Hz. The noise from the power line is suppressed using a 50 Hz notch filter, whereas EOG channels are used for ensuing artifact processing (Mannan, et al., 2018).

### *B. Preprocessing*

EEG signals detected at electrodes positioned on different parts of the scalp, are overlapping, and have some superfluous and misleading information. The signals are then preprocessed to boost the signal-to-noise ratio by removing artifacts. In this work, independent component analysis (ICA) is used to isolate the artifacts inbuilt in the signals acquired from several electrodes. ICA applies a variable representing

the "unmixing" matrix of weights (W). It is multiplied by the matrix of scalp data for creating a matrix of independent component activities. In this work, EEGLAB, which is a MATLAB-based toolkit, is used for implementing the Infomax ICA algorithm, as it is a popularly used technique for the decomposition of mixed signals.

### *C. Feature Extraction*

The obtained preprocessed signals are then applied feature extraction method to the preprocessed EEG signals. In this work, a variant of CSP is used to extract features, while optimizing its parameters to enhance the performance of the BCI system.

*CSP*

It is a popularly used method of feature extraction using spatial filtering for increasing the discriminability of two classes (Zhang, et al., 2015, 2018; Kirar and Agrawal, 2016, pp. 14–21). It establishes linear subspaces in such a way that the variance in one projected class is enhanced to a maximum value while reducing the variance in another class to a minimum value (Ramoser, Muller-Gerking, and Pfurtscheller, 2000). The optimum spatial filters are identified by combined diagonalization of the covariance matrices corresponding to each of the two classes of EEG signals. The covariance matrix of EEG signal E, from each trial, is calculated as:

$$C = \frac{E_{N*T} E_{N*T}^{T}}{trace(E_{N*TE_{N*T}^{T}})} \tag{1}$$

Where, $E_{N*T}$ represents the EEG signal of the trial, N represents number of channels, T denotes number of points in the EEG signal in the trial, and trace(X) is the sum of diagonal values in matrix X. The sum of the covariance matrix for class i of the subject is:

$$C_i = \sum_{m=1}^{M} C(i,m) \tag{2}$$

In CSP, the frequency band for successfully discriminating two tasks is manually established. Another variant of CSP called SWCSP was proposed to avoid repeated experiments to find this frequency band (Park, Lee, and Kim, 2014).

*Spectrally weighted common spatial pattern (SWCSP)*

Feature extraction from the signals preprocessed in the earlier stage is done using SWCSP (Tomioka et al., 2006) (YÜKSEL, 2016). It is employed for extracting the weighted CSP features by using the subject-specific spectral and temporal spectral filters for establishing distinction between various MI tasks. The SWCSP transforms domain of time to frequency and performs optimization of spatial filters by using CSP and spectral filters by Fisher's criterion sequentially and iteratively. The most relevant channels are selected, and irrelevant ones are rejected from extracted SWCSP features. It uses an iterative algorithm to calculate optimum values of the spatial filter and spectral coefficients. It determines a feature vector with J columns as

$$\varnothing_j\left(X,\omega,B_j\right) = \log \omega_j^{T} X B_j B_j^{T} X^{T} \omega_j \tag{3}$$

Where, $\omega_j \in R^N$ is the spatial filter vector and $B_j \in R^{TxT}$ linear temporal filter. It contains the spectral filter coefficients for localized MI signal in frequency domain optimization of spatial filter ($w_j$). Let U be Fourier transformation matrix where

$$U = 1/\sqrt{Te}\,\frac{2\pi kl}{T} \in C^{TxT} \tag{4}$$

$$UU^{T} = I_{TxT} \tag{5}$$

Inserting $UU^T$ into the equation generates a sensor covariance matrix as:

$$\sum{}^{c} B = \left\{ XUU^{T} B_j B_j^{T} UU^{T} X^{T} \right\}^{C} \tag{6}$$

Here,

$$U^{T} B_j, B_j^{T} U = diag(\alpha_1, \alpha_2, \alpha_3 \ldots\ldots \alpha_T) \tag{7}$$

is a diagonal matrix including spectral weights $\alpha_t$ and $\{\}^C$ in Equation 6 represents the expected value within Class c.

$XU \in C^{N*T}$ represents the Fourier transformed input signal and $X_t \in C^N$ represents $i^{th}$ frequency component. The cross-spectrum matrix based on $\alpha_t$ is represented as

$$\sum(\alpha) = \sum_{t=1}^{T} \alpha_t V_k^{c} \in R^{NxN} \tag{8}$$

The $\alpha$ coefficients are calculated by following the optimization function solved with Fisher discriminant analyses (FDAs)

$$\alpha_{opt} = max \frac{s(\omega,\alpha)^1 - s(\omega,\alpha)^2}{var(s(\omega,\alpha)^1 + var(s(\omega,\alpha)^2)} \tag{9}$$

where ($\alpha_t \geq 0$)

$$s(\omega,\alpha)^{c} = \sum_{t=1}^{T} \alpha_t \omega^{T} V_k \omega \tag{10}$$

in which c represents the class label. Both spatial and spectral coefficients are updated alternately at each optimization step. Generalization of spectrum information of the task is represented in the following equation:

$$\alpha_k^{(c)} = \alpha_k^{(c)^{opt}\, q} . \beta_k{}^{p} where(c \in 1,2,3,4) \tag{11}$$

Where, $\beta_{kk=1}^{T'}$ represents the prior information of the spectrum specific to the problem. The values of p and q parameters are dependent on data, preprocessing, and prior information. Hence, their optimal values can be chosen using cross-validation. Finally, the classifier is executed on all SWCSP features in different time intervals to allocate a class to the features.

*Optimized spectrally weighted common spatial pattern (OSWCSP)*

In this work, spatial and spectral filter parameters of SWCSP are identified and iteratively optimized to improve its performance, as shown in Fig. 1. The signals were pre-filtered in a particular frequency band subject wise, as shown in Table I, to attain better performance. The increase in its performance is reflected in the accuracy of classification of the features extracted using SWCSP. Hyperparameter (m) represents a count of spatial filters used for constructing it. All possible values of m were considered and the best value of m giving the highest accuracy is selected. The spectral filter optimization in SWCSP is done by changing hyperparameters (p and q), whereas the prior filter band is varied from subject to subject. Since optimal values of the

http://dx.doi.org/10.14500/aro.10926

Table I
Classification Accuracy on Dataset 2A

| Subject | Frequency range from to | | *P* | q | Accuracy |
|---|---|---|---|---|---|
| 1 | 9 | 32 | 0 | 0.1 | 0.826 |
| 2 | 7 | 30 | 0 | 1.0 | 0.621 |
| 3 | 7 | 28 | 0 | 0.1 | 0.893 |
| 4 | 7 | 30 | 0 | 0.1 | 0.539 |
| 5 | 9 | 32 | 0 | 1.0 | 0.513 |
| 6 | 9 | 32 | 0 | 0.1 | 0.57 |
| 7 | 7 | 28 | 0 | 0.1 | 0.795 |
| 8 | 7 | 28 | 0 | 0.1 | 0.886 |
| 9 | 7 | 28 | 0 | 0.1 | 0.886 |
| Mean | 7 | 28 | 0 | 0.1 | 0.705 |

spatial, as well as the spectral filters, are interdependent, we have employed an iterative method that begins from the basic CSP method for spatial filters and updates one fixing the other alternately, as shown in Fig. 1.

### *D. Classification*

In this work, LDA is used as a classifier as it is reported to offer higher classification accuracy in many MI-based BCIs (Lotte, et al., 2007) (Resalat and Saba, 2016) (Bashashati, et al., 2007). LDA is a technique of dimensional reduction, which is often used for classification based on supervised learning. It classifies a recorded set of observations into pre-configured classes, by finding the combination of a linear feature to establish a distinction between signal classes. It starts with the calculation of interclass variance, which represents separability between different classes. It then calculates the intraclass variance, which is the distance between the mean and sample of each class, and finally calculates a lower-dimensional space, such that interclass variance is maximized and intraclass variance is minimized (Kołodziej, Majkowski, and Rak, 2012).

## III. Results and Discussion

To measure the performance of the proposed approach, MI-based BCI system consisting of signal preprocessing, feature extraction, and feature classification was carried out using MATLAB R2015a. ICA was employed for preprocessing to isolate and discard artifacts from the experimental dataset. The proposed method of OSWCSP was executed for implementing the feature extraction phase of BCI, whereas the LDA method was employed for the classification of these signals into corresponding MI tasks. Experiments were conducted to verify the performance of OSWCSP while optimizing its parameters. Various extensions of CSP were also chosen and their performance was compared with that of the OSWCSP. The proposed approach was executed on the publicly available dataset 2a of BCI Competition IV which has EEG recordings from nine subjects whereas they performed MI tasks. This benchmark dataset consists of 288 trials per session, having 72 trials whereas subjects performed MI tasks of each of four classes. The recorded EEG signals were processed using ICA for removing undesired artifacts, whereas features were extracted using the proposed method of OSWCSP, and LDA was used for classification. The overall efficiency of the system using the proposed feature extraction approach was calculated in terms of classification accuracy for each of the subjects. In the proposed approach of OSWCSP, values of three hyperparameters (m, p, and q) were optimized to improve overall classification accuracy. The improved value of classification accuracy was attained at m = 3, p = 0, and q = 0.1 for subjects 1, 3, 4, 6, 7, 8, and 9, whereas q = 1.0 for subjects 2 and 5. We have used 5-fold cross-validation to achieve a bias-variance trade-off. The k is assigned a value of 5, as it this not prone to high bias or variance. In each cycle, the dataset is shuffled randomly and split into five groups. The 5-fold cross-validation procedure is executed as follows:

- The dataset is shuffled randomly
- Data sample is partitioned into five subsets
- For i = 1–5
  - Train the classification algorithm on all samples except belonging to fold i
  - Test the classifier on a sample of fold i
  - Calculate the percentage Pi of correctly classified sample
- Classification accuracy is calculated as

$$E = \frac{\sum_{i=5}^{k} P_i}{5} \tag{12}$$

in which the data sample is partitioned into five subsets. Iteratively, one of the subsets is used as a testing dataset whereas the remaining subsets are treated as training datasets. Then, the model is fitted to a training set and evaluated on the test dataset, and the average accuracy attained in five such cycles is calculated.

We have optimized the spatial projection, by applying a bandpass filtering dataset for each subject, from 7 to 34 Hz, and CSP projection with m = 3. Patterns corresponding to each of the four classes are calculated on the complete dataset, for eliminating unrelated frequency bands. Spectral filtering is applied on spatially filtered datasets using SWCSP, which has parameters p and q as given in Equation 11, required for tailoring the feature extraction method to specific data. The scaling factors of the spectral filter are selected for each subject using the grid search method, which consists of coarse and fine grid search methods. In coarse grid search, we selected a wide frequency band, which is then narrowed down using fine grid search. The other hyperparameters p and q are varied in the range [0, 1]. It attained the best classification accuracy at m = 3 whereas p and q were varied in a range of 0 and 1. The performance of the proposed optimization is evaluated on the classification of the benchmark dataset, which is then compared with other approaches evaluated on the same benchmark dataset. The performance comparison in terms of classification accuracy, which is the number of correct predictions divided by the total number of predictions, is shown in Table I and Fig. 4.

Classification accuracy attained for all subjects 1, 2, 3, 5, 6, 7, and 8 is higher than the result reported in (Nguyen, et al., 2018). The efficacy of the proposed feature extraction technique is also evident from an improvement in average

Table II
Comparison of Classification Accuracy Rates with Existing Techniques in Nguyen, et.al., 2018

| Subject | LDA | NB | KNN | Ensemble | SVM | FLS | (OSWCSP for feature extraction and LDA for classification) |
|---|---|---|---|---|---|---|---|
| 1 | 0.722 | 0.639 | 0.670 | 0.594 | 0.688 | 0.719 | 0.826 |
| 2 | 0.444 | 0.493 | 0.455 | 0.465 | 0.483 | 0.531 | 0.621 |
| 3 | 0.781 | 0.757 | 0.747 | 0.726 | 0.760 | 0.764 | 0.893 |
| 4 | 0.632 | 0.632 | 0.504 | 0.590 | 0.618 | 0.667 | 0.539 |
| 5 | 0.403 | 0.399 | 0.358 | 0.399 | 0.413 | 0.392 | 0.513 |
| 6 | 0.403 | 0.438 | 0.399 | 0.351 | 0.410 | 0.424 | 0.57 |
| 7 | 0.788 | 0.705 | 0.674 | 0.656 | 0.778 | 0.773 | 0.795 |
| 8 | 0.785 | 0.802 | 0.760 | 0.708 | 0.816 | 0.802 | 0.886 |
| 9 | 0.767 | 0.785 | 0.726 | 0.750 | 0.792 | 0.816 | 0.705 |
| Mean | 0.636 | 0.628 | 0.588 | 0.582 | 0.640 | 0.650 | 0.706 |

Table III
Confusion Matrix Averaged for all Subjects

| Predicted class▶ Actual class▼ | Left | Right | Foot | Tongue |
|---|---|---|---|---|
| Left | 0.85 | 0.09 | 0.02 | 0.04 |
| Right | 0.07 | 0.88 | 0.03 | 0.02 |
| Foot | 0.09 | 0.08 | 0.77 | 0.06 |
| Tongue | 0.07 | 0.06 | 0.08 | 0.79 |

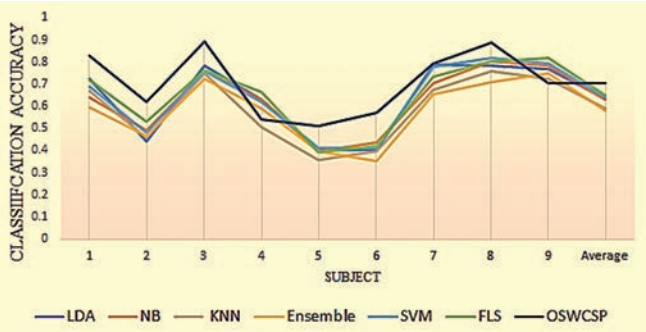


Fig. 4. Classification accuracy.

classification accuracy to 70.6%, as shown in Table II. The confusion matrix of the results is shown in Table III, which depicts correct and incorrect predictions, broken down by class of left hand, right hand, feet, and tongue MI task.

## IV. Conclusion

In this work, the optimized SWCSP approach is proposed for feature extraction from multiclass MI EEG signals. In preprocessing stage, ICA is used for removing artifacts from acquired EEG signals. The next stage of feature extraction is implemented by the proposed OSWCSP method, whereas its parameters are varied to search for their optimal values using the grid search method. The selected features are then input to the LDA classifier. The performance of the proposed approach was evaluated on dataset 2a from BCI Competition IV, which is used as a benchmark by many in the reported literature, using a 5-fold cross-validation process yielding improved performance. The proposed approach yields an average classification accuracy of 0.706, which is better than the accuracy attained using other approaches executed on the same benchmark dataset, as reported in the literature. It has the potential to enhance the robustness and reliability of future EEG-based BCI systems for rehabilitation. The challenge is now to test the efficacy of the proposed approach in a real online BCI system.

## References

Alam, M.N., Ibrahimy, M.I. and Motakabber, S.M.A., 2021. Feature Extraction of EEG Signal by Power Spectral Density for Motor Imagery Based BCI. In: *2021 8th International Conference on Computer and Communication Engineering* (*ICCCE*), pp.234-237.

Bashashati, A., Fatourechi, M., Ward, R.K. and Birch, G.E., 2007. A survey of signal processing algorithms in brain-computer interfaces based on electrical brain signals. *Journal of Neural Engineering*, 4(2), p.R32.

Bernardi, G.B., Pimenta, T.C. and Moreno, R.L., 2019. A Simplified Tool for Testing of Feature Selection and Classification Algorithms in Motor Imagery of Right and Left Hands of EEG Signals. In: *2019 IEEE 10th Latin American Symposium on Circuits and Systems* (*LASCAS*), pp.197-200.

Brunner, C., Leeb, R., M¨uller-Putz, G.R., Schlogl, A. and Pfurtscheller, G., 2008. *BCI Competition 2008-Graz Data Set A*. Institute for Knowledge Discovery (Laboratory of Brain-Computer Interfaces), Graz University of Technology.

Costantini, G., Todisco, M., Casali, D., Carota, M., Saggio, G., Bianchi, L., Abbafati, M. and Quitadamo, L.R., 2009. SVM Classification of EEG Signals for Brain Computer Interface. In: *Proceedings of the 2009 conference on Neural Nets WIRN09: Proceedings of the 19th Italian Workshop on Neural Nets, Vietri sul Mare, Salerno, Italy, May 28-30 2009*, pp.229-233.

Dai, M., Wang, S., Zheng, D., Na, R. and Zhang, S., 2019. Domain Transfer Multiple Kernel Boosting for Classification of EEG Motor Imagery Signals. *IEEE Access*, 7, pp.49951-49960.

Gaur, P., Pachori, R.B., Wang, H. and Prasad, G., 2018. A multi-class EEG-based BCI classification using multivariate empirical mode decomposition based filtering and Riemannian geometry. *Expert Systems with Applications*, 95, pp.201-211.

Kennedy, P.R., Bakay, R.A., Moore, M.M., Adams, K. and Goldwaithe, J., 2000. Direct control of a computer from the human central nervous system. *IEEE Transactions on Rehabilitation Engineering*, 8(2), pp.198-202.

Kirar, J.S. and Agrawal, R.K., 2016. Optimal spatio-spectral variable size subbands filter for motor imagery brain computer interface. *Procedia Computer Science*, 84, pp.14-21.

Kołodziej, M., Majkowski, A. and Rak, R.J., 2012. Linear discriminant analysis as EEG features reduction technique for brain-computer interfaces. *Przeglad Elektrotechniczny*, 88, pp.28-30.

Kothe, C.A. and Makeig, S., 2013. BCILAB: A platform for brain-computer interface development. *Journal of Neural Engineering*, 10(5), p.56014.

Lemm, S., Blankertz, B., Curio, G. and Muller, K.R., 2005. Spatio-spectral filters for improving the classification of single trial EEG. *IEEE Transactions on Biomedical Engineering*, 52(9), pp.1541-1548.

Liu, A., Chen, K., Liu, Q., Ai, Q., Xie, Y. and Chen, A. 2017. Feature selection for motor imagery EEG classification based on firefly algorithm and learning automata. *Sensors*, 17(11), p.2576.

Lotte, F., Bougrain, L., Cichocki, A., Clerc, M., Congedo, M., Rakotomamonjy, A. and Yger, F., 2018. A review of classification algorithms for EEG-based brain-computer interfaces: A 10 year update. *Journal of Neural Engineering*, 15(3), p.31005.

Lotte, F., Congedo, M., Lécuyer, A., Lamarche, F. and Arnaldi, B., 2007. A review of classification algorithms for EEG-based brain-computer interfaces. *Journal of Neural Engineering*, 4(2), p.R1.

Mannan, M.M.N., Kamran, M.A., Kang, S. and Jeong, M.Y., 2018. Effect of EOG

signal filtering on the removal of ocular artifacts and EEG-based brain-computer interface: A comprehensive study. *Complexity*, 2018, p.4853741.

Mason, S.G. and Birch, G.E., 2003. A general framework for brain-computer interface design. *IEEE Transactions on Neural Systems and Rehabilitation Engineering*, 11(1), pp.70-85.

Nguyen, T., Hettiarachchi, I., Khatami, A., Gordon-Brown, L., Lim, C.P., Nahavandi, S., 2018. Classification of multi-class BCI data by common spatial pattern and fuzzy system. *IEEE Access*, 6, pp.27873-27884.

Padfield, N., Zabalza, J., Zhao, H., Masero, V., Ren, J., 2019. EEG-based brain-computer interfaces using motor-imagery: Techniques and challenges. *Sensors*, 19(6), p.1423.

Park, G.H., Lee, Y.R. and Kim, H.N., 2014. Improved filter selection method for filter bank common spatial pattern for eeg-based bci systems. *International Journal of Electronics and Electrical Engineering*, 2(2), pp.101-105.

Ramoser, H., Muller-Gerking, J. and Pfurtscheller, G., 2000. Optimal spatial filtering of single trial EEG during imagined hand movement. *IEEE Transactions on Rehabilitation Engineering*, 8(4), pp.441-446.

Rashid, M., Sulaiman, N., Abdul Majeed, A.P.P., Musa, R.M., Ab Nasir, A.f., Bari, B.S. and Khatun, S. 2020. Current status, challenges, and possible solutions of EEG-based brain-computer interface: A comprehensive review. *Frontiers in Neurorobotics*, 14, pp.25.

Resalat, S.N. and Saba, V., 2016. A study of various feature extraction methods on a motor imagery based brain computer interface system. *Basic and Clinical Neuroscience*, 7(1), p.13.

Selim, S., Tantawi, M.M., Shedeed, H.A. and Badr, A., 2018. A CSP\AM-BA-SVM approach for motor imagery BCI system. *IEEE Access*, 6, pp.49192-49208.

She, Q., Ma, Y.L., Meng, M., Xi, X.G. and Luo, Z.Z., 2017. Noise-assisted MEMD based relevant IMFs identification and EEG classification. *Journal of Central South University*, 24(3), pp.599-608.

Siuly, S. and Li, Y., 2012. Improving the separability of motor imagery EEG signals using a cross correlation-based least square support vector machine for brain-computer interface. *IEEE Transactions on Neural Systems and Rehabilitation Engineering*, 20(4), pp.526-538.

Tan, C., Sun, F., Zhang, W., Liu, S. and Liu, C., 2017. Spatial and Spectral Features Fusion for EEG Classification during Motor Imagery in BCI. In: *2017 IEEE EMBS International Conference on Biomedical and Health Informatics* (*BHI*), pp.309-312.

Tangermann, M., Müller, K.R., Aertsen, A., Birbaumer, N., Braun, C., Brunner, C., Leeb, R., Mehring, C., Miller, K.J., Müller-Putz, G.R., Nolte, G., Pfurtscheller, G., Preissl, H., Schalk, G., Schlögl, A., Vidaurre, C., Waldert, S. and Blankertz, B., 2012. Review of the BCI competition IV. *Frontiers in Neuroscience*, 6, p.55.

Tomioka, R., Dornhege, G., Nolte, G., Blankertz, B., Aihara, K. and Muller, K.R., 2006. Spectrally Weighted Common Spatial Pattern Algorithm for Single Trial EEG Classification. In: *Mathematical Engineering Technical Reports*. University of Tokyo, Tokyo, Japan, Report No. 40.

Wolpaw, J.R., McFarland, D.J. and Vaughan, T.M., 2000. Brain-computer interface research at the Wadsworth Center. *IEEE Transactions on Rehabilitation Engineering*, 8(2), pp.222-226.

Wolpow, J.R., Birbaumer, N., McFarland, D.J., Pfurtscheller, G. and Vaughan, T., 2002. Brain-computer interfaces for communication and control. *Clinical Neurophysiology*, 113(6), pp.767-791.

Yang, H. and Wu, S., 2014. EEG classification for bci based on csp and svm-ga. *Applied Mechanics and Materials*, 459, pp. 228-231.

Yüksel, A., 2016. *Istanbul Technical University Graduate School of Science Engineering and Technology*. Middle East Technical University.

Zhang, D., Yao, L., Zhang, X., Wang, S., Chen, W., Boots, R. and Benatallah, B., 2018. Cascade and Parallel Convolutional Recurrent Neural Networks on EEG-based Intention Recognition for Brain Computer Interface. *Thirty-Second AAAI Conference on Artificial Intelligence*.

Zhang, Y., Zhou, G., Jin, J., Wang, X. and Cichocki, A., 42015. Optimizing spatial patterns with sparse filter bands for motor-imagery based brain-computer interface. *Journal of Neuroscience Methods*, 255, pp.85-91.

# Human Body Posture Recognition Approaches: A Review

Mohammed A. Ali[1], Abir J. Hussain[2], Ahmed T. Sadiq[1]

[1]Department of Computer Sciences, University of Technology, Baghdad, Iraq
[2]School of Computer Sciences and Mathematics, Liverpool John Moores University, Liverpool, England

***Abstract*—Human body posture recognition has become the focus of many researchers in recent years. Recognition of body posture is used in various applications, including surveillance, security, and health monitoring. However, these systems that determine the body's posture through video clips, images, or data from sensors have many challenges when used in the real world. This paper provides an important review of how most essential hardware technologies are used in posture recognition systems. These systems capture and collect datasets through accelerometer sensors or computer vision. In addition, this paper presents a comparison study with state-of-the-art in terms of accuracy. We also present the advantages and limitations of each system and suggest promising future ideas that can increase the efficiency of the existing posture recognition system. Finally, the most common datasets applied in these systems are described in detail. It aims to be a resource to help choose one of the methods in recognizing the posture of the human body and the techniques that suit each method. It analyzes more than 80 papers between 2015 and 2020.**

***Index Terms*—Acceleration based, Computer vision, Health monitoring, Human body posture recognition, Security.**

## I. Introduction

Human body posture recognition (HBPR) is an essential topic in modern technology and focuses on many researchers in computer science and engineering (Patel, Bhatt, and Patel, 2017). Artificial intelligence algorithms are used in these technologies to recognize the position of the human body. In computer vision and electronic devices, such as sensors and smartphones used in many applications (Hameed, Alwan, and Ateia, 2020), the human body's posture is critical. Due to the rapid advancement of image processing and other technologies, HBPR is used in a range of applications and tests, including computer-based intelligent video surveillance and pattern recognition (Lo Presti and La Cascia, 2016; Hsiao, et al., 2018; Zhang, Wu, and Wang, 2020; Wan, et al., 2020).

ARO-The Scientific Journal of Koya University
Vol. X, No.1 (2022), Article ID: ARO.10930, 10 pages
DOI: 10.14500/aro.10930
Received: 26 January 2022; Accepted: 17 May 2022
Regular research paper: Published: 13 June 2022
Corresponding author's e-mail: cs.19.21@grad.uotechnology.edu.iq.iq


In recent years, deep learning technology has been used to achieve successful results in a variety of tasks (Ghafoor, et al., 2021), including image object recognition (Zhao, et al., 2019), classification (Rawat and Wang, 2017), and semantic segmentation (Sun and Wang, 2018), and so on. The use of deep learning technology in HBPR has resulted in rapid growth. The advances were made on engineered networks with excellent estimation capacity, rich datasets (Colleges, et al., 2014; Joo, et al., 2019; Mehta, et al., 2018) for feeding networks, and a more realistic exploration of body models (Kanazawa, et al., no date). Even though there is some current interest in HBPR, there is still a need to summarize the most recent deep learning-based research.

HBPR systems usually use both supervised learning and unsupervised learning. Unsupervised systems rely on rules, while supervised systems use algorithms trained in advance with unique datasets (Gupta, et al., 2020).

The review paper classified HBPR systems into two types: Acceleration-based and vision-based methods (Hsiao, et al., 2018; Abedi, et al., 2020). Fig. 1 shows classification of data capture hardware for human body posture. Posture recognition systems perform sequential data collection from wearable devices or cameras (Zhang and Callaghan, 2020). Acceleration-based methods are divided into two hardware types: Wearable sensors and smartphone devices. The sensors require users to wear multiple accelerometers to collect data (Gupta, et al., 2020; Mo, et al., 2016). Some methods rely on the input data from smartphone sensors such as gyroscopes and accelerometers. These devices recognize the positions of the human body using built-in or stand-alone sensors (Gupta, et al., 2020; Khokhlov, et al., 2018; Voicu, et al., 2019). Many designs, from fitness bands with very limited smartphones to larger implementation platforms, including desktop computers (Khokhlov, et al., 2018). In the final step, they are categorized using the model estimation of the main points of the body through the neural network (Gupta, et al., 2020). Collecting data in the vision-based method utilize one or more conventional cameras and specialized cameras for depth images (Mirza and Al-Talabani, 2021). The vision-based system has the benefit of not requiring users to wear any sensors, but its performance is heavily influenced by visual angle, lighting conditions, and other environmental variables. On the other hand, the accelerometer-based

http://dx.doi.org/10.14500/aro.10930

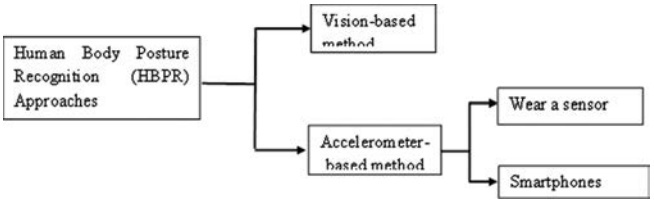


Fig. 1. Classification Hardware to capture and collect dataset.

method requires users to wear a sensor, but it eliminates any external interference. Most cell phones now have a built-in accelerometer, allowing users to construct an accelerometer-based posture system on the mobile platform without the use of extra equipment (Chen and Xue, 2016).

Several reviews have been published during the past decade to summarize the related work on human pose estimation (HPE). For instance, Liu, et al., 2015, a study of HPE based on body parts parsing from numerous input sources, multiple view and single view. Zhang, et al., 2016, discuss the challenges of estimating human pose and include a data-driven analysis of recent approaches to estimating human pose, including depth-based approaches and conventional image-based methods. This research focuses on methods that use RGB and depth image data. Another aspect is presented in the review (Lo Presti and La Cascia, 2016). It highlighted the 3D skeleton-based action classification methods and the new research in this field. Sarafianos, et al., 2016 another paper showed a review of 3D HPE approaches using various inputs (e.g., multiview or monocular, film, or single image). Gong, et al., 2016, this paper provided a review of traditional HPE approaches focused on monocular vision with a few deep learning-based methods. Patel et al., 2017, propose a review discussing how various steps of the human body pose are used by showing various methods used for each step of the system. (Wu, Sharma and Blumenstein, 2017) The three types of datasets were shown, and various state-of-the-art deep learning-based strategies for human behavior detection were proposed (Ben Mabrouk and Zagrouba, 2018). Another paper reviewed the two key measures that make up a video monitoring scheme, behavior representation and behavior simulation. Wang, et al., 2018, this article showed a survey of four types of red green blue-depth (RGB-D) motion recognition: RGB-D based, skeleton based, depth based, and RGB based. Dang, et al., 2019, this review illustrated methods for predicting human pose based on deep learning and their methodologies. Zhang, et al., 2019, covered the latest developments of hand-designed action features in RGB and depth details, modern deep learning-based action feature representation methods, products in human-object interaction recognition, and the emerging technologies hot topic of action detection methods. Chen, Tian, and He, 2020, this paper reviewed four types of monocular HPE analysis and human pose datasets focused on deep learning. The review of Gupta, et al., 2020, concentrated on several recent academic articles on multiple behavior recognition methods, wearable devices, smartphone sensors, and vision-based tools used to recognize.

The main contributions of this review paper are as follows:

- A study of devices used in HBPR systems also identifies each device's limitations and advantages
- Review of essential methods used in HBPR systems
- Classification of a dataset used in HBPR systems into several categories, depending on the hardware used.

The rest of this paper is organized as follows. Section II contains a literature review and compares procedures with practices and their precision. Section III includes the most used datasets and a short description of the information they contain. A discussion of the research regarding its benefits and drawbacks is included in Section IV. Finally, the conclusions and future directions of promising studies that could improve the effectiveness of HBPR appear in Section V.

## II. LITERATURE REVIEW

This paper discusses many methods to discern the human body's pose, whether in cameras, sensors, or smartphones.

### *A. Vision-based Methods*

HBPR has become a common research subject in computer vision (Ding, et al., 2020, Abdulhussein and Raheem, 2020). Posture information is helpful for tasks such as activity detection and content extraction. The method of inferring the locations of 2D or 3D human body parts from still photographs or videos is known as human pose recognition (HPR) (Dang, et al., 2019; Gupta, et al., 2020). Traditional and depth cameras are used to track human body identification in various settings, including sports stadiums, indoor and outdoor events, shopping centers, educational facilities, hospitals, and highways (Zhang and Callaghan, 2020). Estimating the human experience is a challenging problem in computer vision, but it has many real-world applications (Dang, et al., 2019).

From a single image or video, 2D HPR calculates the positions of human joints. HPR 2D algorithms traditionally focus on handcraft feature extraction and sophisticated body models to obtain local representations and global positional structures before deep learning can have a significant effect on vision-based human posture appreciation (Zhang, Wu, and Wang, 2020; Yan, Coenen and Zhang, 2016; Zhou and Zhang, 2020). Single individual posture estimation and multipersonal posture estimation are two types of contemporary 2D human postural estimation approaches based on deep learning (Chen, Tian, and He, 2020; Zhang, Wu, and Wang, 2020).

Color and depth images, as well as human skeletal records, are all readily accessible to researchers. Several location recognition algorithms have been suggested using skeletal data derived from the Kinect (Rahmani and Bennamoun, 2017; Liu, et al., 2020). These algorithms reduce the effect of poor lighting. They also remove the need for pre-processing, such as segmentation and object detection in complex backgrounds, allowing for improved image quality (Ding, et al., 2020).

A photograph or other input form can be used to generate a 3D model of human body joints, known as 3D human pose estimation. Commercial technologies like Kinect with a depth sensor, Vicon with an optical sensor, and the Captury with

multiple cameras have been used for 3D body pose estimation, although these systems only work in extremely limited contexts or require unique markers on the human body to perform (Wu, Sharma and Blumenstein, 2017; Abdulhussein and Raheem, 2020). The three depth sensor-based human labor identification forms are osteoid data, depth image, and methods based on depth and skeleton (Rahmani and Bennamoun, 2017).

### *B. Acceleration-based Methods*

Smartphones are the most helpful tool in our daily lives, and modern technology helps them consistently meet their user's needs and wishes. Smartphone designers continually add new features to the devices to make these systems more usable and functional. Sensors enhance mobile capabilities and play an essential role in environmental awareness. As a result, most smartphones come equipped with a range of sensors to capture a wealth of information about everyday activities. Sensors collect data from body movements and then identify behaviors (Ding, et al., 2020; Gupta, et al., 2020). Accelerometers and gyroscopes are the most common (Kareem, Ali and Jasim, 2020). The accelerometer sensor monitors changes in motion, whereas the gyroscope is used to track the object's orientation. Most commercial smartphones contain at least two, a microsystem or a micro-electro-mechanical system (MEMS; Nandy, Saha and Chowdhury, 2020; Khokhlov, et al., 2018). MEMS-based accelerometers are more practical than mechanical accelerometers. People currently wear or carry these smartphones and wearables with built-in MEMS sensors. These sensors allow the use of many fascinating lifestyle tracking applications. Since smartphones include sensors (gyroscope, accelerometer, compass, etc.) as well as networking capabilities (such as Wi-Fi and Bluetooth), the data gathered from the sensors may be sent to a remote server for analysis and classification (Nandy, Saha and Chowdhury, 2020). Google Fit, Samsung Fitness, and Noom Walk are activity recognition applications for Android OS mobile devices. Likewise, Human Activity Tracker and Pacer are activity recognition apps for iOS devices that gather data from built-in sensors for health-care purposes (Khokhlov, et al., 2018; Wan, et al., 2020; Nandy, Saha and Chowdhury, 2020; Voicu, et al., 2019) support vector machine, k-nearest neighbors algorithm (k-NN), Bootstrap aggregating (Bagging), and Adaptive Boosting (Ada Boost) are some of the human action recognition innovations used by smartphones in recent studies (Ding, et al., 2020; Gupta, et al., 2020).

On the other hand, wearable technology collects data from sensors connected to the subject, used for continuous monitoring. Since human activity includes various physical motions, the recognition of human activity requires data from several sensors mounted on various areas of the person's body (Gupta, et al., 2020). Furthermore, the use of different sensors is now standard as a plug-and-play option. For example, sensors, such as temperature, tone, light, and potentiometers, may be mounted directly on the boards of popular Arduino or Raspberry Pi computers (Vecchio, Mulas, and Cola, 2017). Furthermore, the number of premium sensor products available is constantly increasing, enabling consumers to track various conditions such as air quality, carbon monoxide, ambient pressure, capacity, humidity, gas leakage, and hydrogen (Kamišalić, et al., 2018). Several articles have been published on multiple human activity detection technologies using body sensors or wearable sensors in several environments, including senior centers, detox centers, and systems for identifying mental illnesses (Hsiao, et al., 2018; Wu, Sharma, and Blumenstein, 2017). Motion sensors, such as acceleration, video, proximity, and other wearable sensors, are examples of body sensors. These sensors commonly track driving, sitting, biking, standing, group meetings, reading, and other body movements.

The design of wearable sensors must consider user compatibility. Activity tracking sensors must be light and comfortable. Multiple datasets use activity tracking sensors. Human activities can be classified using statistics after function extraction and modeling, and a machine learning algorithm is implemented. Activity identification requires translating low-level sensor data to higher-level abstractions (Sun and Wang, 2018). Vector machine-based classification, neural network-based classification, and pattern mating-based classification are the most common algorithms (Neili, et al., 2017; Gouiaa and Meunier, 2017; Hassan, et al., 2018).

Table I is a comparison of previous reviews with this review. The comparison was based on the topics covered and studied.

Methods of collecting and capturing image data or other types impact many factors in choosing to build a human body posture recognition system and choosing algorithms and techniques in classification. Table II analyzes the accuracy of these algorithms depending on the type of data used.

## III. DATASET

The dataset has a fundamental role in Human Body Posture Recognition. HBPR, whether through computer vision-based systems or acceleration-based systems using deep learning, requires a large dataset. The dataset size is critical, but the learning improvement can be costly for a large dataset. Each method of determining the body's activities has a specific dataset that depends on the application and the devices used to capture the input. Table III presents the most common datasets available to users that are carefully collected to be trainable and testable.

HMDB51 and UCF 101 are the most often utilized RGB datasets for evaluating proposed methods. These two datasets have been used in virtually all studies of current deep learning-based techniques to test algorithm efficacy. However, the RGBD and skeleton datasets have seen less use in deep learning-based algorithms than the RGB dataset. The fact that these datasets are small scale is one of the primary reasons. Deep learning-based techniques for depth and skeleton data are becoming major research subjects, thanks to the emergence of large scale and complex RGBD and skeleton datasets, such as the NTU RGB+D dataset (Zhang, et al., 2019).

This review paper will divide the dataset according to the type of camera, the samples were collected, RGB images,

http://dx.doi.org/10.14500/aro.10930

and depth images collected by depth cameras.

*A. RGB Dataset*

1. Writing posture dataset (WPD) (Cao, et al., 2017): The WPD was gathered in a laboratory setting with a calibrated binocular camera, and RGB video was captured for each subject. It contains 113,400 pictures taken from 30 people of various genders and heights. For each frame, skeleton data and a position category are supplied
2. MPII (Andriluka, et al., 2014): The dataset is from YouTube videos. It includes 410 human activities, and each image is provided with an activity label
3. Southeast University SEU: This information was initially compiled by Zhao, et al., 2012. Each video in the collection was captured using a side-mounted Logitech C905 CCD camera in daylight circumstances. The dataset was created with the help of 10 male and 10 female drivers. Each film was shot in natural light during the day
4. HMDB51 (Zhao, et al., 2012): The dataset contains many real videos culled from various sources, including films and web videos. There are 6849 video clips in the collection, divided into 51 activity types. Again, they were gathered from various sources (public databases, movies such as YouTube, Google videos, and Prelinger archive)
5. Hollywood2 (Marszałek, Laptev and Schmid, 2009): The dataset consists of 3669 video clips and about 20 of 1 h of the film, with 12 classes of human activities and ten scenery classes. The collection contains video snippets from 69 films. It was suggested that realistic and complex environments be provided (cluttered background, multiple persons.etc.)
6. Olympic (Niebles, Chen and Fei-Fei, 2010): The Olympic Sports dataset includes videos of athletes participating in various sports. It collected all its video sequences from YouTube and used Amazon Mechanical Turk to annotate its class labels
7. UCF101: It was produced by the center for research in Computer Vision, University of Central Florida, the USA, in 2012 (Soomro, Zamir and Shah, 2012). It is an expansion of the UCF50 dataset (Reddy and Shah, 2013), which comprises 50 activity types. It is made of 13,320 videos of 101 realistic action categories taken from YouTube. It delivers the most significant variation in activities and realistic situations (viewpoint, illumination conditions.etc.) (Fig. 2a).

*B. Depth and Skeleton Dataset*

1. MSR-Action3D (Li, Zhang and Liu, 2010): A depth sequence action dataset is recorded by a depth camera. Wanqing Li, a researcher at Microsoft Research Redmond, developed it. It contains 567 depth map sequences of 10 people doing 20 different action types twice or 3 times (Fig. 2b)
2. UTKinect-Action (Xia, Chen and Aggarwal, 2012): The UT-Kinect dataset is a depth sequence action recognition dataset. There are 10 different sorts of actions. RGB, depth, and skeleton joint positions were captured in three channels
3. Northwestern-UCLA (Wang, et al., 2014): The multiview 3D event dataset comprises RGB, depth, and human skeletal data simultaneously recorded by three Kinect cameras. There are 10 activity categories in this dataset. A group of 10 performers carries out each action. This dataset includes data from several perspectives
4. NTU RGB+D datasets (Shahroudy, et al., 2016): NTU RGB+D is a large-scale dataset recognizing RGB-D human actions. It includes 56,880 samples from 40 topics representing 60 action classes. There are three types of activities, 40 everyday acts, nine health-related actions, and

Table I
Summary and Comparison of the Related Review of Human Body Posture Recognition

| No. | Survey, review, and reference | Topic/main focus |
|---|---|---|
| | A survey of human pose estimation: The body parts parsing based methods (Liu, et al., 2015) | The recent advances in vision-based human pose estimation |
| | A survey on human pose estimation (Zhang, et al., 2016) | Discuss the difficulties of human pose estimation and give a data-driven overview of recent approaches |
| | 3D skeleton-based human action classification: A survey (Lo Presti and La Cascia, 2016) | Highlights the motives and challenges of this relatively new research field |
| | 3D human pose estimation: A review of the literature and analysis of covariates (Sarafianos, et al., 2016) | Various inputs (e.g., multiview or monocular, film, or single image) |
| | Human pose estimation from monocular images: A comprehensive survey (Gong, et al., 2016) | Monocular vision with a few deep learning-based methods |
| | Human body posture recognition – A survey (Patel, Bhatt and Patel, 2017) | A different phase of human body posture |
| | Recent advances in video-based human action recognition using deep learning: A review (Wu, Sharma and Blumenstein, 2017) | Three types of datasets, various state-of-the-art deep learning-based strategies |
| | Abnormal behavior recognition for intelligent video surveillance systems: A review (Ben Mabrouk and Zagrouba, 2018). | Two key measures that make up a video monitoring scheme, behavior representation, and behavior simulation |
| | RGB-D-based human motion recognition with deep learning: A survey (Wang, et al., 2018) | There are four types of RGB-D motion recognition: RGB-D based, skeleton based, depth based, and RGB based |
| | Deep learning-based 2D human pose estimation: A survey (Dang, et al., 2019) | Methods for predicting human pose based on deep learning and the methodologies used are discussed |
| | A comprehensive survey of vision-based human action recognition methods (Zhang, et al., 2019) | Review of human action recognition methods and provide a comprehensive overview of recent approaches in human action recognition research |
| | Monocular human pose estimation: A survey of deep learning-based methods ours (Chen, Tian and He, 2020) | Four classes of deep learning-based monocular HPE analysis and human pose datasets |
| | A survey on human activity recognition and classification (Gupta, et al., 2020) | Various methods of activity recognition |
| | Our review | Two famous techniques are capturing and collecting a dataset of human body posters and analyzing modern classification methods |

Table II
Systematic Analysis of Human Body Posture Recognition Algorithm Based on Prior Research

| Paper | Feature | Device | Type image | Method | Dataset | Accuracy (%) |
|---|---|---|---|---|---|---|
| Ding, et al., 2020 | Skeleton | Kinect | RGB-D image | Bagging approach and RIPPER rule learning algorithm | MSR-Action3D | 94.5 |
| | | | | | Microsoft MSRC-12 | 97.6 |
| | | | | | UTKinect- Action | 98.1 |
| | | | | | Baduanjin posture (local dataset) | 99.6 |
| El Amine Elforaici, et al., 2018 | 3D skeleton | Kinect2 | RGB-D image | (CNNs) + SVM classification | Local dataset | |
| | | | | | RGB | 93.3 |
| | | | | | Depth | 95.7 |
| Hsiao, et al., 2018 | Spatial features or body part features. | FSR sensors and infrared array sensors | Pressure sensor data+infrared sensor data | Fuzzy c-means clustering algorithm | Local dataset | 88 |
| Zhang, Wu and Wang, 2020 | Spatiotemporal information | RGB camera | RGB images | Improved two-branch multistage convolutional neural network (M-CNN) | Postures of fall | 98.70 |
| Wan, et al., 2020 | - | Smartphone | Acceleration data | Proposed CNN model | UCI | 92 |
| | | | | | Pamap2 datasets | 91 |
| Chen and Xue, 2016 | - | Android phone | Acceleration data | CNN modified | 31,688 samples from 100 subjects | 93.8 |
| Zhang, Yan and Li, 2018 | 3D body skeletons | RGB camera | RGB images | Multistage CNN architecture | ARM | 94.9 |
| | | | | | Back | 93.9 |
| | | | | | Legs | 94.6 |
| Huang, et al., 2019 | - | Ultra-wide band | Acceleration data | Least square estimation (LSE) method and the improved extended Kalman filtering (iEKF) algorithm | - | - |
| Kale, et al., 2018 | - | Wirelessly (Wi-Fi) acquiring | Sensor data | Artificial neural networks | Dataset of 44,800 samples | 97.58 |
| Ren, et al., 2020 | - | Kinect | RGB-D image | Hybrid fuzzy logic and machine learning approach | A small dataset containing 19,800 | 97.1 |
| Liu, et al., 2020 | Gaussian voxel feature | RGB camera | RGB images | 3D CNN | WPD | 97.77 |
| | | | | | BPD | 98.16 |
| Quan, et al., 2019 | Forward kinematics model of the human skeleton | ASUS Xtion PRO | RGB-D image | Unsupervised learning algorithms, such as GNG and PSO | No dataset used | - |
| Neili, et al., 2017 | Skeleton data | - | RGB-D | ConvNets and SVM classifier | CAD60 | 99.66 |
| Gouiaa and Meunier, 2017 | Shadow images | Camera and two infrared light sources | Synthetic data | CNN | Dataset captured in laboratory | 99 |
| Liang and Hu, 2020 | Coordinate threshold of joint points | Kinect V1 | RGB image | Deep neural network ResNet | MPII | 91 |
| Yan, Coenen and Zhang, 2016 | Hand position | RGB camera | RGB image | CNN | SEU dataset | 99.47 |
| | | | | | Driving-Posture-atNight dataset | 99.3 |
| | | | | | Driving-Posture-inReal dataset | 95.77 |
| Zhou and Zhang, 2020 | Appearance, audio, and skeleton | RGB camera | RGB image | SVM | HMDB51 | 85 |
| | | | | | UCF | 81 |
| | | | | | Hollywood2 | 74 |
| | | | | | Olympic | 76 |
| Jalal, et al., 2020 | Extract full-body human silhouette (energy features) and key points context-aware features | | RGB | Ray optimization+K-Ary tree hashing | UCF50 | 80.9 |
| | | | | | Hmdb51 | 82.1 |
| | | | | | Olympic | 90.83. |
| Liu, Liu and Chen, 2017 | Sequence-based transform | Kinect V1 | RGB+D | CNN | Northwestern- | 92.61 |
| | | | | | UCLA | 73.8 |
| | | | | | NTU RGB+D datasets | 87.21 |
| Liu, *et al*., 2019 | Skeleton posture | Kinect V2.0 | RGB+D | Posture-CNN model | 1620 pose images (including six postures) | 99.01 |

*(Contd...)*

 http://dx.doi.org/10.14500/aro.10930

Table II
*(Continued)*

| Paper | Feature | Device | Type image | Method | Dataset | Accuracy (%) |
|---|---|---|---|---|---|---|
| Rahmani, Mian and Shah, 2018 | Dense trajectories from videos+Dense trajectories from mocap sequences | - | Synthetic data | Robust non-linear knowledge transfer model | INRIA Xmas Motion Acquisition Sequences | 74.1 |
| | | | | | N-UCLA Multiview dataset | 78.1 |
| | | | | | UWA3D Multiview Activity II Dataset | 67.4 |
| Kamel, et al., 2019 | - | | RGB-D | CNN | MSRACTION3D DATASET | 94.51 |
| | | | | | UTD-MHAD DATASET | 88.14 |
| Wang and Liu, 2020 | Direction cosine method | Kinect depth sensor | RGB-D | BP neural network | | Reach more than 90 |
| Xiao, Cui and Li, 2020 | Three-level spatial pyramid feature extraction | - | RGB | Dual aggregation deep network and CXQDA distance metric | UCF50 | 62 |
| | | | | | HMDB51 | 66 |
| | | | | | Hollywood2 | 92 |
| | | | | | Olympic | 89 |
| Zhao and Obonyo, 2020 | - | Wearable Inertial Measurement Units (IMUs) sensors | - | CNN+LSTM | Datasets collected from four workers on construction sites | - |
| Zhou, et al., 2018 | Spatiotemporal information | - | RGB | Two-stream MiCT-Net | UCF101 | 94.7 |
| | | | | | HMDB51 | 70.5 |
| Santhoshkumar and Kalaiselvi Geetha, 2019 | - | - | RGB | FDCNN | (University of York) and GEMEP dataset | 95.4 |
| Cao, et al., 2017 | - | - | RGB | Greedy parsing algorithm | MPII | 79.7 |
| | | | | | COCO | 84.9 |
| Wang, et al., 2016 | Upper and lower body ratio of the human silhouette | Kinect | Depth images | LVQ neural network | - | 97 |
| Kołodziej, et al., 2019 | Statistical parameters | Smartphone, | Acceleration signals | Quadratic discriminant analysis (QDA) | - | 90–95 |
| Kim and Lee, 2020 | - | - | RGB | Proposed a lightweight stacked hourglass network | MPII | 90.8 |
| | | | | | LSP | 91.7 |
| Saini, et al., 2019 | 3D skeleton | Kinect | - | Bidirectional long short-term memory neural network (BLSTM-NN) | KARD dataset | 96.67 |
| | | | | | CAD-60 dataset | 79.58 |
| Ning, Zhang and He, 2018 | - | - | - | Stacked hourglass design and inception-ResNet module | MPII | 91.2 |
| | | | | | LSP | 93.9 |
| Lei et al. (Zhao and Chen, 2020) | Time-domain features+Frequency domain features | Inertial sensor | Sensor- data | SVM | - | 96 |
| Zhang, et al., 2017 | - | Smartphone, RFID | | A hierarchical algorithm with backward reasoning, proposal (multifusion) | - | 85.7 |
| Nandy, Saha and Chowdhury, 2020 | - | Smartphone | - | Ensemble of classifiers | - | 96 |
| Voicu, et al., 2019 | - | Smartphone | - | Neural network | - | 93 |

SVM: Support vector machine

11 joint actions.

## IV. Discussion

This review examined different techniques for recognizing body position and analyzed many papers, results, and algorithms used for each technique. In addition, we mentioned the details of the dataset that is used with each of the techniques. Despite significant advances in body location recognition, there are limitations to the techniques that make them ideal only for specific applications.

We mention and analyze the limitations and benefits in this section. The advantages of vision-based systems are that they are easy to use and do not require cooperation from those watched. Furthermore, they provide the capacity to understand dynamic systems and high-level operations (Wu, Sharma, and Blumenstein, 2017). The disadvantages of vision-based systems include the camera position, the background clutter, and limited coverage. Furthermore, there is a vast range of additional criteria, necessitating the production of


Fig. 2: The samples from dataset: (a) UCF101, RGB image dataset, (b) MSR-Action3D, depth image dataset.

Table III
The Popular Datasets of Human Body Posture Recognition. the (✓) Mark Represents Finding a Feature in the Dataset, but the (X) Mark Means it is Not Found

| Dataset name | Color | Depth | Skeleton | Samples | Classes |
|---|---|---|---|---|---|
| MSR-Action3D (Li, Zhang and Liu, 2010) | X | ✓ | ✓ | 3224 | 20 |
| UTKinect-Action (Xia, Chen and Aggarwal, 2012) | ✓ | X | ✓ | 3795 | 10 |
| writing posture dataset (WPD) (Cao, et al., 2017) | ✓ | X | ✓ | 113,400 | 15 |
| MPII (Andriluka, et al., 2014) | ✓ | X | X | 24,984 | 20 |
| Southeast University SEU (Zhao, et al., 2012) | ✓ | X | X | 24,210 | 4 |
| HMDB51 (Zhao, et al., 2012) | ✓ | X | X | 6849 | 51 |
| Hollywood2 (Marszałek, Laptev and Schmid, 2009) | ✓ | X | X | 3669 | 12 |
| Olympic (Niebles, Chen and Fei-Fei, 2010) | ✓ | X | X | 783 | 16 |
| UCF101 (Reddy and Shah, 2013) | ✓ | X | X | 13,320 | 101 |
| Northwestern-UCLA (Wang, et al., 2014) | X | ✓ | ✓ | 1494 | 10 |
| NTU RGB+D datasets (Shahroudy, et al., 2016) | X | ✓ | ✓ | 56,880 | 60 |

costly training videos (Rahmani and Bennamoun, 2017). In addition, some elements must be handcrafted to solve complex problems. As a result, the key disadvantage of these methods is that they are problem dependent, making them difficult to execute in the real world, despite their high success in action detection (Wu, Sharma, and Blumenstein, 2017). Video editing is computationally effective. The Kinect is less effective outdoors, where a certain amount of solar IR and ferromagnetic radiation can create substantial noise and even wash out the scene produced by it.

Furthermore, the Kinect consumes more energy, has a lower resolution, and is not as quickly and inexpensively available as regular cameras (Zhang, Yan, and Li, 2018). The Kinect also fails to satisfy the criterion of monitoring different individuals. All cameras, including Kinect, have the drawback of invading the subject's privacy, which has led to debates about health surveillance applications for the elderly (Huang, et al., 2019).

One advantage of acceleration-based systems is that they achieve high emotion recognition accuracy (Huang, et al., 2019). Furthermore, they have high real-time efficiency and accuracy (Wang and Liu, 2020). However, one limitation of these systems is that they are restricted to the classification activities for which they were developed (Ravi, et al., 2016). Furthermore, they can burden the subject, jeopardizing the interactive experience (Ding, et al., 2020). Sensors also have the drawback of requiring multiple data processing steps, and they can involve the invasion of the subject's personal space (Huang, et al., 2019). Furthermore, acceleration sensors cannot obtain static information, so they have difficulty identifying locations, shapes, and other objects (Huang, et al., 2019). Furthermore, this method necessitates users to wear sensors on their bodies, which may be inconvenient or cumbersome (Ren, et al., 2020). As a result, interest in wearable sensors is low, and the growth of the technology is slow (Wang and Liu, 2020). Furthermore, wearable sensors reduce user interface while increasing hardware costs (Yan, Coenen, and Zhang, 2016). Finally, since they are battery powered, they must be maintained daily to continue working (Saini, et al., 2019).

Despite its challenges, vision-based technology is often used because cameras of this type are available in many places indoors and outdoors. However, recent developments have reduced the limitations. Furthermore, sensor-based technologies have recently entered many applications and have specificity. However, their main limitations are high price, low data accuracy, and failure to diagnose static objects. Therefore, the application of sensors is limited, unlike the vision-based technology, despite its shortcomings.

## V. Conclusion and Future Work

Human body posture recognition has been extensively studied in recent years, and it plays an essential role in many applications. The methods used to recognize the poses and activities that humans perform are explored in this review paper. Vision-based techniques are discussed, as well as smartphone sensors and wearable sensors. Furthermore, it presents the most common datasets used to describe human body posture. Color or depth color cameras are used to capture data in vision-based systems. Alternately, sensors mounted on the human body while assessing the body's position through a two-dimensional or three-dimensional image, smartphone devices, and wearable sensors obtain data. Each strategy has its own set of benefits and drawbacks.

Because of their precision in the wearing phase, the sensors have a restricted application. Despite its drawbacks, vision-based technology can be advanced by researching and developing modern cameras. It is possible to use sensors on patients, the elderly, and athletes due to the lack of limitations in wearing those instruments. Classifying the data used in this technology are mainly artificial intelligence methods and deep learning. The primary advantage of deep learning is that it removes the need to extract features manually.

Furthermore, deep learning has shown reliable results. As a result, video monitoring and other activities may benefit from vision-based technologies. Deep learning is superior to other approaches to this technology, and it is possible to combine several deep learning algorithms for improved performance.

## References


Abdulhussein, A.A. and Raheem, F.A., 2020. Hand gesture recognition of static letters American sign language (ASL) using deep learning. *Engineering and Technology Journal*, 38(6A), pp.926-937.

Abedi, W.M.S., Ibraheem-Nadher, D. and Sadiq, A.T., 2020. Modified deep learning method for body postures recognition. *International Journal of Advanced Science and Technology*, 29, 3830-3841.

Andriluka, M., Pishchulin, L., Gehler, P. and Schiele, B., 2014. 2D Human Pose Estimation: New Benchmark and State of the Art Analysis. In: *Proceedings of the IEEE Computer Society Conference on Computer Vision and Pattern Recognition*. pp.3686-3693.

Ben Mabrouk, A. and Zagrouba, E., 2018. Abnormal behavior recognition for intelligent video surveillance systems: A review. *Expert Systems with Applications*, 91, pp.480-491.

Cao, Z., Simon, T., Wei, S.E. and Sheikh, Y., 2017. Realtime Multi-person 2D Pose Estimation Using Part Affinity Fields. In: *Proceedings 30th IEEE Conference on Computer Vision and Pattern Recognition, CVPR 2017*, 2017-Janua, pp.1302-1310.

Chen, Y. and Xue, Y., 2016. A Deep Learning Approach to Human Activity Recognition Based on Single Accelerometer. In: *Proceedings 2015 IEEE International Conference on Systems, Man, and Cybernetics, SMC 2015*. IEEE, pp.1488-1492.

Chen, Y., Tian, Y. and He, M., 2020. Monocular human pose estimation: A survey of deep learning-based methods. *Computer Vision and Image Understanding*, 192, p.102897.

Colleges, Gujarat Technological University, 2014. *Microsoft COCO*. Eccv, (June). Colleges, Gujarat Technological University, pp.740-755.

Dang, Q., Yin, J., Wang, B. and Zheng, W., 2019. Deep learning based 2D human pose estimation: A survey. *Tsinghua Science and Technology*, 24, pp. 663-676.

Ding, W., Hu, B., Liu, H., Wang, X. and Huang, X., 2020. Human posture recognition based on multiple features and rule learning. *International Journal of Machine Learning and Cybernetics*, 11(11), pp.2529-2540.

El Amine Elforaici, M., Chaaraoui, I., Bouachir, W., Ouakrim Y. and Mezghani, N., 2018. Posture Recognition Using an rgb-d Camera: Exploring 3d Body Modeling and Deep Learning Approaches. In: *2018 IEEE Life Sciences Conference, LSC*. IEEE, pp.69-72.

Ghafoor, K.J., Rawf, K.M., Abdulrahman, A.O. and Taher, S.H., 2021. Kurdish Dialect Recognition using 1D CNN. *Aro-the Scientific Journal of Koya University*, 9(2), pp.10-14.

Gong, W., Zhang, X., Gonzàlez, J., Sobral, A., Bouwmans, T., Tu, C. and Zahzah, E., 2016. Human pose estimation from monocular images: A comprehensive survey. *Sensors*, 16(12), p.1966.

Gouiaa, R. and Meunier, J., 2017. Learning cast shadow appearance for human posture recognition. *Pattern Recognition Letters*, 97, pp.54-60.

Gupta, A., Gupta, K., Gupta, K. and Gupta, K., 2020. A Survey on Human Activity Recognition and Classification. In: *2020 International Conference on Communication and Signal Processing* (*ICCSP*). IEEE, pp.915-919.

Hameed, F.S., Alwan, H.M. and Ateia, Q.A., 2020. Pose estimation of objects using digital image processing for pick-and-place applications of robotic arms. *Engineering and Technology Journal*, 38(5A), pp.707-718.

Hassan, M.M., Huda, S., Uddin, M.Z., Almogren, A. and Alrubaian, M., 2018. Human activity recognition from body sensor data using deep learning. *Journal of Medical Systems*, 42(6), p.99.

Hsiao, R.S., Chen, T.X., Bitew, M.A., Kao, C.H. and Li, T.Y., 2018. Sleeping posture recognition using fuzzy c-means algorithm. *BioMedical Engineering Online*, 17(S2), p.157.

Huang, X., Wang, F., Zhang, J., Hu, Z. and Jin, J., 2019. A posture recognition method based on indoor positioning technology. *Sensors*, 19(6), p.1464.

Jalal, A., Akhtar, I. and Kim, K., 2020. Human posture estimation and sustainable events classification via Pseudo-2D stick model and K-ary tree hashing. *Sustainability* (*Switzerland*), 12(23), pp.1-24.

Joo, H., Simon, T., Li, X., Liu, H., Tan, L., Gui, L., Banerjee, S., Godisart, T., Nabbe, B., Matthews, I., Kanade, T., Nobuhara, S. and Sheikh, Y., 2019. Panoptic studio: A massively multiview system for social interaction capture. *IEEE Transactions on Pattern Analysis and Machine Intelligence*, 41(1), pp.190-204.

Kale, H., Mandke, P., Mahajan, H. and Deshpande, V., 2018. Human Posture Recognition using Artificial Neural Networks. In: *Proceedings of the 8th International Advance Computing Conference, IACC 2018*. IEEE, pp.272-278.

Kamel, A., Sheng, B., Yang, P., Li, P., Ruimin, S. and Feng, D.D., 2019. Deep convolutional neural networks for human action recognition using depth maps and postures. *IEEE Transactions on Systems, Man, and Cybernetics: Systems*, 49(9), pp.1806-1819.

Kamišalić, A., Fister, I., Turkanović, M. and Karakatič, S., 2018. Sensors and functionalities of non-invasive wrist-wearable devices: A review. *Sensors* (*Switzerland*), 18(6), p.1714.

Kanazawa, A., Black, M.J., Jacobs, D.W., Malik, J., 2018. End-to-end recovery of human shape and pose. *IEEE/CVF Conference on Computer Vision and Pattern Recognition*. pp.7122-7131.

Kareem, A.A., Ali, W.H. and Jasim, M.H., 2020. Design and implementation of a wireless system to locate a user in indoor environments. *Engineering and Technology Journal*, 38(11A), pp.1640-1651.

Khokhlov, I., Reznik, L., Cappos, J. and Bhaskar, R., 2018. Design of Activity Recognition Systems with Wearable Sensors. In: *2018 IEEE Sensors Applications Symposium* (*SAS*). IEEE, pp.1-6.

Kim, S.T. and Lee, H.J., 2020. Lightweight stacked hourglass network for human pose estimation. *Applied Sciences*, 10(18), p.6497.

Kołodziej, M., Majkowski, A., Tarnowski, P., Rak, R.J., Gebert, D. and Sawicki, D., 2019. Registration and analysis of acceleration data to recognize physical activity. *Journal of Healthcare Engineering*, 2019, pp.9497151.

Li, W., Zhang, Z. and Liu, Z., 2010. Action Recognition Based on a Bag of 3D Points. In: *2010 IEEE Computer Society Conference on Computer Vision and Pattern Recognition Workshops*. IEEE, pp.9-14.

Liang, M. and Hu, Y., 2020. Application of Human Body Posture Recognition Technology in Robot Platform for Nursing Empty-Nesters. In: *2020 6th International Conference on Control, Automation and Robotics, ICCAR 2020*. IEEE, pp.91-95.

Liu, G., Lin, L., Zhou, W., Zhang, R., Yin, H., Chen, J. and Guo, H., 2019. A posture recognition method applied to smart product service. In: *Procedia CIRP*, pp.425-428.

Liu, J., Wang, Y., Liu, Y., Xiang, S. and Pan, C., 2020. 3D PostureNet: A unified framework for skeleton-based posture recognition. *Pattern Recognition Letters*,

140, pp.143-149.

Liu, M., Liu, H. and Chen, C., 2017. Enhanced skeleton visualization for view invariant human action recognition. *Pattern Recognition*, 68, pp.346-362.

Liu, Z., Zhu, J., Bu, J. and Chen, C., 2015. A survey of human pose estimation: The body parts parsing based methods. *Journal of Visual Communication and Image Representation*, 32, pp.10-19.

Lo Presti, L. and La Cascia, M., 2016. 3D skeleton-based human action classification: A survey. *Pattern Recognition*, 53, pp.130-147.

Marszałek, M., Laptev, I. and Schmid, C., 2009. *Marszałek-cvpr09-Action in Context*, pp.2929-2936.

Mehta, D., Rhodin, H., Casas, D., Fua, P., Sotnychenko, O., Xu, W. and Theobalt, C., 2018. Monocular 3D Human Pose Estimation in the Wild Using Improved CNN Supervision. In: *Proceedings 2017 International Conference on 3D Vision, 3DV 2017*, pp.506-516.

Mirza, S.F. and Al-Talabani, A.K., 2021. Efficient kinect sensor-based kurdish sign language recognition using echo system network. *ARO The Scientific Journal of Koya University*, 9(2), pp.1-9.

Mo, L., Li, F., Zhu, Y. and Huang, A., 2016. Human Physical Activity Recognition Based on Computer Vision with Deep Learning Model. In: *2016 IEEE International Instrumentation and Measurement Technology Conference Proceedings*. IEEE, pp.1-6.

Nandy, A., Saha, J. and Chowdhury, C., 2020. Novel features for intensive human activity recognition based on wearable and smartphone sensors. *Microsystem Technologies*, 26(6), pp.1889-1903.

Neili, S., Gazzah, S., El Yacoubi, M.A. and Ben Amara, N.E., 2017. Human Posture Recognition Approach Based on ConvNets and SVM Classifier. In: *Proceedings 3rd International Conference on Advanced Technologies for Signal and Image Processing, ATSIP 2017*. IEEE, pp.1-6.

Niebles, J.C., Chen, C.W. and Fei-Fei, L., 2010. Modeling temporal structure of decomposable motion segments for activity classification. *Lecture Notes in Computer Science* (*Including Subseries Lecture Notes in Artificial Intelligence and Lecture Notes in Bioinformatics*), *6312 LNCS* (*PART 2*), pp.392-405.

Ning, G., Zhang, Z. and He, Z., 2018. Knowledge-guided deep fractal neural networks for human pose estimation. *IEEE Transactions on Multimedia*, 20(5), pp.1246-1259.

Patel, P., Bhatt, B. and Patel, B., 2017. Human Body Posture Recognition a Survey. In: *2017 International Conference on Innovative Mechanisms for Industry Applications* (*ICIMIA*). IEEE, pp.473-477.

Quan, W., Woo, J., Toda, Y. and Kubota, N., 2019. Human posture recognition for estimation of human body condition. *Journal of Advanced Computational Intelligence and Intelligent Informatics*, 23(3), pp.519-527.

Rahmani, H. and Bennamoun, M., 2017. Learning action recognition model from depth and skeleton videos. In: *Proceedings of the IEEE International Conference on Computer Vision*. IEEE, pp.5833-5842.

Rahmani, H., Mian, A. and Shah, M., 2018. Learning a deep model for human action recognition from novel viewpoints. *IEEE Transactions on Pattern Analysis and Machine Intelligence*, 40(3), pp.667-681.

Ravi, D., Wong, C., Lo, B. and Yang, G.Z., 2016. Deep Learning for Human Activity Recognition: A Resource Efficient Implementation on Low-power Devices. In: *2016 IEEE 13th International Conference on Wearable and Implantable Body Sensor Networks* (*BSN*). IEEE, pp.71-76.

Rawat, W. and Wang, Z., 2017. Deep convolutional neural networks for image classification: A comprehensive review. *Neural Computation*, 29(9), pp.2352-2449.

Reddy, K.K. and Shah, M., 2013. Recognizing 50 human action categories of web videos. *Machine Vision and Applications*, 24(5), pp.971-981.

Ren, W., Ma, O., Ji, H. and Liu, X., 2020. Human posture recognition using a hybrid of fuzzy logic and machine learning approaches. *IEEE Access*, 8, pp.135628-135639.

Saini, R., Kumar, P., Kaur, B., Roy, P.P., Dogra, D.P. and Santosh, K.C., 2019. Kinect sensor-based interaction monitoring system using the BLSTM neural network in healthcare. *International Journal of Machine Learning and Cybernetics*, 10(9), pp.2529-2540.

Santhoshkumar, R. and Geetha, M.K., 2019. Deep Learning Approach for Emotion Recognition from Human Body Movements with Feedforward Deep Convolution Neural Networks. In: *Procedia Computer Science*, pp.158-165.

Sarafianos, N., Boteanu, B., Ionescu, B. and Kakadiaris, I.A., 2016. 3D human pose estimation: A review of the literature and analysis of covariates. *Computer Vision and Image Understanding*, 152, pp.1-20.

Shahroudy, A., Liu, J., Ng, T.T. and Wang, G., 2016. NTU RGB+D: A Large Scale Dataset for 3D Human Activity Analysis. In: *Proceedings of the IEEE Computer Society Conference on Computer Vision and Pattern Recognition, 2016-Decem*. pp.1010-1019.

Soomro, K., Zamir, A.R. and Shah, M., 2012. *UCF101: A Dataset of 101 Human Actions Classes from Videos in the Wild*. *arXiv*, 2012, 12120402.

Sun, W. and Wang, R., 2018. Fully convolutional networks for semantic segmentation of very high resolution remotely sensed images combined with DSM. *IEEE Geoscience and Remote Sensing Letters*, 15(3), pp.474-478.

Vecchio, A., Mulas, F. and Cola, G., 2017. Posture recognition using the interdistances between wearable devices. *IEEE Sensors Letters*, 1(4), pp.1-4.

Voicu, R.A., Dobre, C., Bajenaru, L. and Ciobanu, R.L., 2019. Human physical activity recognition using smartphone sensors. *Sensors*, 19(3), p.458.

Wan, S., Qi, L., Xu, X., Tong, C. and Gu, Z., 2020. Deep learning models for real-time human activity recognition with smartphones. *Mobile Networks and Applications*, 25(2), pp.743-755.

Wang, J. and Liu, X.H., 2020. Human Posture Recognition Method Based on Skeleton Vector with Depth Sensor. In: *IOP Conference Series: Materials Science and Engineering*, p.012035.

Wang, J., Nie, X., Xia, Y., Wu, Y. and Zhu, S.C., 2014. Cross-view Action Modeling, Learning, and Recognition. In*: Proceedings of the IEEE Computer Society Conference on Computer Vision and Pattern Recognition*, pp.2649-2656.

Wang, P., Li, W., Ogunbona, P., Wan, J. and Escalera, S., 2018. RGB-D-based human motion recognition with deep learning: A survey. *Computer Vision and Image Understanding*, 171, pp.118-139.

Wang, W.J., Chang, J.W., Haung, S.F. and Wang, R.J., 2016. Human posture recognition based on images captured by the kinect sensor. *International Journal of Advanced Robotic Systems*, 13(2), p.54.

Wu, D., Sharma, N. and Blumenstein, M., 2017. Recent Advances in Video-based Human Action Recognition Using Deep Learning: A Review. In: *2017 International Joint Conference on Neural Networks* (*IJCNN*). IEEE, pp.2865-2872.

Xia, L., Chen, C. and Aggarwal, J., 2012. *View Invariant Human Action Recognition Using Histograms of 3D Joints The University of Texas at Austin. CVPR 2012 HAU3D Workshop*, pp.20-27.

Xiao, J., Cui, X. and Li, F., 2020. Human action recognition based on convolutional neural network and spatial pyramid representation. *Journal of Visual Communication and Image Representation*, 71, p.102722.

Yan, C., Coenen, F. and Zhang, B., 2016. Driving posture recognition by convolutional neural networks. *IET Computer Vision*, 10(2), pp.103-114.

Zhang, H., Yan, X. and Li, H., 2018. Ergonomic posture recognition using 3D view-invariant features from single ordinary camera. *Automation in Construction*, 94, pp.1-10.

Zhang, H.B., Lei, Q., Zhong, B.N., Du, J.X. and Peng, J.L., 2016. A survey on human pose estimation. *Intelligent Automation and Soft Computing*, 22(3), pp.483-489.

Zhang, H.B., Zhang, Y.X., Zhong, B., Lei, Q., Yang, L., Du, J.X., Chen, D.S., 2019. A comprehensive survey of vision-based human action recognition methods. *Sensors*, 19(5), p.1005.

Zhang, J., Wu, C. and Wang, Y., 2020. Human fall detection based on body posture spatio-temporal evolution. *Sensors* (*Switzerland*), 20(3), p.946.

Zhang, S. and Callaghan, V., 2020. Real-time human posture recognition using an adaptive hybrid classifier. *International Journal of Machine Learning and Cybernetics*, 12(2), pp.489-499.

Zhang, S., McCullagh, P., Zheng, H. and Nugent, C., 2017. Situation awareness inferred from posture transition and location: Derived from smartphone and smart home sensors. *IEEE Transactions on Human-Machine Systems*, 47(6), pp.814-821.

Zhao, C.H., Zhang, B.L., He, J. and Lian, J., 2012. Recognition of driving postures by contourlet transform and random forests. *IET Intelligent Transport Systems*, 6(2), pp.161-168.

Zhao, J. and Obonyo, E., 2020. Convolutional long short-term memory model for recognizing construction workers' postures from wearable inertial measurement units. *Advanced Engineering Informatics*, 46, p.101177.

Zhao, L. and Chen, W., 2020. Detection and recognition of human body posture in motion based on sensor technology. *IEEJ Transactions on Electrical and Electronic Engineering*, 15(5), pp.766-770.

Zhao, Z.Q., Zheng, P., Xu, S.T. and Wu, X., 2019. Object detection with deep learning: A review. *IEEE Transactions on Neural Networks and Learning Systems*, 30(11), pp.3212-3232.

Zhou, E. and Zhang, H., 2020. Human action recognition toward massive-scale sport sceneries based on deep multi-model feature fusion. *Signal Processing: Image Communication*, 84, p.115802.

Zhou, Y., Sun, X., Zha, Z.J. and Zeng, W., 2018. MiCT: Mixed 3D/2D Convolutional tube for human action recognition. In: *Proceedings of the IEEE Computer Society Conference on Computer Vision and Pattern Recognition*. IEEE, pp.449-458.

# Investigating the Impact of Min-Max Data Normalization on the Regression Performance of K-Nearest Neighbor with Different Similarity Measurements

Peshawa J. Muhammad Ali

Department of Software Engineering, Faculty of Engineering, Koya University, Koya, Kurdistan Region – F.R. Iraq

***Abstract*—K-nearest neighbor (KNN) is a lazy supervised learning algorithm, which depends on computing the similarity between the target and the closest neighbor(s). On the other hand, min-max normalization has been reported as a useful method for eliminating the impact of inconsistent ranges among attributes on the efficiency of some machine learning models. The impact of min-max normalization on the performance of KNN models is still not clear, and it needs more investigation. Therefore, this research examines the impacts of the min-max normalization method on the regression performance of KNN models utilizing eight different similarity measures, which are City block, Euclidean, Chebychev, Cosine, Correlation, Hamming, Jaccard, and Mahalanobis. Five benchmark datasets have been used to test the accuracy of the KNN models with the original dataset and the normalized dataset. Mean squared error (MSE) has been utilized as a performance indicator to compare the results. It's been concluded that the impact of min-max normalization on the KNN models utilizing City block, Euclidean, Chebychev, Cosine, and Correlation depends on the nature of the dataset itself, therefore, testing models on both original and normalized datasets are recommended. The performance of KNN models utilizing Hamming, Jaccard, and Mahalanobis makes no difference by adopting min-max normalization because of their ratio nature, and dataset covariance involvement in the similarity calculations. Results showed that Mahalanobis outperformed the other seven similarity measures. This research is better than its peers in terms of reliability, and quality because it depended on testing different datasets from different application fields.**

***Index Terms*—K-nearest neighbor, Min-max, Normalization, Similarity, Mahalanobis.**

## I. Introduction

The K-nearest neighbor (KNN) has been introduced as supervised learning for the First time by Fix and Hodges in 1951 (Fix and Hodges, 1951). Then, it has been developed by Thomas Cover in 1967 (Cover and Hart, 1976). The algorithm is considered one of the oldest machine learning (ML) algorithms used for classification and regression. The algorithm depends on the similarity or the distance measures between the unknown samples and the closest items in the training set. In regression, the output of the KNN is a value that came from a previously observed output of the closest neighbor called target or from averaging the value of a group of neighbors' target values.

The number of neighbors that may contribute to determining an accurate result for unknown result samples depends on the nature and the statistical properties of the dataset. There is no specific optimize the number of the neighbor that must be considered in the process of determining the results of KNN algorithm. Therefore, examining multiple tests with different numbers of neighbors are the only right process for setting this number. Another factor that also has an impact on the efficiency of the KNN is the type of the KNN itself. KNN comes in two types, equal weight KNN, and weighted KNN. With equal weight KNN, all participating neighbors will evenly contribute to computing the result on an equal base, whereas the contribution of the participated neighbors in the weighted based KNN is changing according to the weights assigned for each neighbor, and the value of each weight could be determined based on the neighbor's distance from the target.

As mentioned before, the core of the KNN's functionality depends on the similarity measurements. There are multiple similarity measuring methods (distance metrics) that used by KNN, such as City block, Euclidean, Chebychev, Cosine, Correlation, Hamming, Jaccard, and Mahalanobis (Cha, 2007). The accuracy of some methods is very sensitive to any change in the distance scale, such as City block, Euclidean, and Chebychev, whereas other methods, such as Mahalanobis and Jaccard, do not depend on the scale of the input features, and the accuracy of the results does not change with the change of the scale. Therefore, examining the impact of the data scale on the KNN performance is another objective of this work.

Data scaling is one of the preprocessing steps that come before the training phase of any ML algorithm. The aim of the scaling step is to accelerate the training phase and to improve the efficiency of any proposed model. The scaling preprocess

ARO-The Scientific Journal of Koya University
Vol. X, No.1 (2022), Article ID: ARO.10955, 7 pages
DOI: 10.14500/aro.10955
Received: 30 March 2022; Accepted: 07 June 2022
Regular research paper: Published: 21 June 2022
Corresponding author's e-mail: peshawa.jammal@koyauniversity.org

http://dx.doi.org/10.14500/aro.10955

is only working with numerical datasets. Although there are different data scaling (data normalization) techniques such as min-max normalization, z-score, soft-max, decimal scaling, max-abs scalar, and quantile transformer, this work focuses on the min-max normalization only.

Min-max data normalization method scales the data to specific ranges such as [0,1] or [−1,1] to eliminate the domination of some of the features over others in the ML techniques using similarity measurements like KNN. Assuming that features in a dataset may come with different ranges, the similarity measures assign more weight to features with larger ranges than those with small ranges. Therefore, min-max data normalization is used to equalize the weight of these features and make them have the same effect on the decision-making process.

There is a disagreement exists in the literature on the impact of min-max data normalization on the regression performance of KNN models with different similarity measures. There is also an ambiguity about how different types of KNN with different similarity measurements may respond to the min-max data normalization. The aim of this research is to study the combined effect of min-max data normalization with these eight similarity measurements on the regression performance of KNN.

The rest of this article is structured as follows: Section 2 explains the related works to this study. Section 3 is the methodology of this research work consisting of three stages: Adopting suitable datasets from the University of California Irvine (UCI) website, implementing min-max feature normalization, range [0,1], and applying and validating KNN on both the original and the normalized datasets. Section 4 summarizes all the observed results, and Section 5 discusses the observed results. Finally, Section 6 concludes this research work.

## II. Related Works

Research works reported different results about the real impact of min-max data normalization on the performance of the KNN models. This disparity in the results is clearly seen in many articles and publications. Some studies recorded very little impact (Ambarwari, Adrian and Herdiyeni, 2020; Dadzie and Kwakye, 2021), whereas others showed a significant increase in the accuracy of the models (Ahsan, et al., 2021; Rajeswari and Thangavel, 2020). Although all mentioned articles utilized the Euclidean KNN, none of them justified the reasons behind this disproportion of the results.

In general, most of the research works that investigated the impact of data normalization were used benchmark datasets, such as the datasets of the repository dataset of the UCI (Ahsan, et al., 2021; Pires, et al., 2020; Bhardwaj, Mishra and Desikan, 2018; Dadzie and Kwakye, 2021; Jayalakshmi and Santhakumaran, 2011; Shorman, et al., 2018). This is because the research goal in those works was to determine the effects of the min-max scaling without considering the nature of the dataset application. In this work, five benchmark datasets from the UCI repository have been adopted.

The common comparison performance measure for regression models is the mean squared error (MSE) (Rajeswari and Thangavel, 2020; Singh, Verma and Thoke, 2015; Jayalakshmi and Santhakumaran, 2011; Shorman, et al., 2018; Bhardwaj, Mishra and Desikan, 2018). In addition to that, methods such as root mean square error (RMSE) (Prasetyo, et al., 2020) and the coefficient of determination (R2) (Aksu, Güzeller and Eser, 2019) can be used as well. However, this work utilizes the MSE method as a performance indicator. The mathematical expressions of the eight different similarity measurements used in this research are shown in Table I.

From the above literature review, it becomes clear that there is no strong vision available on the effects of min-max normalization on the performance of the different types of KNN algorithm. In other words, there is no clear answer to this question "What is/are the condition(s) that makes the performance of the KNN responds positively or negatively to a data scaling method (min-max normalized)?" To the best of our knowledge, there is no comprehensive study that can answer this question clearly. Therefore, the aim of this work is to answer the mentioned question clearly and precisely.

Table I
Similarity Measurements Used with KNN Model

| Similarity Metrics | Mathematical Expression | Notes |
|---|---|---|
| Cityblock | $sim(x,y)=\sum_{i=1}^{n}\lvert x_i-y_i\rvert$ | |
| Euclidean | $sim(x,y)=\sqrt{\sum_{i=1}^{n}(x_i-y_i)^2}$ | |
| Chebychev | $sim\,(x,y)=max_i\,\{\lvert x_i-y_i\rvert\}$ | |
| Cosine | $sim(x,y)=1-\frac{x.y^t}{\sqrt{(x.x^t).(y.y^t)}}$ | $x^t$ and $y^t$ are transpose vectors of the vectors $x$ and $y$. The dot (.) represents dot product. |
| Correlation | $sim(x,y)=1-\frac{(x-\bar{x}).(y-\bar{x})^t}{\sqrt{(x-\bar{x}).(x-\bar{x})^t}\sqrt{(y-\bar{y}).(y-\bar{y})^t}}$ | $\bar{x}=\frac{1}{n}\sum_{i=1}^{n}x_i$ <br> $\bar{y}=\frac{1}{n}\sum_{i=1}^{n}y_i$ |
| Hamming | $sim(x,y)=\frac{\#(x_i\neq y_i)}{n}$ | # is the counting number |
| Jaccard | $sim(x,y)=\frac{\#[(x_i\neq y_i)\cap((x_i\neq 0)\cup(y_i\neq 0))]}{\#[(x_i\neq 0)\cup(y_i\neq 0)]}$ | # is the counting number |
| Mahalanobis | $sim(x,y)=\sqrt{(x-y)C^{-1}(x-y)^t}$ | $C^{-1}$ is the inverse covariance matrix |

$x$ and $y$ are two different records (vectors) that have the same number of attributes $n$, and $sim\,(x, y)$ is the similarity measure between them. $x_i$ and $y_i$ are feature values belonging to the record $x$ and $y$

## III. Methodology

The main aim of this work is to test the efficiency of the KNN algorithm against the min-max data normalization method. To achieve that, KNN has been operated using eight different similarity measurement methods (City block, Euclidean, Chebychev, Cosine, Correlation, Hamming, Jaccard, and Mahalanobis). Through each operation, five benchmark datasets have been fed separately to a regression-based KNN algorithm. For every benchmarked dataset, the accuracy of the KNN will be examined against the scaled and non-scaled datasets. The methodology can be summarized as follows:

- Step 1: Adopting suitable datasets from the UCI website,
- Step 2: Implementing min-max feature normalization, range [0,1],
- Step 3: Applying and validating KNN on both the original and the normalized datasets.
- Step 4: Comparing results and making conclusions.

Fig. 1 explains the methodology of the research work.

### *A. Step 1: The UCI Datasets*

Five different benchmark datasets were downloaded from the ML repository website of the UCI (Dua and Graff, 2019). The reason behind selecting these datasets is the existing variation in the ranges of records among all attributes. Some of the datasets have big differences in their ranges like in the airfoil self-noise dataset (Table II) or very similar ranges like in power plant dataset (Table III). Such a variation is expected to have a role in explaining the impact of min-max normalization on the regression performance of the KNN algorithm with different similarity measurements. The datasets belong to the real applications of physics, life sciences, engineering, and business (Table IV). The dataset's statistical properties are shown in Tables II, III, V-VII.

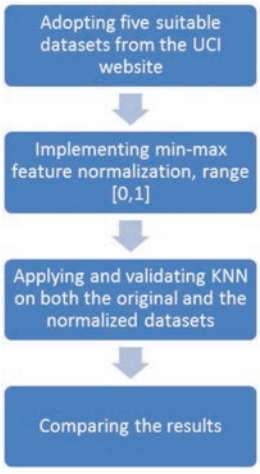


Fig. 1. The methodology of the research work.

Table II
Statistical Properties of the Airfoil Self-noise Dataset (Brooks, Pope and Marcolini, 1989)

| Feature | Max. value | Min. value | Range | Mean | Standard deviation |
|---|---|---|---|---|---|
| F1 | 20,000 | 200 | 19,800 | 2886.380572 | 3152.573137 |
| F2 | 22.2 | 0 | 22.2 | 6.782302063 | 5.918128125 |
| F3 | 0.3048 | 0.0254 | 0.2794 | 0.136548237 | 0.093540728 |
| F4 | 71.3 | 31.7 | 39.6 | 50.86074518 | 15.5727844 |
| F5 | 0.0584113 | 0.000400682 | 0.058010618 | 0.01113988 | 0.013150234 |
| Target | 140.987 | 103.38 | 37.607 | 124.8359428 | 6.898656622 |

### *B. Step 2: Implementing Min-max Feature Normalization, Range [0,1]*

As shown in Equation (1), a normalized data sample *x'* could be obtained from the original data sample *x*. For an attribute, it is mostly dependent on instances with the maximum and minimum values in the same attribute. In this normalization method, the original data sample component values will be transformed to [0,1] range.

$$x' = [(\frac{x - oldMin}{oldMax - oldMin}) * (newMax - newMin)] + newMin \quad (1)$$

Where *x'* is the normalized data sample, *x* is the original data sample, *oldMin* is the minimum data among any attribute of the original dataset, *oldMax* is the maximum data among any attribute of the original dataset, *newMin* is the minimum of the normalized dataset, and *newMax* is the maximum of the normalized dataset.

### *C. Step 3: Applying and Validating KNN on the Datasets*

In this work, eight similarity measurements (City block, Euclidean, Chebychev, Cosine, Correlation, Hamming, Jaccard, and Mahalanobis) were adopted with the KNN algorithm as a regression method. For each similarity measure, 100 tests were conducted on the both of the original and the normalized datasets, with a total number of 1600 tests. The target of applying all tests is to determine the impact of min-max data normalization on the regression performance of KNN by comparing the MSE results observed from the original dataset and the normalized versions. The reason for adopting the eight different similarity measures of KNN is their diversity in dealing with the datasets and their different methodology in determining the nearest neighbors. In all the tests, MSE is computed as a performance measure and 10-fold as a validation technique.

Two types of KNN models were adopted, equal weight KNN and weighted KNN. For each of the type, until 10 neighbors were considered. The tests were adopted on the five datasets for both original and the normalized data. The total number of tests was 1600 tests, as follows: Eight similarity measures, two types of models (weighted and equal weight), until 10 neighbors, two cases raw data and normalized data, for each of the five datasets. The total is ($8 \times 2 \times 10 \times 2 \times 5 = 1600$ tests).

Table III
Statistical Properties of the Combined Cycle Power Plant Dataset (Tüfekci, 2014)

| Feature | Max. value | Min. value | Range | Mean | Standard deviation |
|---|---|---|---|---|---|
| F1 | 37.11 | 1.81 | 35.3 | 19.65123119 | 7.45247323 |
| F2 | 81.56 | 25.36 | 56.2 | 54.30580372 | 12.707893 |
| F3 | 1033.3 | 992.89 | 40.41 | 1013.259078 | 5.938783706 |
| F4 | 100.16 | 25.56 | 74.6 | 73.30897784 | 14.60026876 |
| Target | 495.76 | 420.26 | 75.5 | 454.3650094 | 17.066995 |

 http://dx.doi.org/10.14500/aro.10955

Table IV
Datasets Properties

| Dataset | Number of features | Type of features | Number of instances | Supervised learning | Application |
|---|---|---|---|---|---|
| Airfoil self-noise dataset (Brooks, Pope and Marcolini, 1989) | 5 | Real | 1503 | Regression | Physics |
| Physicochemical properties of protein tertiary structure dataset (Rana, 2013) | 9 | Real | 9146 | Regression | Life sciences |
| Combined cycle power plant dataset (Tüfekci, 2014) | 4 | Real | 9568 | Regression | Energy |
| Concrete compressive strength dataset (Yeh, 1998) | 8 | Real | 1030 | Regression | Civil engineering |
| Real estate valuation dataset (Yeh and Hsu 2018) | 6 | Real | 414 | Regression | Business |

Table V
Statistical Properties of the Physicochemical Properties of Protein Tertiary Structure Dataset (Rana, 2013)

| Feature | Max. value | Min. value | Range | Mean | Standard deviation |
|---|---|---|---|---|---|
| F1 | 32,240.2 | 2783.15 | 29,457.05 | 9873.68162 | 4011.808135 |
| F2 | 11,787.1 | 403.5 | 11,383.6 | 3016.435929 | 1450.041879 |
| F3 | 0.56848 | 0.09362 | 0.47486 | 0.302155567 | 0.062784658 |
| F4 | 343.239 | 10.6891 | 332.5499 | 103.4039974 | 54.9395949 |
| F5 | 4,467,324.7 | 374,315.5155 | 4,093,009.223 | 1,369,092.965 | 558385.2823 |
| F6 | 470.897 | 33.6462 | 437.2508 | 145.5447009 | 69.30473494 |
| F7 | 83,153.57 | 1108.9 | 82,044.67 | 3987.14593 | 1880.513854 |
| F8 | 337 | 0 | 337 | 70.04286027 | 56.50548747 |
| F9 | 47.4559 | 15.5049 | 31.951 | 34.48790348 | 5.930509868 |
| Target | 20.981 | 0 | 20.981 | 7.833154384 | 6.120956974 |

Table VI
Statistical Properties of the Concrete Compressive Strength Dataset (Yeh, 1998)

| Feature | Max. value | Min. value | Range | Mean | Standard deviation |
|---|---|---|---|---|---|
| F1 | 540 | 102 | 438 | 281.1656311 | 104.5071416 |
| F2 | 359.4 | 0 | 359.4 | 73.89548544 | 86.27910364 |
| F3 | 200.1 | 0 | 200.1 | 54.18713592 | 63.99646938 |
| F4 | 247 | 121.75 | 125.25 | 181.5663592 | 21.35556707 |
| F5 | 32.2 | 0 | 32.2 | 6.20311165 | 5.973491651 |
| F6 | 1145 | 801 | 344 | 972.9185922 | 77.75381809 |
| F7 | 992.6 | 594 | 398.6 | 773.5788835 | 80.1754274 |
| F8 | 365 | 1 | 364 | 45.66213592 | 63.16991158 |
| Target | 82.599225 | 2.331807832 | 80.26741697 | 35.81783583 | 16.70567917 |

Table VII
Statistical Properties of the Real Estate Vluation Dataset (Yeh and Hsu, 2018)

| Feature | Max. value | Min. value | Range | Mean | Standard deviation |
|---|---|---|---|---|---|
| F1 | 2013.5833 | 2012.666667 | 0.9166666 | 2013.148953 | 0.281995327 |
| F2 | 43.8 | 0 | 43.8 | 17.71256039 | 11.39248453 |
| F3 | 6488.021 | 23.38284 | 6464.63816 | 1083.885689 | 1262.109595 |
| F4 | 10 | 0 | 10 | 4.094202899 | 2.945561806 |
| F5 | 25.01459 | 24.93207 | 0.08252 | 24.96903007 | 0.012410197 |
| F6 | 121.56627 | 121.47353 | 0.09274 | 121.5333611 | 0.015347183 |
| Target | 117.5 | 7.6 | 109.9 | 37.98019324 | 13.6064877 |

Because our focus in this research work is on variance in the results happening by adopting different similarity measures, therefore, the effect of number of the neighbors (k) did not get too much attention. Instead, the minimum MSE among all of the adopted experiments in each of the similarity measures is observed to be used for the comparison purposes. Determining the effect of number of neighbors (k) on the performance of the KNN is not in the scope of this research. It is noticed that each one of the datasets is responded differently to the increase in the number of neighbors until 10 neighbors, this is because the variance in the nature of the datasets and their statistical properties.

## IV. Results

As mentioned previously, the performance indicator that utilized by this work for checking the efficiency of the proposed KNN is MSE. Throughout the experimental tests, eight models of KNN have been tested each model uses a specific type of similarity measurements. Each model of KNN has been trained and tested with five benchmarked datasets. For each dataset, the efficiency of the proposed KNN was computed in two situations; when the KNN is trained with the original dataset, and second, when the KNN is trained with normalized dataset. All testes were passed through MSE checking. As a result, the overall tests that have been conducted by this work are 1600 tests.

The minimum MSE results of KNN models using different similarity measurements on the five datasets are shown in Table VIII, Figs. 2-6. Each number of the MSE results shown in the Table VIII is the minimum of 20 tests, in other words, 10 tests including until 10 neighbors, and this done for the two cases weighted and equal weight ($10 \times 2 = 20$). Minimum MSE means the best result among all the 20 tests.

## V. Discussion

The MSE results that obtained from five types of the KNN (City block, Euclidean, Chebychev, Cosine, and Correlation) that trained and tested with two datasets (airfoil self-noise and physicochemical) showed a significant improvement in the KNN's efficiency, look at Figs. 2 and 3. However, no significant improvement obtained when the same type of KNN is trained with power plant dataset, Fig. 4. On the other side, the efficiency of the mentioned type of the KNN has been degraded significantly when the KNN trained and tested with concrete strength and house valuation datasets, Figs. 5 and 6. It is clearly observed that performances of three types of the KNN (Hamming, Jaccard, and Mahalanobis) have not been changed. The disparity behavior of the KNN types against scaling and normalizing the training dataset is going back to the mathematical process or concept that each similarity measurement method has following whereas they do data processing. The five similarity measures (City block, Euclidean, Chebychev, Cosine, and Correlation) are sensitive

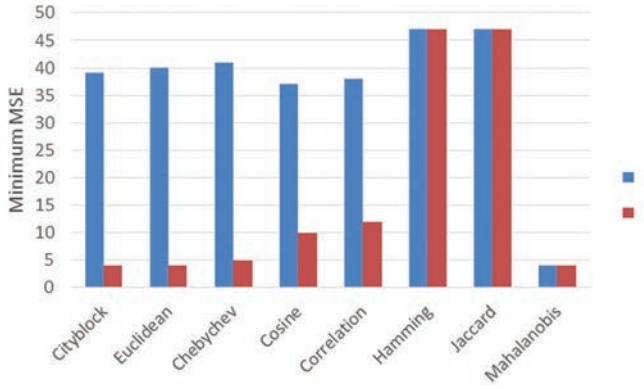


Fig. 2. Minimum MSE values of the KNN models with airfoil self-noise dataset using different similarity measurements (original vs. normalized).

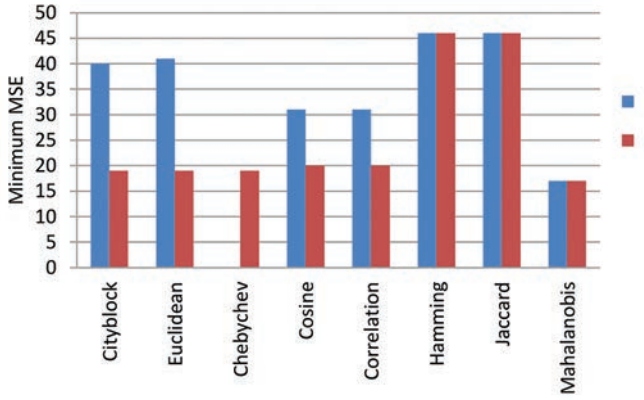


Fig. 3. Minimum MSE values of the KNN models with physicochemical dataset using different similarity measurements (original vs. normalized).

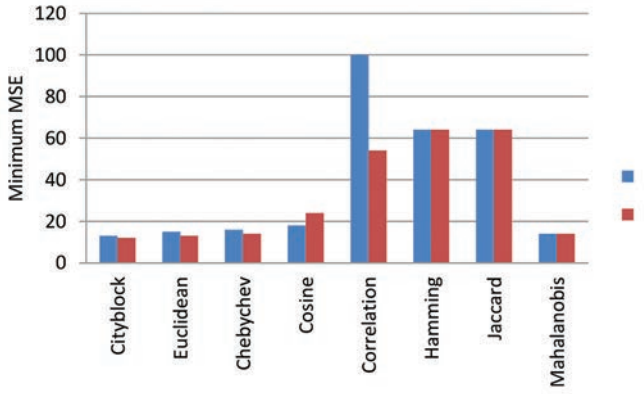


Fig. 4. Minimum MSE values of the KNN models with power plant dataset using different similarity measurements (original vs. normalized).

to the differences exist in the feature ranges, whereas the other three measurements (Hamming, Jaccard, and Mahalanobis) are not sensitive for difference in feature ranges. Hamming and Jaccard are ratio-based similarity measures that cannot be affected by min-max normalization; therefore, their results remained unchanged in all the five datasets, Figs. 2-6. Mahalanobis similarity measurement involves the covariance of the training dataset in the calculations of similarity, which eliminates the effect of min-max normalization.

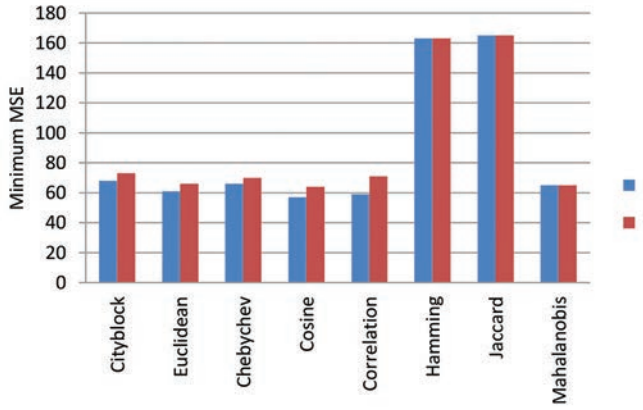


Fig. 5. Minimum MSE values of the KNN models with concrete strength dataset using different similarity measurements (original vs. normalized).

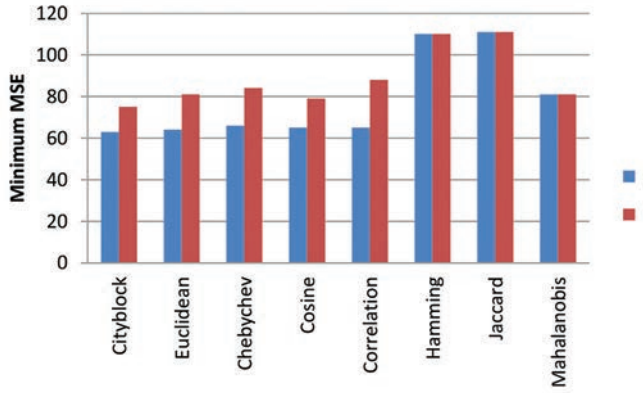


Fig. 6. Minimum MSE values of the KNN models with real estate valuation dataset using different similarity measurements (original vs. normalized).

It is noticeable that the impact of the min-max normalization for the five similarity measures (City block, Euclidean, Chebychev, Cosine, and Correlation) is not always positive, it depends on the nature of the dataset and the differences in the range of the features. An improvement in the results of airfoil self-noise and psychochemical datasets is observed, no significant impact on the results of power plant dataset is observed, and a degradation impact on the results of concrete strength and house valuation datasets is observed. This proves that these measurements are sensitive to the nature of the dataset, more precisely to the differences in the feature ranges. In addition, when the dataset has a homogeneous feature range, it will not be affected by any of the similarity measurements like in the power plant dataset, Tables III, VIII, and Fig. 4. This is also another proof that distance-based metrics of KNN are very sensitive to the differences in the feature ranges.

KNN with Mahalanobis measure provided best results among all the five datasets that have been tested in this research work. Same results observed for the original and the normalized datasets (Table VIII), also, Figs. 2-6.

Comparing the results observed in this research work with the results collected from literatures showed that this

 http://dx.doi.org/10.14500/aro.10955

Table VIII
Minimum MSE Values of the KNN Models Using Different Similarity Measurements (original vs. Normalized)

| No. | KNN models using different similarity measurements | Airfoil self-noise dataset | | Physicochemical dataset | | Power plant dataset | | Concrete strength dataset | | Real estate valuation dataset | |
|---|---|---|---|---|---|---|---|---|---|---|---|
| | | Orig. | Norm | Orig. | Norm | Orig. | Norm | Orig. | Norm | Orig. | Norm |
| 1 | City block | 39 | 4 | 40 | 19 | 13 | 12 | 68 | 73 | 63 | 75 |
| 2 | Euclidean | 40 | 4 | 41 | 19 | 15 | 13 | 61 | 66 | 64 | 81 |
| 3 | Chebychev | 41 | 5 | 42 | 19 | 16 | 14 | 66 | 70 | 66 | 84 |
| 4 | Cosine | 37 | 10 | 31 | 20 | 18 | 24 | 57 | 64 | 65 | 79 |
| 5 | Correlation | 38 | 12 | 31 | 20 | 100 | 54 | 59 | 71 | 65 | 88 |
| 6 | Hamming | 47 | 47 | 46 | 46 | 64 | 64 | 163 | 163 | 110 | 110 |
| 7 | Jaccard | 47 | 47 | 46 | 46 | 64 | 64 | 165 | 165 | 111 | 111 |
| 8 | Mahalanobis | 4 | 4 | 17 | 17 | 14 | 14 | 65 | 65 | 81 | 81 |

Table IX
Comparing the Reliability of this Research with other Previous Literatures

| No. | Research work | Performance of KNN model | Similarity measurement (distance metric) | Number of datasets used | Type of application of datasets |
|---|---|---|---|---|---|
| 1 | Dadzie and Kwakye, 2021 | No significant improvement observed | Not mentioned – probably Euclidean | 1 | 1 |
| 2 | Ambarwari, Adrian and Herdiyeni, 2020 | No significant improvement observed | Not mentioned – probably Euclidean | 1 | 1 |
| 3 | Ahsan, *et al*., 2021 | Improved | Not mentioned – probably Euclidean | 1 | 1 |
| 4 | Rajeswari and Thangavel, 2020 | Improved | Not mentioned – probably Euclidean | 5 | 1 |
| 5 | This research work | Depends on the type of the similarity measure | Eight types of similarity measures are used | 5 | 5 |

research work implemented a better research methodology and analysis, also, the results are more precise and accurate (Table IX). The previous literatures tested the KNN only with Euclidean distance method without considering other similarity measurements, whereas this research analyzed the KNN model results of each of the similarity measurements individually, without generalizing the results. Results showed that some of the KNN models could not respond to the min-max normalization. In some cases, a performance degradation recorded, which has not been mentioned in any of the previous studies. Furthermore, most of the previous literatures depended on testing only one dataset or in best cases depended on using different datasets of one application like in Rajeswari and Thangavel, 2020. This research work depended on five datasets belongs to five different real applications and different in the number of attributes. Therefore, the conclusions of this research are considered more reliable.

The KNN models utilizing Hamming, Jaccard, and Mahalanobis are not responsive to min-max data normalization but may respond positively with other normalization techniques which lay outside the scope of this research work such as z-score, soft-max, decimal-scaling, max-abs-scalar, robust scalar, and quantile transformer.

## VI. Conclusion

It has been concluded from the experiments that min-max normalization may cause performance degradation to the KNN models utilizing similarity measure (City block, Euclidean, Chebychev, Cosine, and Correlation). Therefore, testing datasets with and without min-max data normalization are recommended before considering their results. Attaching min-max with KNN models utilizing (Hamming, Jaccard, and Mahalanobis) is not recommended, because it has no effect on the performance of these models.

The possible degradation impact of using min-max data normalization on the KNN models utilizing similarity measurements (City block, Euclidean, Chebychev, Cosine, and Correlation) return to eliminating the natural domination of one of the attributes by the min-max normalization, and this leads to performance degradation like in the two datasets; concrete strength and house valuation. Therefore, it is better to test the KNN model with both the original dataset and the normalized dataset before deciding if the min-max data normalization is useful or not.

It makes no sense to use min-max normalization with KNN models utilizing (Hamming, Jaccard, and Mahalanobis), because they use the common variance of the dataset in the similarity calculations.

Furthermore, it is not necessary to use min-max data normalization with homogeneous datasets whatever the similarity measurement is, like with power plant dataset.

## References

Ahsan, M.M., Mahmud, M.A.P, Saha, P.K., Gupta, K.D. and Siddique, Z., 2021. Effect of data scaling methods on machine learning algorithms and model performance. *Technologies*, 9, p.52.

Aksu, G., Güzeller, C.O. and Eser, M.T., 2019. The effect of the normalization method used in different sample sizes on the success of artificial neural network model. *International Journal of Assessment Tools in Education*, 6(2), pp.170-192.

Ambarwari, A., Adrian, Q.J. and Herdiyeni, Y., 2020. Analysis of the effect of data scaling on the performance of the machine learning algorithm for plant identification. *Jurnal RESTI (Rekayasa Sistem dan Teknologi Informasi)*, 4(1), pp.117-122.

Bhardwaj, C.A., Mishra, M. and Desikan, K., 2018. *Dynamic Feature Scaling for K-Nearest Neighbor Algorithm*. Available from: https://www.arxiv.org/ftp/arxiv/papers/1811/1811.05062.pdf [Last accessed on 2022 Feb 01].

Brooks, T.F., Pope, D.S. and Marcolini, M.A., 1989. *Airfoil Self-noise and Prediction (NASA Reference Publication). Technical Report 1218*. National Aeronautics and Space Administration, United States.

Cha, S.H., 2007. Comprehensive survey on distance/similarity measures between probability density functions. *International Journal of Mathematical Models and Methods in Applied Sciences*, 4(1), pp.300-307.

Cover, T. and Hart, P., 1976. Nearest neighbor pattern classification. *IEEE Transactions on Information Theory*, 13(1), pp.21-27.

Dadzie, E. and Kwakye, K., 2021. *Developing a Machine Learning Algorithm-Based Classification Models for the Detection of High-Energy Gamma Particles*. Available from: https://www.hal.archives-ouvertes.fr/hal-03425661 [Last accessed on 2022 Feb 01].

Dua, D. and Graff, C., 2019. *UCI Machine Learning Repository*. University of California, School of Information and Computer Science, Irvine, CA, p.27. Available from: http://www.archive.ics.uci.edu/ml [Last accessed on 2022 Feb 01].

Fix, E. and Hodges, J.L., 1951. *Discriminatory Analysis, Nonparametric Discrimination: Consistency Properties*. Technical Report 4, USAF School of Aviation Medicine, Randolph Field, United States.

Jayalakshmi, T. and Santhakumaran, A., 2011. Statistical normalization and back propagationfor classification. *International Journal of Computer Theory and Engineering*, 3, pp.89-93.

Pires, I.M., Hussain, F., Garcia, N.M., Lamesk, P. and Zdravevski, E., 2020. Homogeneous data normalization and deep learning: A case study in human activity classification. *Future Internet*, 12, pp.1-14.

Prasetyo, J., Setiawan, N.A. and Adji, T.B., 2020. Improving normalization method of higher-order neural network in the forecasting of oil production. *E3S Web of Conferences*, 200, p.02016.

Rajeswari, D. and Thangavel, K., 2020. The performance of data normalization techniques on heart disease datasets. *International Journal of Advanced Research in Engineering and Technology*, 11, pp.2350-2357.

Rana, P.S., 2013. *Physicochemical Properties of Protein Tertiary Structure Data Set. UCI Machine Learning Repository*. Available from: https://www.archive.ics.uci.edu/ml/datasets/Physicochemical+Properties+of+Protein+Tertiary+Structure

Shorman, A.R.A., Faris, H., Castillo, P.A., Merelo, J.J. and Al-Madi, N., 2018. The influence of input data standardization methods on the prediction accuracy of genetic programming generated classifiers. In: *Proceedings of the 10th International Joint Conference on Computational Intelligence*. SciTePress, Portugal, pp.79-85.

Singh, B.K., Verma, K. and Thoke, A.S., 2015. Investigations on Impact of Feature Normalization Techniques on Classifier's Performance in Breast Tumor Classification. *International Journal of Computer Applications*, 116(19), pp.975-8887.

Tüfekci, P., 2014. Prediction of full load electrical power output of a base load operated combined cycle power plant using machine learning methods. *International Journal of Electrical Power and Energy Systems*, 60, pp.126-140.

Yeh, I.C. and Hsu, T.K., 2018. Building real estate valuation models with comparative approach through case-based reasoning. *Applied Soft Computing*, 65, pp.260-271.

Yeh, I.C., 1998. Modeling of strength of high-performance concrete using artificial neural networks. *Cement and Concrete Research*, 28(12), pp.1797-1808.

http://dx.doi.org/10.14500/aro.10946

# Effect of Static Magnetic Field on Bone Marrow Cellular Density

Bestoon T. Mustafa[1], Sardar P. Yaba[2] and Asaad H. Ismail[2]

[1]Department of Computer engineering, Faculty of Engineering, Tishk International University- Erbil, Kurdistan Region – F.R. Iraq

[2]Department of Physics, College of Education, Salahaddin University-Erbil, Kurdistan Region – F.R. Iraq

***Abstract*—This study was undertaken to investigate the influence of static magnetic field (SMF) on bone marrow cellular density (BMCD) variation proportionally to bone trabeculae. Female albino Wistar rats exposed with 2.4 ± 0.2 millitesla for 1–4 weeks duration continuously versus 1 h, 2 h, 6 h, and 8 h/day. Trephine biopsy of femurs bone was examined under optical microscope. Data analyzed with ImageJ software. Results showed that short time exposure per day did not enhance the BMCD compare to high exposure period/day. Six hours/day exposure during 1 week increased the marrow cellular density (hypercellularity) significantly ($P \leq 0.05$) compares to bone trabeculae. Contrarily, 8 h/day exposure reduced the BMCD slightly and significantly (hypocellularity, about 50% reduction) due to 1 week and 4 weeks exposure duration, respectively. The SMF has associated bone marrow cellularity tendency of rat's femur.**

***Index Terms*—**Bone marrow, Optical microscope, Static magnetic field, Trephine biopsy

## I. Introduction

Bone marrow examination can be aspiration or biopsy depending on clinical condition (Lee, et al., 2008). Bone marrow specimen can provide a complementary evaluation of hematology-related diseases such as anemia. Bone marrow trephine biopsies (BMTs) are used to diagnose pathological diseases such as hematopoietic disorder, cancers, and infections (Yong, 1992). The procedure of bone marrow biopsy in human can be uncomfortable and rarely hemorrhage or excessive bleeding associated. Therefore, the obtained biopsy information is outstanding to make the final clinical decision (Pedersen, et al., 1993). Bone marrow examination is mostly asked by a specialist since cytometric and microscope examinations of peripheral blood require further investigation.

The effect of pulsed magnetic field (PMF) and static magnetic field (SMF) on biological system is still under investigation (Pirkhider Yaba and Ismail, 2019). Researches have been conducted to investigate the influence of magnetic field on hematology *in vitro* and *in vivo* (Vergallo and Dini, 2018; Mustafa, Yab and Ismail, 2020d). Previously, the influence of PMF on main blood cells was examined. For instance, exposure with 0.97 millitesla (mT) during 50 and 100 days (Cakir, et al., 2009), 5 mT during 1–4 weeks, 3 μT during 15–120 days (Cetin, Bilgili and Eraslan, 2006), and 0.5 and 1.5 mT for 5 selective days (Ciejka, et al., 2011) altered blood parameters in peripheral blood. Regarding SMF exposure, 128 mT:1 h/day for 5 days (Amara, et al., 2006), 10 days (Sihem, et al., 2006), 13 days (Chater, et al., 2006), and 16 mT during 28 days (Djordjevich, et al., 2012) changed peripheral blood cells counts significantly. Since blood cells are originated from bone marrow in animals, the effect of SMF on bone marrow cellular density (BMCD) requires an investigation.

A few studies demonstrated the bone marrow activity-related magnetic field. Human mesenchymal stem cells (HMSCs) metabolism and growth were inhabited under the influence of 20 mT (50 Hz) during 23 days exposure (Yan, et al., 2010). SMF exposure (15 mT) for 5 h exhibited no effect on rats bone marrow stem cells (Sarvestani, et al., 2010). Femurs bone formation was studied under the influence of SMF (Yan, Tomita and Ikada, 1998). Bone calcium content and bone mineral density have increased significantly after 12 weeks exposure. Moderate SMF (3, 15, and 50 mT) effect on biophysical stimulator of osteoblastic differentiation and proliferation studied in human bone marrow (Kim, et al., 2015). Results revealed an increase of calcium release, proliferation, ALP activity, and mineralized nodule formation. Chondrogenic differentiation in human BMSC was stimulated with 0.4 T SMF exposure during 14 days (Amin, et al., 2014). The rate of BMSC viability and proliferation of rats has decreased under the influence of 15 mT SMF (Jouni, Abdolmaleki and Movahedin, 2013). The effect of SMF on BMCD and bone trabeculae density has not been studied previously using trephine biopsy. Here, we investigate the effect of 2.4 mT SMF on BMCD variations in rats' femurs.

ARO-The Scientific Journal of Koya University
Vol. X, No.1 (2022), Article ID: ARO.10946, 6 pages
DOI: 10.14500/aro.10946
Received: 28 February 2022; Accepted: 04 June 2022
Regular research paper: Published: 21 June 2022
Corresponding author's e-mail: bestoon.taha@tiu.edu.iq

## II. Procedure

### A. Housing Animals

In this study, 80 female albino Wistar rats weigh 190 ± 10 g participated and divided into four main groups (Groups 1–4). Each main group of 20 rats was split into five subgroups (A, B, C, D, and E), subgroups of four rats, kept in a plastic cage having about 40 cm of length. The subgroups "A" considered as the control groups and "B–E" exposed with SMF for 1–4 weeks, respectively. The animal house provided within biology department/Salahaddin University-Erbil, Kurdistan Region-Iraq. The standard living atmosphere was 12:12 h darkness/light, temperature of 22 ± 2°C. Rats were housed in bedded plastic cages and received a standard rat chow and drink (tap water).

### B. Experimental Design

To generate SMF, a set-up designed with 6 Helmholtz coils connected in series, Fig. 1. Copper wires connected the coils and a 20 V/12 Amp-DC power supply fed current to the set-up. A digital Teslameter measured the generated SMF. A highly stable and uniform SMF of 2.4 ± 0.2 mT generated in a wide area between the two ends of the set-up. Temperature and magnetic field stability observed and calibrated against operating duration. The set-up was free of sound, vibration and temperature increase during exposure operation (Mustafa, Yab and Ismail, 2020a; Mustafa, Yab and Ismail, 2020b).

### C. Exposure Method

The four main groups of 1–4 exposed to the SMF for a period of 1 h/day, 2 h/day, 6 h/day, and 8 h/day, respectively. In addition, from each main group, subgroups of B, C, D, and E exposed for 1–4 weeks duration, respectively. SMF (2.4 ± 0.2 mT) exposure was applied 7 days a week, between 8:00 AM and 4:00 PM. Control groups maintained at the same room (3 meters away from exposure source) where other groups of rats exposed to SMF.

### D. Bone Collection

Rats were anesthetized with a mixture of xylazine and ketamine hydrochloride. Next, they sacrificed to collect femur bone. The left side femurs was collected from each rat with a blade and cleaned. They kept in a 10% neutral-buffered formalin and taken to perform trephine biopsy (BMT) examination.

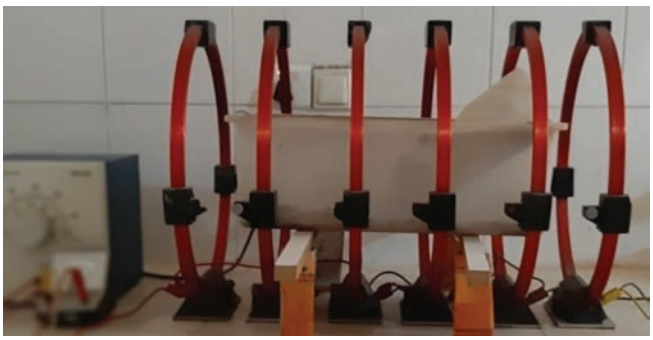

**Fig. 1.** Coil set-up. Six similar coils were used to generate a uniform static magnetic field. The coils were originally bought from PHYWE. Each coil consists of 154 turns and a radius of 20 cm. The length of the set-up was 70 cm.

### E. Bone Marrow Biopsy and Histological Slide Preparation

The methodology of BMT is explained by John D. Bancroft (Suvarna, Layton and Bancroft, 2018). In pathology laboratory, the tissue processing of the bone marrow started as the specimens fixed in formalin and 10% acid hydrochloride for 10 h. Afterward, they inserted into formalin for 14 h. In decalcification process, the specimen placed into ethanol (96%) for 4 h. Later, the ethanol was replaced by xylol 100% for 2 h. Next, the specimen was embedded in paraffin wax overnight. During tissue sectioning process, the paraffin wax blocks were cut with 1–5 μm thickness. The sectioned specimen stained with hematoxylin and eosin, to provide excellent cytomorphology. They were deparaffinized in xylene for 10 min and rosined in distilled water (DW) for 1 min. Then, the samples left in hematoxylin for 40 min, ethanol 5 min, and finally eosin for 10 min. The slides were mounted and monitored by optical microscope device, power of 400× and 600× magnifications.

### F. Data Quantification and Analyses

ImageJ software was used to analyze the microscopic images quantitatively. Particles area were determined of a minimum 10 pixels and larger. The original microscopic images converted and filtered with color threshold with a dark background (Figs. 2 and 3). Manual manipulation used to refine the converted images and qualifying trabeculae networks and the bone marrow distribution. Desired sections of trabeculae bones examined separately. Student's t-test used to determine the statistical significance of variation.

## III. Results of ImageJ analysis

Quantification data of ImageJ is compared with a direct microscopic observation. The hypercellular and hypocellular cellularity of bone marrow were examined in portion of bone trabeculae. Table 1 shows the SMF effect on bone marrow cellularity due to 1 h/day, 2 h/day, 6 h/day, and 8 h/day exposure. Analyzed microscopic images are illustrated in Figs. 2 and 3. Accordingly, the SMF influenced the existence of bone marrow between trabecular networks at high exposure time per day (6 h and 8 h). Eight hours exposure per day during 1 week reduced the BM cellularity slightly. However, 4 weeks exposure decreased BMCD significantly ($P \leq 0.05$). Two weeks and 3 weeks exposure did not alter the bone marrow distribution. The 6 h/day exposure during 1 week declined the density of bone marrow significantly. Other exposure durations did not stimulate the marrow cellularity of the femurs bone.

Trabeculae bone to bone marrow ratio variation is analyzed. Microscopic images were taken of normal and variant portions and examined directly (with eyes) and indirectly using ImageJ software. Decision was made

http://dx.doi.org/10.14500/aro.10946

Table I
Cellular Tendency Response Versus 2.4 mT

| 1 h/day exposure | Cellular effect | 2 h/day exposure | Cellular effect | 6 h/day exposure | Cellular effect | 8 h/day exposure | Cellular effect |
|---|---|---|---|---|---|---|---|
| Control | Normal | Control | Normal | Control | Normal | Control | Normal |
| 1 week | Normal | 1 week | Normal | 1 week | Significant increase ($P \leq 0.05$) | 1 week | Decrease insignificantly |
| 2 weeks | Normal | 2 weeks | Normal | 2 weeks | Normal | 2 weeks | Normal |
| 3 weeks | Normal | 3 weeks | Normal | 3 weeks | Normal | 3 weeks | Normal |
| 4 weeks | Normal | 4 weeks | Normal | 4 weeks | Normal | 4 weeks | Hypocellular ($P \leq 0.05$) |

The bolded area demonstrates the BMCD variations under the influence of SMF

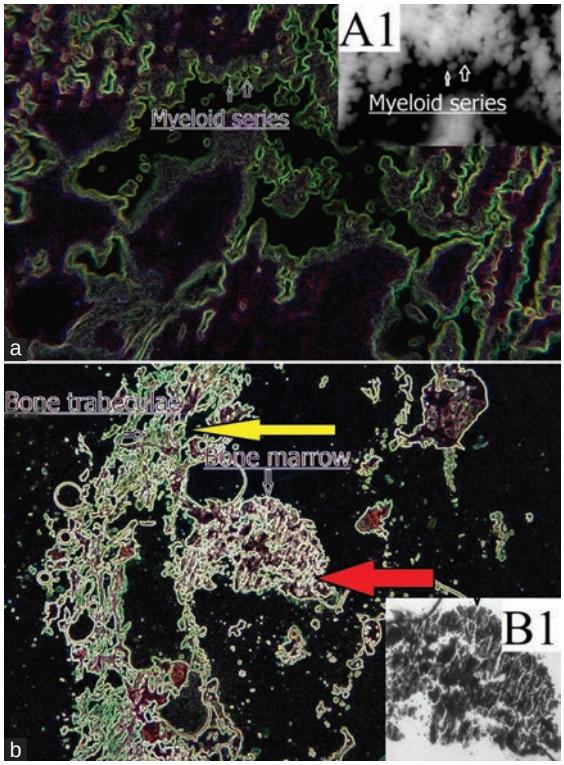


**Fig. 2.** Bone marrow distribution is illustrated. (a) Control image and (b) distribution of bone marrow in two different regions unequally.

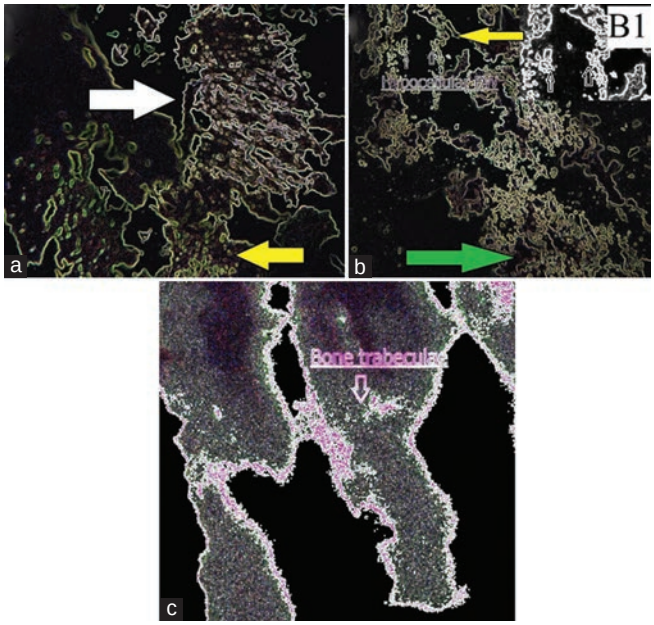


**Fig. 3.** Marrow cells and trabeculae bone distribution are shown with different exposure time per day. (a) Eight hours/day exposure for 1 week (bone marrow reduced insignificantly), (b) 8 h/day for 4 weeks (bone marrow reduced significantly), and (c) 6 h per day exposure (bone trabeculae increased and less marrow found).

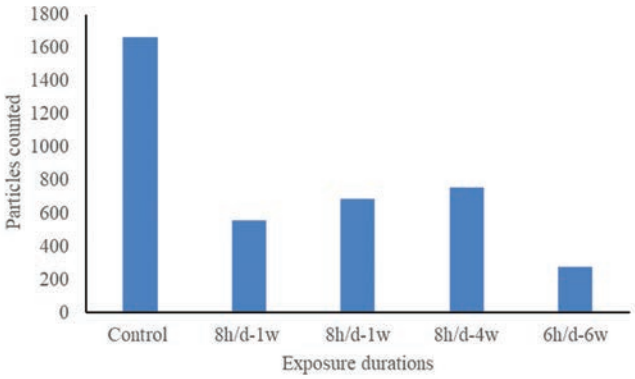


**Fig. 4.** Particle counted with ImageJ software. A minimum size of particles of 10 pixels is taken. Particles with a smaller than that value did not counted.

based on both analyzing methods. Since the ratio of bone trabeculae to marrow should be between 75% and 95%, a direct microscopic image can predict the change. Figs. 2 and 3 show the microscopic observation of bone marrow. Quantitative changes shown in Fig. 4. Fig. 5 represents the particle size variation and distribution under the influence of SMF. Networks of bone trabeculae found in Fig. 2. Image A is a normal distribution of the networks with a soft distribution of bone marrow uniformly. Myeloid cells highlighted as a sample of marrow cells among trabeculae. Image A1 is the filtrated portion of myeloid cells. Image B highlights two regions of bone trabeculae (yellow arrow) and marrow cells (red arrow). Bone marrow reduced slightly in the first region (yellow arrow) in respect to the second region (red arrow). Quantitative data illustrated a cell number decline compare to the control image (Fig. 4). A similar trend appears in image A of Fig. 3 (white and yellow arrows). Therefore, a highly reduction of bone marrow cellularity observed in image B (yellow arrow compares to the green arrow). Quantitatively, the particle numbers are almost half in compare to the control image (1600–800 particles). Image E is a large network of bone trabeculae with a fewer distribution of particles in between. As seen, the marrow cells reduced in ratio to trabeculae. We believe that the cellularity is varied based on a direct analyses of the microscopic images. The statistical analysis revealed a significant variation under the 6 h/day exposure.

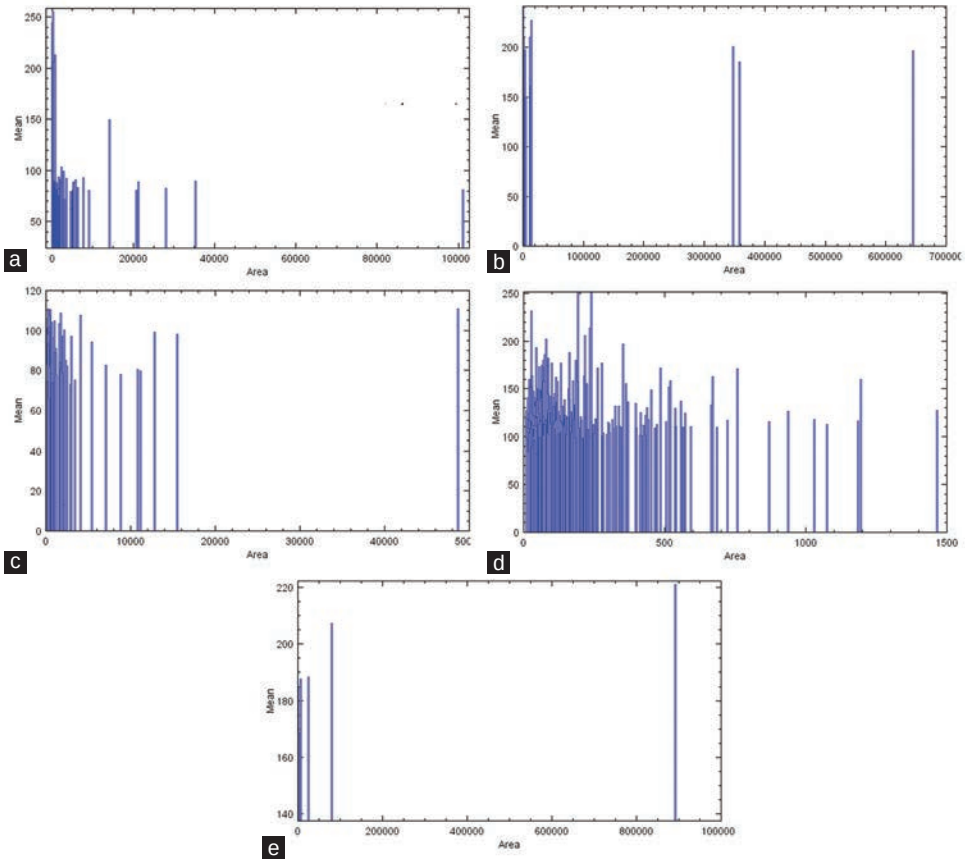


**Fig. 5.** Particles distribution with area. (a) Control, (b-d) 6 h/day exposure and (e) 8 h/day exposure.

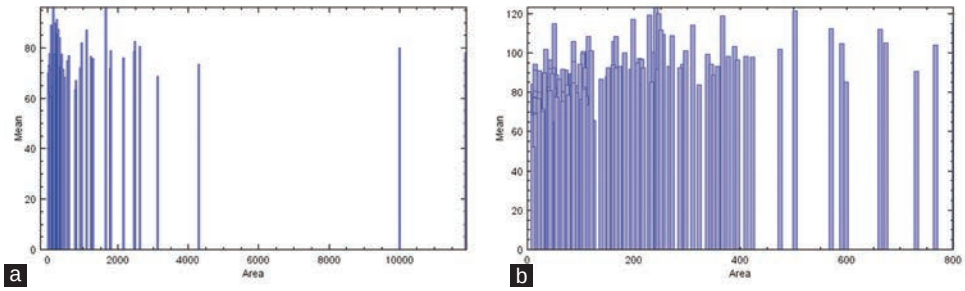


Fig. 6. Particle size distribution in two region of image B of Fig. 3. (a) Less dense and smaller size and (b) higher dense and larger size of particles.

Fig. 4 is the quantitative illustration of particles counted with ImageJ software. High exposure time per day reduced the cellular density in respect of control image. Quantitative data of images A and B of Fig. 3 show almost the same marrow density. Therefore, the BMCD is hypocellular (significant reduction) in image B in contrast to an insignificant reduction within image A.

Particles' area viability is shown in Figs. 5 and 6. Quantitative analysis indicated the presences of SMF influences on the area distribution. The most particle distribution found in control image was <10K pixels (image A). Eight hours exposure per day (1 week) reduced considerably since most of particles measured possessing <10K pixels (images B and C). Significant changes are shown of 4 weeks exposure (image D), analyzed results found the particles with area of <1000 pixels. There is no evidence to prove the area variation related, if only, to the applied magnetic field. However, a correlation can exist since the tendency of the marrow cells was affected with the applied magnetic field.

## IV. Discussion

Our previous studies indicated the *in vivo* influence of 2.4 mT SMF on blood cells (red blood cells (RBCs), white blood cells (WBCs), and platelets-PLTs (Mustafa, Yab and Ismail, 2020d; Mustafa, Yab and Ismail, 2020e; Mustafa, Yab and Ismail, 2020c; Mustafa, Yab and Ismail, 2020b). Rats were exposed with 2.4 mT SMF for short to long time per day for a period of 1–4 weeks. A 6 h/day exposure during 1 week raised WBCs with about 30%, PLTs with 13%, and RBCs reduced with 10%. WBCs declined tremendously under the influence of 8 h/day (4 weeks). RBCs and PLTs counts fluctuated. The present study of bone marrow shows

that our previous results of blood main cells are the response of bone marrow variation under the influence of SMF. We have expected the stimulation or destimulation effect of bone marrow for the influence of the magnetic field, whereas blood main cells are formed within bone marrow during a complex division of hematopoietic stem cells. It is not clear why some of the exposure periods of SMF did not influence the bone marrow. However, we believe that the biological system responses differently even at the same condition and highly controlled external factors.

Stimulating the bone marrow activities can induce bone marrow cell differentiation and stem cells growth rate. Exposed HMSCs with extremely low-frequency magnetic field (20 mT) during 23 days inhabited its growth and metabolism, although not affected the cell differentiation (Yan, et al., 2010). Other studies demonstrated that pulsed electromagnetic field enhanced the bone marrow mesenchymal stem cells proliferation in human and resulted an increase of marrow cell densities (Sun, et al., 2009). A 180 mT SMF effect on bone mineral density examined. No significant variation was found in bone mineral density of femurs among exposed groups of animals. Whereas, the 180 mT has reduced the bone mineral densities significantly in distal regions (Xu, et al., 2010). Osteoporosis also examined under the influence of moderate 0.2–0.6 mT magnetic field (Chen, et al., 2020). It was found that the magnetic field inhibits the adipogenic differentiation of bone marrow-derived mesenchymal stem cells depends on the intensity of exposure.

The marrow and trabeculae bone portions are naturally varied dependently to age. Bone marrow consists of hemopoietic stem cells and fats. The ratio between them is conservative in adults. The normal distribution and density of hematopoietic stem cells are vital and abnormality of it can cause chronic diseases such as cancer (Berg, et al., 1998). Several factors are contributing. Regarding magnetic field, the primitive factor of how bone marrow responds to magnetic field is controversial (Berg, et al., 1998). One anticipation is the chemical characteristics of hematopoietic cells containing protons. Protons interact with magnetic field. The outcome effect is a function of the strength of the field, period of exposure, and the nature of the biological cell. Mustafa, Yab and Ismail (2019) reviewed the influence of various intensities (low, intermediate, and high) of SMF on blood parameters. Several intermediate exposure sources changed blood counts significantly, of which other low and high exposure intensities showed an insignificant effect (Pirkhider Yaba and Ismail, 2019). Despite several studies concerns biological effect of magnetic field, there are studies which claim the safety of magnetic field. Regarding to non-linearity effect of SMF, we showed a significant effect due to high exposure time per day due to 4 weeks treatment, yet no promotion of change found <3 weeks of exposure.

The area distribution of the cells is through charge attraction or repulsion among the cells. The magnetic field produces a magnetic force which rotates the cells into a certain direction (Mustafa, Yab and Ismail, 2020d). If the applied magnetics force overcomes the repulsion force between the cells, they intense in a smaller space or vice versa. Therefore, other factors can contribute such as physiological and psychological effects since the applied magnetic field may not overcome the natural forces in biological system. Other than SMF, external factors were controlled.

## V. Conclusion

We investigated the proportional variation of BMCD to bone trabeculae associated with SMF in femurs albino rats. The short time exposure/day did not change the cellular density of bone marrow. The microscope distribution of the marrow showed in normal pattern. However, the 6 h/day exposure assisted an increase of BMCD (marrow to trabeculae bone) due to 1 week of exposure. Eight hours/day exposure led to reduce cellular density (hypocellularity of trabeculae portion). ImageJ analysis revealed the changes for particles existence under applied magnetic field. We believe that the marrow density variation attributes cell activities and differentiation. This investigation supports the hematological study shows the SMF-related blood components variations.

## References

Amara, S., Abdelmelek, H., Salem, M.B., Abidi, R. and Sakly, M., 2006. Effects of static magnetic field exposure on hematological and biochemical parameters in rats. *Brazilian Archives of Biology and Technology*, 49, pp.889-895.

Amin, H.D., Brady, M.A., St-Pierre, J.P., Stevens, M.M., Overby, D.R. and Ethier, C.R., 2014. Stimulation of chondrogenic differentiation of adult human bone marrow-derived stromal cells by a moderate-strength static magnetic field. *Tissue Engineering Part A*, 20, pp.1612-1620.

Berg, B.C.V., Malghem, J., Lecouvet, F.E. and Maldague, B., 1998. Magnetic resonance imaging of the normal bone marrow. *Skeletal Radiology*, 27, pp.471-483.

Cakir, D.U., Yokus, B., Akdag, M.Z., Sert, C. and Mete, N., 2009. Alterations of hematological variations in rats exposed to extremely low frequency magnetic fields (50 Hz). *Archives of Medical Research*, 40, pp.352-356.

Cetin, N., Bilgili, A. and Eraslan, G., 2006. Effects of pulsed magnetic field chronic exposure on some hematological parameters in mice. *Revue Medicine Veterinaire*, 157, pp.68-71.

Chater, S., Abdelmelek, H., Pequignot, J.M., Sakly, M. and Rhouma, K.B., 2006. Effects of sub-acute exposure to static magnetic field on hematologic and biochemical parameters in pregnant rats. *Electromagnetic Biology and Medicine*, 25, pp.135-144.

Chen, G., Zhuo, Y., Tao, B., Liu, Q., Shang, W., Li, Y., Wang, Y., Li, Y., Zhang, L. and Fang, Y., 2020. Moderate SMFs attenuate bone loss in mice by promoting directional osteogenic differentiation of BMSCs. *Stem Cell Research and Therapy*, 11, pp.1-14.

Ciejka, E., Kleniewska, P., Skibska, B. and Goraca, A., 2011. Effects of extremely low frequency magnetic field on oxidative balance in brain of rats. *Journal of Physiology and Pharmacology*, 62, pp.657.

Djordjevich, D.M., de Luka, S.R., Milovanovich, I.D., Janković, S., Stefanović, S., Vesković-Moračanin, S., Ćirković, S., Ilić, A.Ž., Ristić-Djurović, J.L. and Trbovich, A.M., 2012. Hematological parameters' changes in mice subchronically exposed to static magnetic fields of different orientations. *Ecotoxicology and Environmental Safety*, 81, pp.98-105.

Jouni, F.J., Abdolmaleki, P. and Movahedin, M., 2013. Investigation on the effect of static magnetic field up to 15 mT on the viability and proliferation rate of rat bone marrow stem cells. *In Vitro Cellular and Developmental Biology-Animal,* 49, pp.212-219.

Kim, E.C., Leesungbok, R., Lee, S.W., Lee, H.W., Park, S.H., Mah, S.J. and Ahn, S.J., 2015. Effects of moderate intensity static magnetic fields on human bone marrow-derived mesenchymal stem cells. *Bioelectromagnetics*, 36, pp.267-276.

Lee, S.H., Erber, W., Porwit, A., Tomonaga, M., Peterson, L. and Hematology, I.C.S., 2008. ICSH guidelines for the standardization of bone marrow specimens and reports. *International Journal of Laboratory Hematology*, 30, pp.349-364.

Mustafa, B.T., Yab, S.P. and Ismail, A.H., 2020a. Impacts of materials on the intensity of uniform static magnetic fields using a multi Helmholtz coils design. In: *AIP Conference Proceedings*. AIP Publishing LLC, 020063.

Mustafa, B.T., Yaba, S. and Ismail, A.H., 2020b. Impacts of *In Vivo* Exposure Static Magnetic Field to Blood Viscosity. In: *Materials Science Forum*, Trans Tech Publications Ltd., pp.369-378.

Mustafa, B.T., Yaba, S.P. and Ismail, A.H., 2020c. Experimental Evaluation of the Static Magnetic Field Effect on White Blood Cells: *In Vivo* Study. In: *Materials Science Forum*. Trans Tech Publications Ltd., pp.412-419.

Mustafa, B.T., Yaba, S.P. and Ismail, A.H., 2020d. Influence of the static magnetic field on red blood cells parameters and platelets using tests of CBC and microscopy images. *Biomedical Physics and Engineering Express,* 6, p.025004.

Mustafa, B.T., Yaba, S.P. and Ismail, A.H., 2020e. Moderate range static magnetic field promoted variation of blood parameters: An *in vitro* study. *ARO The Scientific Journal of Koya University*, 8, pp.55-64.

Pedersen, L.M., Jarner, D. and Winge, J., 1993. Bone-marrow biopsy of the iliac bone followed by severe retroperitoneal hemorrhage. *European Journal of Haematology*, 51, pp.52-52.

Pirkhider Yaba, S. and Ismail, A.H., 2019. A review of the effects of magnetic field on main blood cells: *In vivo* and *in vitro* experiments. *ZANCO Journal of Pure and Applied Sciences*, 31, pp.40-50.

Sarvestani, A.S., Abdolmaleki, P., Mowla, S.J., Ghanati, F., Heshmati, E., Tavasoli, Z. and Jahromi, A.M., 2010. Static magnetic fields aggravate the effects of ionizing radiation on cell cycle progression in bone marrow stem cells. *Micron*, 41, pp.101-104.

Sihem, C., Hafedh, A., Mohsen, S., Marc, P.J. and Khmais, B.R., 2006. Effects of sub-acute exposure to magnetic field on blood hematological and biochemical parameters in female rats. *The Turkish Journal of Hematology*, 23, pp.182-187.

Sun, L.Y., Hsieh, D.K., Yu, T.C., Chiu, H.T., Lu, S.F., Luo, G.H., Kuo, T.K., Lee, O.K. and Chiou, T.W., 2009. Effect of pulsed electromagnetic field on the proliferation and differentiation potential of human bone marrow mesenchymal stem cells. *Bioelectromagnetics: Journal of the Bioelectromagnetics Society, The Society for Physical Regulation in Biology and Medicine, The European Bioelectromagnetics Association*, 30, pp.251-260.

Suvarna, K.S., Layton, C. and Bancroft, J.D. 2018. *Bancroft's Theory and Practice of Histological Techniques E-Book*, Elsevier Health Sciences, Amsterdam, Netherlands.

Vergallo, C. and Dini, L., 2018. Comparative analysis of biological effects induced on different cell types by magnetic fields with magnetic flux densities in the range of 1-60 mT and frequencies up to 50 Hz. *Sustainability,* 10, pp.2776.

Xu, S., Okano, H., Tomita, N. and Ikada, Y., 2010. Recovery effects of a 180 mT static magnetic field on bone mineral density of osteoporotic lumbar vertebrae in ovariectomized rats. *Evidence Based Complementary and Alternative Medicine,* 2011, 620984.

Yan, J., Dong, L., Zhang, B. and Qi, N., 2010. Effects of extremely low-frequency magnetic field on growth and differentiation of human mesenchymal stem cells. *Electromagnetic Biology and Medicine*, 29, pp.165-176.

Yan, Q., Tomita, N. and Ikada, Y., 1998. Effects of static magnetic field on bone formation of rat femurs. *Medical Engineering and Physics*, 20, pp.397-402.

Yong, L., 1992. The theory and practice of histological techniques. *Pathology*, 24, p.320.

http://dx.doi.org/10.14500/aro.10898

# Extended-Spectrum β-lactamases and AmpC Production among Uropathogenic Isolates of *Escherichia coli* and Antibiogram Pattern

Aryan R. Ganjo

Department of Pharmacognosy, College of Pharmacy, Hawler Medical University Erbil, Kurdistan Region – F.R. Iraq

***Abstract*—Emergence of drug resistance in *Escherichia coli* due to various mechanisms makes the treatment choices very limited. The objective of this research was to investigate extended-spectrum beta-lactamases (ESBLs) and AmpC lactamases in *E. coli* isolates from urinary tract infections (UTIs) and to assess their antibacterial susceptibility patterns in a health-care context. A total of 70 *E. coli* isolates from clinically assumed cases of UTI patients during the 9 months period. The isolates with bacteriuria ($10^5$ CFU/ml) were identified. ESBL and AmpC were detected phenotypically. Out of the 70 isolates of uropathogenic *E. coli,* ESBL production was detected in 34 (48.6%) isolates and AmpC producer in 27 (38.6%) of isolates in which 14 (20%) of them showed coexistence phenotype of both ESBLs and AmpC and 23 (32.9%) *E. coli* isolates were both ESBL and AmpC non-producer. The findings donated information regarding drug resistance. The level of resistance recorded in ESBL- and AmpC-producing uropathogenic *E. coli* of this study was raising; therefore, it is crucial to have a strict infection control measures and routine monitoring of ESBL- and AmpC-producing bacteria in clinical laboratory.**

***Index Terms*—AmpC, ESBL, *Escherichia coli,* Urinary tract infections.**

## I. Introduction

Increasing resistance to antimicrobials among pathogens that cause common infections is a problem of global proportions given the paucity of novel antibiotics in development (Osthoff, et al., 2015). *Escherichia coli* has been described to be one of the most predominant pathogens for urinary tract infections (UTIs) (Arsalane, et al., 2015; Laxman and Ashok, 2016). Treatment of these infections is often difficult because of the rising bacterial resistance mediated by varying degrees of newly acquired antibiotic resistance of beta-lactamases which is either plasmid or chromosomally mediated (Sheemar, et al., 2016; Alyamani, et al., 2017). Extended-spectrum β-lactamases (ESBLs) and AmpC have become increasingly common globally and have appeared as a major source of multidrug resistance in clinically important *E. coli* (Alqasim, Abu Jaffal and Alyousef, 2018). The hydrolysis of β-lactamases is the most common and efficient process by which microorganisms can become resistant to this category of antibacterial drugs (Rani, et al., 2016). They are typically plasmid-mediated enzymes that are capable of hydrolyzing a wide variety of penicillin and cephalosporin antibiotics such as cefotaxime, ceftriaxone, cefepime, ceftazidime, and monobactam antibiotics, among other things (Thenmozhi, et al., 2014). However, the ESBL-producing bacteria remain susceptible to commercially available β-lactamase inhibitors such as clavulanic acid and sulbactam (Sheemar, et al., 2016). AmpC β-lactamases belong to the molecular Class C as classified by Ambler under a classification scheme of Bush, Jacoby and Medeiros, 1995. The presence of AmpC class β-lactamase demonstrated to be plasmid encoded or chromosomally mediated differentiated from ESBLs by their resistant to cephamycins (e.g. cefoxitin and cefotetan), as well as β-lactam plus β-lactamase inhibitor combination (Kaur, Gupta and Chhina, 2016), cloxacillin and phenylboronic acid, on the other hand, inhibit their activity (Rodríguez-Guerrero, et al., 2022). Furthermore, clinical isolates *E. coli* possessing plasmid encoding AmpC enzymes often are expressed high levels of resistant further constricting the treatment options (Coudron, Moland and Thomson, 2000). Cross-transmission of ESBL- and AmpC-producing bacteria in hospital milieu has been concerned for nosocomial infections globally making the detection of β-lactamases which is extremely important both for epidemiological purposes and for the prevention and control of infection (Madhumati, et al., 2015; Bandekar, et al., 2011). In the developing countries, molecular detection of these enzymes is still costly to be used, hence in the absence of molecular techniques in many clinical laboratories performing specific and sensitive phenotypic tests that provide an effective and reliable alternative to detect ESBL and AmpC beta-lactamase-producing microorganisms (Barua, Shariff and Thukral, 2013), as the genotypic method will confirm the phenotypic method results (Kazemian, et al., 2019). Therefore, the present study was conducted to demonstrate the burden of ESBL and AmpC production in *E. coli* isolated from urine

ARO-The Scientific Journal of Koya University
Vol. X, No.1 (2022), Article ID: ARO.10898, 6 pages
DOI: 10.14500/aro.10898
Received: 29 October 2021; Accepted: 05 June 2022
Regular research paper: Published: 21 June 2022
Corresponding author's e-mail: aryan.ganjo@hmu.edu.krd

specimens taken from patients diagnosed with UTI and their coexistence using phenotypic methods. A comparative analysis of resistant patterns was also done to compare antimicrobial susceptibility among these isolates.

## II. Material and Methods

### A. Identification of Bacterial Isolates

A total of 70 *E. coli* clinical isolates were acquired from patients who appeared with symptoms of UTI and were admitted to Rizgary Teaching Hospital in Erbil city. Isolated microorganisms were identified at the species level using standard microbiological methods and confirmed using the Vitek II. These isolates were grown in trypticase soy broth containing (TSB) and stored at −70°C after the addition of 15% glycerol (Šišková, et al., 2015).

### B. The Antimicrobial Susceptibility Testing

The antimicrobial susceptibility patterns of the bacterial isolates were examined by the disk diffusion method as recommended by the Clinical Laboratory Standard Institute (CLSI) (Humphries, et al., 2018). Each of the stains was standardized to 0.5 McFarland equivalent and aseptically inoculated on Mueller-Hinton agar (MHA). The inoculated plates were allowed to stand for 10 min. Antibiotic disks, namely, ampicillin (10 μg), ampicillin/sulbactam (20 μg), amoxicillin/clavulanate (20/10 μg), imipenem (10 μg), ertapenem (10 μg), ceftazidime (30 μg), ceftriaxone (30 μg), cefepime (30 μg), cefazolin (30 μg), gentamicin (10 μg), levofloxacin (5 μg), nitrofurantoin (300 μg), piperacillin/tazobactam (110 μg), ciprofloxacin (5 μg), and trimethoprim/sulfamethoxazole (1.25/23.75 μg), (Oxoid, UK) were placed on the inoculated plates. Incubation at 37°C for an overnight period was followed by measurement and interpretation of the zones of inhibition in accordance with guidelines (Moroh, et al., 2014).

### C. Screening of ESBL-producing Isolates

Isolated bacteria were examined for their susceptibility to third-generation cephalosporins. After overnight incubation at 37°C, any enhancement of the zone of inhibition of the isolate was indicative of the presence of an ESBL as proposed by CLSI guideline and further tested by confirmatory procedures was performed. Bacteria that produce ESBLs were spotted using the Phenotypic Confirmatory Disk Diffusion Test (PCDDT). Concisely, the 0.5 McFarland standard concentration of bacterial suspension was used to inoculate microorganisms onto the MHA surface. Then, ceftazidime (30 μg) disk alone and the combination of clavulanic acid (30 μg/10 μg), as well as cefotaxime (30 μg) alone, combined with clavulanic acid (10 μg) disks were placed 25 mm apart from each other. The plates were incubated at 37°C for 24 h. Isolate that showed an enhancement in the zone of inhibition and an increase of ≥5 mm diameter of the combination disks in comparison to that of the antibiotic disk alone was interpreted as ESBL producer. *E. coli* ATCC 25922 was used as positive controls (Iroha, et al., 2017).

### D. Screening for AmpC β-lactamase Production

AmpC disk test was used to identify AmpC-producing isolates. The AmpC disks were formed by applying 20 mL of a 1:1 combination of normal saline and ×100 Tris-EDTA to each of the sterile blank paper disks. The disks were stored at refrigerator 4°C. A lawn culture of the a cefoxitin (FOX)-susceptible strain (*E. coli* ATCC 25922) was inoculated onto the surface of MHA plate. A 30 μg cefoxitin disk was placed on the bacterial lawn. The disks of an AmpC were hydrated, and some colonies of the tested bacteria were spread throughout it. After that, with its inoculation surface close to and touching the agar surface, an AmpC disk was placed into an inoculated agar plate. After overnight incubation at 37°C, the results were interpreted. When there is an indentation or destruction in the zone of inhibition, of cefoxitin disk indicated an enzymatic deactivation of the antimicrobial agent (positive result), and is measured as an AmpC producer, in contrast, A lack of distortion, indicating no inactivation of the cefoxitin disk, was interpreted as evidence of a non-AmpC producer. Out of 70 E. coli strains, 34 (48.6%) were ESBL producer, 27 (38.6%) were AmpC producer in which 14 (20%) isolates showed coexistence phenotype of both ESBLs and AmpC and 23(32.9%) E. coli strains were negative, which were both ESBL and AmpC non-producer, as shown in Table II.

## III. Results

The mid-stream urine samples were collected from patients having symptoms, a total of 70 isolates were with significant growth $\geq 10^5$ CFU/ml of *E. coli*. Among these isolates, 20 (28.6%) were male patients whereas 50 (71.4%) belonged to female patients. Through regard to the age groups of patients, maximum proportion 45 (64.3%) were obtained from adults' population, 20 (28.6%) isolates were the elderly, and 5 (7.1%) were belonged to children. Highest percentage were from females 71.4% ($n$ = 50) and 28.6% ($n$ = 20) were obtained from males. Demographic characteristics of patients are presented in Table I.

Out of 70 *E. coli* strains, 34 (48.6%) were ESBL producer, 27 (38.6%) were AmpC producer in which 14 (20%) isolates showed coexistence phenotype of both ESBLs and AmpC and 23(32.9%) *E. coli* strains were negative, which were both ESBL and AmpC non-producer.

Tables III and IV show the comparison of antimicrobial resistance between ESBL and non-ESBL, AmpC and non-AmpC uropathogenic isolates.

Table III reveals the antimicrobial resistance profile of 34 ESBL expressing isolates that are phenotypically positive and 36 non-ESBL producer isolates. The rate of resistance to

Table I
Distribution of Isolates According to Age and Gender

| Age category | Gender | | Total |
|---|---|---|---|
| | Female | Male | |
| Children* | 4 (5.7%) | 1 (1.4%) | 5 (7.1%) |
| Adults** | 34 (48.6%) | 11 (15.7%) | 45 (64.3%) |
| Elderly*** | 12 (17.1%) | 8 (11.5%) | 20 (28.6%) |
| Total | 50 (71.4%) | 20 (28.6%) | 70 (100%) |

*Children: 0–18 years, **adults: 19–64 years, ***elderly: ≥65 years

 http://dx.doi.org/10.14500/aro.10898

all isolates was: In ESBL producer, all isolates were totally resistant for ampicillin, ceftriaxone, and cefazolin. Overall, the highest resistance rate was detected for ceftazidime 94.1%, cefepime 88.2%, and ciprofloxacin 79.4% and the lowest resistant observed for nitrofurantoin 2.9% followed by imipenem and ertapenem 29.4%, while in non-ESBL producer were expressively more susceptible than ESBL producer to most antimicrobial agents.

Of the 70 *E. coli* isolates, 27 (38.6%) were AmpC producers. Antibiotic susceptibility pattern of AmpC-positive isolates disclosed 77.8% to ampicillin, 70.4% ceftriaxone, 66.7% to ciprofloxacin, and 63% to ampicillin/sulbactam, ceftazidime, and trimethoprim/sulfamethoxazole (Table IV), of the 43 (61.4%) non-AmpC producers, the greatest degree of resistance was detected for ampicillin 79.1%, and the lowest rate for nitrofurantoin 2.3% followed by imipenem 14%. A striking resemblance existed between the antibiotic resistance profiles of AmpC producers and non-AmpC-producing isolates.

Table II
Detection of ESBL, AmpC b-lactamase, and ESBL+AmpC among Uropathogenic Isolates

| Microorganism | Phenotypic detection of AmpC- and ESBL-producing *E. coli* isolates | | | |
|---|---|---|---|---|
| | Screening positive ESBL, *n* (%) | Screening positive AmpC, *n* (%) | Both (ESBL+AmpC), *n* (%) | ESBL+AmpC negative, *n* (%) |
| *E. coli* (*n*=70) | 34 (48.6%) | 27 (38.6%) | 14 (20%) | 23 (32.9%) |

*E. coli*: *Escherichia coli*

Table III
Comparison of Antibiotic Resistance Pattern of ESBL- and Non-ESBL-Producing *Escherichia coli*

| Antibiotic | No. (%) of resistant strains | | | | | |
|---|---|---|---|---|---|---|
| | ESBLs producers (*n*=34) | | | Non-ESBLs producers (*n*=36) | | |
| | Resistant, *n* (%) | Intermediate, *n* (%) | Sensitive, *n* (%) | Resistant, *n* (%) | Intermediate, *n* (%) | Sensitive, *n* (%) |
| Ampicillin | 34 (100) | 0 | 0 | 23 (63.9) | 0 | 13 (36.1) |
| Ampicillin/sulbactam | 24 (70.6) | 3 (8.8) | 7 (20.6) | 14 (38.9) | 2 (5.6) | 20 (55.5) |
| Amoxicillin/clavulanate | 17 (50) | 8 (23.5) | 9 (26.5) | 10 (27.8) | 6 (16.7) | 20 (55.5) |
| Ceftazidime | 32 (94.1) | 0 | 2 (5.9) | 10 (27.8) | 0 | 26 (72.2) |
| Ceftriaxone | 34 (100) | 0 | 0 | 11 (30.5) | 1 (2.8) | 24 (66.7) |
| Cefepime | 30 (88.2) | 0 | 4 (11.8) | 4 (11.1) | 0 | 32 (88.9) |
| Cefazolin | 34 (100) | 0 | 0 | 8 (22.2) | 2 (5.6) | 26 (72.2) |
| Ciprofloxacin | 27 (79.4) | 1 (2.9) | 6 (17.7) | 14 (38.9) | 2 (5.6) | 20 (55.5) |
| Ertapenem | 10 (29.4) | 0 | 24 (70.6) | 4 (11.1) | 0 | 32 (88.9) |
| Gentamicin | 18 (52.9) | 2 (5.9) | 14 (41.2) | 7 (19.4) | 0 | 29 (80.6) |
| Imipenem | 10 (29.4) | 0 | 24 (70.6) | 2 (5.6) | 0 | 34 (94.4) |
| Levofloxacin | 18 (52.9) | 0 | 16 (47.1) | 10 (27.8) | 0 | 26 (72.2) |
| Nitrofurantoin | 1 (2.9) | 6 (17.7) | 27 (79.4) | 2 (5.6) | 3 (8.3) | 31 (86.1) |
| Piperacillin/tazobactam | 17 (50) | 4 (11.8) | 13 (38.2) | 6 (16.7) | 1 (2.7) | 29 (80.6) |
| Trimethoprim/sulfamethoxazole | 23 (67.6) | 0 | 11 (32.4) | 12 (33.3) | 0 | 24 (66.7) |

Table IV
Comparison of Antibiotic-Resistant Pattern of AmpC- and Non-AmpC-Producing *Escherichia coli*

| Antibiotic | No. (%) of resistant strains | | | | | |
|---|---|---|---|---|---|---|
| | AmpC producers (*n*=27) | | | Non-AmpC producers (*n*=43) | | |
| | Resistant, *n* (%) | Intermediate, *n* (%) | Sensitive, *n* (%) | Resistant, *n* (%) | Intermediate, *n* (%) | Sensitive, *n* (%) |
| Ampicillin | 21 (77.8) | 0 | 6 (22.2) | 34 (79.1) | 0 | 9 (20.9) |
| Ampicillin/sulbactam | 17 (63) | 2 (7.4) | 8 (29.6) | 19 (44.2) | 2 (4.7) | 22 (51.1) |
| Amoxicillin/clavulanate | 12 (44.4) | 6 (22.2) | 9 (33.4) | 15 (34.9) | 8 (18.6) | 20 (46.5) |
| Ceftazidime | 17 (63) | 0 | 10 (37) | 25 (58.1) | 0 | 18 (41.9) |
| Ceftriaxone | 19 (70.4) | 0 | 8 (29.6) | 26 (60.5) | 1 (2.3) | 16 (37.2) |
| Cefepime | 14 (51.9) | 0 | 13 (48.1) | 14 (32.6) | 0 | 29 (67.4) |
| Cefazolin | 15 (55.6) | 1 (3.7) | 11 (40.7) | 15 (34.9) | 1 (2.3) | 27 (62.8) |
| Ciprofloxacin | 18 (66.7) | 3 (11.1) | 6 (22.2) | 23 (53.5) | 0 | 20 (46.5) |
| Ertapenem | 7 (25.9) | 0 | 20 (74.1) | 7 (16.3) | 0 | 36 (83.7) |
| Gentamicin | 9 (33.3) | 0 | 18 (66.7) | 16 (37.2) | 1 (2.3) | 26 (60.5) |
| Imipenem | 6 (22.2) | 0 | 21 (77.8) | 6 (14) | 0 | 37 (86) |
| Levofloxacin | 14 (51.9) | 0 | 13 (48.1) | 14 (32.6) | 0 | 29 (67.4) |
| Nitrofurantoin | 3 (11.1) | 3 (11.1) | 21 (77.8) | 1 (2.3) | 5 (11.6) | 37 (86.1) |
| Piperacillin/tazobactam | 9 (33.3) | 1 (3.7) | 17 (63) | 14 (32.6) | 4 (9.3) | 25 (58.1) |
| Trimethoprim/sulfamethoxazole | 17 (63) | 0 | 10 (37) | 19 (44.2) | 0 | 24 (55.8) |

## IV. Discussion

UTIs have been established to be the most encountered bacterial infection and leading patients to pursue medical care (Giwa, et al., 2018). *E. coli,* in particular, showing multiple resistance to β-lactam antibiotics, especially penicillin and third generation of cephalosporin. Among these, ESBL- and AmpC-producing strains have been reported to be responsible for serious hospital-acquired infections globally (Lee, et al., 2015), with the spread of ESBL- and AmpC-producing strains all over the world, it is necessary to know the risk of prevalence of these strains in hospitals. In the present study out of 70 isolates, 20 (28.6%) were obtained from male patients and 50 (71.4%) were from female patients. Different studies conducted by other researchers found that 48.01% were male and 51.98% were female, that showed the higher occurrence of UTI in female (Alqasim, Abu Jaffal and Alyousef, 2018). The current results are in agreement with earlier study that only 35.6% of isolates were from men patients (Bakshi, et al., 2019). Other research has been shown that ESBL-producing *E. coli* incidences were significantly higher in females 73.6% than males 26.4% (Senbayrak, et al., 2017). It has been revealed that the high UTI prevalence in female can be attributed to many factors such as anatomical differing that allow quick admission of bacteria to the urinary tract (Rowe and Juthani-Mehta, 2013; Foad, 2016). The findings of this study show that bacterial proliferation was most pronounced in the 19–64 age range and least bacterial growth was detected in children and elderly among the isolates. Similarly, a research conducted in Nepal's South Terai found the identical results (Yadav and Prakash, 2017). The frequency of UTI rises with age and sexual activity, poor hygiene, use of contraceptives, earlier antibiotic usage, and prolonged catheterization duration, all are predisposing factors for the UTI (Kizilay, et al., 2020). Among 70 strains of *E. coli*, the number of ESBLs positive strains was 34 (48.6%) and ESBLs negative strains was 36 (51.4%) by double-disk synergy method. According to an Iranian investigation, ESBL production was identified in 40.8% of all the isolates tested (Seyedjavadi, Goudarzi and Sabzehali, 2016), whereas other study reported 42.5% of the isolates recovered from outpatients (Koshesh, et al., 2016). Another investigation from tertiary care hospital in Istanbul revealed that 44.7% and 22.8% of isolates were ESBL enzyme producer among inpatients and outpatients, respectively (Senbayrak, et al., 2017). Based on the results of this study, the number of isolates that were found to be positive for AmpC screening were 27 (38.6%) which is in accordance to the previous published studies. Numerous studies from different states of the world have conveyed the presence of AmpC producers in isolates of *E. coli,* the percentage of AmpC production in *E. coli* was 57.7%, 40.8%, and 32%, respectively (Fam, et al., 2013, Barua, Shariff and Thukral, 2013; Madhumati, et al., 2015). The present study revealed that 14 (20%) were coproducers of ESBL + AmpC. As many other study had been reported that there is not high incidence of phenotypic coexistence of ESBL/AmpC β-lactamases, 11.5% of coexistence occurred in India (Nayar, et al., 2012). Another study described that the coexistence phenotype of both ESBLs and AmpC was 11.5% of the isolates (Nasir, et al., 2015). In the existing study, ESBL production was found to be higher than AmpC production. Higher prevalence of ESBL-producing *E. coli* was seen possibly because of geographic areas and sample distinction can also be another reason. This study correlates with the former study by Mandal, et al., 2020, that established ESBL much higher in their isolates and the existence of ESBL and AmpC was 30.92% and 18.4%, correspondingly. This study also corroborates the earlier finding that higher ESBLs production was observed in 52.6% of isolates and AmpC production was perceived only in 8% of isolates (Gupta, et al., 2013). Furthermore, the resistance rate to cephalosporin was also high 100% and 82% resistance to cephalexin and ceftriaxone, respectively. This result was predictable because this group of drugs was widely used in both hospital and community settings. This result supported the outcomes realized by other researchers. It has been reported the highest resistance rate to antibiotics was piperacillin 86.6%, ceftriaxone 66.5%, and cefotaxime 66% and the most sensitivity was to the imipenem 90% and amikacin 80% (Hoseini, et al., 2017). Numerous studies have documented a remarkable increase in resistant degree to antibiotics such as penicillin, 2$^{nd}$ and 3$^{rd}$ generation cephalosporin (Bakshi, et al., 2019). These results exhibited a high frequency of resistance among *E. coli* isolates to the common antibiotics which are used routinely in the treatment of UTIs. Few options such as amikacin and carbapenems remain the utmost effective drugs against these resistant pathogens (Al-Zarouni, et al., 2008, Giwa, et al., 2018). It has been realized the clinical outpatient ESBL-producing isolates displayed high resistance to all cephalosporins, ranging from 25% (cefepime) to 100% (cefuroxime) (Ibrahimagić, 2016). In another study, all ESBL-producing isolates were resistant toward β-lactam and cephalosporins (ampicillin, cefotaxime, ceftriaxone, and ceftazidime), most ESBL producers were susceptible against imipenem (89.7%), nitrofurantoin 82.8%, and amikacin 72.4% (Kayastha, et al., 2020). The results of the present study exhibited that the rate of resistance to the β-lactam group (ampicillin and amoxicillin) was high, which might be due to the improper use of this class of antibiotics in the health-care setting. These results are in agreement with another study (Rahamathulla and Harish, 2016; Tillekeratne, et al., 2016). It is noticeable that the ESBL- and AmpC-producing *E. coli* were often resistant to other antibiotics such as aminoglycosides and fluoroquinolones. This could be due to coexistence of genes encoding drug resistance to those classes of antibiotics.

## V. Conclusion

The present study highlights the incidence of ESBL and AmpC beta-lactamase-producing uropathogenic *E. coli* which alarming and crucial action needs because therapeutic choices may be limited due to the high percentage of drug-resistant bacteria. There is necessity to assume continued surveillance of the resistant bacteria and their underlying mechanisms so as to control further spread of the infections.

## References


Alqasim, A., Abu Jaffal, A. and Alyousef, A.A., 2018. Prevalence of multidrug resistance and extended-spectrum β-lactamase carriage of clinical uropathogenic *Escherichia coli* isolates in Riyadh, Saudi Arabia. *International Journal of Microbiology*, 2018, p.3026851.

Alyamani, E.J., Khiyami, A.M., Booq, R.Y., Majrashi, M.A., Bahwerth, F.S. and Rechkina, E., 2017. The occurrence of ESBL-producing *Escherichia coli* carrying aminoglycoside resistance genes in urinary tract infections in Saudi Arabia. *Annals of Clinical Microbiology and Antimicrobials*, 16, p.1.

Al-Zarouni, M., Senok, A., Rashid, F., Al-Jesmi, S.M. and Panigrahi, D., 2008. Prevalence and antimicrobial susceptibility pattern of extended-spectrum beta-lactamase-producing *Enterobacteriaceae* in the United Arab Emirates. *Medical Principles and Practice*, 17, pp.32-36.

Arsalane, L., Zerouali, K., Katfy, K. and Zouhair, S., 2015. Molecular characterization of extended spectrum β-lactamase-producing *Escherichia coli* in a university hospital in Morocco, North Africa. *African Journal of Urology*, 21, pp.161-166.

Bakshi, R., Sehgal, V.K., Kansal, P. and Kaur, S., 2019. Detection of extended-spectrum beta lactamases and AmpC beta lactamases producing uropathogenic *Escherichia coli* in a tertiary care hospital. 8, p.23503.

Bandekar, N., Vinodkumar, C., Basavarajappa, K., Prabhakar, P. and Nagaraj, P., 2011. Beta lactamases mediated resistance amongst gram negative bacilli in burn infection. *International Journal of Biological and Medical Research*, 2, pp.766-770.

Barua, T., Shariff, M. and Thukral, S., 2013. Detection and characterization of AmpC B-lactamases in Indian clinical isolates of *Escherichia coli, Klebsiella pneumoniae* and *Klebsiella oxytoca*. *Universal Journal of Microbiology Research*, 1, pp.15-21.

Bush, K., Jacoby, G.A. and Medeiros, A.A., 1995. A functional classification scheme for beta-lactamases and its correlation with molecular structure. *Antimicrobial Agents and Chemotherapy*, 39, p.1211.

Coudron, P.E., Moland, E.S. and Thomson, K.S., 2000. Occurrence and detection of AmpC beta-lactamases among *Escherichia coli, Klebsiella pneumoniae*, and *Proteus mirabilis* isolates at a veterans medical center. *Journal of Clinical Microbiology*, 38, pp.1791-1796.

Fam, N., Gamal, D., El Said, M., Aboul-Fadl, L., El Dabei, E., El Attar, S., Sorur, A., Fouad, S. and Klena, J., 2013. Detection of plasmid-mediated AmpC beta-lactamases in clinically significant bacterial isolates in a research institute hospital in Egypt. *Life Science Journal*, 10, pp.2294-2304.

Foad, M.F., 2016. Phenotypic detection and antimicrobial susceptibility profile of ESBL, AmpC and carbapenemase producing gram-negative isolates from outpatient clinic specimens. *International Journal of Current Microbiology and Applied Sciences*, 5, pp.740-752.

Giwa, F.J., Ige, O.T., Haruna, D.M., Yaqub, Y., Lamido, T.Z. and Usman, S.Y., 2018. Extended-spectrum beta-lactamase production and antimicrobial susceptibility pattern of uropathogens in a tertiary hospital in Northwestern Nigeria. *Annals of Tropical Pathology*, 9, p.11.

Gupta, V., Rani, H., Singla, N., Kaistha, N. and Chander, J., 2013. Determination of extended-spectrum β-lactamases and AmpC production in uropathogenic isolates of *Escherichia coli* and susceptibility to fosfomycin. *Journal of Laboratory Physicians*, 5, p.90.

Hoseini, N., Sedighi, I., Nejad, A.S.M. and Alikhani, M.Y., 2017. Phenotypic and genotypic detection of AmpC enzymes in clinical isolates of *Escherichia coli* and *Klebsiella pneumoniae*. *Journal of Krishna Institute of Medical Sciences*, 6, pp.10-18.

Humphries, R.M., Ambler, J., Mitchell, S.L., Castanheira, M., Dingle, T., Hindler, J.A., Koeth, L. and Sei, K., 2018. CLSI methods development and standardization working group best practices for evaluation of antimicrobial susceptibility tests. *Journal of Clinical Microbiology*, 56, pp.e01934-17.

Ibrahimagić, A., 2016. Prevalence and antimicrobial resistance of betalactamase-producing gram-negative isolates from outpatient clinical and environmental samples in the Zenica-Doboj Canton, Bosnia and Herzegovina. *Journal of Health Sciences*, 6, p.337.

Iroha, I., Okoye, E., Osigwe, C., Moses, I., Ejikeugwu, C. and Nwakaeze, A., 2017. Isolation, phenotypic characterization and prevalence of ESBL-producing *Escherichia coli* and *Klebsiella* species from orthopedic wounds in National Orthopedic Hospital Enugu (NOHE), South East Nigeria. *Journal of Pharmaceutical Care and Health Systems*, 4, pp.1-5.

Kaur, S., Gupta, V. and Chhina, D., 2016. AmpC β-lactamases producing gram-negative clinical isolates from a tertiary care hospital. *Journal of Mahatma Gandhi Institute of Medical Sciences*, 21, pp.107-110.

Kayastha, K., Dhungel, B., Karki, S., Adhikari, B., Banjara, M.R., Rijal, K.R. and Ghimire, P., 2020. Extended-spectrum β-lactamase-producing *Escherichia coli* and *Klebsiella* species in pediatric patients visiting international friendship children's hospital, Kathmandu, Nepal. *Infectious Diseases: Research and Treatment*, 13, p.1178633720909798.

Kazemian, H., Heidari, H., Ghanavati, R., Ghafourian, S., Yazdani, F., Sadeghifard, N., Valadbeigi, H., Maleki, A. and Pakzad, I., 2019. Phenotypic and genotypic characterization of ESBL-, AmpC-, and carbapenemase-producing *Klebsiella pneumoniae* and *Escherichia coli* isolates. *Medical Principles and Practice*, 28, pp.547-551.

Kizilay, F., Aliyev, B., Şimşir, A., Kalemci, M.S., Köse, T., Taşbakan, M. and Pullukçu, H., 2020. Carbapenem-resistant *Klebsiella pneumonia* infection outbreak in a tertiary urology clinic: Analysis of influencing factors with a controlled trial. *Turkish Journal of Medical Sciences*, 50, pp.239-247.

Koshesh, M., Mansouri, S., Hashemizadeh, Z. and Kalantar-Neyestanaki, D., 2016. Identification of extended-spectrum β-lactamase genes and ampc-β-lactamase in clinical isolates of *Escherichia coli* recovered from patients with urinary tract infections in Kerman, Iran. *Archives of Pediatric Infectious Diseases*, 5, p.e37968.

Laxman, C.V. and Ashok, P.A., 2016. Profile and antimicrobial susceptibility pattern of urinary bacterial isolates at a tertiary care hospital in central India. *European Journal of Biomedical*, 3, pp.560-564.

Lee, C.H., Lee, Y.T., Kung, C.H., Ku, W.W., Kuo, S.C., Chen, T.L. and Fung, C.P., 2015. Risk factors of community-onset urinary tract infections caused by plasmid-mediated AmpC β-lactamase-producing *Enterobacteriaceae*. *Journal of Microbiology, Immunology and Infection*, 48, pp.269-275.

Madhumati, B., Rani, L., Ranjini, C. and Rajendran, R., 2015. Prevalence of AMPC beta lactamases among gram negative bacterial isolates in a tertiary care hospitals. *International Journal of Current Microbiology and Applied Sciences*, 4, pp.219-227.

Mandal, D.K., Sah, S.K., Mishra, S.K., Sharma, S., Kattel, H.P., Pandit, S., Yadav, P.K., Laghu, U., Lama, R. and Sah, N.P., 2020. Carriage of extended-spectrum-β-lactamase-and AmpC-β-lactamase-producing *Enterobacteriaceae* (ESBL-PE) in healthy community and outpatient department (OPD) patients in Nepal. *Canadian Journal of Infectious Diseases and Medical Microbiology*, 2020, p.5154217.

Moroh, J.L., Fleury, Y., Tia, H., Bahi, C., Lietard, C., Coroller, L., Edoh, V., Coulibaly, A., Labia, R. and Leguerinel, I., 2014. Diversity and antibiotic resistance of uropathogenic bacteria from Abidjan. *African Journal of Urology*, 20, pp.18-24.

Nasir, K.M., Preeti, S., Vikili, C. and Singh, N.P., 2015. Prevalence of ESBL and AmpC βlactamase in gram negative bacilli in various clinical samples at tertiary care hospital. *International Research Journal of Medical Sciences*, 3, p.1-6.

Nayar, R., Arora, V.M. and Duggal, S., 2012. Antibiotic impregnated tablets for screening ESBL and AmpC beta lactamases. *The IOSR Journal of Pharmacy*, 2, 207-209.

Osthoff, M., Mcguinness, S.L., Wagen, A.Z. and Eisen, D.P., 2015. Urinary tract infections due to extended-spectrum beta-lactamase-producing gram-negative bacteria: Identification of risk factors and outcome predictors in an Australian tertiary referral hospital. *International Journal of Infectious Diseases*, 34,

pp.79-83.

Rahamathulla, M.P. and Harish, B.N., 2016. Molecular characterization of ESBL and AmpC β-lactamases among blood isolates of *Klebsiella pneumoniae* and *Escherichia coli*. *Microbiology Research Journal International*, 12, pp.1-19.

Rani, S., Rao, K., Ravinder, S. and Kanakadurga, P., 2016. Prevalence of extended spectrum beta lactamases (ESBL) producing *Pseudomonas aeruginosa* isolates from burn patients. *Proceedings of the International Journal of Contemporary Medical Research*, 5, pp.1297-1300.

Rodríguez-Guerrero, E., Callejas-Rodelas, J.C., Navarro-Marí, J.M. and Gutiérrez-Fernández, J., 2022. systematic review of plasmid AmpC type resistances in *Escherichia coli* and *Klebsiella pneumoniae* and preliminary proposal of a simplified screening method for ampC. *Microorganisms*, 10, p.611.

Rowe, T.A. and Juthani-Mehta, M., 2013. Urinary tract infection in older adults. *Aging Health*, 9, pp.519-528.

Senbayrak, S., Boz, E.S., Cevan, S., Inan, A., Engin, D.O., Dosoglu, N., Cobanoglu, N., Dagli, O., Davarci, I. and Aksaray, S., 2017. Antibiotic resistance trends and the ESBL prevalence of *Escherichia coli* and *Klebsiella* spp. urinary isolates in in-and outpatients in a tertiary care hospital in İstanbul, 2004-2012. *Jundishapur Journal of Microbiology*, 10, p.e13098.

Seyedjavadi, S.S., Goudarzi, M. and Sabzehali, F., 2016. Relation between blaTEM, blaSHV and blaCTX-M genes and acute urinary tract infections. *Journal of Acute Disease*, 5, pp.71-76.

Sheemar, S., Chopra, S., Mahajan, G., Kaur, J. and Chouhan, Y.S., 2016. Extended spectrum beta-lactamase and AmpC producing *Klebsiella pneumoniae*: A therapeutic challenge. *Tropical Journal of Medical Research,* 19, p.114.

Šišková, P., Černohorská, L., Mahelová, M., Turková, K. and Woznicová, V., 2015. Phenotypes of *Escherichia coli* isolated from urine: Differences between extended-spectrum β-lactamase producers and sensitive strains. *Journal of Microbiology, Immunology and Infection*, 48, pp.329-334.

Thenmozhi, S., Moorthy, K., Sureshkumar, B. and Suresh, M., 2014. Antibiotic resistance mechanism of ESBL producing *Enterobacteriaceae* in clinical field: A review. *International Journal of Pure and Applied Bioscience*, 2, pp.207-26.

Tillekeratne, L.G., Vidanagama, D., Tippalagama, R., Lewkebandara, R., Joyce, M., Nicholson, B.P., Nagahawatte, A., Bodinayake, C.K., De Silva, A.D. and Woods, C.W., 2016. Extended-spectrum ß-lactamase-producing *Enterobacteriaceae* as a common cause of urinary tract infections in Sri Lanka. *Infection and Chemotherapy*, 48, pp.160-165.

Yadav, K. and Prakash, S. 2017. Screening of ESBL producing multidrug resistant *E. coli* from urinary tract infection suspected cases in Southern Terai of Nepal. *Journal of Infectious Diseases and Diagnosis*, 2, p.2.

 http://dx.doi.org/10.14500/aro.10877

# Role of Laser Produced Silver Nanoparticles in Reversing Antibiotic Resistance in Some Multidrug-Resistant Pathogenic Bacteria

Abubaker H. Hamad[1], Mahmoud A. Chawsheen[1], Ahmed A. Al-Naqshbandi[2]

[1]Department of General Science, Faculty of Education, Soran University, Erbil, Kurdistan Region - F.R. Iraq

[2]Department of Laboratory, Rizgary Teaching Hospital, Erbil, Kurdistan Region - F.R. Iraq

***Abstract*—Silver nanoparticles (Ag NPs) were produced through nanosecond laser in deionized water. These nanoparticles were characterized by UV–VIS spectrometer and transmission electron microscopy. VITEK®2 compact system was used to identify *Escherichia coli* (ESBL strain) and *Staphylococcus aureus* (MRSA strain) as multidrug-resistance (MDR) bacteria. The antibacterial activity of Ag NPs, ampicillin (AMP), and their combinations was tested against both bacterial isolates through standard microbiological culturing techniques. Our data show that both of *E. coli* and *S. aureus* were highly resistant to AMP. Ag NPs alone reduced growth in both bacterial isolates considerably. Growth declined drastically in both bacteria when AMP was used in combination with Ag NPs. The minimal inhibitory concentration of combined agents for *E. coli* was 20 μg/ml Ag NPs + 1 mg AMP/ml and for *S. aureus* was 10 μg/ml Ag NPs + 1 mg AMP/ml. The results show that the Ag NPs have great potentials in enhancing the antimicrobial activities of drugs that used to be ineffective against MDR bacteria. Administering combinations of antibiotic(s) with Ag NPs may help in treating patients suffering from infections caused by MDR bacteria. Further *in vivo* and *in vitro* investigations are required to evaluate the side effects of these combinations.**

***Index Terms*—Ampicillin, Antibacterial activity, Laser ablation, Nanosecond laser, Silver nanoparticles.**

## I. Introduction

The unnecessary prescriptions of antibiotics have increasingly made these drugs less effective in treating pathogen-associated diseases. As a consequence, antimicrobial resistance (AMR) spreads worldwide and becoming life-threatening problem (Al-Naqshbandi, Chawsheen and Abdulqader, 2019; WHO, 2020). To overcome this dilemma, physicians and researchers have tried various approaches and formulated different therapeutics for treatment (Weber-Dąbrowska, et al., 2006; Opal, 2016; Greenberg, et al., 2018). For their unique properties, nanoparticles (NPs) were thoroughly investigated in this regard (Hajipour, et al., 2012). Since silver NPs (Ag NPs) showed antibacterial effects against wide range of pathogenic bacteria, they were also studied for this purpose for many years now (Chaloupka, Malam and Seifalian, 2010). Ag NPs antibacterial effects have proven to be in a dose dependent manner (Marassi, et al., 2018) and presented as a promising agent for medical, industrial, and food packaging applications (Haider and Kang, 2015, Simbine, et al., 2019). The mechanisms by which the NPs eliminate bacteria are through: Attachment and penetration of bacterial cell wall, generation of reactive oxygen species (ROS), alterations in bacterial signaling pathways, and eventually cytolysis and leakage of proteins and carbohydrates (Rajesh, Dharanishanthi and Kanna, 2015; Dakal, et al., 2016).

As a strategy to eradicate multidrug-resistant (MDR) bacteria, scientists tried to promote the antibacterial effects of Ag NPs either by combining them with other NPs, such as $TiO_2$ (Hamad, et al., 2015c), or through applying different combinations of these NPs with antibiotics (Brown, et al., 2012; Allahverdiyev, et al., 2011). Furthermore, it has been confirmed that the purity of NPs modulates their antibacterial effects, the more pure NPs are the more bactericidal effects they have (Perito, et al., 2016).

Ag NPs are synthesized either by biological, chemical, or physical methods. Each of these methods has its own advantages and disadvantages (Zhang, et al., 2016). Laser produced Ag NPs, in deionized water, have considerable advantage over those produced through other methods. This is mainly due to their high purity as these NPs without any reductants, stabilizing and capping agents (Sportelli, et al., 2018). (Perito, et al., 2016) generated Ag NPs through pulsed laser ablation in liquid with a small average size in diameter and a narrow size distribution. It was concluded that the Ag NPs are significantly effective against Gram-positive bacteria (GPB) and Gram-negative bacteria (GNB). It was also reported that the minimal inhibitory concentration (MIC) values for laser produced Ag NPs at least comparable or lower

ARO-The Scientific Journal of Koya University
Vol. X, No.1 (2022), Article ID: ARO.10877, 7 pages
DOI: 10.14500/aro.10877
Received: 14 September 2022; Accepted: 15 June 2022
Regular research paper: Published: 30 June 2022
Corresponding author's e-mail: abubaker.hamad@soran.edu.iq

than those reported for chemically produced Ag NPs. Brasil, et al., 2018, reported synergism in the antibacterial activity of ternary mixtures involving Ag NPs, chitosan and the antibiotics azithromycin, levofloxacin, or tetracycline, against both GPB and GNB strains. The antibacterial activities were performed by *in vitro* antimicrobial susceptibility testing and checkerboard assays. Enhancement of the antibacterial activity was observed in the most combination and the MIC of the drugs was reduced to 97% from 37%. Hwang, et al., 2012, investigated synergistic combination effects between Ag NPs and the common antibiotics such as ampicillin (AMP), kanamycin, and chloramphenicol against different representative pathogenic bacteria. The antibacterial susceptibility and synergistic effects were confirmed through MIC and fractional inhibitory concentration index.

In this study, we tried to uncover the impact of laser produced Ag NPs on pathogenic MDR GPB and GNB. We also aimed to investigate the outcomes of applying different combinations of these NPs and AMP against the same types of bacteria.

## II. Experimental Set-Up

### A. Materials

Ag NPs were generated from a pure Ag bulk plate with a purity of 99.99% and dimensions of 25 mm × 25 mm × 2 mm. The sample was cleaned and sonicated before performing laser ablation in deionized water.

### B. Ag NPs Production

Ag NPs were produced by placing the target on the bottom of a Pyrex glass dish, containing about 15–20 ml of deionized water. A 7.22 W Green marker nanosecond laser (Semiconductor laser: Laserline-Laserval Violino) was used to produce the NPs with the following beam parameters: Wavelength $\lambda$ = 532 nm, frequency $f$ = 30 kHz, laser power $P$ = 7.22 W, pulse width $\tau$ = 5 ns, spot size $D$ = 50 μm, scan speed $v$ = 250 mm/s, laser pulse energy $E_{pulse}$ = 241 μJ, and laser fluence $F_{laser}$ = 12.2 J/cm$^2$. The water level above the sample target was about 2 mm. The ablation process continued for 10 min. The effects of water level on the laser beam intensity and focal length were considered. The experimental setup is shown in Fig. 1.

### C. Material Characterization

The colloidal NPs were characterized using a UV–VIS spectrometer (Analytic Jena, SPECORD 250, dual beam) and Transmission Electron Microscopy (TEM) (JEOL 2000 FX AEM + EDX model). A copper microgrid mesh was used for sample preparation for the TEM analyses. After placing a drop of colloidal NPs onto the mesh, the substrate was allowed to dry at room temperature. This process was repeated several times to deposit sufficient amounts of NPs on the copper microgrid mesh. A microbalance scale (Sartorius BL 210S, with readability $d$ = 0.1 mg) was used to indicate the concentration of the colloidal NPs by weighing the bulk targets before and after the production process of colloidal NPs. A hair dryer was used to dry the target samples after the NPs generation to record the weight of the ablated materials with greater accuracy.

### D. Antibacterial Activity Analysis

The MIC of bacterial strains, antibiotic, Ag NPs, and their combinations was determined using macrodilution method (Dakal, et al., 2016). The Ag NPs concentrations, antibiotic, and their combinations in 5 ml of nutrient broth were inoculated with 0.5 ml of tested bacteria at a concentration of $10^8$ colony-forming units (CFU)/ml. The values of MIC were determined as the lowest concentration of NPs that inhibited bacteria after 24 h of incubation at 37°C using McFarland DensiCHEK plus (bioMérieux, France) (a turbidimetric device for measuring suspended bacteria based on standards optically mimicking bacterial suspensions) (Zamora and Perez-Gracia, 2012). MDR strains of both *Staphylococcus aureus* (*S. aureus*) and *Escherichia coli* (*E. coli*) bacteria were identified using VITEK®2 compact system protocols.

## III. Results

### A. Generation of Ag NPs

Fig. 2a shows absorption spectra of laser fabricated Ag NPs by a nanosecond laser in deionized water. The Ag NPs have a weak and a strong absorption peak at 250 and 400 nm, respectively. The strong absorption peak formation is due to surface plasmon resonance of the Ag NPs, and the weak absorption peak formation is due to interband transitions (Hamad, Li and Liu, 2015a). Fig. 2b shows the size distribution of the NPs. The size of laser produced Ag NPs was between few nanometers to about 60 nm, and some of them were up to 120 nm. The average size of laser

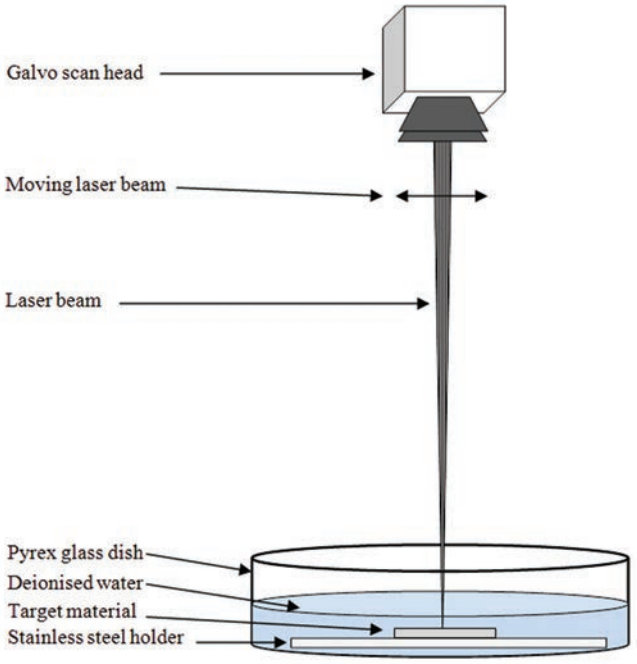


Fig. 1. Experimental set-up to produce Ag NPs in deionized water.

http://dx.doi.org/10.14500/aro.10877

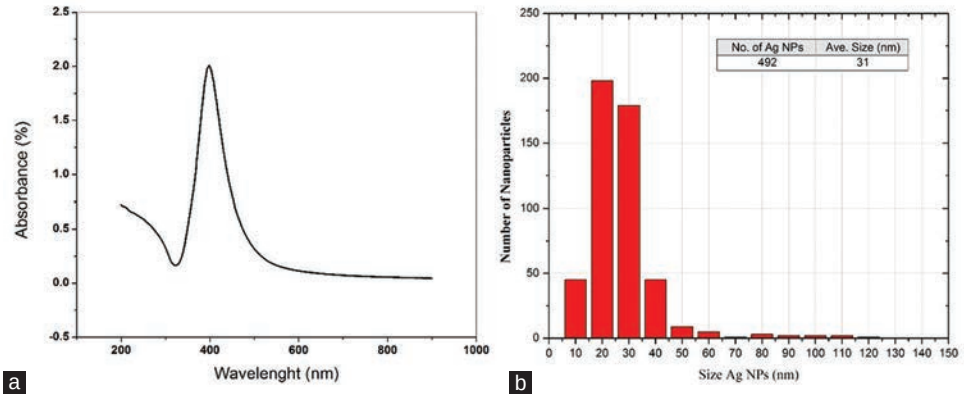


Fig. 2. (a) Absorption spectra of the Ag NPs and (b) size distribution histogram of the Ag NPs.

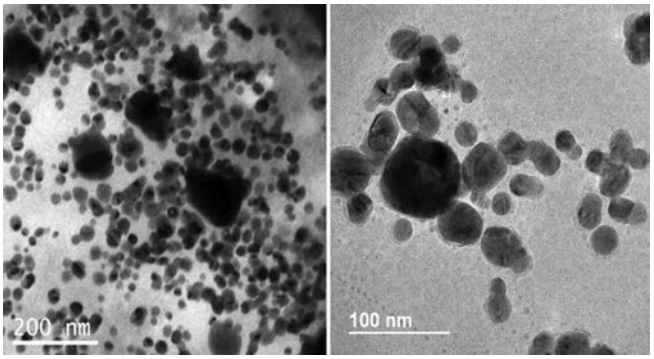


Fig. 3. TEM images of laser-generated Ag NPs in deionized water.

produced Ag NPs is about 31 nm.

Fig. 3 shows the TEM images of laser produced Ag NPs and their semi-spherical shapes. A big and few ultrafine Ag NPs can be seen in these images.

### *B. Antibacterial Activity of the Ag NPs With and Without Antibiotics*

Fig. 4 shows survival rates of *S. aureus*, GPB, and *E. coli*, GNB, after treating them with AMP and/or Ag NPs. Both *S. aureus* and *E. coli* were highly resistant to AMP. Our data show synergetic effects of the Ag NPs and AMP combinations in comparison with the control, Ag NPs, and AMP-treated groups. As shown in Fig. 4a, different combinations of Ag NPs + AMP inhibited the growth of *S. aureus* bacteria completely, even with the lowest Ag NPs concentration (20 μg/ml). In contrast to *S. aureus*, *E. coli* were somehow resistant to the first combination (Fig. 4b).

To uncover the impact of lower concentrations of Ag NPs (≤20 μg/ml) on the outcomes of combined treatments (AgNPs + AMP) against both types of bacteria, another experiment was carried out and the data are shown in Fig. 5.

Accordingly, it can be noted that the Ag NPs combined with AMP were more effective against *S. aureus* than *E. coli* bacteria. In addition, our data show that the impact of Ag NPs on the combinations (AgNPs + AMP) was in a dose-dependent manner (Fig. 5). As shown in Fig. 5a, the fourth treated group (10 μg/ml Ag NPs + AMP) was able to kill all *S. aureus* bacteria, whereas for *E. coli*, even 20 μg/ml Ag NPs in the fifth combination could not kill *E. coli* bacteria entirely and this was consistent with the previous experiment (Figs. 4b and 5b).

For more visibility, Fig. 6 shows the effects of our combinations on both GPB and GNB at concentrations equal or <20 μg/ml of Ag NPs and 1 mg/1 ml AMP. It can be seen that the impact of the combination is similar on both types of bacteria, but still is higher against *S. aureus* in comparison with *E. coli* bacteria.

## IV. Discussion

This study was carried out to address possible roles of Ag NPs in reversing AMP resistance in multidrug-resistant GPB and GNB. We used AMP in our experiments because typically, it is effective against both GPB and GNB. Unfortunately, there is growing evidence suggesting that AMP globally become less effective nowadays in eradicating different types of pathogenic bacteria, which is mainly due to the emergence of AMR in these bacteria as a consequence of excessive use of this drug (Katzung and Trevor, 2012; Krzyżaniak, Pawłowska and Bajorek, 2016; Chawsheen, AL-Naqshbandi and Abdulqader, 2020; Al-Naqshbandi, et al., 2021). In our experiments, bacteria were treated with Ag NPs, AMP, and their combinations. Efficacy of these treatments was evaluated by measuring survival rates of the studied bacteria. Our data show that Ag NPs have the ability to kill *S. aureus* and *E. coli* bacteria but to a limited level that is not exceeding 69%. Our data also show that *E. coli* bacteria are more resilient to Ag NPs than *S. aureus.* Combinations of AgNPs + AMP can effectively eliminate both types of bacteria, especially *S. aureus* that was more sensitive to all combinations than *E. coli.* In spite of the fact that Al-Ogaidi, 2017, used a different method for Ag NPs preparation, but our results came in agreement with theirs regarding different antibacterial activity of Ag NPs, AMP, and their combinations against the targeted bacteria (Al-Ogaidi, 2017).

The antibacterial activity of the Ag NPs can be explained on the basis of metallic silver (Ag°) and ionic silver ($Ag^+$) NPs which being released from the Ag NPs. In other words, the antibacterial activity of the Ag NPs is due to their ability to release Ag ions that are able to bind strongly with electron donor groups such as biological molecules consisting of O, N, and S (Juan, et al., 2010; Hajipour, et al., 2012; Sportelli, et al., 2018).

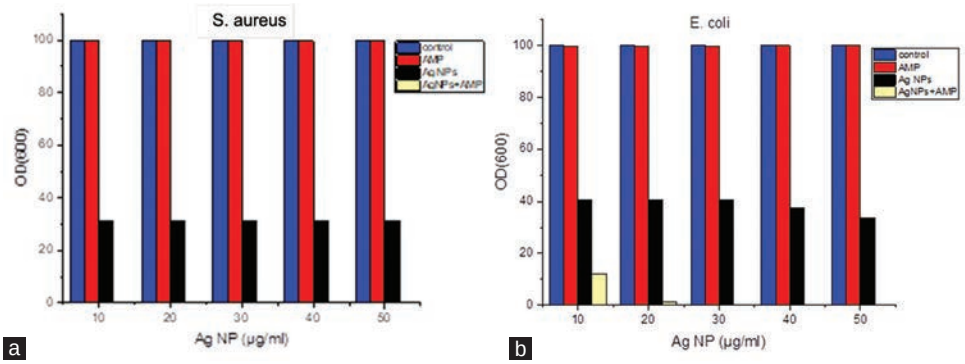


Fig. 4. Survival rate (optical density) of *Staphylococcus aureus* (a) and *Escherichia coli* (b) bacteria after been treated with or without AMP (1 mg/1 ml) and/or ascending concentrations of Ag NPs (10, 20 30, 40, and 50 µg/ml).

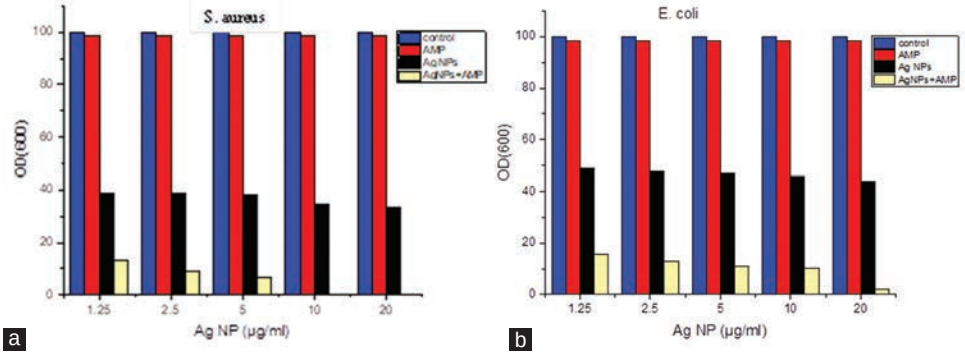


Fig. 5. Survival rate (optical density) of *Staphylococcus aureus* (a) and *Escherichia coli* (b) bacteria after been treated with or without AMP (1 mg/1 ml) and/or ascending concentrations of Ag NPs (1.25, 2.5, 5, 10, and 20 µg/ml).

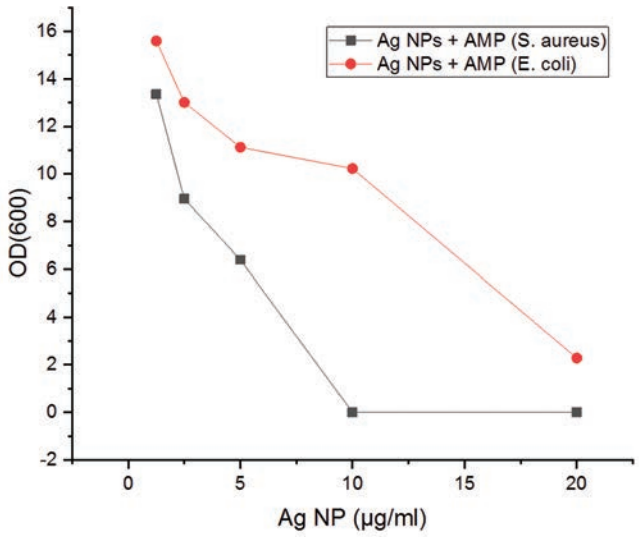


Fig. 6. Effects of (Ag NPs + AMP) on *Staphylococcus aureus* and *Escherichia coli* bacteria. In this experiment, 1 mg of AMP was used in combination with ascending concentrations of Ag NPs (1.25, 2.5, 5, 10, and 20 µg/ml).

### *A. Antibacterial Mechanism of Ag NPs*

There are several proposed mechanisms of action that may explain the impact of Ag NPs, separately or in combination with AMP, on bacterial survival rates. When Ag NPs attach to bacterial cell membrane important functions of this structure such as respiration and permeability will be disrupted (Feng, et al., 2000). Later on, these NPs will penetrate bacterial cells and causes formation of pits in their membranes. Ag NPs may also interact with thiol (organosulfur compound) groups of respiratory chain and transport proteins (sulfur-containing proteins), and eventually preventing them from functioning properly (Morones, et al., 2005). In addition, silver metal or silver ion leads to generation of free radicals and ROS which may damage DNA and denature proteins (Liao, Li and Tjong, 2019). Beside Ag NPs, Ag ions which release either from Ag metals or Ag NPs may interact with nucleic acids and cytoplasmic components, or lead to inhibition of respiratory chain enzymes. These ions may also damage membrane permeability (Russell and Hugo, 1994), thus affecting passive diffusion rate across cell membrane. Furthermore, Ag ions may take role in the adhesion of the Ag NPs to the cell membrane through offering electrostatic interactions between the Ag ions and the negatively charged cell membrane. As a result, structural integrity of the bacterial cell may be compromised through cytoplasmic shrinkage that detaching it from the cell wall and consequently lead to bacterial death (Prasher, Singh and Mudila, 2018). More detail of the antibacterial mechanism of the Ag NPs can be found in our previous review paper (Hamad, Khashan and Hadi, 2020).

### *B. Antibacterial Mechanism of Ag NPs Conjugated AMP*

In the case of Ag NPs conjugated AMP, Allahverdiyev, et al., 2011, reported that the Ag NPs produce a complex with

antibiotics through possible binding sites which include S, N, and OH (Allahverdiyev, et al., 2011). Interactions between Ag NPs and AMP increase the density and concentration of the antibiotic on the surface of the bacteria. In this regard, Ag NPs play the role of the carrier that deliver and facilitate the way in for AMP "hydrophobic compound" to reach inside the bacterial cell. Afterword, the cell wall will be destroyed by AMP through its well-known mechanism of action and then increases its permeability for these NPs (Biggs and Kucers, 1986). Ag NPs prevent DNA from unwinding and consequently interfere with the duplication process in the affected bacteria (Fayaz, et al., 2010; Allahverdiyev, et al., 2011). Furthermore, Fayaz, et al., 2010, reported that Ag-AMP core-shell compound interacts with the bacteria over the cell wall which prevents the generation of cross-links in the peptidoglycan layers, as a result, the cell wall will be lysis (Fig. 7).

Functionalized Ag NPs, capped by stable citrate, were used as a sensing probe for detection of AMP in urine samples based on color changing and shift localized surface plasmon resonance to longer wavelength known as red shift phenomenon. They found out that pH and temperature have a direct impact on hydrolysis of AMP. After the addition of the antibiotic, Ag NPs aggregated and then AMP conjugates with the surface of the these NPs through sulfur bond and electrostatic force ($F_e$), and replacement of citrate ions from the surface of NPs will take place (Shrivas, et al., 2017).

Even though our data showing that *S. aureus* are more sensitive than *E. coli* to Ag NPs, there are some studies suggesting that "at the same concentration," Ag NPs are more effective against GNB than GPB because of their thinner cell wall (Pandey, et al., 2014).

In the case of *E. coli* bacteria, silver ions interact with the respiratory chain enzymes and prevent the respiratory chain at a low potential point (Holt and Bard, 2005). The Ag NPs in the bacterial cell tend to "interfere with the bacterial growth signaling pathway by modulating tyrosine phosphorylation of putative peptide substrates critical for cell viability and division (Shrivastava, et al., 2007)." A low molecular weight area in the bacterial cell will be produced when the Ag NPs enter the cell and then the bacteria aggregate to protect their DNA. After that, the NPs interact with the respiratory chain, which leads to the death of bacterial cell (Rai, Yadav and Gade, 2009). In the case of GPB, *S. aureus*, peptidoglycan layer is 30 nm thick and negatively charged, which makes it less vulnerable against Ag NPs in comparison with the GNB, *E. coli*, where the thickness of peptidoglycan layer is about 3–5 nm. The thickness and negative charge of the peptidoglycan layer renders the Ag ions produced from Ag metals inactive, as a result, makes GPB to be more resistant against antimicrobial drugs. In addition, lipopolysaccharides (LPS) part in cell membrane of the GNB prevents and protects the microorganisms from the chemical reactions and keeps the structural integrity of the cell membrane. However,

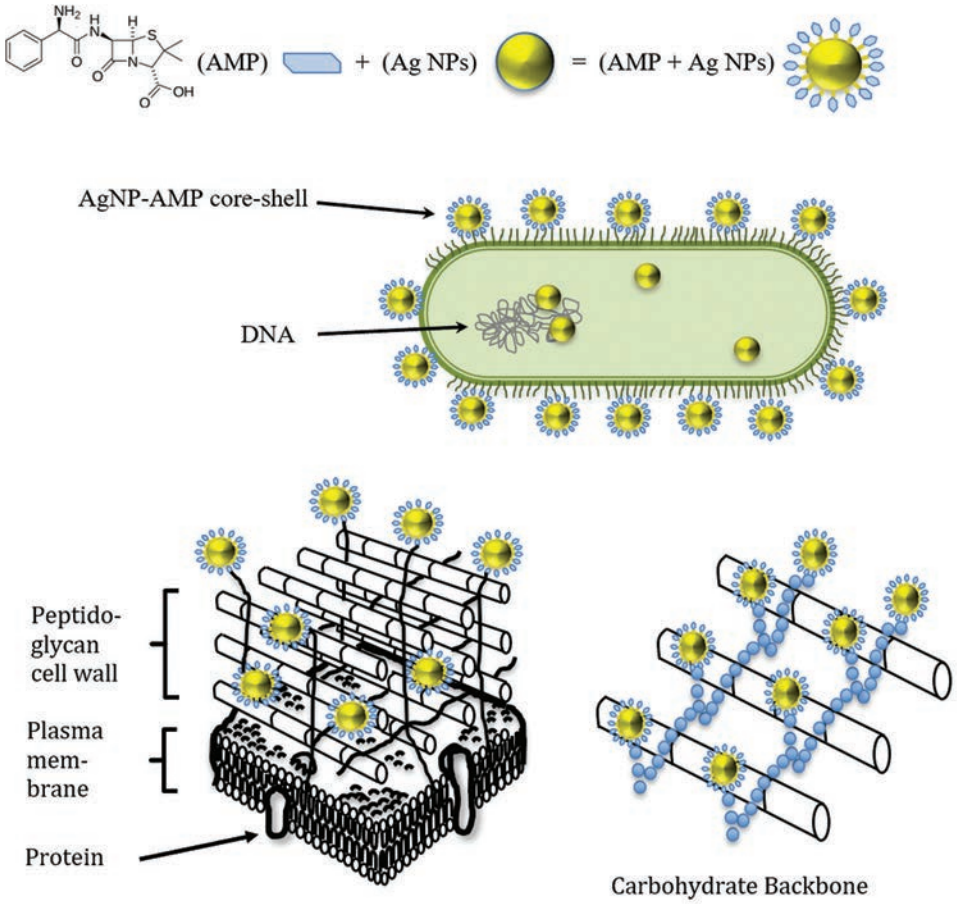


Fig. 7. Possible mechanism of AMP conjugated Ag NPs against microorganisms (Fayaz, et al., 2010).

negatively charged LPS promotes the connection between the NPs and the cell membrane which makes the bacterial cells more susceptible to antimicrobial drugs (Prasher, Singh and Mudila, 2018).

Laser-generated Ag NPs have negative zeta potentials of about −42.3 mV (zeta deviation = 7.65 mV) (Hamad, et al., 2015b), thus, the NPs are negatively charged particles. On the other hand, *S. aureus* bacteria are GPB, they are positively charged bacteria. The electrostatic interaction between NPs and bacteria is the key prominent force facilitating the Ag NPs binding to surface of *S. aureus* bacteria. Due to that, Ag NPs combined with AMP are more effective against *S. aureus* than *E. coli* bacteria. The surface electrostatic interaction changes in accordance with surface charge of the nanomaterials. In the case of the positively charged Ag NPs, strong electrostatic forces help in combining of positively charged Ag NPs to GNB or negatively charged bacterial outer membrane or cell wall (Poh, et al., 2018). Last but least, the surface charge properties of the Ag NPs when conjugated with the AMP should be taken into account, as the surface charge of the NPs is related to the NPs' stability in the aqueous solution (Mafuné, et al., 2000).

## V. Conclusions

The Ag NPs which fabricated using a nanosecond laser in deionized water have the ability to generate bactericidal effects against both MDR GPB and GNB. Different combinations of Ag NPs and AMP are able to reverse antibiotic resistance in these bacteria; this is more likely through compromising the structural integrity of cell membrane, damaging cytoplasmic compartments, interfering with cellular signaling pathways, and blocking DNA duplication process.

## VI. Authors' Contribution Statement

AH, AA, and MC: Evenly participated in designing the research. AA: Carried out biological experiments. AH: Prepared and validate Ag NPs. MC and AH: Evenly contributed in writing the manuscript.

## References

Allahverdiyev, A.M., Kon, K.V., Abamor, E.S., Bagirova, M. and Rafailovich, M., 2011. Coping with antibiotic resistance: Combining nanoparticles with antibiotics and other antimicrobial agents. *Expert Review of Anti-Infective Therapy*, 9, pp.1035-1052.

Al-Naqshbandi, A.A., Chawsheen, M.A. and Abdulqader, H.H., 2019. Prevalence and antimicrobial susceptibility of bacterial pathogens isolated from urine specimens received in Rizgary hospital-Erbil. *Journal of Infection and Public Health*, 12, pp.330-336.

Al-Naqshbandi, A.A., Hassan, H.A., Chawsheen, M.A. and Qader, H.H.A., 2021. Categorization of bacterial pathogens present in infected wounds and their antibiotic resistance profile recovered from patients attending rizgary hospital-Erbil. *ARO The Scientific Journal of Koya University*, 9, pp.64-70.

Al-Ogaidi, I.A. Z., 2017. Detecting the antibacterial activity of green synthesized silver (Ag) nanoparticles functionalized with ampicillin (Amp). *Baghdad Science Journal*, 14, pp.117-125.

Biggs, B.A. and Kucers, A., 1986. Penicillins and related drugs. *The Medical Journal of Australia*, 145, pp.607-611.

Brasil, M.S., Filgueiras, A.L., Campos, M.B., Neves, M.S., Eugênio, M., Sena, L.A., Sant'anna, C.B., Silva, V.L.D., Diniz, C.G. and Sant'ana, A.C., 2018. Synergism in the antibacterial action of ternary mixtures involving silver nanoparticles, chitosan and antibiotics. *Journal of the Brazilian Chemical Society*, 29, pp.2026-2033.

Brown, A.N., Smith, K., Samuels, T.A., Lu, J., Obare, S.O. and Scott, M.E., 2012. Nanoparticles functionalized with ampicillin destroy multiple-antibiotic-resistant isolates of *Pseudomonas aeruginosa* and *Enterobacter aerogenes* and methicillin-resistant *Staphylococcus aureus*. *Applied. Environmental. Microbiology*, 78**,** 2768-2774.

Chaloupka, K., Malam, Y. and Seifalian, A.M., 2010. Nanosilver as a new generation of nanoproduct in biomedical applications. *Trends in Biotechnology*, 28, pp.580-588.

Chawsheen, M.A., AL-Naqshbandi, A.A. and Abdulqader, H.H., 2020. Bacterial profile and antimicrobial susceptibility of isolates recovered from lower respiratory tract infection for patients in Rizgary hospital, Erbil. *Aro-the Scientific Journal of Koya University*, 8, pp.64-70.

Dakal, T.C., Kumar, A., Majumdar, R.S. and Yadav, V., 2016. Mechanistic basis of antimicrobial actions of silver nanoparticles. *Frontiers in Microbiology*, 7, pp.1831.

Fayaz, A.M., Balaji, K., Girilal, M., Yadav, R., Kalaichelvan, P.T. and Venketesan, R., 2010. Biogenic synthesis of silver nanoparticles and their synergistic effect with antibiotics: A study against gram-positive and gram-negative bacteria. *Nanomedicine*, 6, pp.103-109.

Feng, Q.L., Wu, J., Chen, G.Q., Cui, F.Z., Kim, T.N. and Kim, J.O., 2000. A mechanistic study of the antibacterial effect of silver ions on *Escherichia coli* and *Staphylococcus aureus*. *Journal of Biomedical Materials Research*, 52, pp.662-668.

Greenberg, M., Kuo, D., Jankowsky, E., Long, L., Hager, C., Bandi, K., MA, D., Manoharan, D., Shoham, Y. and Harte, W., 2018. Small-molecule AgrA inhibitors F12 and F19 act as antivirulence agents against gram-positive pathogens. *Scientific Reports*, 8, pp.1-12.

Haider, A. and Kang, I.K., 2015. Preparation of silver nanoparticles and their industrial and biomedical applications: A comprehensive review. *Advances in Materials Science and Engineering*, 2015, p.165257.

Hajipour, M.J., Fromm, K.M., Ashkarran, A.A., De Aberasturi, D.J., De Larramendi, I.R., Rojo, T., Serpooshan, V., Parak, W.J. and Mahmoudi, M., 2012. Antibacterial properties of nanoparticles. *Trends in Biotechnology*, 30, pp.499-511.

Hamad, A., Li, L. and Liu, Z., 2015a. A comparison of the characteristics of nanosecond, picosecond and femtosecond lasers generated Ag, $TiO_2$ and Au nanoparticles in deionised water. *Applied Physics A*, 120, pp.1247-1260.

Hamad, A., Li, L., Liu, Z., Zhong, X.L. and Wang, T., 2015c. Picosecond laser generation of Ag-$TiO_2$ nanoparticles with reduced energy gap by ablation in ice water and their antibacterial activities. *Applied Physics A*, 119, pp.1387-1396.

Hamad, A., Li, l., Liu, Z., Zhong, X.L., Liu, H. and Wang, T., 2015b. Generation of silver titania nanoparticles from an Ag-Ti alloy via picosecond laser ablation and their antibacterial activities. *Royal Society of Chemistry Advances*, 5, pp.72981-72994.

Hamad, A.H, Khashan, K.S. and Hadi, A.A., 2020. Silver nanoparticles and silver ions as potential antibacterial agents. *Journal of Inorganic and Organometallic Polymers and Materials*, 30, 1-18.

Holt, K.B. and Bard, A.J., 2005. Interaction of silver (I) ions with the respiratory chain of *Escherichia coli:* An electrochemical and scanning electrochemical microscopy study of the antimicrobial mechanism of micromolar Ag+. *Biochemistry*, 44, pp.13214-13223.

Hwang, I.S., Hwang, J.H., Choi, H., Kim, K.J. and Lee, D.G., 2012. Synergistic effects between silver nanoparticles and antibiotics and the mechanisms involved. *Journal of Medical Microbiology*, 61, pp.1719-1726.

Juan, L., Zhimin, Z., Anchun, M., Lei, L. and Jingchao, Z., 2010. Deposition of silver nanoparticles on titanium surface for antibacterial effect. *International Journal of Nanomedicine*, 5, p.261.

Katzung, B.G. and Trevor, A.J., 2012. *Basic and Clinical Pharmacology*. McGraw Hill Professional, New York.

Krzyżaniak, N., Pawłowska, I. and Bajorek, B., 2016. Review of drug utilization patterns in NICU s worldwide. *Journal of Clinical Pharmacy and Therapeutics*, 41, pp.612-620.

Liao, C., Li, Y. and Tjong, S.C., 2019. Bactericidal and cytotoxic properties of silver nanoparticles. *International Journal of Molecular Sciences*, 20**,** 449.

Mafuné, F., Kohno, J.Y., Takeda, Y., Kondow, T. and Sawabe, H., 2000. Structure and stability of silver nanoparticles in aqueous solution produced by laser ablation. *The Journal of Physical Chemistry B*, 104, pp.8333-8337.

Marassi, V., Di Cristo, L., Smith, S.G.J., Ortelli, S., Blosi, M., Costa, A.L., Reschiglian, P., Volkov, Y. and Prina-Mello, A., 2018. Silver nanoparticles as a medical device in healthcare settings: A five-step approach for candidate screening of coating agents. *Royal Society Open Science*, 5, pp.171113.

Morones, J.R., Elechiguerra, J.L., Camacho, A., Holt, K., Kouri, J.B., Ramírez, J.T. and Yacaman, M.J., 2005. The bactericidal effect of silver nanoparticles. *Nanotechnology*, 16, pp.2346-2353.

Opal, S.M., 2016. Non-antibiotic treatments for bacterial diseases in an era of progressive antibiotic resistance. *Critical Care*, 20, p.397.

Pandey, J.K., Swarnkar, R., Soumya, K.K., Dwivedi, P., Singh, M.K., Sundaram, S. and Gopal, R., 2014. Silver nanoparticles synthesized by pulsed laser ablation: As a potent antibacterial agent for human enteropathogenic gram-positive and gram-negative bacterial strains. *Applied Biochemistry and Biotechnology*, 174, pp.1021-1031.

Perito, B., Giorgetti, E., Marsili, P. and Muniz-Miranda, M., 2016. Antibacterial activity of silver nanoparticles obtained by pulsed laser ablation in pure water and in chloride solution. *Beilstein Journal of Nanotechnology*, 7, pp.465-473.

Poh, T.Y., Ali, N.A.B., Mac Aogáin, M., Kathawala, M.H., Setyawati, M.I., Ng, K.W. and Chotirmall, S.H., 2018. Inhaled nanomaterials and the respiratory microbiome: Clinical, immunological and toxicological perspectives. *Particle and Fibre Toxicology*, 15, p.46.

Prasher, P., Singh, M. and Mudila, H., 2018. Silver nanoparticles as antimicrobial therapeutics: Current perspectives and future challenges. *3 Biotechnology*, 8, p.411.

Rai, M., Yadav, A. and Gade, A., 2009. Silver nanoparticles as a new generation of antimicrobials. *Biotechnology Advances*, 27, pp.76-83.

Rajesh, S., Dharanishanthi, V. and Kanna, A.V., 2015. Antibacterial mechanism of biogenic silver nanoparticles of *Lactobacillus acidophilus*. *Journal of Experimental Nanoscience*, 10, pp.1143-1152.

Russell, A. and Hugo, W., 1994. Antimicrobial activity and action of silver. *Progress in Medicinal Chemistry*, 31, pp.351-70.

Shrivas, K., Sahu, J., Maji, P. and Sinha, D., 2017. Label-free selective detection of ampicillin drug in human urine samples using silver nanoparticles as a colorimetric sensing probe. *New Journal of Chemistry*, 41, pp.6685-6692.

Shrivastava, S., Bera, T., Roy, A., Singh, G., Ramachandrarao, P. and Dash, D., 2007. Characterization of enhanced antibacterial effects of novel silver nanoparticles. *Nanotechnology*, 18, p.225103.

Simbine, E.O., Rodrigues, L.D.C., Lapa-Guimaraes, J., Kamimura, E.S., Corassin, C.H. and De Oliveira, C.A.F., 2019. Application of silver nanoparticles in food packages: A review. *Food Science and Technology*, 67, pp.1942-1956.

Sportelli, M.C., Izzi, M., Volpe, A., Clemente, M., Picca, R.A., Ancona, A., Lugarà, P.M., Palazzo, G. and Cioffi, N., 2018. The pros and cons of the use of laser ablation synthesis for the production of silver nano-antimicrobials. *Antibiotics* (*Basel*), 7, p.67.

Weber-Dąbrowska, B., Zimecki, M., Kruzel, M., Kochanowska, I. and Łusiak-Szelachowska, M., 2006. Alternative therapies in antibiotic-resistant infection. *Advances Medical Sciences*, 51, pp.242-244.

World Health Organization, 2020. *Antimicrobial Resistance*. Geneva: World Health Organization. Available from: https://www.who.int/news-room/fact-sheets/detail/antimicrobial-resistance [Last accessed on 2020 Jul 22].

Zamora, L.L. and Perez-Gracia, M.T., 2012. Using digital photography to implement the McFarland method. *Journal of the Royal Society Interface*, 9, pp.1892-1897.

Zhang, X.F., Liu, Z.G., Shen, W. and Gurunathan, S., 2016. Silver nanoparticles: Synthesis, characterization, properties, applications, and therapeutic approaches. *International Journal of Molecular Sciences*, 17, p.1534.

# Design, Modeling, and Characterization of Hot Electron Light Emission and Lasing in Semiconductor Heterostructure-VCSOA with Optical Gain up to 36 dB

Hawro I. Yaba and Faten A. Chaqmaqchee

Department of Physics, Faculty of Science and Health, Koya University, Koya, Kurdistan Region - F.R. Iraq

***Abstract*—Vertical-cavity semiconductor optical amplifiers (VCSOAs) are interesting devices for optical communication applications. In this work, we have studied the characteristics of gain spectra and amplifier bandwidth in reflection mode at 1300 nm *GaInNAs/GaAs* hot electron light emission and lasing in semiconductor heterostructure-VCSOA structure using MATLAB program. The device contains 16 $Ga_{0.7}In_{0.3}N_{0.038}As_{0.962}$ multiple quantum wells (QWs) in its intrinsic region; the active region is bounded between eight pairs of *GaAs/AlAs* top distributed Bragg reflectors (DBRs) mirror and 25 pairs of *AlAs/GaAs* bottom DBRs mirror. Simulation results suggest that the resonance cavity of QW of HILLISH-VCSOA is varied with temperature and number of DBRs periods. We compare the relation between the wavelength and gain at a different single-pass gain in both reflection and transmission modes. The highest gain at around 36 dB is observed in reflection mode. Moreover, we calculated the amplifier bandwidth at different periods of top mirror's reflectivity, in which when the peak reflection gains increases, the amplifier bandwidth decreases.**

***Index Terms*—Hot electron, Vertical-cavity semiconductor optical amplifier, *AlAs* DBRs, *GaInNAs/GaAs* QWs, optical characterization.**

## I. Introduction

III–V compound semiconductors have aided the development of modern electrical and optoelectronic devices significantly. They offer a wide range of potential uses in nanometer-scale optoelectronics applications (Razeghi, 2000; Chaqmaqchee and Lott, 2020; Lee, et al., 2022). Adding small quantities of nitrogen into III–V alloys have a significant influence on the fundamental band gap (Yu, et al., 2000) and cause a redshift in emission wavelength (Zhao, et al., 2005). This discovery has applications in technology of dilute III–V nitride semiconductors devices. The bandgap of the *GaInNAs* semiconductor layer can be worked by incorporating N into *InGaAs*; increasing the N concentration in *GaInNAs* reduces the energy gap, resulting in higher refractive index values ( Walukiewicz, et al., 1999; Ungan, et al., 2013). As a result, the propensity for the refractive index to grow as the bandgap energy decreases is the same as in traditional III–V semiconductors (Uesugi, K., Morooka, N. and Suemune, I., 1999). The dilute III–V nitrides compound can be used in long-wavelength optoelectronic as local area network and metropolitan area network (Gönül, Köksal and Bakır, 2007).

*GaInNAs* may be grown pseudomorphically on GaAs in the 1.3 μm optical communications window, enabling the utilization of high-quality Al(Ga)As/GaAs distributed Bragg reflectors (DBRs) using MatLab program (Abubaker, S.A., 2021; Chaqmaqchee, et al., 2011; Chaqmaqchee, 2021) with possible cost savings over *InP*-based techniques. Vertical cavity surface-emitting lasers (VCSELs) and vertical-cavity semiconductor optical amplifiers (VCSOAs) are closely related and have many of the same advantages. They are probably low-cost devices that can be used instead of in-plane SOAs (Royo, Koda and Coldren, 2002). They have low fiber-coupling losses and low noise figures and can be fabricated into two-dimensional arrays, unlike in-plane SOAs and they allow high-fiber coupling efficiency and are insensitive to polarization (Hepburn, et al., 2005). An important feature of VCSOAs is the narrow signal gain bandwidth, which allows VCSOAs to function as optical filters with gain. The optical gain not only depends on the wavelength of the incidence signal but also on the intensity inside the semiconductor optical amplifier (Kimura, et al., 2003).

The VCSOA (Bjorlin, 2002; Gauss, et al., 2011) can be amended into hot electron light emission and lasing in semiconductor heterostructure (HELLISH)-VCSOA structure, which differs from the HELLISH-VCSEL structure by reducing the number of top DBR layers (Wah and Balkan, 2004; Chaqmaqchee, 2016). HILLISH-VCSOA is a device that utilizes hot carrier transport parallel to the layers of the p–n junction. The junction contains a *GaInNAs*/*GaAs* quantum well (QW) in the depletion region. Briefly, the electric field

ARO-The Scientific Journal of Koya University
Vol. X, No. 1 (2022), Article ID: ARO.10969, 5 pages
DOI: 10.14500/aro.10969
Received: 25 April 2022; Accepted: 27 June 2022
Regular research paper: Published: 30 June 2022
Corresponding author's e-mail: hawro.ibrahim7@gmail.com

http://dx.doi.org/10.14500/aro.10969

applied along the layers provides heating of the electrons and holes in their respective channels through tunneling and thermionic emission processes (O'brien, et al., 1999). Because electrons have smaller effective masses and higher motilities, are excited to higher energy levels than holes. Therefore, they have a higher non-equilibrium temperature than the hole. Hot electrons are injected by the main tunneling into the QW, resulting in emitting light at longer wavelengths (Chaqmaqchee, Balkan and Herrero, 2012).

In this work, the influence of temperature on the cavity resonance together with active material bandgap energy of the HILISH-VCSOA was studied using MatLab program. We compare the gain spectra in both reflection mode and transmission modes at different single-pass gain. In addition, the amplifier bandwidth as a function of peak reflection gain is calculated at fixed bottom DBR mirrors and different number of top DBR periods.

## II. Design, Modeling, and Simulation Method

The VCSOA design is adapted here using MatLab Program to make a *GaInNAs*-based HELLISH-VCSOA structure, which differs from the HELLISH-VCSEL structure by reducing the number of top DBR layers. The VCSOA design is shown in Fig. 1a and is optimized at a wavelength of 1300 nm. The active region is arranged with a cavity length of $3\lambda/(2n_c)$ and formed by four ($Ga_{0.7}In_{0.3}N_{0.038}As_{0.962}$)/*GaAs* QWs and each stack with another four layers. It is enclosed between two 150 nm thick doped cladding layers Si doped ($n$=1×10$^{17}$ cm$^{-3}$) on the bottom side, and C doped (p=n=1×10$^{17}$ cm$^{-3}$) on the top side and bounded by 25 periods *GaAs*/*AlAs* bottom DBRs and eight periods *GaAs*/*AlAs* top DBRs, both DBRs are undoped, except for the first period in each mirror joining the cavity (Balkan, et al., 2000). The use of MQWs, placed at the electric field antinode of 3/2 cavity length, is done to provide optical gain Fig. 1b. The number of QW can be modified from 3 to 9 according to HELLISH-VCOSAs design. The most important problem with such devices is the variation of resonance wavelength, which increases with increasing the number of QWs. Obviously, the maximum photon energy in the device is for a case with 3 QWs which can be found elsewhere (Ghadimi and Ahmadzadeh, 2020).

The gains in reflection mode ($G_R$) and transmission mode ($G_t$) operation (Adams, et al., 1985; Bjorlin, et al., 2001) can be calculated using:

$$G_r = \frac{\left(\sqrt{R_f} - \sqrt{R_b}\, g_s\right)^2 + 4\sqrt{R_f R_b}\, g_s \sin^2 \varnothing}{\left(1 - \sqrt{R_b}\, g_s\right)^2 + 4\sqrt{R_f R_b}\, g_s \sin^2 \varnothing} \quad (1)$$

$$G_t = \frac{(1-R_f)(1-R_b) g_s}{\left(1 - \sqrt{R_b}\, g_s\right)^2 + 4\sqrt{R_f R_b}\, g_s \sin^2 \varnothing} \quad (2)$$

where, $R_f$, $R_b$, and $g_s$ are the reflectivity of the top DBR mirror,the reflectivity of the bottom DBR mirror, and the single-pass gain, respectively.

The QW material gain ($g$) can be approximated by Piprek, Bjorlin and Bowers, 2001:

$$g = g_0 \ln\left(\frac{N + N_s}{N_{tr} - N_s}\right) \quad (3)$$

where, $g_0$, $N$, $N_{tr}$, and $N_s$ are the gain coefficient, the QW carrier densitythe transparency carrier density concentration, and fitting parameters, respectively.

The gain bandwidth in the reflected and transmitted modes can be given by Bjorlin, et al., 2001; Erol, 2008:

$$\Delta f_r = \frac{c}{\pi n L}.arcsin\left[4\sqrt{R_f R_b}\, g_s \left(\frac{1}{\left(1 - \sqrt{R_f R_b}\, g_s\right)^2} - \frac{2}{\left(\sqrt{R_t} - \sqrt{R_b}\right)^2}\right)\right]^{-1/2} \quad (4)$$

$$\Delta f_t = \frac{c}{\pi n L}.arcsin\left[\frac{\left(1 - \sqrt{R_f R_b}\, g_s\right)^2}{4\sqrt{R_f R_b}\, g_s}\right]^{1/2} \quad (5)$$

where, $c$ and $L$ are the velocity of light in vacuum and the cavity length, respectively.

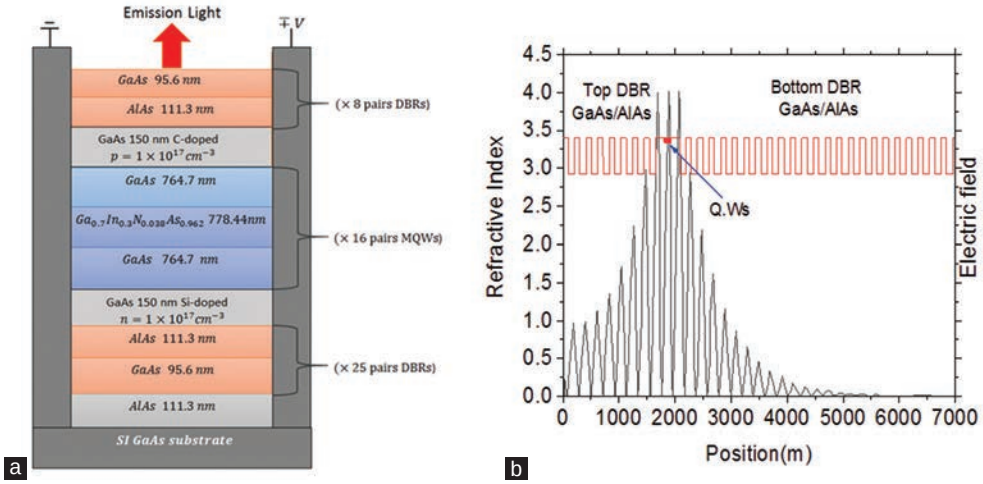


Fig. 1. (a) The schematic diagram illustrates the layer structure of the simple bar HELLISH-VCSOA, (b) refractive index profile, and the electric field intensity distribution that forms standing.

## III. Results and Discussion

The resonance cavity of HELLISH-VCSOA at various temperatures is shown in Fig. 2. The result shows that when the temperature increases the resonance cavity of the QW shifts to a longer wavelength and the resonance cavity matches with a longer wavelength (1300 nm) due to a higher temperature of 300 K (Su, et al., 2006).

The reflectivity spectra of the *GaInNAs* of HELLISH-VCSOA structure with different periods (8, 11, 14, and 17) are shown in Fig. 3. When the number of top mirrors of *AlAs*/*GaAs* increased, the reflectivity increased larger than 99% which lead to a high gain bandwidth, whereas low mirror reflectivity causes a lower gain and high saturation power.

The temperature dependence of the cavity resonance together with the *GaInNAs*/*GaAs* active material bandgap energy curve is plotted in Fig. 4. The behavior of an active medium area is extremely changed with temperature. It shows from the figure that by increasing temperature to 300 K, the material bandgap reduced to ~1.005 eV which used for long-wavelength optical communication system. Theoretically, a redshift of the active material peak wavelength at a rate of 0.38 nm/K was predicted, whereas the resonance cavity moves with the temperature at around 0.18 nm/K (Potter and Balkan, 2004).

In Figs. 5 and 6, the gain spectra in reflection and transmission modes for *GaInNAs*/*GaAs* HELLISH-VCSOAs can be plotted according to Equations 1 and 2 with using various single-pass gains of 1.068, 1.07, 1.072, 1.074, and 1.076. By increasing the single-pass gain from 1.068 to 1.076, the gain spectra are increased from nearly 10.09 dB to 34.838 as shown in Fig. 5 and the gain increased from 10.2 to the as shown in Fig. 6, whereas the bandwidth gets narrower at about 0.0008 nm with increasing single-pass gain. The optical gain in reflection mode is higher than the optical gain in transmission mode under using same single-pass gain. Thus, the higher gain with narrow bandwidth can be useful for filtering application (Chaqmaqchee, et al., 2020). The inset

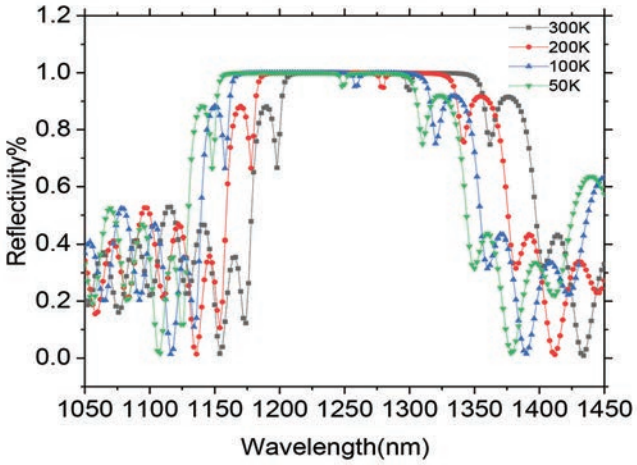


Fig. 2. The resonance cavity of quantum well as a function of different temperatures.

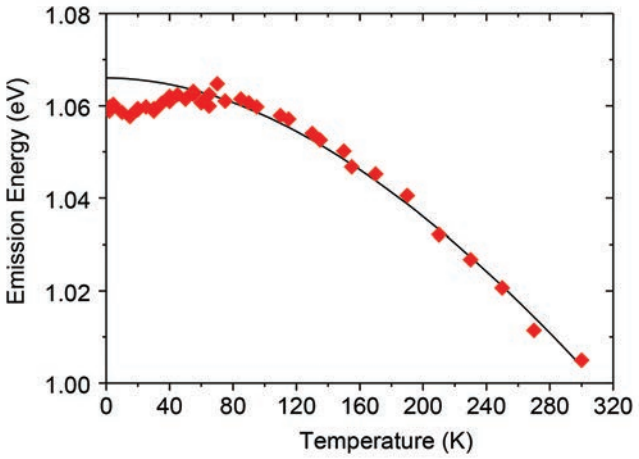


Fig. 4. The red square points represent the calculated temperature dependence of bandgap energy for the device active area (*GaInNAs*/*GaAs* QW) using the BAC model, whereas the expected cavity resonance position is plotted with a continuous line.

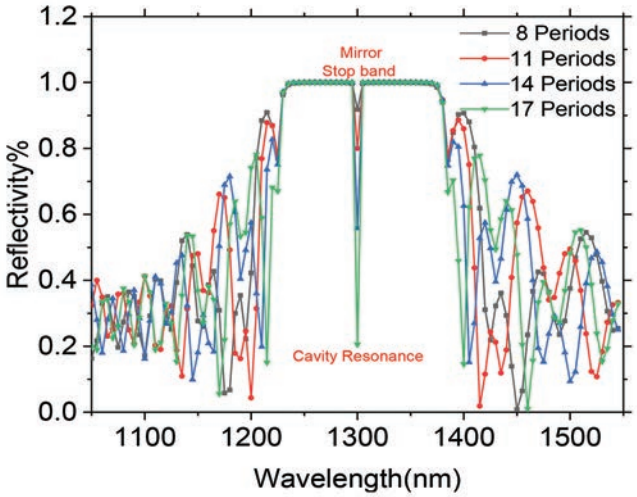


Fig. 3. Reflectivity spectrum for a cavity *GaInNAs* VCSOAs of refractive index (n=3.34) placed between varied top DBRs periods and fixed bottom DBRs of 25 periods and cavity resonance at 1300 nm.

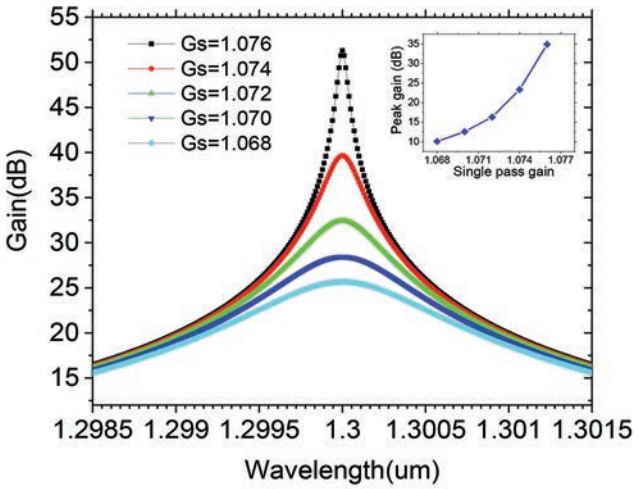


Fig. 5. Reflection VCSOA gains spectra for different *Gs* values, where $R_f$=86.7%, $R_b$=99.7%, and $L_c$=3λ/2$L_c$, the inset shows maximum peak gain versus single-pass gain.

http://dx.doi.org/10.14500/aro.10969

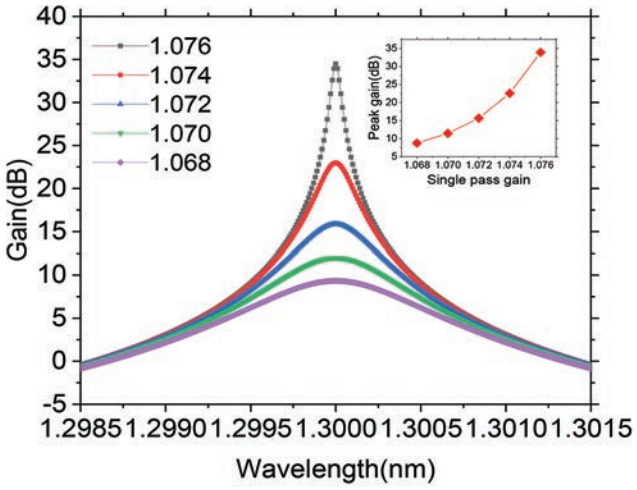


Fig. 6 Transmission VCSOA gains spectra for different *Gs* values, where $R_f$=86.7%, $R_b$=99.7%, and $L_c$=3λ/2$L_c$, the inset shows maximum peak gain versus single-pass gain.

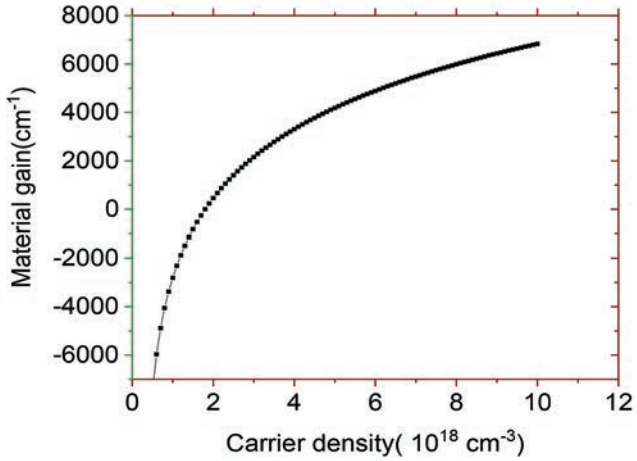


Fig. 7. Material gain versus carrier density curve for *GaInNAs*/*GaAs* QW active region.

of figures shows the peak gains versus single-pass gain. As a results, the optical gain in reflection mode is about 34.838 *dB* and in transmission mode is around 34.069 *dB*.

Fig. 7 illustrates the material gain against the carrier density curve for *GaInNAs*/*GaAs* QW active region. The gain was calculated using the Equation 3, which recommended a fit parameter of $g_0$=3650 $cm^{-1}$ and transparency carrier density parameter of $N_{tr}$=1.8×$10^{18}$ $cm^{-3}$ (Chaqmaqchee, 2016). The material gain depends on QW of carrier density and its logarithmic inclination, but this model allows for an accurate description of the material gain at low carrier densities. It shows at lower and higher carrier densities, the logarithmic gain model is limited, as it does not calculate the saturation of the material, where the gain cannot be estimated from a linear profile.

Fig. 8 shows amplifier bandwidth versus peak reflection gain for *GaInNAs* of 25 periods of bottom DBR mirrors and different top DBR mirrors reflectivity. The figure shows that when the peak reflection gains increase, the amplifier bandwidth decreases. High gain and shorter amplifier

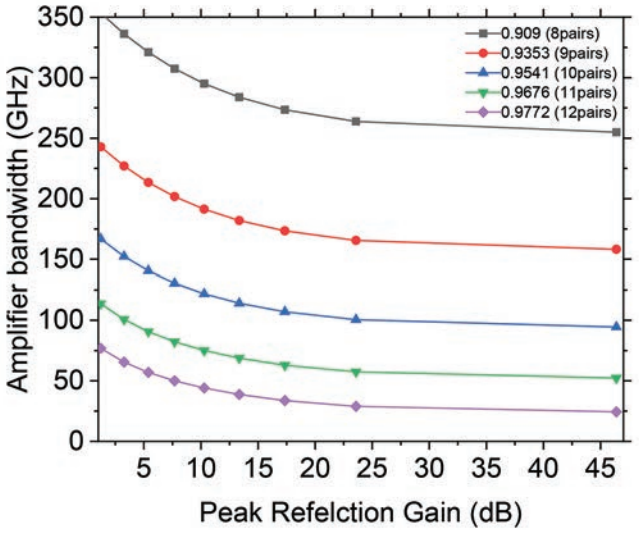


Fig. 8. Amplifier bandwidth versus peak reflection gain using the fixed 25 *pairs* bottom mirror of 0.99 reflectivity and different pairs of top *mirror's reflectivity.*

bandwidth are possible because of the increased reflectivity. The small bandwidths are advantageous for filter applications to reduce the noise figure, whereas the larger bandwidths are desirable for devices used in applications with multiple channels (Chaqmaqchee and Balkan, 2012).

## IV. Conclusion

In this paper, we use the program to investigate and calculating the resonance cavity, the reflectivity of QW, gain, and amplifier bandwidth. The resonance cavity matches the longer wavelength at 300 K without changing the reflectivity. The reflectivity was larger than 99% by increasing the number of periods. The gain in reflection and transmission mode varies proportionally with the single-pass gain. We have achieved high optical gain and narrower bandwidth at around 36 dB with single-pass gains of 1.076, where the gain in reflection mode is higher than the gain in transmission mode for the same single-pass gain. Moreover, the amplifier bandwidth as a function of peak reflection gain for HELLISH-VCSOA at different top DBR periods is measured. High amplifier bandwidth is achieved at around 270 GHz at peak reflection gain of 36 dB with front mirrors reflectivity of ~ 91%.

## V. Acknowledgments

The authors are grateful to the Department of Physics at Koya University for allowing this work.

## References

Adams, M.J., Collins, J.V. and Henning, I.D., 1985. Analysis of semiconductor laser optical amplifiers. IEE Proceedings J (Optoelectronics), 132(1), pp.58-63.

Abubaker Salh, S., 2021. A comparison of top distributed bragg reflector for 1300 nm vertical cavity semiconductor optical amplifiers based on III-V

compound. *ARO-the Scientific Journal of Koya University*, 9(2), pp.26-29.

Adams, M.J., Collins, J.V. and Henning, I.D., 1985. Analysis of semiconductor laser optical amplifiers. *IEE Proceedings Journal*, 132(1), pp.58-63.

Balkan, N., Serpengüzel, A., O'Brien-Davies, A., Sökmen, I., Hepburn, C., Potter, R., Adams, M.J. and Roberts, J.S., 2000. VCSEL structure hot electron light emitter. *Materials Science and Engineering: B*, 74(1-3), pp.96-100.

Bjorlin, E.S., Riou, B., Abraham, P., Piprek, J., Chiu, Y.Y., Black, K.A., Keating, A. and Bowers, J.E., 2001. Long wavelength vertical-cavity semiconductor optical amplifiers. *IEEE Journal of Quantum Electronics*, 37(2), pp.274-281.

Bjorlin, E.S., 2002. Long-wavelength Vertical-cavity *Semiconductor Optical Amplifiers.* University of California, Santa Barbara Long-wavelength Vertical-cavity.

Chaqmaqchee, F., Abubekr Salh, S. and Mohammed Sabri, M., 2020. Optical analysis of 1300 nm GaInNAsSb/GaAs vertical cavity semiconductor optical amplifier. *Zanco Journal of Pure and Applied Sciences*, 32(2), pp.87-92.

Chaqmaqchee, F.A., 2021. A comparative study of electrical characterization of P-doped distributed bragg reflectors mirrors for 1300 nm vertical cavity semiconductor optical amplifiers. *ARO-the Scientific Journal of Koya University*, 9(1), pp.89-94.

Chaqmaqchee, F.A.I, Balkan, N. and Herrero, J.M., 2012. Top-Hat HELLISH-VCSOA for optical amplification and wavelength conversion for 0.85 to 1.3μm operation. *Nanoscale Research Letters*, 7(525), pp.1-6.

Chaqmaqchee, F.A.I. and Balkan, N., 2012. Gain studies of 1.3-μm dilute nitride HELLISH-VCSOA for optical communications. *Nanoscale Research Letters*, 7(1), pp.1-4.

Chaqmaqchee, F.A.I. and Lott, J.A., 2020. Impact of oxide aperture diameter on optical output power, spectral emission, and bandwidth for 980 nm VCSELs. *OSA Continuum*, 3(9), pp.2602-2613.

Chaqmaqchee, F.A.I., 2016. Optical design of dilute nitride quantum wells vertical cavity semiconductor optical amplifiers for communication systems. *ARO-The Scientific Journal of Koya University*, 4(1), pp.8-12.

Chaqmaqchee, F.A.I., Mazzucato, S., Oduncuoglu, M., Balkan, N., Sun, Y., Gunes, M., Hugues, M. and Hopkinson, M, 2011. GaInNAs-based Hellish-vertical cavity semiconductor optical amplifier for 1.3 μm operation. *Nanoscale Research Letters*, 6(1), pp.1-7.

Erol, A., 2008. *Dilute III-V Nitride Semiconductors and Material Systems: Physics and Technology*. Springer, Berlin, Germany.

Ghadimi, A. and Ahmadzadeh, M., 2020. Effect of variation of specifications of quantum well and contact length on performance of InP-based Vertical Cavity Surface Emitting Laser (VCSEL). *Journal of Optoelectronical Nanostructures*, 5(1), pp.19-34.

Gönül, B., Köksal, K. and Bakır, E., 2007. A theoretical investigation of carrier and optical mode confinement in GaInNAs QWs on GaAs and InP substrates. *Physica Status Solidi C*, 4(2), pp.671-673.

Hepburn, C.J., Wah, J.Y., Boland Thoms, A. and Balkan, N., 2005. GaInNAs and GaAs, top-hat vertical-cavity semiconductor optical amplifier (VCSOA) based on longitudinal current transport. *Physica Status Solidi (c)*, 2(8), pp.3096-3099.

Kimura, T., Bjorlin, S., Piprek, J. and Bowers, J.E., 2003. High-temperature characteristics and tunability of long-wavelength vertical-cavity semiconductor optical amplifiers. *IEEE Photonics Technology Letters*, 15(11), pp.1501-1503.

Lee, Q.Y., Chou, C.J., Lee, M.X. and Lee, Y.C., 2022. Detecting the knowledge domains of compound semiconductors. *Micromachines*, 13(3), p.476.

O'brien, A., Balkan, N., Boland-Thoms, A., Adams, M., Bek, A., Serpengüzel, A., Aydinli, A. and Roberts, J., 1999. Super-radiant surface emission from a quasi-cavity hot electron light emitter. *Optical and Quantum Electronics*, 31(2), pp.183-190.

Piprek, J., Bjorlin, E.S. and Bowers, J.E., 2001. Modeling and optimization of vertical-cavity semiconductor laser amplifiers. *In Physics and Simulation of Optoelectronic Devices IX*, 4283, pp.129-138.

Potter, R.J. and Balkan, N., 2004. Optical properties of GaNAs and GaInAsN quantum wells. *Journal of Physics: Condensed Matter*, 16(31), p.S3387.

Razeghi, M., 2000. Optoelectronic devices based on III-V compound semiconductors which have made a major scientific and technological impact in the past 20 years. *IEEE Journal of Selected Topics in Quantum Electronics*, 6(6), pp.1344-1354

Royo, P., Koda, R. and Coldren, L.A., 2002. Vertical cavity semiconductor optical amplifiers: Comparison of Fabry-Perot and rate equation approaches. *IEEE Journal of Quantum Electronics*, 38(3), pp.279-284.

Su, S.T., Tang, S.F., Chen, T.C., Chiang, C.D., Yang, S.T. and Su, W.K., 2006. Temperature dependent VCSEL optical characteristics based on graded Al x Ga 1-x As/GaAs distributed Bragg reflectors: Reflectivity and beam profile analyses. *In Vertical-Cavity Surface-Emitting Lasers X*, 6132, pp.165-174.

Uesugi, K., Morooka, N. and Suemune, I., 1999. Reexamination of N composition dependence of coherently grown GaNAs band gap energy with high-resolution x-ray diffraction mapping measurements. *Applied Physics Letter*s, 74(9), pp.1254-1256.

Ungan, F., Yesilgul, U., Sakiroglu, S., Kasapoglu, E., Sari, H. and Sökmen, I., 2013. Nonlinear optical absorption and refractive index in GaInNAs/GaAs double quantum wells under intense laser field and applied electric field. *Journal of Luminescence*, 143, pp.75-80.

Wah, J.Y. and Balkan, N, 2004. Low field operation of hot electron light emitting devices: Quasi-flat-band model. *IEE Proceedings-Optoelectronics*, 151(6), pp.482-485.

Walukiewicz, W., Shan, W., Ager, J.W. 3rd., Chamberlin, D.R., Haller, E.E., Geisz, J.F., Friedman, D.J., Olson, J.M. and Kurtz, S.R, 1999. *Nitrogen-induced Modification of the Electronic Structure of Group III-NV Alloys*. National Renewable Energy Lab.(NREL), Golden, CO, pp.520-29583.

Yu, K.M., Walukiewicz, W., Shan, W., Wu, J., Beeman, J.W., Ager, J.W., Haller, E.E. and Ridgway, M.C., 2000. *Synthesis of III-N x-V 1-x Thin Films by N Ion Implantation*. MRS Online Proceedings Library (OPL), Germany, p.647.

Zhao, X., Palinginis, P., Pesala, B., Chang-Hasnain, C.J. and Hemmer, P., 2005. Tunable ultraslow light in vertical-cavity surface-emitting laser amplifier. Optics Express, 13(20), pp.7899-7904.

http://dx.doi.org/10.14500/aro.10924

# Detection of Sperm DNA Integrity and Some Immunological Aspects in Infertile Males

Sarmad N. Mageed[1], Shukur R. Hamasharef [2] and Ahmed F. Shallal[3]

[1]Department of Medical Microbiology, Faculty of Science and Health, Koya University, Koya, Kurdistan Region – F.R. Iraq

[2]Department of Medical Instrumentations Engineering Technology, College of Engineering Techniques, Alkitab University, Kirkuk – F.R. Iraq

[3]Department Medical Laboratory Science, College of Science, University of Raparin, Rania-Sulaymaniyah, Kurdistan Region – F.R. Iraq

***Abstract*—Immunoinfertility caused by anti-sperm antibodies (ASAs) represents about 10–20% of infertility among couples, which interfere with sperm motility and ability to penetrate cervical mucus, sperm-oocyte binding, fertilization, and embryo development. In addition, deoxyribonucleic acid (DNA) damages are increasingly found with infertile cases affecting male reproduction potency and progeny. This study aims to assess the semen, presence of ASAs, and DNA fragmentation index in normozoospermic patients. A total number of 116 cases with an average age of 20–51 years old, and duration of infertility at 4.70 ± 2.77 are classified into 77 and 39 primary and secondary types of infertility, respectively. Mixed agglutination reaction test was used to estimate the ASAs in semen (direct method) and in seminal plasma and blood serum (indirect method), for both immunoglobulins IgG and IgA. Acridine orange test was used to detect DNA fragmentation index. The results showed a significant difference ($P > 0.05$) for those with a secondary type of infertility at means 24.37 and 31.48 for IgG, and 14.46 ± 1.76 and 6.86 ± 0.39 for IgA by both direct and indirect methods, respectively. The direct method showed a significant difference only for the sperm tail, while that for indirect method was in sperm mid-piece. The mean of DFI for all cases was 38.25 ± 2.08, at 41.61 ± 2.19 and 31.63 ± 4.29, for both primary and secondary cases, respectively. The percentage of ASAs revealed no significant difference with DFI, except in some parts of sperm.**

***Index Terms*—Acridine orange test; Anti-sperm antibodies; Deoxyribonucleic acid fragmentation index; Mixed agglutination reaction.**

## I. Introduction

Sertoli cells forming tight junctions of the blood-testis barrier provide immunologic protection from sperm antigens. The immune response that spermatozoon evokes when exposed to the systemic immune defense system once the barrier is disrupted leads to anti-sperm antibodies (ASAs). However, the presence of naturally occurring ASA is a well-known cause of infertility in men and women, but the antigens for these antibodies are poorly characterized. Antibodies attached to the sperm impair their motility or recognition, and their ability for bounding with the ovum, or might lead to sperm destruction female reproductive tract immune system (El-Sherbiny, et al., 2021). In addition, the detected levels of ASAs within semen samples from infertile men had been associated with specific male genital tract pathology (e.g., testicular trauma, surgery and torsion). Sperm ASAs believed to have an adverse impact on male fertility through two mechanisms of action:

1. Directly interfering with sperm surface interactions (e.g., fertilization) and
2. Indirectly by mediating the release of cytokines that can impair sperm function, possibly including deoxyribonucleic acid (DNA) integrity (Muscianisi, et al., 2021).

DNA within the sperm head characterized by its hypercondensation core due to histones partially being replaced by the protamines during spermiogenesis. The protamines were positively charged DNA proteins that compacted the sperm nucleus into a hydrodynamic form that allowed sperm to move and penetrate egg membranes. There is clinical evidence that damage to sperm DNA integrity of the infertile men results in impaired embryo development and pregnancy in mice and humans, sperm; has shown an elevation in DNA damage aneuploidy, and other genetic abnormalities. Morphological defects in DNA integrity and chromatin organization have been associated with increased DNA fragmentation (Zhang, et al., 2022).

### *A. The Spermatozoa*

Germ cells of the male go on meiosis to begin their multifarious alteration into spermatozoa, highly specialized cells by the initiation of puberty. Spermatogenesis needs 24 days (Houda, et al., 2021). Each ejaculation of fertile men

ARO-The Scientific Journal of Koya University
Vol. X, No.1 (2022), Article ID: ARO.10924, 7 pages
DOI: 10.14500/aro.10924
Received 01 January 2022; Accepted: 07 June 2022
Regular research paper: Published: 30 June 2022
Corresponding author's e-mail: sarmad.mageed@koyauniversity.org

typically contains from 15 million sperm to over 200 million sperm per milliliter (ml) of semen which is considered a normal sperm count, only one normal sperm precisely enters an ovum. Sperm may live only 44 h in the female genital system. The spermatozoa are characterized by its polarized cell composed of a head and tail or flagellum. The head and tail are covered by a sperm plasma membrane, head contains a nucleus that holds the male genome, in which the DNA condensing core and linker histones has been partially replaced during spermiogenesis by protamines, and the acrosome, a large secretory granule that is oriented over the anterior area of the sperm nucleus, stores enzymes needed to penetrate the egg. In the middle piece, there are mitochondria which are spirally arranged around the first portion of the tail and are responsible for oxidative phosphorylation and provide much of the energy. The first part of the tail is consist of the flagella axoneme that contains nine courses (longitudinally arranged) in the peripheral of two central tubules; the peripheral tubules are arranged as groups of double tubules (Houda, et al., 2021).

### *B. Immunological Aspects of Spermatozoa*

The risk factors of ASA development are conditions that may disrupt the blood-testis barrier (Maverakis, Moudgil and Sercarz, 2006). Obstruction of the ductal system is associated with the development of ASAs. After vasectomy, approximately 60% of men develop ASAs. Whereas approximately one-third of patients with congenital bilateral absence of vas deferens are found to have ASAs. Thus, most studies have not found testicular torsion to be a risk factor for the presence of ASAs. Conflicting data also exist for cryptorchidism, varicoceles, and testicular biopsy abnormal postcoital tests, particularly when immotile sperm with a shaking motion is noticed, are highly suggestive of the presence of ASAs. Couples with unexplained infertility as well as cases with impaired sperm motility or sperm agglutination have also been to have a higher incidence of ASAs (Rose, 2008; Tahiat, et al., 2021).

*Formation of immune markers*

There are many assays for investigating the presence of ASAs, for example, the direct assays detect the presence of ASAs on the patient's sperm, and indirect assays measure ASAs in the patient's serum and generally require ASA-negative donor sperm. Because it is the sperm that reaches the female reproductive tract, not serum, direct assays have the advantage of only detecting sperm-bound immunoglobulin (Ig). The presence of ASAs in the serum is not always associated with the presence of these antibodies on sperm. In addition, IgM class antibodies that may be present in serum do not usually make it to the semen. However, the immunobead assay and the mixed agglutination reaction are commonly used for the detection of ASAs. These assays utilize synthetic beads or red blood cells that will bind to antibodies bound to the sperm surface. Scoring is based on the percentage of motile sperm with bead or red blood cell binding (Abu-Raya, et al., 2020).

### *C. Sperm DNA Chromatin Structure and Fertility*

Sperm DNA damage may lead to or considered the cause of infertility elsewhere negative impact on male fertility potential. It may be initiated by a multifactorial etiology such as drugs, chemotherapy, radiation therapy, smoking, and environmental toxins, genital tract inflammation, testicular hyperthermia, varicoceles, and hormonal factors (Selvam, et al., 2021; Mateo-Otero, et al., 2022). Also from paternal DNA damage as well as maternal DNA damage, the fertilization and subsequent embryonic development afflict. The tests for spermatozoon DNA integrity appears to be a threshold of sperm DNA damage beyond which embryo development and pregnancy are impaired, and studies have shown that the spermatozoa of infertile men possess more DNA damage than, and impaired pre-implantation development, increased abortion, and an increased incidence of disease in the offspring, including childhood cancer, with a high percentage of spermatozoa with DNA damage, have a reduced potential for natural fertility (Liu, et al., 2022).

## II. Materials and Methods

### *A. Methodology*

The study was carried out at Kirkuk Private Laboratory, Kirkuk, Iraq. This study included two aspects, the first one is the immunological aspect, through which some immunological aspects were measured, which included ASAs (IgA and IgG) in semen and blood serum using agglutination reaction (direct and indirect methods). The second is the molecular aspect, including determination of the integrity of sperm DNA. The DNA fragmentation index (DFI) was also estimated using mixed acridine orange test (AOT).

## III. Results

### *A. Descriptive Parameters and Semen Analysis*

The studies involved 116 normozoospermic male cases and were distributed into two groups, primary and secondary, according to the type of infertility. The primary group included 77 individuals with primary infertility representing (66.38%) of total cases, whereas, 39 cases represent (33.62 %) of total cases as the secondary infertility type. The semen of all cases was analyzed to evaluate the sperm integrity based on a number of parameters (Björndahl and Brown, 2022) (Table I). Sperm parameters for a primary and secondary

Table I
Sperm Parameters for all Subjects According to the WHO Criteria (Björndahl and Brown, 2022)

| Parameters | Subjects* | Björndahl and Brown, 2022 reference values |
|---|---|---|
| Sperm concentration (million/mL) | 46.80±0.6 | ≥15 |
| Progressive sperm motility (%) | 35.70±0.83 | ≥32% |
| Non-progressive sperm motility (%) | 28.30±0.654 | |
| Immotile sperm (%) | 36.0±0.92 | |
| Total progressive motility/*ejaculate* | 39.91±1.93 | >32 |
| Normal sperm morphology (%) | 31.291±0.86 | ≥4% |

Data are Mean±S.E. (Cooper, et al., 2010), (Björndahl and Brown, 2022)

http://dx.doi.org/10.14500/aro.10924

infertile patients were within normal values, except for sperm morphology which showed lower limits than those specified by the WHO (Björndahl and Brown, 2022) (Table II).

The mean age of the primary infertility was 34.84 ± 0.644 years, and their duration of infertility was 4.727 ± 0.29 years, at age category 20–48 years. The secondary type had a mean age of 35.82 ± 6.808 years, at 5.0 ± 0.497 years for infertility duration; with age category 23–51 years.

Sperm's concentration, progressive sperm motility, non-progressive sperm motility, total progressive sperm motility/ejaculate, and normal sperm morphology for 20–29 and 30–39 age groups were within normal values, according to the WHO criteria (Björndahl and Brown, 2022). However, normal sperm morphology for age group 40–49 years and percentage of progressive sperm motility and normal sperm morphology for age group ≥50 years were less than the lower limits of the WHO values (Björndahl and Brown, 2022) (Table III).

The mean of IgG percentage for 97 positive cases was 23.88 ± 1.75 detected by a direct method, showed no significant difference ($P < 0.05$) with the mean 27.41 ± 2.41 of 71 positive cases for IgG percentage that detected by indirect method (Fig. 1). For the primary infertility subjects, no significant difference ($P < 0.05$) was recorded between the direct and indirect methods of IgG detection (Fig. 2). Whereas a significant difference ($P < 0.05$) was achieved for those with the secondary type of infertility with both methods (Fig. 3).

Surprisingly, the percentage of IgA antibodies by the direct and indirect methods, for all subjects with primary and secondary infertility types showed significant correlation ($P > 0.05$) (Figs. 4-6). Fig. 7 shows an image of positive react sperm with latex particles coated with monoclonal ASAs.

Table II
Sperm Parameters for Primary and Secondary Types of Infertility

| Parameter | Type of infertility | | (Björndahl and Brown, 2022) reference values |
|---|---|---|---|
| | Primary* | Secondary** | |
| Sperm concentration (million/mL) | 46.766[a]±2.10 | 44.153[a]±2.76 | ≥15 |
| Progressive sperm motility (%) | 36.026[a]±0.95 | 34.692[a]±1.63 | ≥32 (%) |
| Non-progressive sperm motility (%) | 29.402[a]±0.75 | 26.769[b]±1.25 | |
| Immotile sperm (%) | 34.428[b]±0.95 | 38.641[b]±1.86 | |
| Total progressive motility/ *ejaculate* | 40.081[a]±2.40 | 36.511[a]±3.19 | >32 |
| Normal sperm morphology (%) | 31.974[a]±1.04 | 29.437[a]±1.57 | ≥4% |

(Mean±SE), *no. of primary infertile men=77. **No. of secondary infertile subjects=39. Different superscripts within each row are significantly different ($P<0.05$). Same superscripts within each row are non-significantly different ($P>0.05$)

## IV. Discussion

Sperm's normal chromatin structure is essential for the correct transmission of paternal genetic information; as there is a negative correlation between defective sperm chromatin structure (DNA breaks) and fertility, a lower rate of implantation, a higher rate of abortion, and illnesses in offspring that can be explained as multifactorial oxidative stress (Selvam, et al., 2021).

Different results for Igs in several studies, as well as the present study, might be due to different subclasses of Igs (Shibahara, et al., 2021). The genital tract secretions that included IgA have various molecular properties from those of IgA in other body fluids. Containing polymeric (p), dimeric, and tetrameric IgA reflect the dominance of S-IgA, with J chain and other secretory components (SCs) are essential during the selective transepithelial transport of pIgA; and mIgA is present in low quantities. The male and female genital secretions contained relatively similar properties of typical S-IgA, pIgA, and mIgA. The IgA1 and IgA2 subclasses are present in genital secretions in proportions differ from other body fluids (Lavelle and Ward, 2021), whereas in semen, IgA1 percentage dominates and was detected in similar levels in the serum (Woof and Mestecky, 2015). The findings showed no significant difference between the direct and indirect techniques for detecting both classes of IgA according to their distributions on sperm parts in all subjects, including the primary and secondary types of infertility, which have been confirmed by previous studies. ASAs affect virtually all components of sperm, diminished sperm-oocyte binding, faulty zona pellucida penetration cervical mucus penetration, and sperm survival (Silva, Ramalho-Santos and Amaral, 2021). Furthermore, the ASAs linked to abnormal embryo development by retarding the cleavage process, blocking the initiation of the embryo, and most significantly affecting fertilization rates when localized both at the head and the tail tip levels of sperm. Previous data showed an effect of ASAs on actual DNA lack of the sperm cell. In the present study, the IgG and IgA antibodies were detected by the direct method according to their bounding with the sperm head and exhibited no significant difference for all samples and those of secondary type infertility (Chereshnev, et al., 2021). Nevertheless, significant correlations were noticed between the two classes of antibodies, IgG and IgA, which detected bounding to the sperm heads in subjects with primary type infertility (Ata, et al., 2021; Audu, et al., 2021). However, bounded IgG and IgA antibodies to the sperm head directly may inhibit fertilization. It is found that the presence of ASAs has negative effects on sperm-oocyte

Table III
Sperm Parameters According to the Age Group

| Age groups (years)/sperm parameters | 20–29 | 30–39 | 40–49 | ≥50 | Björndahl and Brown, 2022 |
|---|---|---|---|---|---|
| Sperm concentration (million/mL) | 39.882±4.03 | 50.4533±2.18 | 40.727±2.80 | 35.50±9.50 | ≥15 |
| Progressive sperm motility (%) | 34.079±2.80 | 37.035±0.99 | 33.181±1.34 | 26.50±1.55 | ≥32% |
| Non-progressive sperm motility (%) | 30.173±1.81 | 27.120±0.78 | 31.41±1.38 | 27.50±1.00 | |
| Immotile (%) | 35.748±2.79 | 35.845±1.18 | 35.409±1.51 | 46.0±1.00 | |
| Total progressive motility/ejaculate | 36.444±4.66 | 43.678±2.60 | 30.870±2.22 | 26.89±2.03 | >32 |
| Normal morphology (%) | 30.823±2.60 | 32.442±1.06 | 29.300±1.48 | 14.00±1.00 | ≥4% |

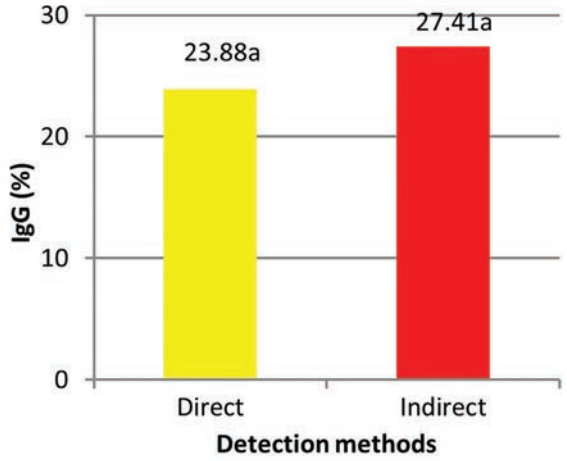


Fig. 1. Means of IgG by direct and indirect detection methods for primary and secondary subjects. Same superscripts above the column indicate non-significant difference ($P < 0.05$). No. of positive cases using direct method = 97. No. of positive cases using indirect method = 71.

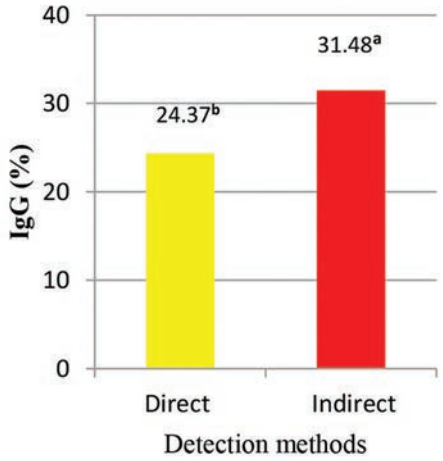


Fig. 3. The IgG means detected by direct and indirect methods for secondary infertility subjects. Different superscripts within the column are significantly different ($P < 0.05$). No. of positive cases using direct method = 27. No. of positive cases using indirect method = 19.

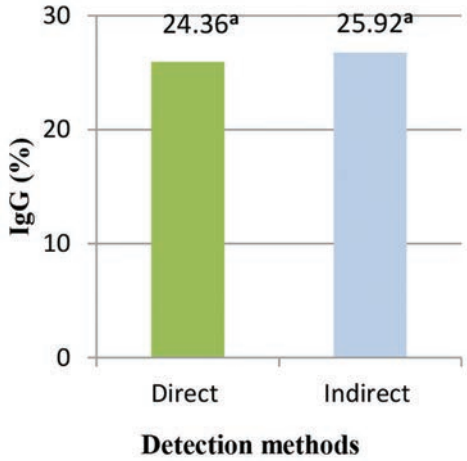


Fig. 2. The IgG means detected by direct and indirect methods for primary infertility cases. Same superscript above the bars indicates non-significant difference ($P < 0.05$). No. of positive cases using direct method = 70. No. of positive cases using indirect method = 57.

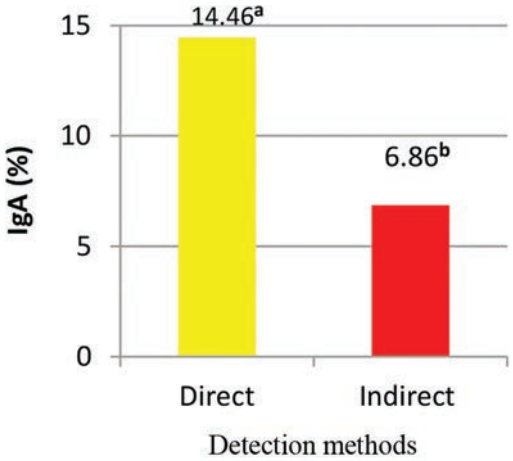


Fig. 4. The IgA means detected by direct and indirect methods for primary and secondary subjects. Different superscripts above the column indicate no significant ($P < 0.05$). No. of positive cases using direct method = 88. No. of positive cases using indirect method = 27.

binding, penetration, fertilization, and post-fertilization events (Vickram, et al., 2019). IgA isotype of ASA demonstrated the lowest pregnancy rate. Moreover, the antibodies directed on sperm mid-piece show significance in percentage in all subjects and those with primary and secondary types of infertility that disagreed with a previous study. Whereas only subjects with secondary type infertility showed a significant differences as related to detected IgG and IgA by indirect methods were bounded to the sperm tail, all subjects and those with primary type showed no significant difference (Barbonetti, et al., 2019).

The results showed significant differences between detected IgG in serum and the round cells count. Furthermore, the IgG bound the sperm mid-piece had a highly significant correlation with the round cells. Regarding the DFI and IgA, there was a significant correlation, because ASAs may promote the release of cytokines and may be associated with increased semen leukocyte concentration (Tennakoon, Yasawardene and Weerasekera, 2012). As related to the sperm parameters of subjects with primary infertility and those with secondary infertility, many studies reported large and overlapping differences, whereas this study showed no significant difference in sperm parameters in exception to the non-progressive sperm motility, which had a significant difference between the two types of infertility that agreed by other studies. The studied cases with primary type of infertility showed an increasing level of DNA fragmentation compared to other cases with a secondary type of infertility which are in agreement with similar studies and reported that the incidence of sperm DNA damage is higher in primary infertile patients who may harm fertility potential (Garolla, et al., 2021). All outcomes of involved cases and those with primary type infertility indicated a significant difference between the IgG and IgA detected by a direct method according to sperm tail bound. These findings were in disagreement with a study that investigated the impact of different Ig classes based on their

http://dx.doi.org/10.14500/aro.10924

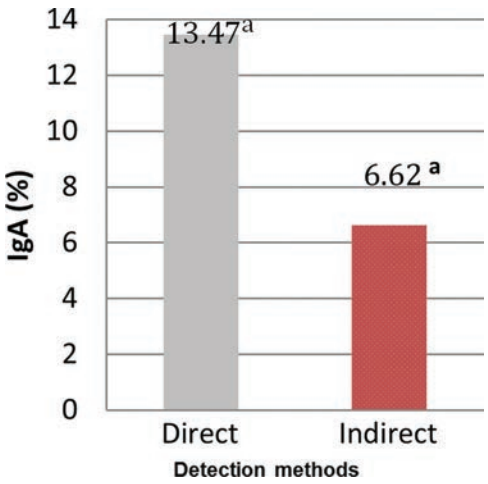


Fig. 5. The IgA means detected by direct and in direct method for primary infertility subjects. Same script above the bars indicates no significant ($P < 0.05$). No. of positive cases using direct method = 64. No. of positive cases using indirect method = 21.

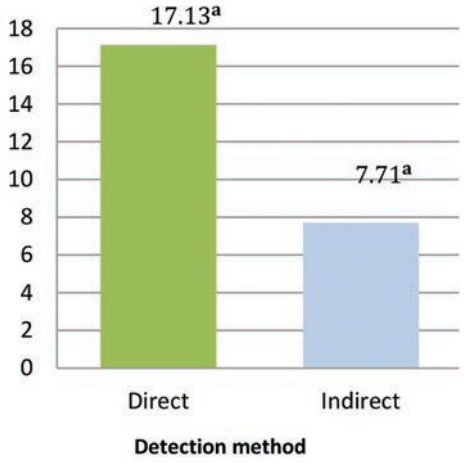


Fig. 6. The IgA means detected by direct and indirect method for secondary infertility subjects. Same script above the bars indicates no significant ($P < 0.05$). No. of positive cases using direct method = 24. No. of positive cases using indirect method = 6.

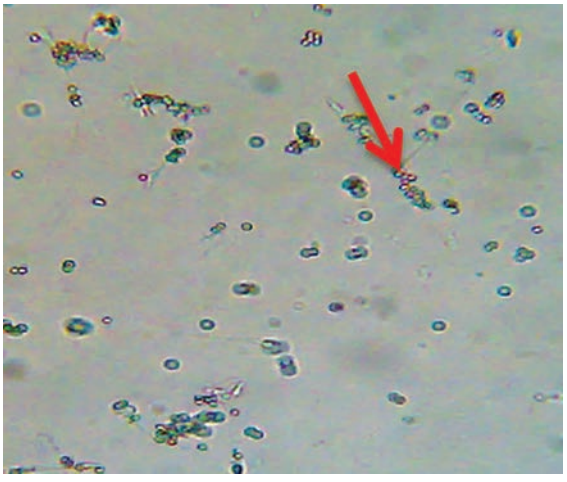

Fig. 7. Spermatozoa attached to latex particles (red arrow) ×60.

bounded site. The concentrations of IgA and IgG in semen (detected by direct method) were not correlated; however, the results were in contradiction with the fact that IgA may be because of its secretory origin. Other studies found that prostate and vesicle infection and subclinical reproductive tract infection might lead to dysfunction of sperm and changes in semen parameters, and the latter lead to infertility (Tennakoon, Yasawardene and Weerasekera, 2012). Some possible mechanisms of the development of infertility are linked either to inhibition of spermatogenesis resulting from testicular damage or an autoimmune process. The IgA detected in seminal plasma (indirect method) and according to its bound with sperm (mid-piece and tail) had a significant correlation with round cells count. Whereas the direct method of IgA detection showed a significant correlation between the bounding site of sperm (head and tail) and the count of round cells. The detected IgG by an indirect method that is bound to the mid-piece and tail showed a significant difference with normal sperm morphology but had no significant difference with the direct method. Whereas IgA detection by indirect method bound to the sperm head and mid-piece showed a significant difference compared to normal sperm morphology. On the other hand, no significant difference was recorded with the direct method that is bound to different sites of the sperm.

The origin of IgA present in the sperm and pre-ejaculate has yet to be confirmed. However, it appears that both local syntheses, primarily in the penile urethra and circulation, contribute to the Ig pool in these fluids, based on the molecular characteristics (Chantler, Sharma and Sharman, 1989; Sadecki, et al., 2022). The sperm parameters such as total progressive sperm motility/ejaculate and round cells count were significantly correlated with DFI that was agreed by a previous study, whereas the other sperm parameters such as normal sperm morphology and the sperm count did not correlate with DFI. According to the age category, the studied cases demonstrated lower records of sperm morphology in the age group 40–49 and ≥50 years. These outcomes were in agreement with several investigation studies of aging effect on fertility (Ahmed, et al., 2019; Silva, Ramalho-Santos and Amaral, 2021). In addition, the progressive sperm motility for the age category ≥50 years was below the reference value of the WHO (Björndahl and Brown, 2022) that was in agreement with similar studies (Stewart and Kim, 2011). No correlation was found between DFI and IgG detected by both direct and indirect methods, which are compatible with the results of another study (Mateo-Otero, et al., 2022). As related to correlation within sperm parts, however; significant results were recorded that were agreed by several studies investigating the correlation between ASA presence and DNA damages (Selvam, et al., 2021). Conflicting evidence was observed on the relationship between the presence of ASAs and sperm characteristics including concentration, motility, and morphology in the sperm (Dacheux and Dacheux, 2014). The majority of published studies found no link between the presence of ASAs and sperm concentration or motility and morphology (Chereshnev, et al., 2021). There were

significant correlations between the sites of sperm to which the IgA bound detected in semen plasma indirectly and on the sperm directly with DNA fragmentation.

## V. Conclusions

The findings of the study led to the following conclusion:

1. The ASAs interfere in different manners with sperm parameters
2. The ASAs detected indirectly in seminal plasma (IgA) class and in serum (IgG) have strong correlation with total progressive sperm motility and with round cells counts
3. Sperm parts (head, mid-piece, and tail) attached to the different ASAs class correlate and with sperm parameters in different manners, by which showed no significant difference except for the sperm tail. However, the indirect method for ASAs showed a significant difference in sperm mid-piece
4. There was no correlation between the levels of the ASA and the percentage of DFI, except in some parts of sperm.

## VI. Acknowledgment

Authors highly appreciate Kirkuk Private Laboratory for their extreme assistance and endless kindness during the period of sampling and dealing with cases under study. A special thanks and appreciation are directed to the people from whom samples were taken for the study, which was the basis on which the experiments and analyzes were built. Authors are also grateful for the insightful comments offered by our expertise colleagues at the university, particularly M. Furat at the computing department. The generosity and expertise of one and all have improved this study in innumerable ways and saved us from many errors; those that inevitably remain are entirely our own responsibility.

## References

Abu-Raya, B., Michalski, C., Sadarangani, M. and Lavoie, P.M., 2020. Maternal immunological adaptation during normal pregnancy. *Frontiers in Immunology*, 11, pp.575197.

Ahmed, T.A., Ahmed, S.M., El-Gammal, Z., Shouman, S., Ahmed, A., Mansour, R. and El-Badri, N., 2020. Oocyte aging: The role of cellular and environmental factors and impact on female fertility. *Advances in Experimental Medicine and Biology*, 8, pp.109-123.

Ata, N., Turkler, C., Ulug, P. and Mertoglu, C., 2021. Is there a role of antisperm antibodies in women with unexplained infertility-a Turkish pilot cross sectional case control study. *Annals of Medical Research*, 28(9), pp.1615-1619.

Audu, O., Musa, B., Adeiza, M.A, Muhammed, A., Ahmad, A., Ega, B., Opaluwa, S.A. and Shuaib, B.I., 2021. Sero-prevalence of IgG and IgA antisperm antibodies in men with infertility attending two major hospitals in Zaria, Nigeria. *Health Science Journal*, 15(5), pp.1-5.

Barbonetti, A., Castellini, C., D'Andrea, S., Cordeschi, G., Santucci, R., Francavilla, S. and Francavilla, F., 2019. Prevalence of anti-sperm antibodies and relationship of degree of sperm auto-immunization to semen parameters and post-coital test outcome: A retrospective analysis of over 10 000 men. *Human Reproduction*, 34(5), pp.834-841.

Björndahl, L. and Brown, J.K., 2022. The sixth edition of the WHO laboratory manual for the examination and processing of human semen: Ensuring quality and standardization in basic examination of human ejaculates. *Fertility and Sterility*, 117, pp.246-251.

Chantler, E., Sharma, R. and Sharman, D., 1989. Changes in cervical mucus that prevent penetration by spermatozoa. *In Symposia of the Society for Experimental Biology*, 43, pp.325-336.

Chereshnev, V.A., Pichugova, S.V., Beikin, Y.B., Chereshneva, M.V., Iukhta, A.I., Stroev, Y.I. and Churilov, L.P., 2021. Pathogenesis of autoimmune male infertility: Juxtacrine, paracrine, and endocrine dysregulation. *Pathophysiology*, 28(4), pp.471-488.

Cooper, T.G., Noonan, E., von Eckardstein, S., Auger, J., Baker, H.W., Behre, H.M., Haugen, T.B., Kruger, T., Wang, C., Mbizvo, M.T. and Vogelsong, K.M. (2010). World Health Organization reference values for human semen characteristics. *Human Reproduction Update*, 16, pp.231-245.

Dacheux, J.L. and Dacheux, F., 2014. New insights into epididymal function in relation to sperm maturation. *Reproduction*, 147(2), pp.R27-R42.

El-Sherbiny, A.F., Ali, T.A., Hassan, E.A., Mehaney, A.B. and Elshemy, H.A., 2021. The prognostic value of seminal anti-sperm antibodies screening in men prepared for ICSI: A call to change the current antibody-directed view point of sperm autoimmunity testing. *Therapeutic Advances in Urology*, 13, p.1-9.

Garolla, A., Pizzol, D., Carosso, A.R., Borini, A., Ubaldi, F.M., Calogero, A.E., Ferlin, A., Lanzone, A., Tomei, F., Engl, B., Rienzi, L., De Santis, L., Coticchio, G., Smith, L., Cannarella, R., Anastasi, A., Menegazzo, M., Stuppia, L., Corsini, C. and Foresta, C. 2021. Practical clinical and diagnostic pathway for the investigation of the infertile couple. *Frontiers in Endocrinology* (*Lausanne*), 11, pp.1032.

Houda, A., Nyaz, S., Sobhy, B.M., Bosilah, A.H., Romeo, M., Michael, J.P. and Eid, H.M., 2021. Seminiferous tubules and spermatogenesis. In: *Male Reproductive Anatomy*. IntechOpen, London.

Lavelle, E.C. and Ward, R.W., 2022. Mucosal vaccines-fortifying the frontiers. *Nature Reviews Immunology*, 22, pp.236-250.

Liu, C.L., Li, P., Cai, G.F., Morse, A., Liu, J., Chen, Z.H., Zhang, X. and Sun, L., 2022. Optimal follow-up duration for assessment of birth defects after *in vitro* fertilization-embryo transfer: A multicenter 5-year cohort study in China. *Frontiers in endocrinology* (*Lausanne*), 13, p.382.

Mateo-Otero, Y., Llavanera, M., Recuero, S., Delgado-Bermúdez, A., Barranco, I., Ribas-Maynou, J. and Yeste, M., 2022. Sperm DNA damage compromises embryo development, but not oocyte fertilisation in pigs. *Biological Research*, 55(1), pp.1-12.

Maverakis, E., Moudgil, K.D. and Sercarz, E.E., 2006. Generation of T-cell antigenic determinants in autoimmunity and their recognition. In: *The Autoimmune Diseases*. Academic Press, Cambridge. pp.179-191.

Muscianisi, F., De Toni, L., Giorato, G., Carosso, A., Foresta, C. and Garolla, A., 2021. Is HPV the novel target in male idiopathic infertility? A systematic review of the literature. *Frontiers in Endocrinology*, 12, p.643539.

Rose, N.R., 2008. Immunologic Diagnosis of Autoimmunity: In O'Gorman, M.R. and Donnenberg, A.D., editors. *Handbook of Human Immunology*. 2nd ed. CRC Press, Boca Raton, New York, pp.378-380.

Sadecki, E., Weaver, A., Zhao, Y., Stewart, E.A. and Ainsworth, A.J., 2022. Fertility trends and comparisons in a historical cohort of US women with primary infertility. *Reproductive Health*, 19(1), pp.1-11.

Selvam, M.K., Ambar, R.F., Agarwal, A. and Henkel, R., 2021. Etiologies of sperm DNA damage and its impact on male infertility. *Andrologia*, 53(1), p.e13706.

Shibahara, H, Wakimoto, Y, Fukui, A and Hasegawa, A., 2021. Anti-sperm antibodies and reproductive failures. *American Journal of Reproductive Immunology*, 85, e13337.

Silva, A.F., Ramalho-Santos, J. and Amaral, S., 2021. The impact of antisperm antibodies on human male reproductive function: An update. *Reproduction*,

162(4), pp.R55-R71.

Stewart, A.F. and Kim, E.D., 2011. Fertility concerns for the aging male. *Urology*, 78(3), pp.496-499.

Tahiat, A., Yagoubi, A., Ladj, M.S., Belbouab, R., Aggoune, S., Atek, L., Bouziane, D., Melzi, S., Boubidi, C., Drali, W. and Bendahmane, C., Iguerguesdaoune, H., Taguemount, S., Soufane, A., Oukil, A., Ketfi, A., Messaoudi, H., Boukhenfouf, N., Ifri, M.A., Madani, T.B., Belhadj, H., Benhala, K.N., Khiari, M., Cherif, N., Smati, L., Arada, Z., Zeroual, Z., Bouzerar, Z., Ibsaine, O., Maouche, H., Boukari, R. and Djenouhat, K., 2021. Diagnostic and predictive contribution of autoantibodies screening in a large series of patients with primary immunodeficiencies. *Frontiers in Immunology*, 12, p.1130.

Tennakoon, V., Yasawardene, S.G. and Weerasekera, D.S., 2012. Antisperm antibodies: Incidence, isotypes and location on spermatozoa, their implications on fertilization and on pregnancy rate at a selected Centre in Sri Lanka. *Sri Lanka Journal of Obstetrics and Gynaecology*, 32(1), pp. 8-16.

Vickram, S, Dhama, K., Chakraborty, S., Samad, H.A., Latheef, S.K., Sharun, K. Archana K., Khurana, S.K., Tiwari, R., Bhatt, P. and Chaicumpa, W., 2019. Role of antisperm antibodies in infertility, pregnancy, and potential for contraceptive and antifertility vaccine designs: Research progress and pioneering vision. *Vaccines* (*Basel*), 7(3), p.116.

Woof, J.M. and Mestecky, J., 2015. *Mucosal immunoglobulins*. In: Mucosal Immunology. Elsevier/Academic Press, Amsterdam, pp.287-324.

Zhang, X., Deng, C., Liu, W., Liu, H., Zhou, Y., Li, Q., Zheng, H., Wang, Q., Jiang, M., Pang, T. and Ma, C., Huang, C., Zhao, Q. and Tang, Y., 2022. Effects of varicocele and microsurgical varicocelectomy on the metabolites in semen. *Scientific Reports*, 12(1), pp.1-10.

# Synchro Software-Based Alternatives for Improving Traffic Operations at Signalized Intersections

Nasreen A. Hussein

Department of Civil Engineering, College of Engineering, University of Duhok,
Kurdistan Region – F.R. Iraq

***Abstract*—*Traffic* congestion is a considerable problem in urban arterials, especially at signalized intersections. Signalized intersections are critical elements of the highway system, thus improving their performance would significantly influence the overall operating performance of the system in terms of delay and level of service (LOS). The aim of this study is to assess the capacity performance of two signalized intersections in Duhok city, namely, Zari land intersection and Salahaddin Mosque intersection using the procedure in the Highway Capacity Manual and Synchro software. Total intersection delay, LOS, and volume to capacity ratio (v/c) were the measures of effectiveness used for comparison purposes. Different optimization alternatives have been tested to improve current and future performance. The results have shown that the Zari land intersection is currently operating at LOS F with an average delay of 590 s/veh and high values of v/c at specific movements. Results of optimization show that the scenario of creating an overpass with a change in cycle length and adding one additional lane in each direction is the best alternative to improve its performance to the LOS D with the maximum v/c ratio of 0.86. For Salahaddin Mosque intersection, the delay can be reduced from 544 s/veh (LOS F) with high values of v/c at the major street through movement to an average delay of 70 s/veh (LOS E) and maximum v/c ratio of 1, when cycle length and geometrics are changed, and approaching traffic from the minor street is prohibited.**

***Index Terms*—Level of service, Optimization, Signalized intersections, Synchro software.**

## I. Introduction

Signalized intersections are critical elements of highway system, thus improving the performance of these intersections significantly influences the overall operating performance of the highways, as the comfort of drivers and passengers is affected by the operational conditions of signalized intersections. An important parameter in explaining the operational conditions of signalized intersections is the concept of level of service (LOS) through measuring the control delay (HCM, 2010). Delay at signalized intersections is the time lost due to prevailing conditions including geometric characteristics, traffic, and control conditions present at the intersections.

Reduction in capacity and increase in delay at signalized intersections could be a reflection of poor signal timing as well as inadequate road geometry variables (Chen, Qi and Sun, 2014; Potts, et al., 2007). Efficient movement for pedestrians and orderly, maximizing the volume movement through an intersection, and increasing the capacity are depending on the properly designed and timed traffic signals (Koonce, et al., 2008). One of the effective methods to reduce delay at signalized intersections is improving the flow of traffic. Therefore, the alternatives of developing the optimal signal timing and improving geometrics using optimization software can make an efficient impact to reduce delay and improve the LOS at these intersections (He, et al., 2013; Roy, Barua and Das, 2015; Zhang, Sun and Kondyli, 2017). These problems can have a negative effect on drivers' comfort and LOS if not solved and optimized.

The literature covers a wide variety of researches indicating that one of the effective methods to reduce traffic congestion and delay and improving the performance of signalized intersections is the optimization of signal timing (Sunkari, 2004; Siddiqui, 2015; Udomsilp, et al., 2017; Ratrout and Assi, 2019). Others found that appropriate intersection improvement alternatives to achieve efficient operations include changing traffic signal timing, introducing additional lanes, and modifying the geometric conditions (Nyantakyi, et al., 2013; Roy, Barua and Das, 2015; Al-Allaff, et al., 2015; Zhang, Sun and Kondyli, 2017; Ragab and Abo El-Naga, 2019). Although, the focus of this research is using Synchro software and highway capacity manual (HCM) 2010 calculations, the findings from past published studies related to the evaluation and optimization of traffic performance at signalized intersections involved using different optimization software. Zhang, Sun and Kondyli (2017) used VISSIM software package to evaluate different optimization solutions and find a suitable alternative with the best performance measure or control delay. Based on the data of a representative intersection in Shanghai/China, introducing an additional right turn lane in one direction was found to be effective in reducing delay by 27.3% and improving traffic efficiency for the whole intersection.

ARO-The Scientific Journal of Koya University
Vol. X, No. 1 (2022), Article ID: ARO.10915, 9 pages
DOI: 10.14500/aro.10915
Received: 05 December 2021; Accepted: 27 June 2022
Regular research paper: Published: 30 June 2022
Corresponding author's e-mail: nasreen.hussein@uod.ac

http://dx.doi.org/10.14500/aro.10915

Several studies have been carried out on evaluating and improving signalized intersections. Jrew and Abojaradeh (2009) carried out a study to evaluate the operational analysis of Wadi-Saqra intersection in Amman city/Jordan, using HCM and Highway Capacity Software (HCS). For optimization process, the authors utilized the Synchro software to solve the current and future problems depending on different proposed alternatives. It was found that changing traffic signal timing, prohibiting left turn movement, and constructing an overpass for one direction did not improve the LOS. However, constructing two overpasses or one overpass and a tunnel will improve the LOS from F to C (Jrew and Abojarade, 2009). Similar findings have been reported by Joni and Hikmat (2017), where the LOS improved from F to C by implementing the strategy of constructing one overpass in one direction of a signalized intersection in Samawa city/Iraq (Joni and Hikmatt, 2017). Furthermore, Ziboon, et al. (2019) used Synchro 10 software to evaluate Al-FALLAH intersection in Baghdad city/Iraq by analyzing delay time, degree of saturation, and LOS. The authors found that the intersection is performing at LOS F under existing conditions (the year 2018) during peak hours. The authors suggested that the unique alternative to improve the performance of the intersection is the construction of an overpass for Al-Falah Street. After the implementation of the suggested geometric design, the intersection will operate at LOS D with an average delay of 41.3 s/veh in the design year (2038) (Ziboon, Qasim and Yousif, 2019).

Siddiqui (2015) found that optimizing cycle length using Synchro software was effective in reducing average delay by 30–35% for both off-peak and PM peak hours. To solve the current and future traffic congestion in a signalized intersection in Dhaka/Bangladesh, Roy, Barua and Das (2015) utilized VISSIM simulation computer program. The authors recommended four alternative proposals including prohibiting right turning movement at all approaches, changing the signal timing, constructing one overpass for one direction, and constructing two overpasses for two directions. The results showed that the third and fourth alternatives were significant in improving the LOS, however, the third alternative was more cost effective. In addition, in a study to manage traffic control and reduce delay at intersections, Udomsilp et al. (2017) focused on setting the optimal cycle length and helping in the application of a reversible lane that includes two traffic signals in a short distance along the selected road. To show an improvement in travel time, a comprehensive analysis was performed between actual signal timing and optimal cycle length. The travel time results indicated that periodic signal timing control by Synchro during peak hours was better than off-peak hours.

A genetic algorithm (GA)-based signal optimization program is developed by Park, Messer, and Urbanik (1999) during an oversaturated condition. The program optimizes different traffic signal parameters simultaneously including cycle length, green split, off set, and phase sequence. In addition, the intersection's performance was evaluated with Transyt-7F software. The authors found that the GA provided better signal timing plans as compared with Transyt-7F program. Besides, Ratrout and Assi (2019) developed a model to optimize signal timing, intersection space (space optimization and lane allocation), and phasing arrangement together. The authors utilized Transyt-7F, Synchro, and HCS 2010 to assess the developed model. The results showed that optimizing both time and spacing plan together produce lower intersection delay as compared to the optimization of the timing plan only. In Jordan, Al-Allaff et al. (2015) conducted a study to improve traffic management system on a network of two main arterials having eight signalized intersections. Synchro 8 program and HCS 2000 were used to evaluate the performance of each intersection. The evaluation output illustrated that the six intersections were operating at high saturation condition with LOS F and two intersections have LOS D. The authors suggested two alternatives. The first alternative was changing the timing plan and the second alternative included modifying the geometric conditions with changing the timing plan. Based on the analysis of data, it was found that with an improvement in the saturation flow, the LOS of the intersections improved from LOS F to LOS C, D, and E.

Another study focused on average delay and LOS estimation at two three-legged intersections in Mansoura city/Egypt (Ragab and Abo El-Naga, 2019). To develop models and analyze the selected intersections, VISSIM micro-simulation software was used. The authors investigated three strategies; first: Original strategy, second: Optimization of signal cycle time, and third: Increasing of lane width. The simulation results illustrated that the second and third strategies resulted in a reduction in delay and improving the LOS from D to C.

The purpose of this study is to assess the performance of two selected signalized intersections in Duhok city and develop the optimum signal timing and geometric improvement using Synchro 8 software. Delay and LOS of each movement and approach of the intersections and for the whole intersections are evaluated using both HCM procedure and Synchro software. Different alternatives and suggestions are proposed to solve the current and future problems including, creating an overpass, changing the cycle length, adding lanes, and prohibiting approaching traffic. Evaluating, analyzing, and optimizing the existing traffic signal of the intersection are also performed by applying the suggested alternatives with and without changing the geometric conditions using Synchro computer program. The future condition of all the intersections is assessed using traffic growth factor. It is important to note that Synchro software calculates intersection and approach delays either based on Chapter 16 of the HCM 2000 or chapter 31 of HCM 2010. Synchro is a macroscopic traffic signal timing tool that can be utilized to optimize signal timing parameters such as cycle lengths, splits, offsets, and phase order for isolated intersections, and make coordinated traffic signal timing plans for arteries and networks. It has no limitations on the number of links and nodes. Synchro is simple in usage and rapid in modeling (Sabra, Wallace and Lin, 2000). For the mentioned reasons, this program was chosen in this study.

Details of sites selection, collection of traffic volume data, geometric characteristics, signal timing, and assessment approach are described in this paper. Assessment results are also presented and discussed.

## II. Study Area Description

The area of the study consists of two intersections with different urban streets. The presence of various entertainment places in addition to the presence of restaurants, schools, mosques, buildings, and shopping centers has increased the traffic and thus increased the traffic congestion. The selected intersections are Zari land intersection which is consisting of four legs and Salahaddin Mosque intersection which is consisting of three legs. Both intersections are located in non-Central Business District area. The geometric plan of the existing intersections is shown in Fig. 1.

## III. Data Collection Methods

To evaluate the performance of traffic flow at the selected signalized intersections, both field survey and video recording technique using a fixed camera were used in the present study as data collection method. Two methods were used to identify the main input data required for the HCM and selected software program. In good weather condition and based on the information from Duhok Traffic Directorate, the data were collected at the selected signalized intersections for 3 normal days, from 7:30 AM to 10:30 AM to find the morning peak hour. The 3 days were providing a suitable sample to

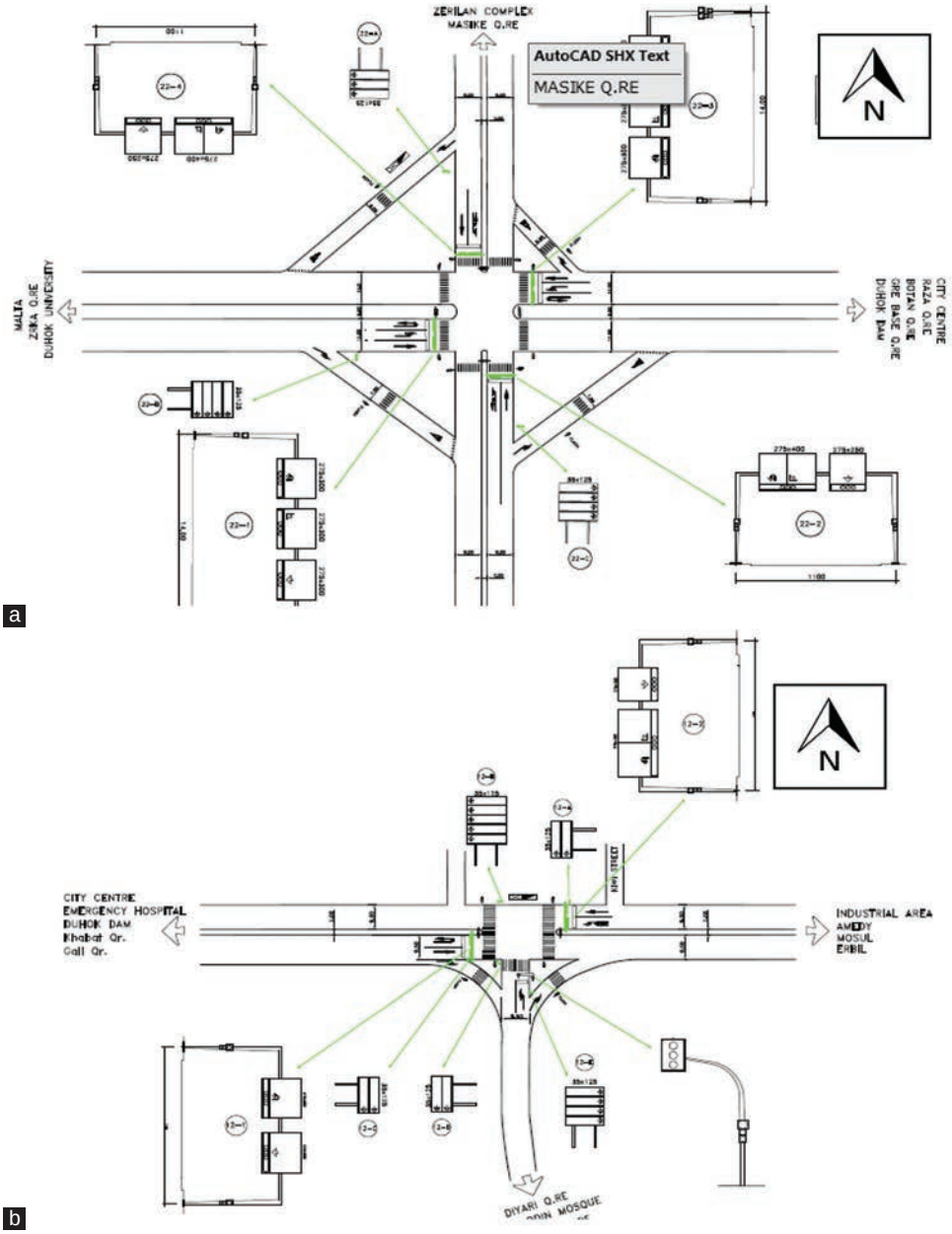


Fig. 1. Geometric plan of (a) Zari land intersection and (b) Salahaddin Mosque intersection.

 http://dx.doi.org/10.14500/aro.10915

cover most ranges of traffic conditions under the usual traffic circumstances. A video recording technique using a fixed camera was used in the present study as data collection method for the two selected signalized intersections. Using video recording technique made the selection difficult, as it was necessary to find a good point located on a high place (such as a building) to cover a sufficient approach length (at least 100 m to the stop line). The recorded videos were reviewed and the required data were extracted manually. The advantage of this method is that it allows for a large number of events to be recorded at the same time. The two signalized intersections were visited (field observation) for collecting both geometric characteristics using a measuring tape and recording signal settings using a stopwatch for all approaches of the selected intersections.

### *A. Traffic Volume Data*

Traffic volume data were collected using video recording technique and manual counting of vehicles from the recorded data for 3 normal days from 7:30 AM to 10:30 AM for each 15 min interval to find the variation of flow and determine the peak and off-peak hours. The count started and ended at the same time at each approach. The data collected covers:

1. Traffic volume with composition to indicate % of heavy vehicles
2. Traffic volume with turn types (through, left turn and right turning traffic volume) counts to indicate the proportion of the left and right turn movements
3. In this study, the highest peak hour volume in the morning hours is selected for each approach in the intersection to simulate the worst situation in the intersection to be used in the capacity analysis based on the peak hour factor (PHF) of each approach and in the capacity analysis based on the PHF of each movement
4. Growth rate of traffic volume.

### *B. Geometrical Characteristics and Signal Timing Data*

In addition to the traffic data, geometric data should be collected as input during the optimization process by Synchro software. Field survey and manual method characterized using a measuring tape are also used in this study to collect the required geometric characteristics of each intersection. The geometric characteristics include area type, approach width, number of approach lanes, presence of median, width of median, presence of shared lane on each approach, right turn channelized or not, right turn control type (yield, signal, and free), presence of bus stop, and parking. Signal timing data including type of control, total cycle length, green, yellow, red time, all red (clearance interval), and phase plan were obtained from signal indication during the field survey by a stop watch.

## IV. Results and Discussion

The peak hour volume and the PHF for each approach were found from manual counting of the traffic volume data from video recording technique. The PHFs for all approaches and each movement within each approach for Zari land intersection and Salahaddin Mosque intersection is given in Table I.

### *A. Evaluation of Existing Condition*

The analysis was performed based on the existing traffic volumes, signal timing, and geometric configurations for both intersections using the (HCM, 2010) steps and Synchro software. The ratio of demand flow rate to capacity (v/c), average control delay, and LOS are the main performance indices in the evaluation process with HCM 2010 and Synchro software. Operational analysis or determination of LOS based on HCM 2010 includes; input values (considering details of intersection flows, signalization), and geometrics, volume adjustment, saturation flow rate, capacity analysis, delay computation, and LOS. The results of movement delay calculation for Zari land intersection in Table II illustrated that the intersection is operating at LOS F with high intersection delay (747) s/veh during the morning peak hour.

It can be seen that the delay level is unacceptable for EB, which may be due to inadequate phase plan and distribution of green time and more specifically due to low number of lanes allocated for the through movement and capacity problems. In general, the delay is high, and the demand is over capacity. This is due to the reason that the delay may increase rapidly with minor changes in the demand when comparing the WB and EB situations. For the application of Synchro software, the abstracted and collected data required for the software were fed into the program for each movement, each approach, and for the whole intersection. The existing peak traffic flow in Synchro software is shown in Fig. 2.

Table I
PHF Values for Zari Land Intersection and Salahaddin Mosque Intersection

| PHF Values for Zari land Intersection | | | |
|---|---|---|---|
| Direction | PHF by approach | Movement | PHF by movement |
| NB | 0.92 | L | 0.94 |
| | | TH | 0.88 |
| | | R | 0.94 |
| SB | 0.91 | L | 0.89 |
| | | TH | 0.83 |
| | | R | 0.88 |
| WB | 0.94 | L | 0.84 |
| | | TH | 0.93 |
| | | R | 0.84 |
| EB | 0.88 | L | 0.85 |
| | | TH | 0.95 |
| | | R | 0.79 |
| PHF values for Salahaddin Mosque intersection | | | |
| Direction | PHF by approach | Movement | PHF by movement |
| NB | 0.85 | L | 0.81 |
| | | R | 0.86 |
| WB | 0.95 | L | 0.89 |
| | | TH | 0.83 |
| EB | 0.84 | L | 0.90 |
| | | TH/R | 0.94 |

Table II
HCM 2010 Calculations by Movement – Zari Land Intersection

| Hand calculations by movement | | | | | | | | | | | |
|---|---|---|---|---|---|---|---|---|---|---|---|
| Direc/LnGrp | v/c Ratio | g/c Ratio | Unif Delay d1 (sec) | Progr Fact PF | Lane Grp Cap | Cal Term k | Incr Delay d2 (sec) | Lane Grp Delay | Lane Grp LOS | Delay by APP (s/veh) | LOS by App |
| WB/L | 0.66 | 0.27 | 71 | 1 | 770 | 0.5 | 4.4 | 75.4 | E | 459 | F |
| WB/TR | 2.31 | | 78 | 1 | 392 | 0.5 | 597 | 675 | F | | |
| EB/L | 0.48 | 0.20 | 72 | 1 | 663 | 0.5 | 2.48 | 74.5 | E | 1266 | F |
| EB/TR | 4.19 | | 81 | 1 | 348 | 0.5 | 1442 | 1523 | F | | |
| SB/L | 1.46 | 0.22 | 81 | 1 | 395 | 0.5 | 221 | 302 | F | 278 | F |
| SB/TR | 1.34 | | 81 | 1 | 384 | 0.5 | 170 | 251 | F | | |
| NB/L | 0.90 | 0.19 | 71 | 1 | 497 | 0.5 | 22 | 93 | F | 201 | F |
| NB/TR | 1.44 | | 74 | 1 | 472 | 0.5 | 210 | 284 | F | | |
| Intersection | | | | | | | | | | 747 | F |

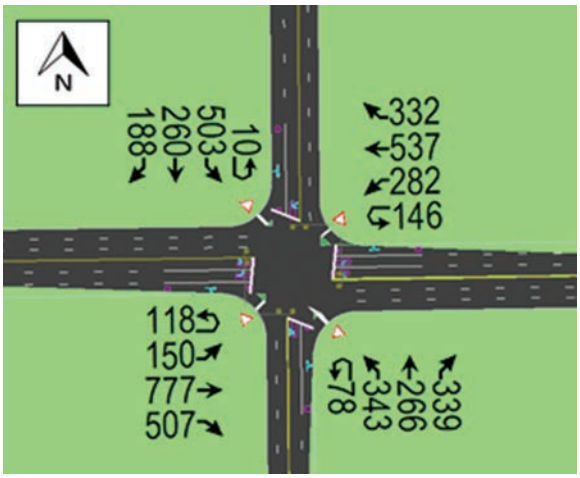


Fig 2. The existing peak traffic flow in Synchro software – Zari land intersection.

Assessment of the average delay per vehicle in each lane group, each approach, and for the whole intersection (operational analysis by movement) is shown in Table III. The results illustrated that the intersection is operating at LOS F with a high delay (589.8) s/veh during the morning peak hour.

The results of HCM application for movement delay calculation for Salahaddin Mosque intersection in Table IV illustrated that the intersection is operating at LOS F with a high delay (608.9) s/veh during the morning peak hour. The v/c ratio of the through movement is much higher than that of the left turn movement at both WB and EB. This imbalance results in much higher delay experienced by one movement than the other.

The average delay time of the left movement for both WB and EB approaches was 33.2 and 30.4 s/veh, respectively, which is equivalent to the LOS C and indicates that the traffic continues smoothly or the approach green time is reasonable for the volume in left movements. However, the extremely high average delay through movements likely indicates a breakdown of vehicular traffic flow. The HCM delay model produces reasonable results for undersaturated conditions but compared to other delay models, predicts higher delays for oversaturated conditions. The existing peak traffic flow in Synchro software is shown in Fig. 3.

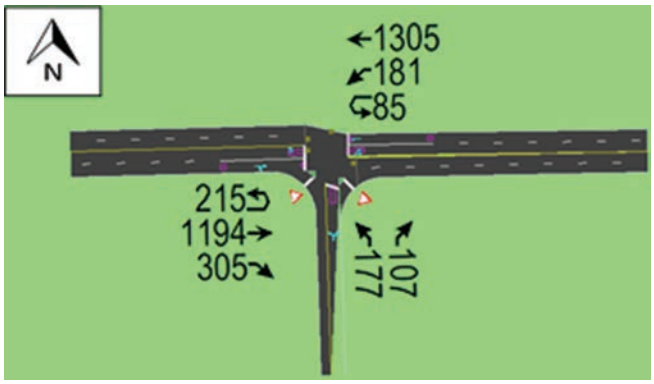


Fig. 3. The existing peak traffic flow in Synchro – Salahaddin Mosque intersection.

Assessment of the average delay per vehicle in each lane group, each approach, and for the whole intersection (operational analysis by movement) is shown in Table V. The results illustrated that the intersection is operating at LOS F with high a delay (544.3) s/veh during the morning peak hour. Similar to the Zari land intersection, the result of delay analysis for Salahaddin Mosque intersection using both HCM 2010 and Synchro software applications indicates a nearly reasonable matching between the software generated and the calculated delay values using movement analysis.

In general, the analysis results of both intersections by HCM 2010 procedure and Synchro software application indicate a nearly reasonable matching between the software generated delay and the calculated delay values using movement analysis. However, a comparison is made by the paired samples t-test using SPSS V.27 program to determine whether there is a difference between average delay calculated by HCM and Synchro software (Synchro, 2011). The results indicate that there is no statistically significant difference between two mean values of delay with mean of delay difference of 21.38 s and $P = 0.23$. The difference between both results may be due to the reason that although Synchro computes control delay for the signalized intersections according to the HCM method, it offers an alternative calculation of delay based on an expected distribution of traffic volumes for the intersection which is called the percentile delay for different traffic volume levels to differentiate it from the HCM control delay.

 http://dx.doi.org/10.14500/aro.10915

Table III
Synchro Application by Movement – Zari Land Intersection

| Synchro by movement | | | | | | | | |
|---|---|---|---|---|---|---|---|---|
| Direc/LnGrp | v/c ratio | G/C RATIO | Progr Fact PF | Cal Term k | Ln Grp Delay | Ln Grp LOS | Delay by APP (s/veh) | LOS by App |
| WB/L | 0.48 | 0.27 | 1 | 0.5 | 82.2 | F | 1182.9 | F |
| WB/TR | 4.11 | | 1 | 0.5 | 583.7 | F | | |
| EB/L | 0.64 | 0.20 | 1 | 0.5 | 76.8 | E | 404.3 | F |
| EB/TR | 2.21 | | 1 | 0.5 | | F | | |
| SB/L | 1.57 | 0.22 | 1 | 0.5 | 313.5 | F | 276.3 | F |
| SB/TR | 1.36 | | 1 | 0.5 | 233.3 | F | | |
| NB/L | 0.95 | 0.19 | 1 | 0.5 | 100.8 | F | 172.5 | F |
| NB/TR | 1.36 | | 1 | 0.5 | 222.9 | F | | |
| Intersection | | | | | | | 589.8 | F |

Table IV
HCM 2010 Calculations by Movement – Salahaddin Mosque Intersection

| Hand calculations by movement | | | | | | | | | | | |
|---|---|---|---|---|---|---|---|---|---|---|---|
| Direc/LnGrp | v/c Ratio | g/c Ratio | Unif Delay d1 (sec) | Progr Fact PF | Lane Grp Cap | Cal Term k | Incr Delay d2 (sec) | Lane Grp Delay | Lane Grp LOS | Delay by APP (s/veh) | LOS by App |
| WB/L | 0.47 | 0.353 | 30.7 | 1 | 635 | 0.5 | 2.5 | 33.2 | C | 721.4 | F |
| WB/T | 2.76 | 0.353 | 39.5 | 1 | 655 | 0.5 | 796.3 | 835.8 | F | | |
| EB/L | 0.34 | 0.353 | 29 | 1 | 692 | 0.5 | 1.4 | 30.4 | C | 562.8 | F |
| EB/TR | 2.33 | 0.353 | 39.5 | 1 | 685 | 0.5 | 603.1 | 642 | F | | |
| NB/LR | 1.15 | 0.148 | 52 | 1 | 291 | 0.5 | 99.6 | 151.6 | F | 151.6 | F |
| Intersection | | | | | | | | | | 608.9 | F |

Table V
Synchro Application by Movement – Salahaddin Mosque Intersection

| Synchro by movement | | | | | | | | |
|---|---|---|---|---|---|---|---|---|
| Direc/Ln Grp | v/c Ratio | g/c Ratio | Progr Fact PF | Cal Term k | Ln Grp Delay | Ln Grp LOS | Delay by APP (s/veh) | LOS by App |
| WB/L | 0.48 | 0.35 | 1 | 0.5 | 33.8 | C | 562.9 | F |
| WB/T | 2.42 | 0.35 | 1 | 0.5 | 665.6 | F | | |
| EB/L | 0.37 | 0.35 | 1 | 0.5 | 31.5 | C | 593.2 | F |
| EB/TR | 2.45 | 0.35 | 1 | 0.5 | 677.4 | F | | |
| NB/LR | 1.22 | 0.15 | 1 | 0.5 | 169.8 | F | 169.8 | F |
| Intersection | | | | | | | 544.3 | F |

It computes the uniform delay (d1) for the 90$^{th}$ percentile volume, the 70$^{th}$ percentile volume, the 50$^{th}$ percentile volume, the 30$^{th}$ percentile volume, and the 10$^{th}$ percentile volume. For instance, if the traffic is observed for 100 cycles, the 90$^{th}$ percentile would be the 90$^{th}$ busiest. The five delay calculations are averaged to find the average delay (Siddiqui, 2015). Furthermore, running the Synchro models with default parameters contributes to the difference between both delays estimations.

### *B. Optimization of the Existing Conditions*

Synchro software provides good improvement in reducing the intersection delay and improving the LOS through optimization and implementation of suitable alternatives. The optimization results include some major and important measures of effectiveness such as degree of saturation, intersection delay, and LOS. As there is a nearly reasonable agreement for the results of delay analysis by movement between HCM (2010) calculation and Synchro 8, the existing Synchro models obtained from analysis by movement were optimized using the optimization tool within Synchro. The improvement suggestions for both intersections with their output results are presented in the following sections.

#### *The improvement proposals of the Zari land intersection*

Zari land intersection runs as nearly 590 s/veh as average delay and at LOS F. The intersection is oversaturated and considered unsafe. Hence, an improvement scenario must be implemented. According to the HCM (2010), the situation of the intersection is critical when both delay levels and v/c ratios are unacceptable. Therefore, the full range of possible geometric and signal design improvements should be considered as suggestions. Different improvement scenarios were proposed for this purpose such as:

1. Proposal 1: Optimization by changing the cycle length
2. Proposal 2: Optimization by adding a lane for through movement for all approaches
3. Proposal 3: Optimization by changing the cycle length and adding a through lane for all approaches
4. Proposal 4: Optimization by creating an overpass for the main street

5. Proposal 5: Optimization by creating an overpass for the main street, changing the cycle length, and adding a left turn lane for WB and EB and adding a through lane for SB and NB.

The optimization by changing the geometric elements started by adding a lane either for through movement in the major street or for the left turning movement in the minor street. From the field survey measurements, it was observed that the number of lanes in these approaches can be increased by decreasing the lane width (with keeping the width of lanes greater than a minimum value of 2.4 m as recommended by HCM [2010]) which is actually practicable in the field. This is done in Synchro by remarking the approaching lanes and setting the lane width to the maximum allowable width for each approach. This certainly will result in rearranging of queuing vehicles at the stop line. Optimization by creating an overpass for the main street (WB-EB) was another proposal. This proposal was applied as this intersection suffers from high traffic volume and particularly at the through movement. Furthermore, there is an enough space for constructing the overpass. Creation of an overpass was more effective when both cycle time optimization and adding an extra lane for through movement in the main street and a lane for the left turning movement in the minor street were implemented.

The results of all proposed improvements for the existing condition and after optimization for all approaches of this intersection are illustrated in Table VI. The intersection results for cycle length, delay, reduction in delay, and LOS from the base scenario and different optimization methods are reported in Table VII. Comparing to the existing condition, the delay has been decreased considerably and it can be noticed that for the proposals 1, 2, 3, and 4, the delay values have been reduced by 16.72%, 79.41%, 81.79%, and 76.03%, respectively. However, the intersection is still operating at LOS F. The reason behind this is the excessive number of vehicles that cannot be accommodated sufficiently by the intersection and particularly by the insufficient number of the left turn lanes in the main street (WB-EB) and through lanes in the minor street (NB-SB). The reduction in delay is more evidence in proposal 5 indicating 93.37% of reduction resulting the better improvement in LOS values from F to D according to LOS criteria for signalized intersections given in HCM (2010).

*The improvement proposals of the Salahaddin Mosque intersection*

Salahaddin Mosque intersection runs as nearly 545 s/veh as an average delay and at LOS F. The intersection is oversaturated, and therefore, an improvement scenario must be implemented. Different improvement scenarios were proposed for this purpose such as:

1. Proposal 1: Optimization by changing the cycle length
2. Proposal 2: Optimization by adding a lane for through movement for the main street and adding an exclusive left turn lane for the minor street
3. Proposal 3: Optimization by changing the cycle length and adding a through lane for the main street and adding an exclusive left turn lane for the minor street

Table VI
Proposed Improvements for the Existing Condition and After Optimization – Zari Land Intersection

| Suggested proposal | Delay (s/veh) | | | | LOS | | | |
|---|---|---|---|---|---|---|---|---|
| | WB | EB | NB | SB | WB | EB | NB | SB |
| Existing condition | 1182.9 | 404.3 | 172.5 | 276.3 | F | F | F | F |
| Proposal 1 | 439.6 | 660.9 | 368.6 | 402.8 | F | F | F | F |
| Proposal 2 | 86.2 | 164 | 74.8 | 144.7 | F | F | E | F |
| Proposal 3 | 109.9 | 88.3 | 94.6 | 148.8 | F | F | F | F |
| Proposal 4 | 51.4 | 27.6 | 172.5 | 276.3 | D | C | F | F |
| Proposal 5 | 36.3 | 19.4 | 41.5 | 54.4 | D | B | D | D |

4. Proposal 4: Optimization by changing the cycle length, adding a lane for through movement for the main street, and prohibiting approaching traffic from NB.

The results of all proposed improvements for the existing condition and after optimization for all approaches of this intersection are illustrated in Table VIII. The intersection results for cycle length, delay, reduction in delay, and LOS from the base scenario and different optimization methods are reported in Table IX. Comparing to the existing condition, the delay has been decreased considerably and it can be noticed that for the proposals 1, 2, and 3, the delay values have been reduced by 7.31%, 69.68%, and 73.14%, respectively. However, the intersection is still operating at LOS F. This is due to the reason that the larger number of phases in a traffic light results in a longer waiting time and having a lower share of green time. Therefore, prohibiting the approaching traffic from NB (the minor street with left and right turn only) will certainly increase the capacity of the intersection after sharing the green time of this approach between two other approaches of the intersection.

The reduction in delay is more evidence in proposal 4 indicating 87.12% of reduction resulting the better improvement in LOS values from F to E. The proposal 4 is implemented in Synchro by remarking the approaching lanes and setting the lane width to the maximum allowable width for each approach in addition to optimizing the cycle length and prohibiting approaching traffic from NB. This certainly will result in rearranging of queuing vehicles at the stop line.

### *C. Evaluation of the Future Condition*

The future traffic volume expected to use the highway facilities should be taken into consideration in the design of new highways or implementation of improvements to the existing facilities. To make accurate estimates for future, usually, a period of 15–20 years is used in calculation of growth factor or traffic forecast factor. Synchro software is used to analyze the future data for both intersections based on proposals 5 for Zari land intersection and proposal 4 for Salahaddin Mosque intersection with the “3%” traffic growth factor. Zari land intersection under the proposed improvement of optimization by creating an overpass for the main street, changing the cycle length, and adding a left turn lane for WB and EB and adding a through lane for SB and NB was evaluated for the future traffic volume using Synchro software. Based on the proposal 5 and 3% of traffic

 http://dx.doi.org/10.14500/aro.10915

Table VII
Average Delays and LOS for Existing and Different Improvement Scenarios – Zari Land Intersection

| Synchro output | Existing condition | After optimization | | | | |
|---|---|---|---|---|---|---|
| | | Proposal 1 | Proposal 2 | Proposal 3 | Proposal 4 | Proposal 5 |
| Cycle length (sec) | 198 | 150 | 198 | 150 | 198 | 120 |
| Max V/C ratio | 4.1 | 2.71 | 1.5 | 1.2 | 1.57 | 0.86 |
| Delay (s/veh) | 589.8 | 491.2 | 121.4 | 107.4 | 141.4 | 39.1 |
| Reduction in delay % | | 16.72 | 79.41 | 81.79 | 76.03 | 93.37 |
| LOS | F | F | F | F | F | D |

Table VIII
Proposed Improvements for the Existing Condition and After Optimization – Salahaddin Mosque Intersection

| Suggested proposal | Delay | | | LOS | | |
|---|---|---|---|---|---|---|
| | WB | EB | NB | WB | EB | NB |
| Existing condition | 562.9 | 593.2 | 169.8 | F | F | F |
| Proposal 1 | 514.5 | 544.3 | 229.4 | F | F | F |
| Proposal 2 | 181.3 | 168.9 | 50.8 | F | F | D |
| Proposal 3 | 141.5 | 163.9 | 76.3 | F | F | E |
| Proposal 4 | 61.2 | 79.3 | | E | E | |

Table IX
Average Delays and LOS for Existing and Different Improvement Scenarios – Salahaddin Mosque Intersection

| Synchro output | Existing condition | After optimization | | | |
|---|---|---|---|---|---|
| | | Proposal 1 | Proposal 2 | Proposal 3 | Proposal 4 |
| Cycle length (sec) | 122 | 150 | 122 | 150 | 140 |
| Max V/C ratio | 2.45 | 2.32 | 1.38 | 1.31 | 1.09 |
| Delay (s/veh) | 544.3 | 504.5 | 165 | 146.2 | 70.1 |
| Reduction in delay % | | 7.31 | 69.68 | 73.14 | 87.12 |
| LOS | F | F | F | F | E |

growth factor, the intersection will operate at LOS F with an average control delay of 484.7 s. Although the intersection will be under worst operating condition with LOS F, there will be 17.82% reduction in delay comparing to the existing condition for the upcoming 15 years based on the improvement suggested in proposal 5. Salahaddin Mosque intersection under the proposed improvement of optimization by changing the cycle length and prohibiting approaching traffic from NB was evaluated for the future traffic volume using Synchro software. Based on the proposal 4 and 3% of traffic growth factor, the intersection will operate at LOS F with an average control delay of 865.3 s. It was found that no benefit could be obtained by optimizing the cycle length and prohibiting approaching traffic from NB for future condition as compared to the existing condition.

## V. Conclusion

At present, transportation authorities have to implement effective countermeasures to resolve the existing congestion problems and improve the traffic operation of signalized intersections. Effective traffic signal control is essential to ensure smooth and arranged traffic operation of urban roads. In this study, traffic performance of two signalized intersections during morning peak hour is evaluated and optimized based on the methodology in the (HCM) 2010 and Synchro 8 software. It has been confirmed that the current state of the intersections exhibits weak performance, due to the extreme values of vehicular waiting times (delay) that have been detected. Zari land intersection using HCM 2010 methodology is estimated to be operating at LOS F with a delay of 747 s/veh and at LOS F with a delay of 589.8 s/veh when using Synchro software. For Salahaddin Mosque intersection, the HCM results illustrated that the intersection is operating at LOS F with a delay of 608.9 s/veh, whereas from Synchro software, the intersection is operating at LOS F with delay of 544.3 s/veh. Several proposals were assessed for both intersections to improve traffic operation such as changing the cycle length, adding lanes, creating an overpass, and prohibiting approaching traffic.

Compared to the baseline scenario or existing conditions, for Zari land intersection, the delay has been decreased considerably and it was found that for the alternative proposals; 1, 2, 3, and 4, the delay values have been reduced by 16.72%, 79.41%, 81.79%, and 76.03%, respectively. However, the intersection is still operating at LOS F. The reduction in delay is more evidenced in proposal 5 with 93.37% of reduction and an improvement in LOS from F to D. For Salahaddin Mosque intersection, the delay has been decreased considerably and it was found that for proposals 1, 2, and 3, the delay values have been reduced by 7.31%, 69.68%, and 73.14%, respectively. However, the intersection is still operating at LOS F. It also indicated that implementing the proposal 4 improved the intersection LOS from F to E, with a significant decrease in control delay of 87.12|% and volume to capacity ratio.

Synchro software was used to analyze the future data for both intersections based on proposal 5 for Zari land intersection and proposal 4 for Salahaddin Mosque intersection with the traffic growth factor of 3%. It was found that the Zari land intersection will operate at the LOS F with 17.82% reduction in delay compared to current condition. Furthermore, the Salahaddin Mosque intersection will operate at the LOS F and no benefit could be obtained by optimizing the cycle length, adding a lane for through movement of the main street, and prohibiting approaching traffic from NB for future condition as compared to the current condition. The situation of the intersection is critical when both delay levels and v/c ratios are unacceptable. Therefore, the full range of possible geometric and signal design improvements should be considered as suggestions. It can be concluded that the approach used in evaluating the existing condition and

optimization methods used herein proved to be successful in addressing the study objectives. A future extension of this work should be performed to evaluate the traffic performance for other types of intersections that have not been considered in this study such as network analysis and coordinating intersections.

## VI. Acknowledgment

The author would like to thank "Duhok Traffic Directorate" to their support and assistance of accomplishing this study.

## References

Al-Allaff, R.A., Jrew, B., Abojaradeh, M. and Msallam, M., 2015. Evaluation and Improvement of Traffic Flow and Traffic Network Management System in Al-Shmesani Amman Jordan. *7th Traffic Safety* Conference from 12-13 May 2015 in Amman, Jordan.

Chen, P., Qi, H. and Sun, J., 2014. Investigation of saturation flow on shared right-turn lane at signalized intersections, *Transportation Research Record: Journal of the Transportation Research Board*, 2461, pp.66-75.

HCM, 2010. *Highway Capacity Manual, Transportation Research Board, National Research Council*. USA, Washington, DC.

He, S., Wang, W., Zhang, J. and Yang, J., 2013. An improved optimization method for isolated signalized intersection based on the temporal and spatial resources integration. *Procedia Social and Behavioral Sciences*, 96, pp.1696-1706.

Joni, H.H. and Hikmatt, M.M., 2017. Assessment at Al-Ameer signalized intersection in Samawa city. In: *Third International Conference on Building, Construction and Environmental Engineering*, Egypt.

Jrew, B.K. and Abojarade, M.A., 2009. Evaluation and Improvement of Wadi-Saqra Signalized Intersection in Amman City. *The 4th Conference in Scientific Research in Jordan*, Jordan Society for Scientific Research, 7 November 2009, Amman Jordan. Highway and Traffic in Jordan, pp.3-19.

Koonce, P., Rodegerdts, L., Lee, K., Quayle, S., Beaird, S., Braud, C., Bonneson, J., Tarnoff, P. and Urbanik, T., 2008. *Traffic Signal Timing Manual*. USDOT-FHWA, Project HOP-08-024, USA, Washington DC.

Nyantakyi, E.K., Adams, C.A., Borkloe, J.K. and Pobee, D., 2013. Synchronization of signalised intersections: A case study of three major intersections on the 24th February road, Kumasi, Ghana. *International Journal of Engineering Research and Applications*, 3(4), pp.2566-2590.

Park, B., Messer, C.J. and Urbanik, T., 1999. Traffic signal optimization program for oversaturated conditions genetic algorithm approach. *Transportation Research Record*, 1683, pp.133-142.

Potts, I.B., Ringert, J.F., Bauer, K.M., Zegeer, J.D., Harwood, D.W. and Gilmore, D.K., 2007. Relationship of lane width to saturation flow rate on urban and suburban signalized intersection approaches, transportation research record. *Journal of the Transportation Research Board*, 2007, pp.45-51.

Ragab, M. and Abo El-Naga, I., 2019. Measures to improve traffic operations at signalized intersection in urban areas. *International Journal for Traffic and Transport Engineering*, 9(4), pp.408-418.

Ratrout, N. and Assi, K., 2019. Development and evaluation of a quick method for optimizing a space and timing plan for isolated signalized intersection. *Transport*, 36(2), pp.1-12.

Roy, C.K., Barua, S. and Das, A., 2015. A Study on Feasible Traffic Operation Alternatives at Signalized Intersection in Dhaka City. In: *International Conference on Recent Innovation in Civil Engineering for Sustainable Development* (IICSD-2015), DUET Gazipur, Bangladesh.

Sabra, Z., Wallace, C.H.E. and Lin, F., 2000. Traffic Analysis Software Tools. *Transportation Research Board* (*TRB*)/*National Research Council*, Transportation Research Circular E-C014.

Siddiqui, S., 2015. Signal Timing Evaluation and Optimization. Technical Report.

SPSS, 2021. Statistical Package for the Social Sciences, Version 27, 2021.

Sunkari, S., 2004. The benefits of retiming traffic signals. *ITE Journal*, 74(4), pp.26-29.

Synchro, 2011. Synchro Studio 8 User Guide.

Udomsilp, K., Arayakarnkul, T., Watarakitpaisarn, S., Komolkiti, P., Rudjanakanoknad, J. and Aswakul, C., 2017. Traffic data analysis on sathorn road with synchro optimization and traffic simulation. *Engineering Journal*, 21(6), pp.57-67.

Zhang, Y., Sun, D.J. and Kondyli, A., 2017. An empirical framework for intersection optimization based on uniform design. *Journal of Advanced Transportation*, 2017(4), pp.1-10.

Ziboon, A.T., Qasim, Z.I. and Yousif, M.A., 2019. Traffic performance evaluzation and aanalysis of Al-Fallah intersection in Baghdad City utilizing synchro.10 software. *Journal of Engineering and Sustainable Development*, 23(6), pp.25-34.

# General Information

**ARO's Mission:** ARO seeks to publish those papers that are most influential in their fields or across fields and that will significantly advance scientific understanding. Selected papers should present novel and broadly important data, syntheses, or concepts. They should merit the recognition by the scientific community and general public provided by publication in ARO, beyond that provided by specialty journals.

We welcome submissions from all fields of natural science and technology, and from any source. We are committed to the prompt evaluation and publication of submitted papers. ARO is published biannually; selected papers are published online ahead of print.

## Submission

Manuscripts should be submitted by the correspondent authors of the manuscript via the on-line submission page. Regardless of the source of the word-processing tool, only electronic Word (.doc, .docx, .rtf) files can be submitted on-line. There is no page limit. Only online submissions are accepted to facilitate rapid publication and minimize administrative costs. Submissions by any other one but the authors will not be accepted. The submitting author takes responsibility for the paper during submission and peer review. If for some technical reason submission through the email is not possible, the author can contact aro.journal@koyauniversity.org for support. Before submitting please check ARO's guide to authors thoroughly to avoid any delay in the review and publication process.

Authors are explicitly responsible for the language of their texts. Paper should be submitted in a well written in understandable English. Authors should not expect the editor or editorial board to rewrite their paper. Prior to submission, authors should have their paper proofread by a possible academic native speaker of English.

- Submit the Article with contact Information
- File name should be your article tittle
- Don't submit your article in multiple journal, we are taking only minimum time for review process. please don't waste our time
- Once the paper is accepted, it can't be withdrawn
- Please follow publication ethics and regulation
- Avoid plagiarism and copied material
- Strictly Follow ARO's Template

## Terms of Submission

Papers must be submitted on the understanding that they have not been published elsewhere and are not currently under consideration by another journal or any other publisher. ARO accepts original articles with novel impacts only. Post conference papers are not accepted "as is", however, regular papers on the same topic but with a different title can be submitted. The new paper should contain significant improvements in terms of extended content, analysis, comparisons with popular methods, results, figures, comments, etc. Please do not forget that the publication of the same or similar material in ARO constitutes the grounds for filing of an (auto) plagiarism case.

The submitting author is responsible for ensuring that the article’s publication has been approved by all the other co-authors. It is also the authors’ responsibility to ensure that the articles emanating from a particular institution are submitted with the approval of the necessary institution. Only an acknowledgement from the editorial office officially establishes the date of receipt. Further correspondence and proofs will be sent to the author(s) before publication unless otherwise indicated. It is a condition of submission of a paper that the authors permit editing of the paper for readability. All enquiries concerning the publication of accepted papers should be addressed to aro.journal@koyauniversity.org.

### Peer Review

All manuscripts are subject to peer review and are expected to meet standards of academic excellence. Submissions will be considered by an editor and "if not rejected right away" by peer-reviewers, whose identities will remain anonymous to the authors.

# Guide to Author

We welcome submissions from all fields of science and from any source. We are committed to the prompt evaluation and publication of submitted papers. Selected papers are published online ahead of print. Authors are encouraged to read the instructions below before submitting their manuscripts. This section arranged into an overview speedy guidelines below and more detailed at the bottom section of this page

### Manuscript Preparation

Submitting your manuscript will be in two stages namely before final acceptance and after.

***Stage one:***

At the first stage manuscript needs to be prepared electronically and submitted online via the online submission page in a Word (.doc, .docx, .rtf) format of one column double-spaced page, Times New Roman font type, and 12 p font size. A pdf version of the submitted manuscript should be submitted too. All authors' names, affiliations, e-mail addresses, and mobile phone numbers should be typed on a cover page, indicating the correspondent author.

***Stage two:***

- File type: MS-Word version 2003 or later.
- Format: The preferred format of the manuscript two-column template with figures and captions included in the text. This template can be downloaded via the following link. Please follow instructions given in the template; http://aro.koyauniversity.org/about/submissions#onlineSubmissions
- Text: All text is in Times New Roman font. The main text is 10-point, abstract is 9-point font and tables, references and captions are 8-point font.
- Figures: Figures should be easily viewed on a computer screen.

### Units of Measurement

Units of measurement should be presented simply and concisely using System International (SI) units.

### Title and Authorship Information

The following information should be included;

- Paper title.
- Full author names.
- Affiliation.
- Email addresses.

## Abstract

The manuscript should contain an abstract. The abstract should be self-contained and citation-free and should not exceed 200 words.

## Introduction

This section should be succinct, with no subheadings.

## Materials and Methods

This part should contain sufficient detail so that all procedures can be repeated. It can be divided into subsections if several methods are described.

## Results and Discussion

This section may each be divided by subheadings or may be combined.

## Conclusions

This should clearly explain the main conclusions of the work highlighting its importance and relevance.

## Acknowledgements

All acknowledgements (if any) should be included at the very end of the paper before the references and may include supporting grants, presentations, and so forth.

### References

References must be included in the manuscript and authors are responsible for the accuracy of references. Manuscripts without them will be returned. ARO is following Harvard System of Referencing. (Learn how to import and use Harvard Styling in your Microsoft Office by following this link:
http://bibword.codeplex.com/releases/view/15852)

## Preparation of Figures

Upon submission of an article, authors are supposed to include all figures and tables in the PDF file of the manuscript. Figures and tables should be embedded in the manuscript. Figures should be supplied in either vector art formats (Illustrator, EPS, WMF, FreeHand, CorelDraw, PowerPoint, Excel, etc.) or bitmap formats (Photoshop, TIFF, GIF, JPEG, etc.). Bitmap images should be of 300 dpi resolution at least unless the resolution is intentionally set to a lower level for scientific reasons. If a bitmap image has labels, the image and labels should be embedded in separate layers.

## Preparation of Tables

Tables should be cited consecutively in the text. Every table must have a descriptive title and if numerical measurements are given, the units should be included in the column heading. Vertical rules should not be used.

## Copyright

# ARO Reviewer/Associate Editor Application Form

ARO is a scientific journal of Koya University (p-ISSN: 2410-9355, e-ISSN: 2307-549X) which aims to offer a novel contribution to the study of Science. The purpose of ARO is twofold: first, it will aim to become an ongoing forum for debate and discussion across the sciences and Engineering. We hope to advance our problem solving capacity and deepen our knowledge regarding a comprehensive range of collective actions. Second, ARO accepts the challenges brought about by multidisciplinary scientific areas and aspires to expand the community of academics who are able to learn from and help to produce advances in a variety of different disciplines.

The Journal is seeking reviewers who can provide constructive analysis of papers thus enhancing overall reputation of the Journal. If any expert is interested in participating of the review process, we highly encourage you to sign up as a reviewer for our Journal and help us improve our presence in domain of your expertise. Appropriate selection of reviewers who have expertise and interest in the domain relevant to each manuscript are essential elements that ensure a timely, productive peer review process. We require proficiency in English.

## How to apply

To apply for becoming a reviewer of ARO, please submit the application form by following the link:
http://aro.koyauniversity.org/user/register
To apply for becoming a member of the Editorial Board of ARO, please submit the application form by following the link: http://aro.koyauniversity.org/pages/view/AEB

Both Associate Editor and Reviewers should specify their areas of research and expertise. Applicants must have a doctorate (or an equivalent degree), and if Master degree they need to have significant publishing experience. Please note that;

- You will need to write your full official name.
- Please provide an email which reflects your official name, such as nameOne.NameTwo@... , or your institute's official email.
- All data need to be written in English.

**Note:** For more information, kindly visit the following websites:

1. aro.koyauniversity.org.
2. http://libweb.anglia.ac.uk/referencing/harvard.htm.
3. http://bibword.codeplex.com/releases/view/15852.


INDEXED IN
EMERGING SOURCES CITATION INDEX
CLARIVATE ANALYTICS


PRESERVED IN
CLOCKSS


PRESERVED IN
LOCKSS


PKP
PUBLIC
KNOWLEDGE
PROJECT


DOAJ
SEAL


INDEXED IN
DOAJ


Journal
TOCs
The latest Journals Tables of Contents


ingenta


Dimensions


ZEITSCHRIFTEN
DATENBANK


SHERPA
RoMEO


scinapse


Scilit


ScienceGate


ROAD
DIRECTORY
OF OPEN ACCESS
SCHOLARLY
RESOURCES


ResearchGATE
scientific network


OAJSE


Microsoft
Academic


OCLC
WorldCat


Google
Scholar


Crossref


BASE


publons


ACADEMIA


Koya University is a young University established in 2003 and it is located in the city of Koya (Koysinjaq), short distance to the East of regional capital city of Erbil (Arbil, Hewlêr) in Kurdistan Region of Iraq. It is on the foothills of beautiful High Mountain. Its campus has been carefully laid out to embrace the beautiful mountainous nature. The Koya University has a Faculty system which enhances the interactions between similar academic fields. Today, Koya University has four Faculties: Engineering, Science and Health, Humanities and Social Sciences and Education in addition to the School of Medicine, which all consist of twenty-five scientific departments in different fields, such as Petroleum Engineering, Geotechnical Engineering, Software Engineering, Physics, Chemistry, Clinical Psychology, Social Science, Medical Microbiology and Sport Education.

ARO-The Scientific Journal of Koya University is a biannual journal of original scientific research, global news, and commentary in the areas of Science and Technology. ARO is a Peer-reviewed Open Access journal with CC BY-NC-SA 4.0 license. It provides immediate, worldwide and barrier-free access to the full text of research articles without requiring a subscription to the journal, and has no article processing charge (APC). ARO Journal seeks to publish those papers that are most influential in their fields or across fields and that will significantly advance scientific understanding. ARO Journal is a member of ROAD and Crossref agencies and has got ESCI, DOAJ seal, SHERPA/RoMEO deposit policy, and LOCKSS archiving policy.

# ARO

The Scientific Journal of Koya University

Koya University (KOU)
University Park
Danielle Mitterrand Boulevard
Koya KOY45, Kurdistan Region - Iraq

DOI: 10.14500/2307-549X p-ISSN: 2410-9355 e-ISSN: 2307-549X